Recovering Uplift Histories from Noisy Landscapes

Matthew Morris

Imperial College London

Department of Earth Science and Engineering

Supervisors: Dr. Gareth Roberts, Dr. Fred Richards & Dr. Alex Lipp

This dissertation is submitted for the degree of
Doctor of Philosophy
in Earth Sciences Research

February 2026

Abstract

The shape of modern-day topography is determined at large scales by its tectonic and erosional history. However at smaller scales, other processes—climatic or lithologic variability for instance—that can be considered as geomorphic noise, can determine landscape geometries. This presents a challenge when using topography to recover tectonic information such as uplift rate histories. In this dissertation I seek to overcome this challenge by developing an inverse modelling framework to recover uplift histories from topography generated in the presence of geomorphic noise. I first demonstrate how noise added to models of landscape evolution produces complexity at local scales and variability in geomorphic properties at larger scales. By generating ensembles of models, where noise is incorporated using strategies informed by observations of Earth's topography, I show how uncertainties in predicted landscape geometries and derived metrics can be quantified. In Chapter 3 I then expand upon the challenge of addressing complexity at local scales in the context of inverse modelling. When comparing topography using existing Euclidean approaches, small differences in noisy elevations that are initially inserted into landscape evolution simulators generate resultant landscapes with contrasting drainage planforms. These differences in local elevation hamper the recovery of tectonics from topography. Instead, I leverage techniques from Optimal Transport theory, namely the Wasserstein distance, to develop a method that 'sees through' local complexity to recover uplift rates from topography. In Chapter 4 I then demonstrate how such approaches can be used to recover uplift rate histories from noisy synthetic landscapes. Calibrated Wasserstein-based objective functions successfully recover rates of uplift that vary in space and time. Uncertainties in calculated values are quantified via a probabilistic inverse modelling framework. The success of this approach suggests that future attempts to invert real topography with appropriately calibrated models can yield meaningful information about tectonic histories on geologic timescales.

Publications arising from this dissertation

A version of Chapter 2 has been published as:

M. J. Morris and G. G. Roberts (2025). Impact of noise on landscapes and metrics generated with stream power models. *Earth Surface Dynamics* **13** (5), 1003–1038. DOI: 10.5194/esurf-13-1003-2025

Part of Chapter 3 has been published as:

M. J. Morris et al. (2023). Towards inverse modeling of landscapes using the Wasserstein Distance. *Geophysical Research Letters* **50** (14), e2023GL103880. DOI: 10.1029/2023GL103880

A version of Chapter 4 has been published as:

M. J. Morris et al. (2026). Seeing Through Geomorphic Complexity to Recover Tectonics From Topography: Inverting Landscapes for Uplift Histories Using the Wasserstein Distance. *Journal of Geophysical Research: Earth Surface* **131** (4), e2025JF008966. DOI: https://doi.org/10.1029/2025JF008966

Declaration

Declaration of Originality

I hereby declare that this dissertation, submitted for the degree of Doctor of Philosophy at Imperial College London and Associateship of the Royal School of Mines, is original research undertaken by me. Unless explicitly stated in the text, this thesis is the result of my own work.

Copyright Declaration

The copyright of this thesis rests with the author. Unless otherwise indicated, its contents are licensed under a Creative Commons Attribution-Non Commercial 4.0 International Licence (CC BY-NC). Under this licence, you may copy and redistribute the material in any medium or format. You may also create and distribute modified versions of the work. This is on the condition that: you credit the author and do not use it, or any derivative works, for a commercial purpose. When reusing or sharing this work, ensure you make the licence terms clear to others by naming the licence and linking to the licence text. Where a work has been adapted, you should indicate that the work has been changed and describe those changes. Please seek permission from the copyright holder for uses of this work that are not included in this licence or permitted under UK Copyright Law.

Acknowledgements

It has been an enormous pleasure, and, without doubt, a privilege, to explore problems that I find interesting for the past three and a half years. I am thankful to EPSRC for funding me to do so. I am extremely grateful that throughout this time I have worked with people who have supported me with advice, feedback, and guidance, all of which have helped both the work contained in this dissertation, and me. Gareth Roberts has been an outstanding supervisor from whom I could not have asked any more from. Fred Richards and Alex Lipp have both provided wonderful support and guidance as co-supervisors. I acknowledge the work of Emily Siddle, whose MSci research project I co-supervised and results of which were generated in collaboration and used to produce Figures 4.24–4.26. I am also appreciative of the high performance computing resource at Imperial that I have made use of throughout this project.

I am fortunate to have been able to see the outdoors during what has been a landscape modelling project. Thanks to Sam Mitchell for permitting me to assist him during fieldwork in Greece, and to teaching staff within ESE, in particular Alex Whittaker, for the opportunity to share my enthusiasm with undergraduates. I returned from each trip with a renewed sense of vigour and perspective that fieldwork provides.

Thanks to my peers and friends within ESE who have enriched this experience by being themselves, in particular James, Banusha, and Giulia. Thanks especially to Amy for continuing to support and encourage me. A special thanks to Eric, whose friendship has been so valuable.

Finally, the support I have felt from my family throughout this journey has been immense. I am grateful for their wisdom and love.

Contents

Abstract **3**

List of Tables **10**

List of Figures **10**

1 Introduction **15**

1.1 Overview 15

1.2 Landscape evolution modelling 19

1.3 Inverse modelling 23

1.4 Outline 25

1.4.1 Dissertation objectives and research questions 25

1.4.2 Dissertation structure 26

2 Impact of Noise on Landscapes and Metrics Generated with Stream Power Models 28

2.1 Introduction 29

2.2 Methodology 31

2.2.1 Generating synthetic landscapes 32

2.2.2 Generating noisy functions and their verification 35

2.2.3 Experimentation strategy 41

2.2.4 Identifying steady state landscapes for experimentation 45

2.2.5 Mapping noise-specific geometries of landscapes 50

2.2.6 Geomorphic metrics 52

2.3 Results 67

2.3.1 Scenario A: Noise only inserted into the initial condition 67

2.3.2 Scenario B: Quenched noise 77

2.3.3 Scenario C: Spatio-temporal noise . . . 82
2.3.4 Scenario D: Addition of un-eroded noise . . . 84
2.4 Discussion . . . 85
2.4.1 Distributions of geomorphic metrics and determinism . . . 85
2.4.2 An assumption of steady state . . . 92
2.4.3 Drainage planform variability and maximum drainage sizes . . . 93
2.4.4 Comparison to natural landscapes . . . 95
2.4.5 Limitations and recommendations . . . 96
2.5 Conclusions . . . 97

3 Introducing the Wasserstein distance as a tool for inverting landscapes 99
3.1 Introduction . . . 100
3.2 Euclidean statistics . . . 101
3.3 Wasserstein statistics: theory . . . 102
3.4 Calculating Wasserstein distances in one dimension . . . 105
3.5 Wasserstein distance in two dimensions . . . 107
3.5.1 Marginal distributions . . . 112
3.6 Exploring Wasserstein statistics with synthetic landscapes . . . 113
3.7 Conclusions . . . 118

4 Seeing through geomorphic complexity to recover tectonics from topography: Inverting landscapes for uplift histories using the Wasserstein distance 120
4.1 Introduction . . . 121
4.2 Methodology . . . 126
4.2.1 Forward model . . . 126
4.2.2 Inversion strategy . . . 130
4.2.3 Experimentation strategy . . . 136
4.2.4 Comparisons with existing approaches . . . 138
4.3 Results . . . 139
4.3.1 Experiment 1: Recovering timing of a single uplift event from landscapes with different noisy starting conditions . . . 139
4.3.2 Experiment 2: Recovering a more complex uplift history when noise is known . 140

4.3.3 Experiment 3: Recovering a complex uplift history when noisy starting conditions differ . . . 146
4.3.4 Experiment 4: Recovering a complex uplift history from a landscape with spatio-temporal changes in uplift . . . 153
4.4 Discussion . . . 155
4.4.1 Recovering tectonic information from noisy landscapes . . . 155
4.4.2 Recommendations, implications and future work . . . 161
4.5 Conclusions . . . 164

5 Discussion **168**
5.1 Summary of key findings . . . 168
5.2 Returning to the research questions . . . 170
5.3 Future work . . . 171
5.3.1 Application to observed topography . . . 171
5.3.2 Further exploration of forward model parameters . . . 174
5.3.3 Extending Optimal Transport-based objective functions . . . 174

Bibliography **175**

List of Tables

1.1 Examples of landscape evolution models 20

2.1 Maximum amplitude of noise added to initial conditions, or each time step 40

4.1 Parameter values for Neighbourhood Algorithm 138

4.2 Summary of results for Experiments 1–4 155

List of Figures

1.1 Illustration showing different processes that generate uplift 17

1.2 Schematic diagram showing the relationship between forward and inverse modelling . . 23

2.1 Introduction to geometries and power spectra of landscapes generated using the Stream Power model 34

2.2 Evolving landscapes with and without initial sink-filling 36

2.3 Landscapes without inserted noise 38

2.4 Planforms of drainage networks in landscapes without inserted noise 39

2.5 Noise functions (maps) used to generate initial conditions for landscape models 42

2.6 Verifying the distributions of noisy functions added to landscapes 43

2.7 Schematic summarising the scenarios tested and approach to extracting metrics 47

2.8 Guide to *scenarios*, *ensembles* and *models* in this study 48

2.9 Identifying steady state landscapes 50

2.10 Identifying steady state landscapes with quenched noise 52

2.11 Identifying steady state landscapes with spatio-temporal noise 54

2.12 Steady state landscapes generated with different initial conditions 54

2.13 Steady state landscapes generated with different initial conditions using a 400 × 400 km grid. 55

2.14 Landscape response time maps 56

2.15 Differences in elevations and drainage network planforms due solely to changing arrangements of initial noise 57

2.16 Variability of drainage areas due to noise 58

2.17 Variability of drainage basin areas due to noise in landscapes without initial sink-filling 58

2.18 Probability of drainage within landscapes generated by different arrangements of initial noise 59

2.19 Drainage probability maps for 'square' landscapes with no initial sink-filling 60
2.20 Probability of drainage within landscapes generated by 100 different arrangements of initial, quenched, and spatio-temporal noise 61
2.21 Spectral (two-dimensional Fourier) analysis of steady state landscapes generated with noise in the initial condition 62
2.22 Impact of assumed value of concavity index on recovery of uplift rates from chi-analyses 64
2.23 Geomorphic metrics for an example 'square' landscape generated with white noise only in the initial condition 67
2.24 Comparing geomorphic metrics from 'square' steady state landscapes initialised with red, white or blue noise 70
2.25 Geomorphic metrics for 'square' landscapes with no initial sink-filling 71
2.26 Geomorphic metrics of steady state 'escarpment' landscapes initialised with red, white or blue noise 72
2.27 Impact of noise on recovered uplift rates from $z(\chi)$ 73
2.28 Geomorphic metrics of steady state 'domal' landscapes initialised with red, white or blue noise 76
2.29 Impact of amplitude of initial red, white or blue noise on geomorphic metrics recovered from steady state 'square' landscapes 77
2.30 Impact of amplitude of initial red, white or blue noise on geomorphic metrics recovered from steady state 'square' landscapes 78
2.31 Comparison of geomorphic metrics for steady state 'square' landscapes evolving with initial or quenched noise 79
2.32 Comparison of geomorphic metrics for steady state 'square' landscapes evolving with initial or quenched zero-mean noise 80
2.33 Trade off between recovered parameters from slope-area data 82
2.34 Comparison of geomorphic metrics for 'steady state' 'square' landscapes evolving with initial or spatio-temporal noise 83
2.35 Comparison of geomorphic metrics for 'steady state' 'square' landscapes evolving with initial or spatio-temporal zero-mean noise 84
2.36 Impact of un-eroded noise on metrics: An example 86
2.37 Examples of geometries of river profiles and associated metrics in landscapes with un-eroded white noise 88

2.38 Geometries of river profiles and associated metrics generated with un-eroded red noise 89
2.39 Geometries of river profiles and associated metrics generated with un-eroded blue noise 90
2.40 Impact of noise on variance of geomorphic metrics from steady state landscapes 94

3.1 Schematic illustrating how a Wasserstein distance is calculated between two probability density functions 104
3.2 Comparison of Euclidean and Wasserstein misfit for synthetic one-dimensional functions 107
3.3 Wasserstein and Euclidean (RMS) misfit between observed (target) and theoretical (source) topographic transects 109
3.4 A simple example of calculating a Wasserstein distance for a 2D density function . . . 111
3.5 Misfit between two dimensional, $z(x, y)$, theoretical landscapes 115
3.6 Two-dimensional Wasserstein distances for synthetic landscapes 116
3.7 Inverse modelling of noisy synthetic landscapes: Euclidean and Wasserstein statistics . 118

4.1 Noisy starting conditions and their impact on landscape geometries: Generation of target 'observed' landscapes 125
4.2 Schematic summarising approach to inverting landscapes for uplift histories in the presence of noise 127
4.3 Tectonic information—landscape response times—within a fluvial landscape 131
4.4 Comparing 'observed' and theoretical landscapes with Euclidean and Wasserstein metrics 141
4.5 Constructing a Wasserstein-based objective function in one dimension to support the search for true uplift histories 142
4.6 Comparing 'observed' and theoretical domal landscapes with Euclidean and Wasserstein metrics 143
4.7 Comparing 'observed' and theoretical landscapes with Euclidean and Wasserstein metrics with different maximum amplitudes of initial noise 144
4.8 Examples of multi-dimensional Euclidean and Wasserstein-based search spaces for models with same initial noise—objective functions when uplift rate is allowed to vary in time 147
4.9 Examples of multi-dimensional Euclidean and Wasserstein-based search spaces for models with same initial noise—objective functions when uplift rate is allowed to vary in time 148

4.10 Testing Wasserstein-based parameter spaces for models with same initial noise by varying values of weighting parameters μ_1 and μ_2 149
4.11 Misfit convergence for Powell's Algorithm 150
4.12 Misfit convergence for Neighbourhood Algorithm 150
4.13 Best-fitting uplift histories recovered from inverse modelling of landscapes with initial noise conditions identical to the 'observed' landscape generated using different optimisation techniques 151
4.14 Posterior distributions of RMS misfit for Experiment 2 152
4.15 Posterior distributions of Wasserstein-based misfit for Experiment 2 153
4.16 Examples of misfit spaces (objective functions) and Neighbourhood Algorithm search for uplift rate history for models with initial conditions different to the 'observed' landscape 155
4.17 Best-fitting landscapes extracted from ensemble of inverse models with initial conditions different to 'observed' landscape: Comparison of Euclidean and Wasserstein-based approaches 156
4.18 Distribution of calculated uplift rates from ensemble of inverse models generated with Euclidean statistics and different initial noise conditions compared to true uplift rates . 157
4.19 Distribution of calculated uplift rates from ensemble of inverse models generated with different initial conditions and Wasserstein-based objective functions compared to true values 158
4.20 Recovered uplift histories from inverse modelling of river profiles 159
4.21 Inverse modelling of domal topography to recover uplift rate histories 160
4.22 Assessing sensitivity of calculated uplift rates recovered from noisy landscapes 161
4.23 Residual misfit of best-fitting models initialised under different noisy starting conditions 162
4.24 Theoretical landscapes generated with blue and white noise initial conditions 164
4.25 Theoretical landscapes generated with pink and red noise initial conditions 165
4.26 Uplift histories recovered from landscapes with different colours (distributions) of initial noise 166

Chapter 1

Introduction

1.1 Overview

Understanding where, when, and how Earth's surface has grown and decayed throughout geologic time has been of interest to geomorphologists for more than a century and remains of concern to date, not least because the constraints provided by histories of topographic evolution are relevant for understanding a variety of geological, biological, and environmental processes. For instance, the uplift of mountains and the erosion of their mass into sedimentary basins can influence the distribution of natural resources and hazards (e.g., Kirby et al., 2008; Hadler Boggiani et al., 2025; Zwaan et al., 2025), constrain patterns and rates of mantle convection (e.g., Champion et al., 2008; Hoggard et al., 2020; Stephenson et al., 2024), generate climatic, atmospheric, and biologic feedbacks (e.g., Barnosky and Carrasco, 2002; Kitoh, 2004; Finarelli and Badgley, 2010; Stokes and Perron, 2020), and influence glacio-eustasy (e.g., Chappell, 1974; Simms et al., 2016; Mitrovica et al., 2020; Thompson et al., 2025).

Figure 1.1 illustrates several possible mechanisms that may drive uplift at Earth's surface. For instance, orogenesis, driven by tectonic plate convergence, leads to crustal thickening and generates high topography such as the Himalaya or Andes. Such orogenic loads can produce flexural basins in their proximity, but generate flexural uplift at the forebulge more distally (Turcotte and Schubert, 2014). Excess positive temperatures within the convecting asthenospheric mantle can also drive transient topographic uplift, often termed dynamic support. Finally, changes in base level driven by normal faulting or glacio-eustasy can driven relative uplift, or lead to isostatic uplift due to erosional unloading. However, recovering information about surface uplift on geologic timescales is challenging for several reasons. A primary concern is the removal of useful topographic information due to erosion,

thus limiting the temporal extent of recovered uplift histories. A secondary and related concern is how surface processes, including erosive ones, operate to sculpt topography in ways that can bear little or no relation to tectonic processes that drive topographic growth. For example, the roles of biotic, climatic, and lithologic variability, as well as internal hydraulics, have been shown to influence landscape evolution across a variety of scales (seconds to millions of years, < 1 m to continents, e.g., Molnar and England, 1990; Lifton and Chase, 1992; Hurst et al., 2013; Bursztyn et al., 2015; Forte et al., 2016; Gallen, 2018; Scheingross et al., 2020). The variations in elevation and topographic form that are caused by such processes might be considered as 'noise', for two reasons. First, due to their difference in scale relative to larger scale tectonic signals, and second, due to a lack of information about their variance in space and time. Both factors hence complicate the recovery of uplift histories from topography. A challenge, therefore, is to develop methods that can 'see through' local complexity (such as differences in drainage network geometries) generated by noisy processes in order to reliably identify tectonic information.

Several families of techniques exist that seek to identify and quantify tectonic signals from topography, across the scales of interest. Arguably the least equivocal of these approaches utilises stratigraphic information, such as dated marine terraces (sub-horizontal surfaces formed at the coastline by marine erosion and deposition, bounded by sub-vertical slopes, and often occurring in stair-like sequences, on scales 10^{-1}–10^{2} km; e.g., Sahagian, 1988; Rowley et al., 2013; Fernandes and Roberts, 2020). A second family makes use of chemical information contained within rocks and sediments to derive tectonic and erosional histories (e.g., thermochronology, cosmogenic radionuclide dating, clumped isotope thermometry; Wellman and McDougall, 1974; Karlstrom et al., 2007; Harel et al., 2016; Stucky de Quay et al., 2019; Hagbi et al., 2024). A third suite of approaches utilise properties of topography likely to be sensitive to uplift, such as elevations, the geometries of fluvial networks and hill slopes, or landscape area-elevation relationships (hypsometries; e.g., Davis, 1899; King, 1953; Penck, 1953; Hack, 1960; Howard, 1994; Rosenbloom and Anderson, 1994; Kirby and Whipple, 2001). Challenges in obtaining sufficient data, uncertainties in laboratory methods, and underlying methodological assumptions with all three of these families means that, in general, a multi-faceted approach for calculating uplift histories is beneficial.

One way in which a more complete repository of surface uplift histories can be produced is by developing methods that can augment the spatial extent of existing spot measurements. A subset of the third family (i.e., those that use properties of topography) seeks to do so by inverting suites of longitudinal

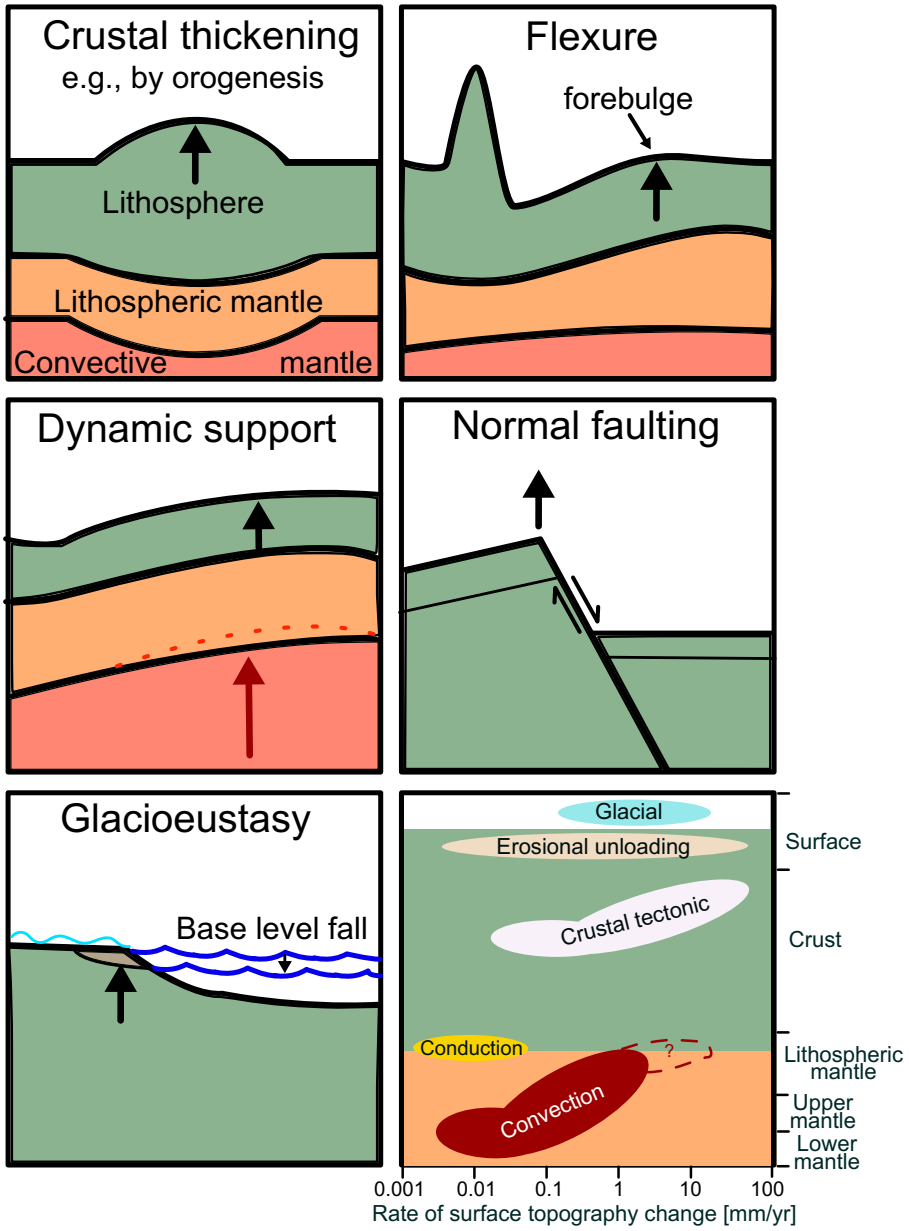


Figure 1.1: **Illustration showing different processes that generate uplift.** Top left: Isostatic uplift driven by crustal thickening, e.g., due to plate convergence. Black arrow indicates surface uplift. Top right: Uplift of forebulge as a flexural response to lithospheric loading. Middle left: Dynamic support generating surface uplift due to, for instance, an increase in the thickness of the thermal boundary layer, marked by dotted red line. Middle right: Relative uplift of footwall of a normal fault. Lower left: Relative uplift of land surface following eustatic fall. Brown filled polygon highlights potential for upstream fluvial incision. Lower right: Schematic summary of rates of surface vertical change associated with these processes, adapted from Faccenna and Becker (2020). Isostatic processes on green background, dynamic processes on orange background. Region encasing question mark highlights potential for convective processes to generate more rapid vertical changes (e.g., Hartley et al., 2011).

river profiles (elevation as a function of along-stream distance) to recover histories of uplift on regional and continental scales (e.g., Pritchard et al., 2009; Roberts and White, 2010; Barnett-Moore et al., 2014; Fox et al., 2014; Goren et al., 2014a; Glotzbach, 2015; Fernandes et al., 2019; Wang et al., 2022). The success of this technique is reliant on rates of tectonic uplift manifesting in river profiles as knickzones: perturbations of wavelengths $O(10^1–10^3)$ km and amplitudes $O(10^2–10^3)$ m for instance, from equilibrium concave-up states (e.g., Tanner, 1971). However, underlying assumptions involving the stability of drainage network planforms and the role of non-fluvial erosion may limit the applicability of these methods to regions where fluvial erosion in long-lived channel networks sets the landscape form. For instance, assumptions of planform stability are challenging to justify in regions where topography has laterally advected (such as via transverse faulting), but also potentially given evidence that drainage networks remain dynamic, with drainage capture causing rapid changes in upstream drainage area, throughout their lifetime (e.g., Willett et al., 2014; Beeson et al., 2017; Hoskins et al., 2023; Gelwick et al., 2024). Inverse modelling of entire landscapes (not just their fluvial networks) for their uplift histories has sought to overcome these assumptions (e.g., Croissant and Braun, 2014; Barnhart et al., 2020d; O'Malley et al., 2021). However, previous studies comparing observed and theoretical landscapes have used Euclidean-based statistics (such as root-mean-square calculations) that inherently struggle to 'see through' local (e.g., pixel-wise) differences in elevation that may be caused by noisy surface processes. Thus, alternative approaches for comparing entire landscapes that can capture a more global perception of differences are required.

The primary goal of this dissertation is to develop a method for inverting noisy topography—topography generated when the uplift and erosive processes governing its evolution are noisy—to recover histories of uplift on regional to continental scales and million year timescales. I do so by making use of numerical models of landscape evolution. The justification for using landscape simulators over, for instance, analogue models, lies in the flexibility with which they can represent a range of tectonic and surface processes, and the speed with which they can represent geologic timescales. Initially, the role of noise in landscape evolution is assessed by representing noisy surface processes within landscape evolution models by their spectral characteristics, and examining the variability in geomorphic properties of ensembles of simulated landscapes that arises from noise. I then demonstrate the challenges that arise when noise is added to landscape evolution models when seeking to invert a landscape for its uplift history. I explore ways in which the presence of noise can be overcome through a series of landscape evolution model-based experiments that build in their complexity. Finally, I develop and test a probabilistic inverse modelling framework. I demonstrate how it recovers the uplift histories of

synthetic landscapes when noise is present. The methodology developed in this dissertation extends previous approaches to invert topographic features for their tectonic signals and makes such approaches applicable to larger portions of Earth's surface, in particular those with evidence of channel migration throughout their lifetime. In the remainder of this chapter I provide context on landscape evolution modelling and inverse modelling, before describing the research questions addressed in this dissertation and its structure.

1.2 Landscape evolution modelling

Hypotheses that relate modern-day landscape form to its geologic and geomorphologic evolution have benefitted from qualitative observations made since at least the late 19th century (e.g., Gilbert, 1877; Davis, 1899; Powell, 1964). In more recent decades, theories of landscape evolution have benefitted from application of quantitative techniques and then in conjunction, the advancement of computational power (e.g., Howard, 1994; Coulthard, 2001; Salles et al., 2020). A combination of these two factors laid the foundation for the use of computer-based numerical models of landscape evolution.

Landscape evolution models (LEMs) rely on the concept that many processes governing landscape evolution can be described by conservative transport laws and thus represented as mathematical equations. One reason why it is convenient to do so is to reduce the number of variables used to describe how a landscape evolves. Therefore these equations often represent simplifications of the natural environment. Such simplification expedites the calculation of changes in landscapes through space and time through analytical or numerical techniques. Fundamentally, LEMs are designed to simulate the evolution of geomorphic systems (e.g., rivers, soils, hillslopes, etc.) forwards in time. In general, forward models seek to predict data arising from some cause(s). Various types of LEM exist, typically differing in their scale (either in space or time), the geomorphic processes that they describe (fluvial, non-fluvial, atmospheric, etc), or computational implementation (implicit versus explicit methods, gridding choices, etc). A list of examples, which is by no means exhaustive, is given in Table 1.1.

In general, the temporal and spatial evolution of landscapes can be described by their uplift and erosion, such that

$$\frac{\partial z}{\partial t} = E(x, y, t) + U(x, y, t) \tag{1.1}$$

where z is elevation (e.g., above sea level), t is time, E is erosion rate, and U is uplift rate. x and y are spatial coordinates. In tectonically active regions landscape form is often driven by fluvial erosion where

Model Name	Example Reference	Description and Key Feature
SIBERIA	Willgoose et al. (1991a)	Simulates transport-limited fluvial erosion on long timescales
CASCADE	Braun and Sambridge (1997)	Stream power-based erosion and landscape evolution using irregularly discretised (non-raster) grids
CHILD	Tucker et al. (2001)	Channel-based approach with stochastic rainfall component and sediment transport
CAESAR-Lisflood	Coulthard et al. (2013)	Channel-scale landscape evolution coupled to a hydrodynamic model
TTLEM	Campforts et al. (2017)	Stream power-based landscape evolution that minimises numerical diffusion
SPACE	Shobe et al. (2017)	Combines detachment-limited and transport-limited fluvial erosion
HyLands	Campforts et al. (2020a)	Landslide-focused evolution on decadal to centennial timescales
GoSPL	Salles et al. (2020)	Global scale implementation of stream power model
FastScape-LEM	Bovy (2021)	Implicit implementation of stream power model
CHONK	Gailleton et al. (2024)	Cellular automaton and graph theory approach to large-scale landscape evolution

Table 1.1: **Examples of landscape evolution models.**

its rate is set by how efficiently bedrock can be eroded (sometimes referred to as 'detachment-limited'; Howard, 1994). In transport-limited fluvial settings, or non-fluvial regions such as hill slopes, erosion is often represented by a diffusive component (Culling, 1960; Rosenbloom and Anderson, 1994; Sklar and Dietrich, 1998). Therefore, erosion rate E in Equation 1.1 is often described with an advective and a diffusive component

$$E(x, y, t) = -vA(x, y)^m \nabla z^n + \kappa \nabla^2 z, \tag{1.2}$$

where v, m, n and κ are erosional constants that can sometimes be calibrated using independent information and A is upstream drainage area (the catchment encompassing all water feeding to that location). The first term on the right-hand-side of Equation 1.2 is commonly known as the stream power model (e.g., Howard and Kerby, 1983; Howard, 1994; Whipple and Tucker, 1999). The second term is the diffusive component, in this case scaled linearly by the term κ, representing diffusivity.

Several computational packages exist that implement Equations 1.1 and 1.2 on the regional to continental spatial scales and the geological timescales that are relevant for this dissertation ($O(10^6 - 10^8$ yr) . Two examples of popular packages currently used within the geomorphic community are Basin and Landscape Dynamics (Badlands; Salles, 2016; Salles and Hardiman, 2016), and Landlab (Hobley et al., 2017). In this dissertation I generate stream power-based LEMs using Landlab, due to its open source nature, extensive documentation, and flexibility in available model components.

Simulating landscape evolution within the Landlab framework, or indeed other simulation frameworks, also requires additional model choices by the user. Often a first step is determining the type of grid to be used. Landlab enables raster, hexagonal, or Voronoi-Delaunay irregular grid types to be used. Whilst unstructured and irregular grids have been used in some landscape simulators (e.g., Braun and Sambridge, 1997; Tucker et al., 2001; Salles, 2019), the numerical models that I create in Chapters 2–4 utilise a raster grid with square grid cells. I choose this grid type for its simple structure and for its compatibility with other components of the landscape evolution models that I generate (e.g., sink-filling, flow-routing).

As a landscape simulation proceeds, artificial water is fluxed across the domain in a process known as flow-routing. The aim of the calculations that perform this task is to route continuous pathways from high elevations to open (flux-permitting) boundaries. Several options exist how to perform this calculation, that can be generally categorised as single flow direction (SFD) methods (e.g., O'Callaghan and Mark, 1984) or multiple flow direction (MFD) methods (e.g., Quinn et al., 1991; Tarboton, 1997; Seibert and McGlynn, 2007). MFD approaches permit packages of water to be split from a single upstream grid pixel across two or more downstream grid pixels. However they are more computationally expensive than SFD approaches, which do not permit such splitting. For this reason I adopt a single flow direction method of flow routing. I choose the 'D8' method, which permits water to flow into the grid pixel with the steepest gradient of its eight (four cardinal, four diagonal) neighbours (O'Callaghan and Mark, 1984). I note that both SFD and MFD approaches have been shown to have limitations that can impact interpretations from natural or synthetic landscapes (see e.g., Shelef and Hilley, 2013; Prescott et al., 2025).

The models generated in Chapters 2–4 evolve with both stream power-based (advective) and diffusive erosion, following Equation 1.2. Both processes are typically considered to shape natural topography, for instance certain sediment transport processes such as soil creep (e.g., due to bioturbation) are often assumed to be linearly diffusive (e.g., Fernandes and Dietrich, 1997). However it has been previously shown that combining the stream power model with a linear diffusion equation in a numerical landscape evolution model can produce problems with scale and the form of longitudinal river profiles (see e.g., Howard, 1994; Perron et al., 2008; Hergarten, 2020; Hergarten and Pietrek, 2023; Litwin et al., 2025). As Hergarten (2020) explains, a scale dependence exists in models where rivers have a width of one grid pixel. If the same river network were to exist on grids of different resolution, the network on the finer resolution grid would have a lower overall proportion of drainage area than that of the coarser

grid. If diffusively eroded material enters the river from adjacent grid cells, the erosion rate required to balance the additional uplift rate is higher, thus river channels steepen in a way which depends on grid scale, and deviates from analytical solutions. This is compounded in cases where diffusively eroded material enters rivers from non-fluvial regions and is not explicitly treated as separate (for instance, it has the same erodibility as river bedrock). Whilst there exist numerical models which are capable of making this distinction (e.g., SPACE; Shobe et al., 2017; Yuan et al., 2019a), I circumvent this issue by either forbidding deposition of diffusively eroded material, or using a diffusivity coefficient, κ, of zero. The former approach is akin to sediment from hillslopes leaving the model domain within one model timestep, and limits most of the capacity for diffusive processes to limit advective fluvial processes, a choice which is probably appropriate at scales larger than individual catchments (O'Malley et al., 2021; Litwin et al., 2025). I note that coupling the stream power model to a diffusion equation is incorporated in previous studies (e.g., Campforts et al., 2017; O'Malley et al., 2021).

Forward models of landscape evolution have been applied across a range of tectonic settings and timescales to identify uplift and erosional conditions. For example, Kooi and Beaumont (1994) explored the evolution of a topographic escarpment, analogous to a scenario of continental rifting. Landscape models have also been used to understand the evolution of convergent tectonic settings (e.g., Koons, 1989; Beaumont et al., 1992). The role of mantle convection in generating transient topographic swells (dynamic topography) has been explored (e.g., Braun et al., 2013; Ruetenik et al., 2016). Some forward modelling approaches have coupled landscape evolution models with mantle convection models (e.g., Bahadori et al., 2022; Neuharth et al., 2022; Yuan et al., 2024), though the concept of coupling surface and geodynamic processes dates more than a century (Ransome, 1896; Moretti and Turcotte, 1985; Stephenson and Lambeck, 1985; Molnar and England, 1990). However, as forward models become increasingly complicated (for instance by incorporating a greater number of parameters or being coupled to other models), it becomes harder to distinguish the respective contributions of each parameter. Often, adding model complexity is done at the expense of, even to the point of rendering it prohibitively expensive or unfeasible, investigating the assumptions and choices made in existing models (e.g., numerical formulation, gridding, initial and boundary conditions). Such validations themselves can become extensive (e.g., Barnhart et al., 2020b,d,e; Gasparini et al., 2024).

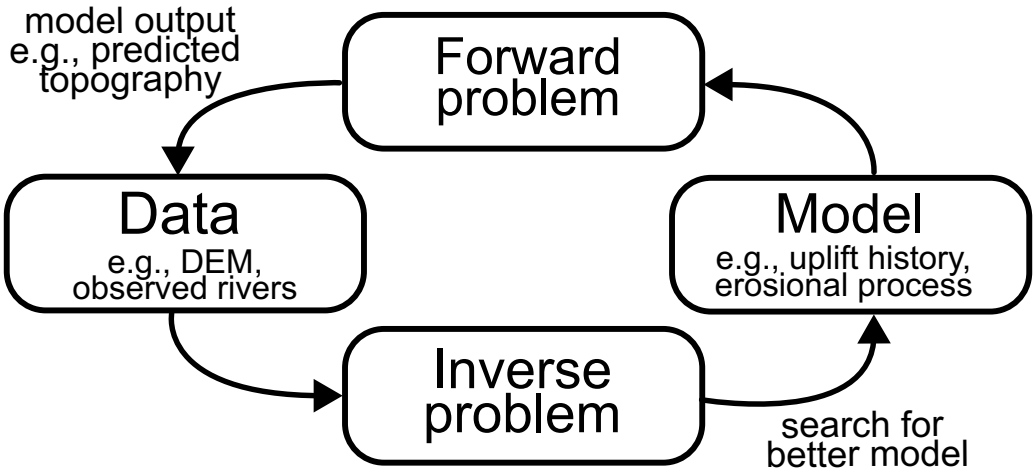


Figure 1.2: **Schematic diagram showing the relationship between forward and inverse modelling.** Observations are used for the inverse problem to hypothesise a model, that when run in a forward sense, generates predictions that can be quantitatively compared to observed data.

1.3 Inverse modelling

In contrast to forward modelling approaches, inverse methods seek to infer the causes of observed data (e.g., Figure 1.2). A well-known example of an inverse problem is X-ray computed tomography (CT), which infers the internal structure of an object (such as a human) from the attenuation of X-rays (Kaplan et al., 1969; Hunt, 1970). In general, inverse approaches are attractive because they seek to reproduce observations, and can tell us things about the Earth, for instance, that cannot be directly measured (such as its internal structure, or histories of topographic evolution; e.g., Bullard et al., 1965; Backus and Gilbert, 1967; Worthington et al., 1974; van der Beek and Braun, 1999). Some inverse problems have linear or analytical solutions, which makes them generally amenable to solve. An inverse problem for which there is no obvious analytical solution (such as a stream power model and diffusion-based formulation to landscape evolution) is solved by posing a forward model that hypothesises how observed data might be explained, running (often many) iterations of the forward model where parameter values are altered between each model, and measuring differences between the observed data and model output, aiming to minimise misfit in subsequent updates of the parameters inserted into the forward model or construct a probability distribution of each model parameter.

Solving an inverse problem is not always straightforward. Two common challenges are non-uniqueness and computational expense. Consider a range of models, generated as solutions to an inverse problem, that all have equally good fits to an observed dataset. The solution is therefore non-unique (also phrased as the inverse problem being *ill-posed*, though strictly ill-posedness can also occur when solutions do not exist or are unstable; Hadamard, 1902), especially if the models are generated with parameter values

that vary considerably from each other (e.g., Backus and Gilbert, 1967; Keilis-Borok and Yanovskaja, 1967). Non-uniqueness can arise when observed data contains noise, and can be accounted for by (often subjectively) imposing additional information (e.g., prior knowledge, smoothing) on model solutions (e.g., Backus and Gilbert, 1967; Jackson, 1979). In reality, solutions to an inverse problem may not necessarily reproduce observed data in exactness, but instead within some tolerable uncertainty based on heuristics that define the degree of accuracy required of the solution. uncertainty. Quantifying uncertainties may give estimates of noise in the observed data, how well the forward model represents the true nature of the problem, and the appropriateness of any underlying assumptions. I discuss in Chapter 2 how it might be reasonable to expect landscapes to always be considered as noisy, and explicitly incorporate this view, and quantify the resultant uncertainties in the inverse model developed in Chapters 3 and 4.

Implicit within the considerations outlined above is the requirement to run many forward models. Whether or not this becomes computationally expensive is dependent on the nature of the forward model. For example, it is typically more computationally efficient to solve inverse problems that involve linear equations (such as calculating Earth's gravitational field) than those involving non-linear or partial differential equations, such as Equation 1.2. In the context of landscape evolution, this is relevant because previous work that has inverted suites of longitudinal river profiles for histories of uplift made use of a linearised approach, in part for its computational efficiency compared to a preceding non-linear approach (Pritchard et al., 2009; Roberts et al., 2012a; Fox et al., 2014; Goren et al., 2014a; Rudge et al., 2015). Forward models of landscape evolution in two-dimensions are, however, more computationally expensive, making inverse approaches more challenging. Key to overcoming this challenge is the use of optimisation algorithms—techniques that seek to efficiently identify well-fitting models, thus reducing the total number of models that need to be run during an inversion. Optimisation algorithms can broadly be classified into two categories. Global optimisation techniques seek to locate the maximum or minimum value of a function for its entire range of possible values, whereas local optimisation techniques identify local extrema (for instance, within a subset of the function). In practice, a user may wish to apply a global optimisation algorithm when information about the structure of the function that is to be minimised (or maximised) is poor, or when local extrema are known to be present. Local search algorithms may be more effective when evaluating the function in the region of the global optimum. When seeking to invert topography for its uplift history, it is highly likely that the role of noise means local minima are expected to be present. In Chapter 4 I explore the use of three different optimisation algorithms within the inverse method that I develop.

At the heart of an inverse problem is the construction of an *objective function*: a quantified way in which predictions are compared to observations. In this dissertation I compare two families of objective functions. The first family uses Euclidean statistics to compare observed and predicted elevations, in line with previous studies seeking to invert topography for histories of uplift (e.g., Croissant and Braun, 2014; Barnhart et al., 2020e; O'Malley et al., 2021; Petit et al., 2025). The second family makes use of a branch of mathematics called Optimal Transport theory, originating from Monge (1781), that seeks to identify efficient ways to move 'mass' from one location to another. A cost exists with the movement of mass, and the optimal transportation is associated with the minimal cost. To my knowledge, this is the first time that Optimal Transport theory has been applied to landscape evolution. I note that this is different from other concepts of optimality that have been applied to landscape evolution, which in general describe how drainage networks can be described as having configurations that minimise total energy dissipation. Such optimal channel networks are not discussed further in this dissertation (e.g., Rinaldo et al., 1992; Rodríguez-Iturbe et al., 1992; Ijjasz-Vasquez et al., 1993; Ijjász-Vásquez et al., 1993; Rigon et al., 1993).

1.4 Outline

1.4.1 Dissertation objectives and research questions

The primary aim of this dissertation is to develop an inverse methodology for accurately recovering histories of uplift from topography generated in the presence of noise. As explained, the major challenge in doing so lies in 'seeing through' local complexity in order to identify larger scale tectonic signals. Four research questions emerge from this challenge, which will be addressed in subsequent chapters:

1. How can naturally occurring geomorphic noise be described, characterised, and represented in landscape evolution models?

2. What are the consequences of adding noise to landscape evolution models?

3. How can topography be quantitatively compared in a way that 'sees through' local variability?

4. Can Euclidean or Wasserstein-based objective functions be used to recover uplift histories from transient noisy topography?

1.4.2 Dissertation structure

Chapter 2

Research questions 1 and 2 are addressed in this chapter. I first present a case for considering geomorphic processes that shape topography on shorter timescales than tectonic processes as noise. It is demonstrated how the spectral treatment of geomorphic noise can aid with its implementation in numerical simulations of landscape evolution. Three scenarios are presented in which noise is added to landscape simulators in different ways. For each scenario, an ensemble of models is generated in which different precise arrangements or distributions of noise are added to models. The consequences for resultant topography are examined. The work contained within this chapter has been published in Morris and Roberts (2025).

Chapter 3

Research question 3 is addressed in this chapter by exploring the use of Wasserstein statistics to compare topographies. The performance of Wasserstein-based objective functions is assessed alongside more widely used Euclidean statistics. I first introduce the Wasserstein distance, which stems from Optimal Transport theory, and illustrate its behaviour by comparing a series of analytical functions. Euclidean and Wasserstein-based objectives functions that quantitatively compare 'observed' and theoretical landscapes are then constructed. The performance of these objective functions in identifying tectonic information is tested. It is found that Wasserstein-based objective functions can recover tectonic information more effectively than Euclidean ones when landscapes have differences due to noise. Some of the work contained within this chapter has been published in Morris et al. (2023).

Chapter 4

Research question 4 is addressed in this chapter, where the methods developed in Chapter 3 are expanded upon and used to invert transient landscapes for their histories of uplift. First, the sensitivity of Euclidean and Wasserstein-based objective functions to the timing of tectonic uplift is demonstrated. I found that both approaches can identify uplift signals, even in the presence of noise. A synthetic landscape is then inverted for its uplift history where theoretical landscapes are generated using noisy initial topography that is identical to the 'observed' landscape. Three algorithms that seek to identify optimal solutions by efficiently searching model parameter space are tested. It is found that accurate uplift histories can be recovered using both Euclidean and Wasserstein-based objective functions and

a probabilistic algorithm. Finally, I demonstrate how Wasserstein-based objective functions can accurately recover tectonic information from topography when theoretical landscapes contain different noisy starting conditions to the 'observed' topography. A version of this chapter has been submitted to Journal of Geophysical Research: Earth Surface.

Chapter 5

Chapter 5 summarises the findings of the preceding chapters to critically assess whether the research questions and objectives of the dissertation have been met. The results are synthesised to outline an inverse framework that can recover tectonic information from topography. The successes and limitations of the framework are discussed, opening up directions for possible future work. Finally, I highlight the advances of this work beyond existing techniques for recovering tectonic information from topography, and the potential of this work to be applied to further portions of Earth's surface in order to constrain, for instance, locations of mineral enrichment.

Chapter 2

Impact of Noise on Landscapes and Metrics Generated with Stream Power Models

Publication Note

A version of this chapter has been published as:

> **Morris, M. J.** and G. G. Roberts (2025). 'Impact of Noise on Landscapes and Metrics Generated with Stream Power Models'. *Earth Surface Dynamics* 13, 1003–1038, DOI: 10.5194/esurf-13-1003-2025

For reproducibility purposes, code and data relevant to this chapter can be found at 10.5281/zenodo.16926470.

Abstract

The Stream Power Model (SPM) has become a cornerstone of quantitative geomorphology, widely used to predict landscape evolution including the generation, moderation, and lowering of Earth's topography, sedimentary flux and biogeochemical processes. It is well known that landscape geometries predicted by the SPM can be strongly influenced by noise. However, its impact on the uncertainties or probabilities of, for instance, drainage planform geometries and widely used metrics is poorly understood. Noise can be incorporated into SPM simulations in a variety of ways. For instance, random, low amplitude, topographic anomalies are often inserted into starting conditions to enhance the realism of calculated drainage networks. Spatio-temporal or quenched (frozen) noise also influence the trajectories of evolving landscapes. The goal of this chapter is to establish how noise impacts the probabilities of landscape geometries and the reliability of tectonic and erosional information recovered from them. A series of landscape evolution models are run in which different arrangements, distributions, and implementations of noise are added to models evolving under the same tectonic and erosional forcings

to an equilibrium state. Uncertainties that arise from incorporating different arrangements of typical (*uniform*; white) and naturalistic initial, quenched and spatio-temporal noise are quantified. I focus on three conclusions. First, tectonic rates and values of erosional-geometric parameters (e.g., concavity and steepness indices, Hack exponents) recovered via metrics-based approaches (e.g., slope-area, χ, length-area) are uncertain in the presence of noisy initial conditions. Recovered values from individual landscapes generated with the same distribution but different specific arrangement of noise are at least as uncertain as ranges attributed to, for instance, changes in aridity. In fact, even noise with amplitudes that are $< 1\%$ of cumulative uplift can cause tectonic rates to no longer be recoverable to within a factor of two of true values. These results emphasise the sensitivity of metrics that rely on calculating derivatives (e.g., slope-area, χ) to noise. Secondly, whilst noise can make landscape geometries highly uncertain (different in different simulations), the distributions of their geomorphic properties (e.g., hypsometries, channel length-area relationships, Hack exponents) appear to have well defined statistical properties (e.g., expected values and variance). Finally, I suggest that a useful way to assess the impact of noise on SPM predictions is to generate ensembles of hundreds to thousands of models in which different arrangements of the chosen distribution of noise are inserted. Doing so can provide means to quantify uncertainty in predicted geometries and derived metrics, which can be substantial.

2.1 Introduction

It is well established that processes acting to shape Earth's topography leave behind some record of their history. Therefore interrogation of surface topography can, one hopes, yield insight into how these processes operate and intertwine. Various observational and theoretical approaches exist to make such interrogations (e.g., Anderson and Anderson, 2010). One family of approaches makes use of partial differential equations (PDEs), often solved numerically, to predict evolution of topography in space and time. The Stream Power Model (SPM) is perhaps the most widely used (see e.g., Howard, 1994; Rosenbloom and Anderson, 1994; Whipple and Tucker, 1999; Tucker and Hancock, 2010; Lague, 2014; Salles, 2016; Hobley et al., 2017, and references therein). A wide variety of metric-based (e.g., slope-area or χ analyses; see Section 2.2.6, forward and inverse modelling studies utilise the SPM to derive information about uplift, erosion, climate and biogeochemical processes from real and synthetic landscapes (e.g., Howard, 1994; Whipple and Tucker, 1999; Baldwin et al., 2003; Zaprowski et al., 2005; Roberts and White, 2010; Roberts et al., 2012b; Ferrier et al., 2013; Croissant and Braun, 2014; Forte et al., 2016; Harel et al., 2016; Mitchell and Yanites, 2019; Campforts et al., 2020b; Lipp et al., 2020, 2021; Salles et al., 2023; DeLisle and Yanites, 2024). However, one complication to this endeavour is the presence of noise, which is considered in two categories.

The first category of noise, obfuscating the recovery of tectonic information, is termed as 'scientific'. This refers to things which cannot be known, such as the many areas within a landscape that have unknown or poorly understood histories, where information necessary to recover tectonic information

has been removed by erosion, for instance. This category also includes noise that can be attributed to measurement or observational uncertainties due to, for example, fluctuations or changes in landscape form that are too rapid or slow to be recorded directly (Lague, 2014; Ancey et al., 2015; Forte et al., 2016; Chen et al., 2022; Roberts and Wani, 2024).

The second category of noise considered, and the focus of this chapter, is computational. A usual strategy in landscape evolution models is for computational noise to be inserted as random elevations within a model starting condition to enable realistic drainage networks to form (see e.g., Willgoose et al., 1991b; Tucker and Slingerland, 1994; Braun and Sambridge, 1997; Smith et al., 1997; Tucker et al., 2001; Coulthard et al., 2012; Goren et al., 2014b, and references therein). Typically, initial topographic roughness is drawn from a random uniform distribution (i.e., white noise). Other types of noise have been incorporated into landscape simulations, such as those with normal distributions or generated using specific algorithms (e.g., Perlin noise; diamond square algorithm), though they are less common (Fournier et al., 1982; Perlin, 1985, 2002; Perron and Fagherazzi, 2012; Mudd et al., 2018; Etherington, 2022; Ruiz Sánchez-Oro et al., 2024). The choice of noise (e.g., its distribution) has important implications for landscape geometries, however the often assumed white noise is not necessarily representative of observed topography or processes driving landscape evolution (see e.g., Ijjász-Vásquez et al., 1992; Perron and Fagherazzi, 2012; Kwang and Parker, 2019; Wapenhans et al., 2021). Whilst specific details of palaeotopography may not be knowable, spectral analysis of modern topography provides insight into the distributions of elevations that one might wish to replicate when deciding on the distributions of noise to be used within, for instance, model starting conditions (Perron et al., 2008; Audet, 2011; Roberts et al., 2019; Wapenhans et al., 2021). It is noted that alternative approaches to generate realistic channel planforms exist outside of adding random elevations. One option is to randomise flow directions (e.g., Salles, 2016; Salles and Hardiman, 2016). However given the prevalence of adding noisy random elevations to encourage LEMs to channelise, attention is focused on the consequences of doing so in this chapter.

The presence of noise within natural and modelled landscapes is known to complicate the recovery of geomorphic information. Roberts et al. (2012a) and Smith et al. (2022) showed how solutions recovered from channel slope-upstream drainage area data become unstable when noise is added to longitudinal profiles. Castelltort and Yamato (2013) highlight how the steepness of slopes present in noisy initial conditions added to LEMs can unsatisfactorily influence the geometry of resultant drainage basins. Wapenhans et al. (2021) demonstrate that adding white noise to longitudinal river profiles extracted

from a landscape evolution model leads to changes in power spectra that increase their similarity to power spectra of observed rivers. Addition of quenched noise to landscape evolution models can have similar effects (Birnir et al., 2001; Wapenhans et al., 2021). Several studies have sought to recover erosional parameter values using SPMs by maximising the similarity of predicted topography to observed landscapes (Croissant and Braun, 2014; Barnhart et al., 2020e). It is likely that the presence of noise contributes to a range of acceptable values being recovered (Willgoose et al., 2003). Inverse approaches such as these require the construction of a misfit function to quantitatively compare observations to model predictions. However, inserted noise is known to impact drainage planforms, which can persist throughout a model run time (Ijjász-Vásquez et al., 1992; Willgoose et al., 2003; Perron and Fagherazzi, 2012; Hancock et al., 2016; Kwang and Parker, 2019). An important challenge is to generate misfit functions that are insensitive to noise so that insight into the processes that drive topographic change such as uplift can be recovered with accurate assessment of uncertainties (Willgoose et al., 2003; Morris et al., 2023).

In this chapter I seek to establish an understanding of the role of noise within landscape evolution models and its consequences for a variety of commonly used geomorphic metrics and tools. Four scenarios are designed in order to assess how different distributions of noise and the way in which they are inserted into the SPM impact the variance of basic geometric properties: elevations, planforms, hypsometry, spectral content, and fluvial information: longitudinal profiles, slope-area relationships, χ-elevation profiles, length-area relationships. The variance of erosional parameter values and uplift rates calculated from widely used metrics (slope-area, χ) is also assessed, quantifying the impact of noise on the reliability of information recovered. Given the ubiquity of assumed steady state in studies making use of the SPM, I focus on assessing the impact of noise on landscapes that are demonstrably at, or very close to, topographic steady state, which is defined here as (practically) no elevation change in any grid cell between successive model time steps, and explained further in Section 2.2.4 (Willett and Brandon, 2002).

2.2 Methodology

In this section I introduce how synthetic landscapes and noisy functions are generated. I then describe how steady state conditions are identified, and the modelling strategy used to assess the impact of noise on geomorphic metrics.

2.2.1 Generating synthetic landscapes

In this study, landscape evolution is modelled using a widely accepted grid-based framework in which a partial differential equation (PDE) governing the rate of change, and evolution, of elevations is implemented. Gridding, flow routing, and numerical PDE solver libraries that are part of the Landlab toolkit are utilised to generate synthetic landscapes (Hobley et al., 2017; Barnhart et al., 2020a; Hutton et al., 2020). The erosional model and uplift rates are defined, and noise is added, such that

$$\frac{\partial z}{\partial t} = -KA^m \nabla z^n + \kappa \nabla^2 z + U + \eta, \tag{2.1}$$

where z is elevation, t is time, and K, m, n, and κ are erosional constants. I note that this is akin to Equations 1.1, and 1.2, and is simply re-defined here for clarity. The erosional processes (first two terms on RHS of Equation 2.1) can be regarded as being a simple version of the (advective) stream power model, and erosion that, phenomenologically at least, mimics diffusion, for instance 'transport-limited' or hill-slope processes (see e.g., Howard, 1994; Rosenbloom and Anderson, 1994). For simplicity—to avoid the complexities that arise when shocks are expected or thresholds are incorporated—and to aid assessment of the impact of noise, a linear version of the stream power model is implemented, i.e., the slope exponent $n = 1$ (the n notation is included for completeness; see e.g., Pritchard et al., 2009; Lague, 2014; Roberts and Wani, 2024). Upstream drainage area, $A = A(x, y, t)$, uplift rate, $U = U(x, y, t)$, and noise, $\eta = \eta(x, y, t)$ can vary as a function of space, (x, y), and time.

Each synthetic landscape in this study is generated by the following steps (Figure 2.1). First, a uniform Cartesian (*raster*) grid with dimensions of 100 × 100 km and cell size of 1 × 1 km is generated. Elevations at the boundaries of the domain are fixed at zero (i.e., Dirichlet conditions). Each 'east', 'west', 'south' or 'north' boundary is individually set to be *open/active* (i.e., flux across it is permitted) or *closed/inactive* (i.e., flux is forbidden; see Hobley et al., 2017, for details). An initial (noisy) topography is then added to the grid. It is the choice of this initial topography, subsequent additive noise, and their consequences on resultant landscape evolution and associated metrics that are the foci of this chapter. Topographic depressions are then filled to permit continuous flowlines and minimise the chance of internally draining regions forming (Barnes et al., 2014). Erosional parameters $m = 0.5$ and $K = 10^{-3}$ /kyr. Erosional 'diffusivity' $\kappa = 100$ m^2 /kyr. Diffusion is calculated using the explicit finite-volume method within the Landlab model component `LinearDiffuser`, with deposition turned off. The advection component of erosion is calculated using the FastScape erosion scheme, and flow routing is performed with the 'D8' algorithm (O'Callaghan and Mark, 1984; Braun and Willett, 2013).

In other words, the basic modelling framework is purposefully simple and designed to honour the assumptions that underpin the calculation of many geomorphic metrics. Each synthetic landscape is evolved forwards in time for 100 Myr, with uplift, flow-routing, erosion, and diffusion taking place at each model time step. A model time step, $\Delta t = 10$ kyr, is used. This satisfies the Courant-Friedrich-Lewy (CFL) condition, defined as

$$C = \frac{u\Delta t}{\Delta x} \leq C_{max}, \tag{2.2}$$

where C is the Courant number, u is velocity (e.g., at which a signal propagates across a discretised grid), and Δx is the length interval (i.e., the cell dimension, 1 km, in this case). The time step of 10 kyr is also sufficiently large that computational runtime is reasonable, and provides numerical stability and demonstrable convergence.

Three categories of landscape configuration

Three categories of relatively simple synthetic landscapes are generated, designed to resemble widely studied natural and computational end-members: a 'block' of topography uplifted at a constant rate, escarpment evolution, and evolution of a topographic swell/dome (see e.g., Beaumont et al., 1992; Kooi and Beaumont, 1994; Tucker and Slingerland, 1994; Braun and van der Beek, 2004; Pelletier, 2007; Anderson and Anderson, 2010; Roberts and White, 2010; Braun et al., 2013; Paul et al., 2014; Hobley et al., 2017; O'Malley et al., 2021; Gasparini et al., 2024). The first category has open boundary conditions along each edge of the model domain, for all other (*core*) grid cells uplift rate is constant, $U(x, y) = 0.2$ m/kyr. This category is henceforth referred to as producing 'square' landscapes. The second category has open boundary conditions along the east and west edges of the model domain only; no flux is permitted along the north and south boundaries. Uplift is again as a 'block' with $U = 0.2$ m/kyr. This category produces 'escarpment' landscapes. The third category has open boundaries and a Gaussian uplift function, decaying from the centre of the domain towards its edges with the form

$$U(x, y) = U_{max} \exp\left\{-\left[\frac{(x - x_0)^2}{2\sigma_x^2} + \frac{(y - y_0)^2}{2\sigma_y^2}\right]\right\}, \tag{2.3}$$

where $U(x, y)$ is uplift rate, $x_0 = y_0 = 50$ km are the central coordinates of the dome, and $\sigma_x = \sigma_y = 20$ km are the standard deviations (spreads) in the x and y directions. The function is scaled by maximum uplift rate, $U_{max} = 0.2$ m /kyr. This category produces 'domal' landscapes. Examples of the 'square', 'escarpment', and 'domal' landscape are shown in Figure 2.1. This nomenclature is maintained throughout to describe the three categories of landscape configuration.

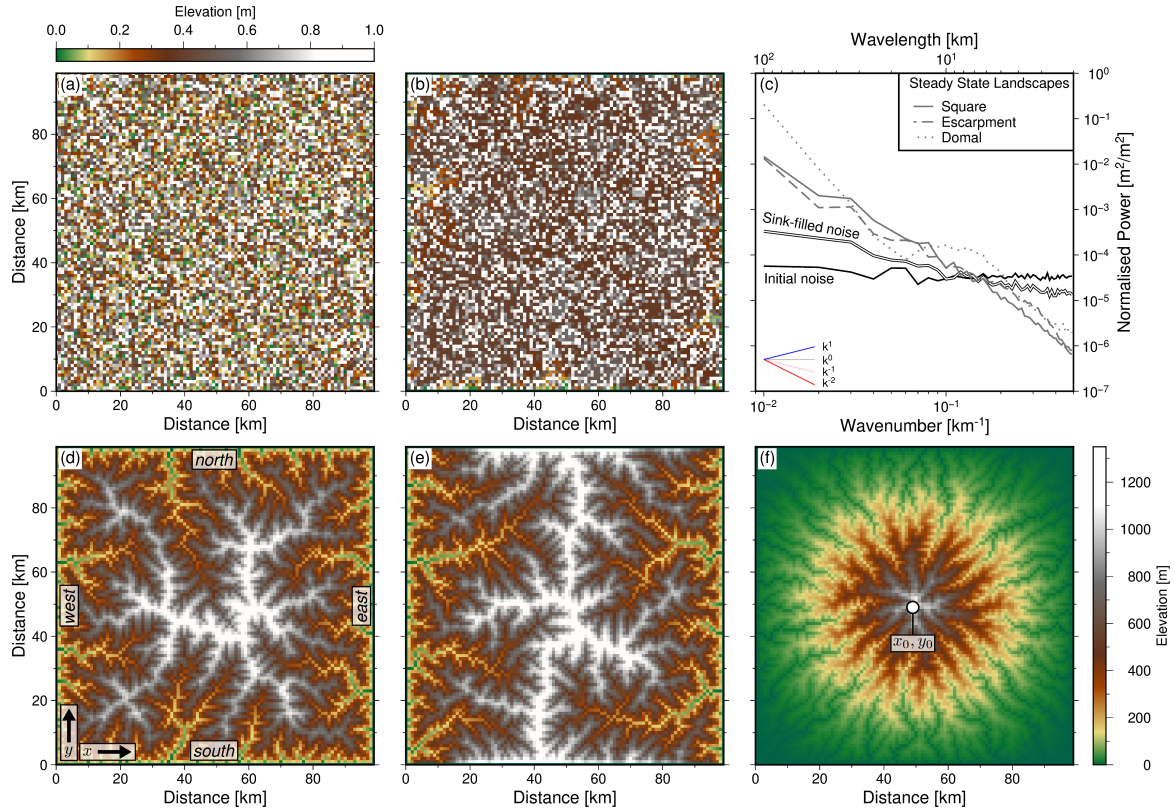


Figure 2.1: **Introduction to geometries and power spectra of landscapes generated using the Stream Power model.** (a) Initial white ('uniform') noise; typically used when parametrising landscape evolution models to ensure realistic looking drainage planforms emerge. (b) The white noise function shown in panel (a) once sinks have been filled; a standard step that seeks to ensure drainage networks are continuous. (c) Normalised power spectrum—$\phi(k)$, where ϕ is radially averaged (in the frequency domain) spectral power, and k is wavenumber, i.e., spatial frequency—of initial (panel a) and sink-filled noise (panel b), and of the three steady state landscapes shown in panels (d)–(f). Normalisation is for visual purposes only. Note graticule showing power spectral slopes of theoretical blue ($\phi \propto k$), white ($\phi \propto k^0$), pink ($\phi \propto k^{-1}$) and red ($\phi \propto k^{-2}$) noise. (d-f) Steady state landscapes generated with uplift rates that are constant in space and time, unless otherwise indicated (see body text for details). (d) 'Square' landscape generated with fixed, open, boundaries. (e) 'Escarpment' landscape with closed north and south boundaries. (f) 'Domal' landscape generated with uplift rate modulated by a (spatial) Gaussian function (see Equation 2.3).

Other Modelling Choices

Whilst the framework for initialising and running a single model is purposefully straightforward, there are choices within this model setup that have the potential to impact elements of landscape evolution, that have not been explored in major detail. Nonetheless, two choices that I have briefly explored are the grid size and the role of initial sink-filling.

The choice to use a 100 × 100 km grid, with cell size of 1 × 1 km is motivated by balancing a requirement for a large enough grid to capture scales of interest (e.g., multiple watersheds), and computation time. A single simulation at this grid size and resolution and 100 Myr of modelled time takes approximately

90 seconds to run using a desktop computer with an Intel i7-6700 CPU and 64 gigabytes of RAM. In comparison, increasing the grid size to 400 × 400 km grid, maintaining a cell size of 1 × 1 km, requires approximately 17 minutes of runtime (ensuring that the CFL stability conditions are satisfied). Given these practical considerations and the goal to develop statistical insight, experimentation using a 100 × 100 km grid is reasonable though experimentation that incorporates other scales would be valuable future work.

For a subset of the models generated in this chapter, I explore the impact of excluding the initial sink-filling step. Omitting the filling of initial sinks prevents the early formation of continuous flowlines from the interior to the exterior of the domain. Thus, regions of internal drainage are produced at early model time steps. Due to the absence of initial sink-filling, youthful drainage networks tend to be shorter than those in landscapes with filled initial sinks. A consequence of not filling sinks is that it takes longer for rivers to reach the centre of the domain (see Figure 2.2). However, after 100 Myr of evolution, there appears to be little difference between sink-filled or unfilled landscapes. The impact of sink-filling on landscape planforms, drainage basin sizes, and geomorphic metrics is shown in the Results section (Figures 2.17, 2.19 and 2.25).

2.2.2 Generating noisy functions and their verification

Introduction to noise in landscape simulators

In this section I describe how different distributions of noise can be produced and inserted into landscape evolution models. The resultant functions are used to define starting conditions and the additive noise inserted into the scenarios examined. I then demonstrate how the spectral content and characteristics, e.g., colours of noise, of such functions and of evolved landscapes can be assessed.

The impact of examining 'end-members'—red, white and blue noise—is focussed on for the following reasons. First, topography and many other natural phenomena (e.g., mantle convective support of Earth's surface, potential fields) tend to have red noise characteristics (see e.g., Bell, 1975; Rapp, 1989; Pelletier, 1999; Birnir et al., 2001; Turcotte, 2007; Singh et al., 2011; Valentine and Davies, 2020; Holdt et al., 2022, and references therein). For a landscape to have red noise characteristics it would have amplitudes of elevation that are inversely proportional to spatial frequencies, k (i.e., wavenumber), where $k = 1/\lambda$, λ is wavelength. Wavelength can be thought of as broadly synonymous with scale. In other words, as horizontal scales increase, so do vertical scales; wide features have big amplitudes, and narrow features have small amplitudes. Landscapes with red noise characteristics

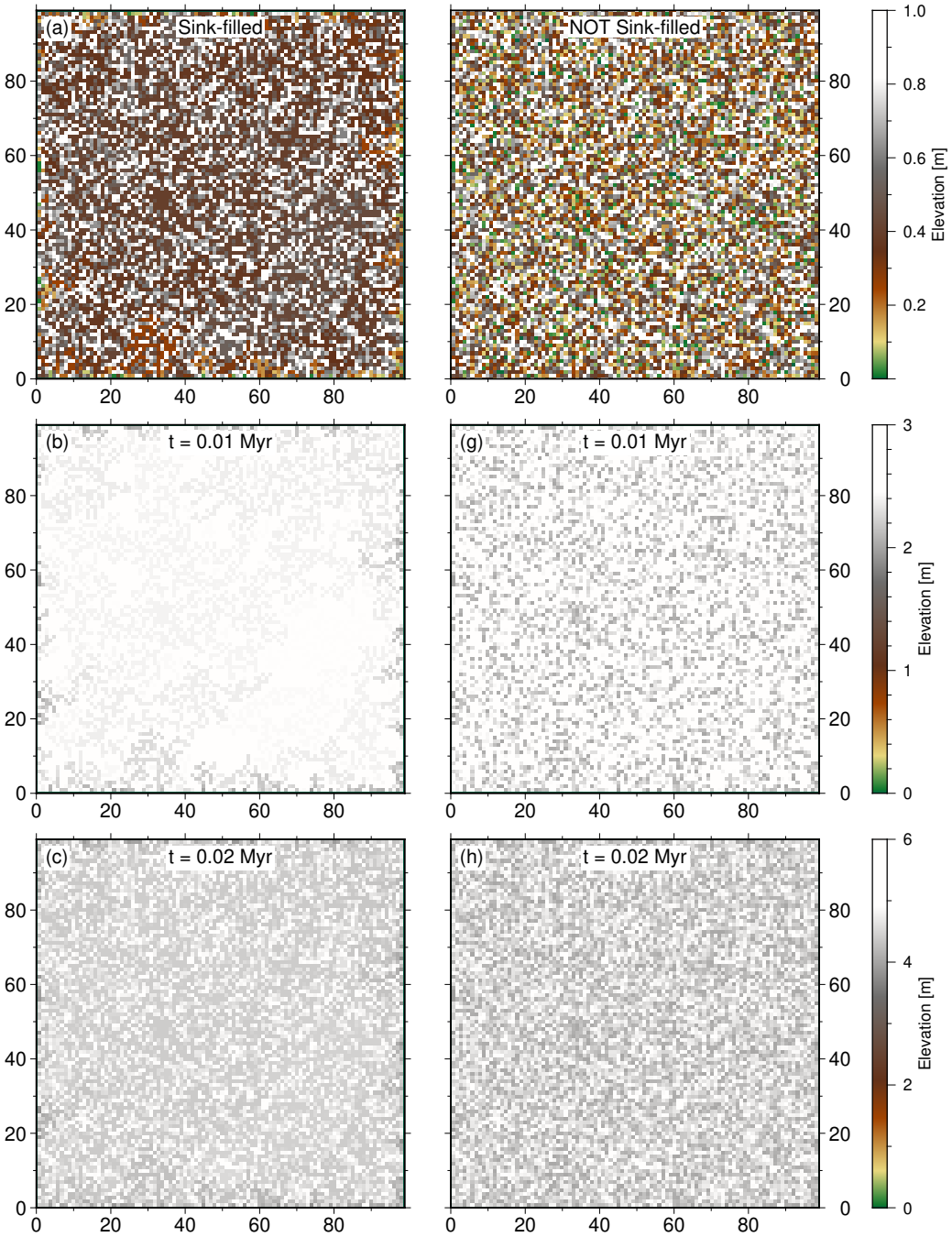


Figure 2.2: **Evolving landscapes with and without initial sink-filling.** Left column shows an initial condition which has been sink-filled, and a series of juvenile topographies. Right column shows the initial topography without sink-filling, and the resulting topographies. Note changing colour scales.

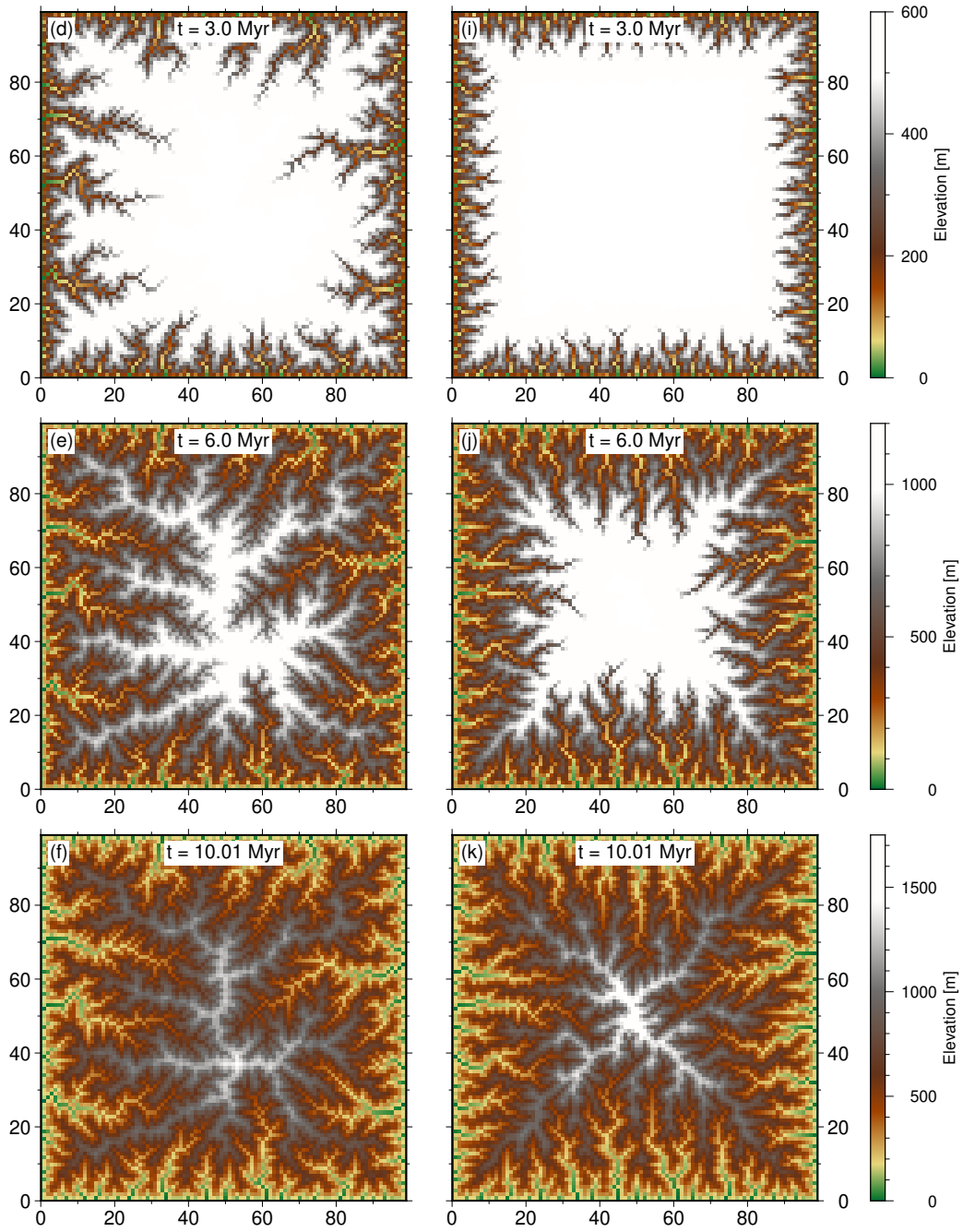


Figure 2.2: **Evolving landscapes with and without initial sink-filling.** See above caption.

have spectral power, $\phi(k)$ proportional to k^{-2}, where $\phi = Z^2$ with $Z = Z(k)$ being elevations in the frequency domain. I discuss how such signals can be identified in the following section. In contrast, white noise (amplitudes are scale-invariant; $\phi \propto k^0$), which appears to characterise some long-timescale atmospheric temperature variations and fossil records, for instance, is often assumed to be appropriate for parametrising landscape evolution models (see e.g., Ijjász-Vásquez et al., 1993; Howard, 1994; Smith et al., 1997; Kirchner and Weil, 1998; Pelletier, 1998; Yacobucci, 2005; Castelltort and Yamato, 2013; Adams et al., 2015; Gray et al., 2017; Lyons et al., 2020; Shen et al., 2021; Cullen et al., 2022). Blue

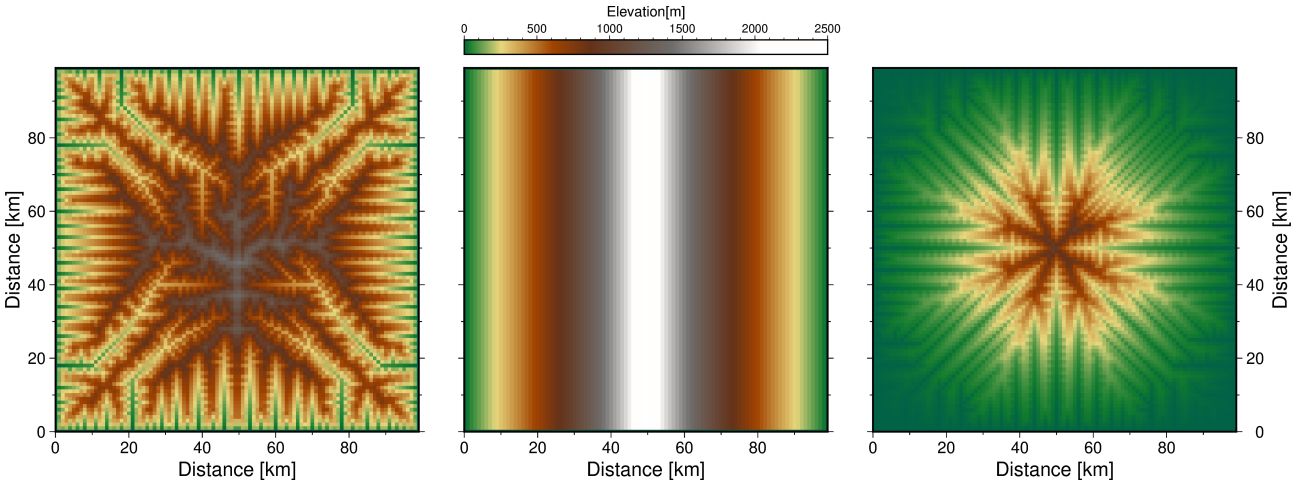


Figure 2.3: **Landscapes without inserted noise.** (a) 'Square', (b) 'escarpment' and (c) 'domal' landscapes but without added noise.

noise, which appears to be a property of (at least some) systems that exhibit shockwave behaviour (e.g., perhaps at small scales in fluvial landscapes; Wapenhans et al., 2021; Wang et al., 2022; Roberts and Wani, 2024) would indicate that landscapes have vertical amplitudes proportional to wavenumbers, i.e., narrow features have big amplitudes, wide features have small amplitudes ($\phi \propto k$).

Models with no initial noise

The inclusion of a starting topography, which is often noisy, within landscape evolution models, encourages drainage networks with realistic appearances to form. Excluding this step leads to drainage networks forming on a 'numerically flat' surface, and having unnaturally straight planforms. Figures 2.3 and 2.4 show examples of 'square', 'escarpment' and 'domal' landscapes and planform geometries generated using the same procedures and parametrisations as models containing noise, but with no inserted noise, either at the starting condition or throughout model run time.

Generating white, red and blue noise

In order to generate a two-dimensional function, $z(x, y)$, i.e., map of elevations, with a specific distribution (colour) of noise a random uniform (white noise) function of size $N_x \times N_y$ is first created, where N_x and N_y are equal to the number of cells in the x and y directions. Amplitudes are set to $0 \leq z \leq 1$ m. Such functions are straightforwardly generated using a variety of random number generators, such as Python's `numpy.random.uniform`, which is utilised. Generating white noise in this way is standard procedure in most simulations of two-dimensional landscape evolution (see e.g., Braun and Sambridge, 1997; Tucker et al., 2001; Goren et al., 2014b; Gray et al., 2017; Lyons et al., 2020; Morris et al.,

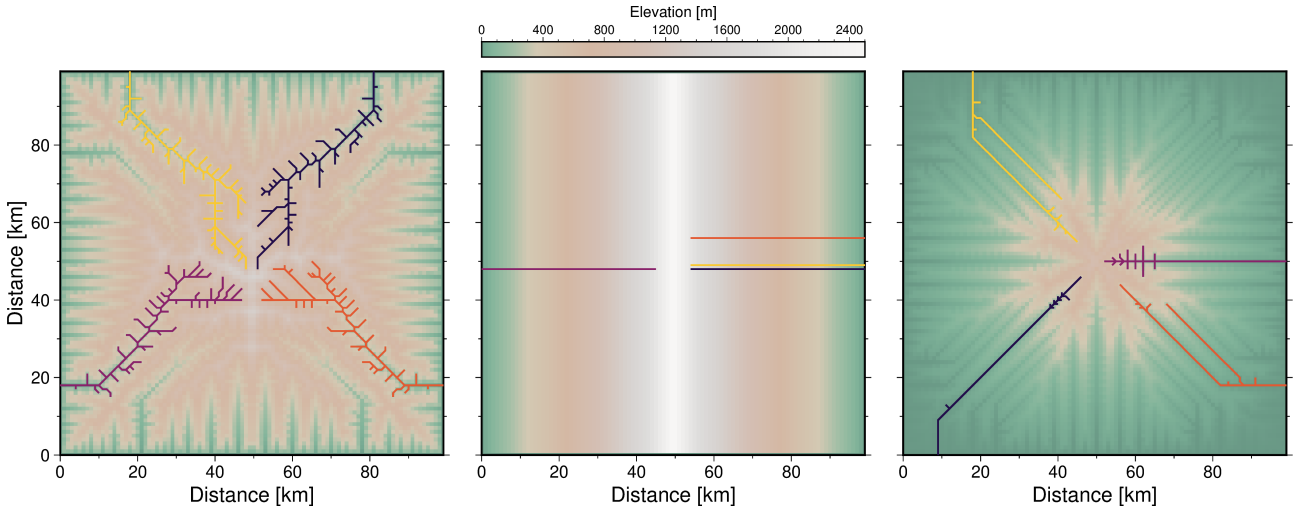


Figure 2.4: **Planforms of drainage networks in landscapes without inserted noise.** Coloured lines = four largest drainage networks within the (a) 'square', (b) 'escarpment' and (c) 'domal' landscapes shown in Figure 2.3.

2023). Many white noise functions with different specific arrangements of elevations can be generated rapidly by re-running such algorithms with different 'seed' numbers. Seed numbers are sometimes set 'under-the-hood' using, for instance, computer clock time (see e.g., Press et al., 1992, for extended discussion of random number generation). In contrast, a unique seed number for each model is defined (and recorded) in this study, ensuring reproducibility.

Maps of elevation (e.g., white noise) in the spatial domain can be converted into the frequency domain using a two-dimensional discrete Fourier transform, such that

$$Z(k_x, k_y) = \sum_{j=0}^{N_x-1} \sum_{k=0}^{N_y-1} z(x, y) e^{-2\pi i(k_x/N_x + k_y/N_y)}, \tag{2.4}$$

where k_x and k_y are the wavenumbers in the x and y directions, $i = \sqrt{-1}$, j and k are index positions in the two-dimensional $z(x, y)$ array (Cooley and Tukey, 1965; Press et al., 1992; Perron et al., 2008).

The wavenumber content of white noise functions, $Z_w(k_x, k_y)$, is used to generate other functions that have different distributions (colours of noise), $Z_\eta(k_x, y_y)$, in four steps. First, $Z_w(k_x, k_y)$ is rearranged by shifting the zero-wavenumber component to the centre of the array. Second, the array is multiplied by the square root of the radial wavenumber, $f = f(k_x, k_y)$, raised to the power p,

$$Z_\eta(k_x, k_y) = Z_w(k_x, k_y)\sqrt{(f/f^*)^p}, \tag{2.5}$$

where $f^* = 1$ /km ensures dimensionality. The radial wavenumber, f, is given by

$$f(k_x, k_y) = \sqrt{(k_x - N_x/2)^2 + (k_y - N_y/2)^2}. \tag{2.6}$$

The exponent p controls how rapidly elevations change in the wavenumber domain. When $p < 0$ longer wavelength signals have greatest amplitudes. The opposite is true when $p > 0$. Red noise, Z_r, is generated using $p = -2$, and blue noise, Z_b, with $p = 1$. White noise maps have $p = 0$. Third, the Z_η (Z_r or Z_b) array is converted from the frequency domain into the spatial domain by, first, reversing the shifting of zero-wavenumber components, and then calculating the inverse 2D discrete Fourier transform of the real components of $Z_\eta(k_x, k_y)$.

Finally, the resultant function $z_\eta(x, y)$ is normalised to ensure that elevations are between 0 and 1 m. Normalisation is achieved by adding the minimum elevation to the entire array, and dividing through by the new maximum elevation:

$$z_\eta(x, y) = \frac{|z_\eta(x, y) + z_\eta^{min}|}{z_\eta^{max}}. \tag{2.7}$$

These steps are repeated multiple times to generate M functions with red, blue or white noise characteristics (Figure 2.5). Corresponding histograms of these noisy distributions are shown in Figure 2.6. To test the impact of different amplitudes of noise, $z_\eta(x, y)$ was scaled by a factor α (see Table 2.1). Histograms of elevations for these noisy functions are shown in Figure 2.6

Max. noise [m], α	% of $U\mathrm{d}t$	% of $\int_{t=0}^{\tau} U\mathrm{d}t$
0.002	10^{-1}	10^{-5}
0.2	10	10^{-3}
2	10^2	10^{-2}
20	10^3	10^{-1}
200	10^4	1

Table 2.1: Maximum amplitude of noise added to initial conditions, or each time step as percentage of uplift rate, $U = 0.2$ m/kyr, or cumulative uplift after $\tau = 100$ Myr.

Power spectra

The noise characteristics of these functions are verified by first inserting them into Equation 2.4 and then calculating their power spectra,

$$\phi(k_x, k_y) = \frac{1}{N_x^2 N_y^2} |Z_\eta(k_x, k_y)|^2. \tag{2.8}$$

Since two-dimensional power spectra, $\phi(k_x, k_y)$, can be challenging to interpret they are usually visualised in one dimension (i.e., $\phi(k)$; see e.g., McKenzie and Bowin, 1976; McKenzie and Fairhead, 1997; Perron et al., 2008; Watts and Moore, 2017). There are two quite widely used methods. The first approach calculates mean power between specific radial frequencies (from the zero-shifted power spectrum) by averaging within annuli, in this case I average within sequential annuli of width $\delta f = 1$ km^{-1} (see e.g., McKenzie and Bowin, 1976). Figure 2.5 shows the power spectra of 100 red, white and blue noise functions generated in this way. It demonstrates that these functions have respective power spectra that on average are proportional to k^{-2}, k^0 and k, as expected.

The second approach simply collapses the two-dimensional spectra into one dimension, such that each 'pixel' $\phi(k_x, k_y)$ can be plotted as $\phi(k)$ (see e.g., Perron et al., 2008; Watts and Moore, 2017). In practice, if appropriate values of δf are chosen, the one dimensional spectra from both approaches are very similar. Collapsed power spectra of elevations are presented, following transformation $z(x, y) \rightarrow Z(k_x, k_y) \rightarrow \phi(k) = Z^2(k)$, in later figures because they demonstrate the solutions to Equation 2.8 directly. Also shown in these figures is mean power,

$$\overline{\phi(k)} = \langle \phi(k) \rangle, \tag{2.9}$$

where the angle brackets denote the average value for a wavenumber band centred on wavenumber k. Averaging is performed within logarithmically equally spaced bands. The Code statement at the beginning of this chapter explains where Python scripts to generate and verify noise maps can be found.

2.2.3 Experimentation strategy

Figures 2.7 and 2.8 summarise the approach to experimentation. The goal of this strategy is to establish the impact of noise on landscape evolution in a series of increasingly complex, and perhaps more realistic, scenarios.

In scenario A, I examine the consequences of a widely used approach—insertion of noise only into the starting condition of a landscape evolution model (see e.g., Braun and Sambridge, 1997; Tucker et al., 2001; Braun and Willett, 2013; Goren et al., 2014b; Barnhart et al., 2020a,d,e). The impact of different distributions (i.e., red, white, blue) and amplitudes of noise is examined. Each ensemble examined (e.g., *white noise, 'square' landscape*; *white noise, 'escarpment' landscape*; *white noise, 'domal' landscape*; *red noise 'square' landscape*, etc.) contains $M = 100$ or $M = 1000$ individual models. Within an ensemble, each model has the same boundary conditions, uplift function, erosional parameter values,

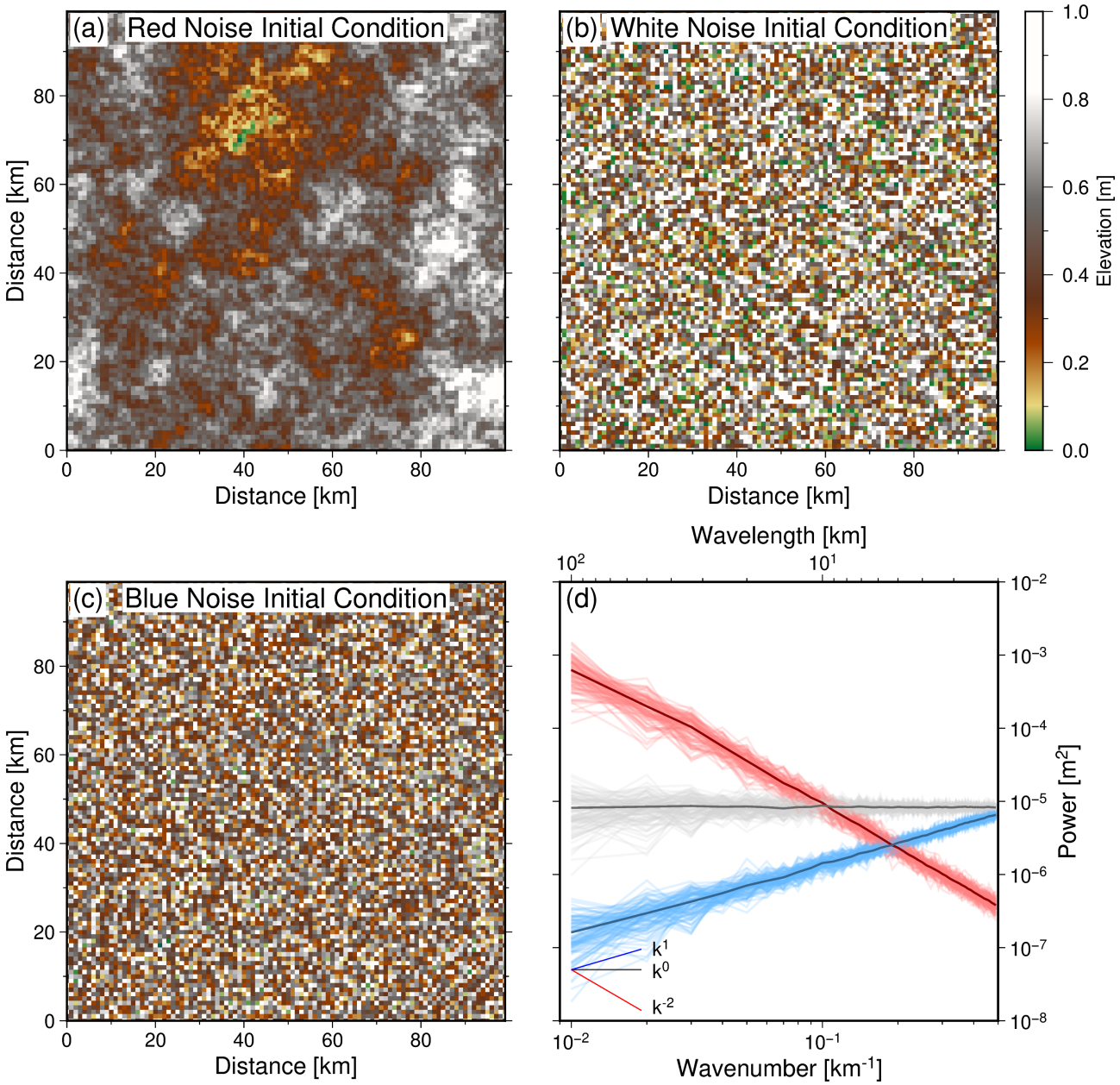


Figure 2.5: **Noise functions (maps) used to generate initial conditions for landscape models.** (a–c) Examples of functions with red, white and blue noise characteristics. (d) Thin red lines = radially averaged (in the frequency domain) power spectra, $\phi(k)$, of the 100 red noise functions used in this study (see body text for details). Thin grey and blue lines = respective power spectra of the 100 white and blue noise functions used in this study. Thick lines = average values for each suite of coloured functions. Note graticule showing theoretical spectral slopes for red ($\phi \propto k^{-2}$, where k = wavenumber), white ($\phi \propto k^0$), and blue ($\phi \propto k$) noise.

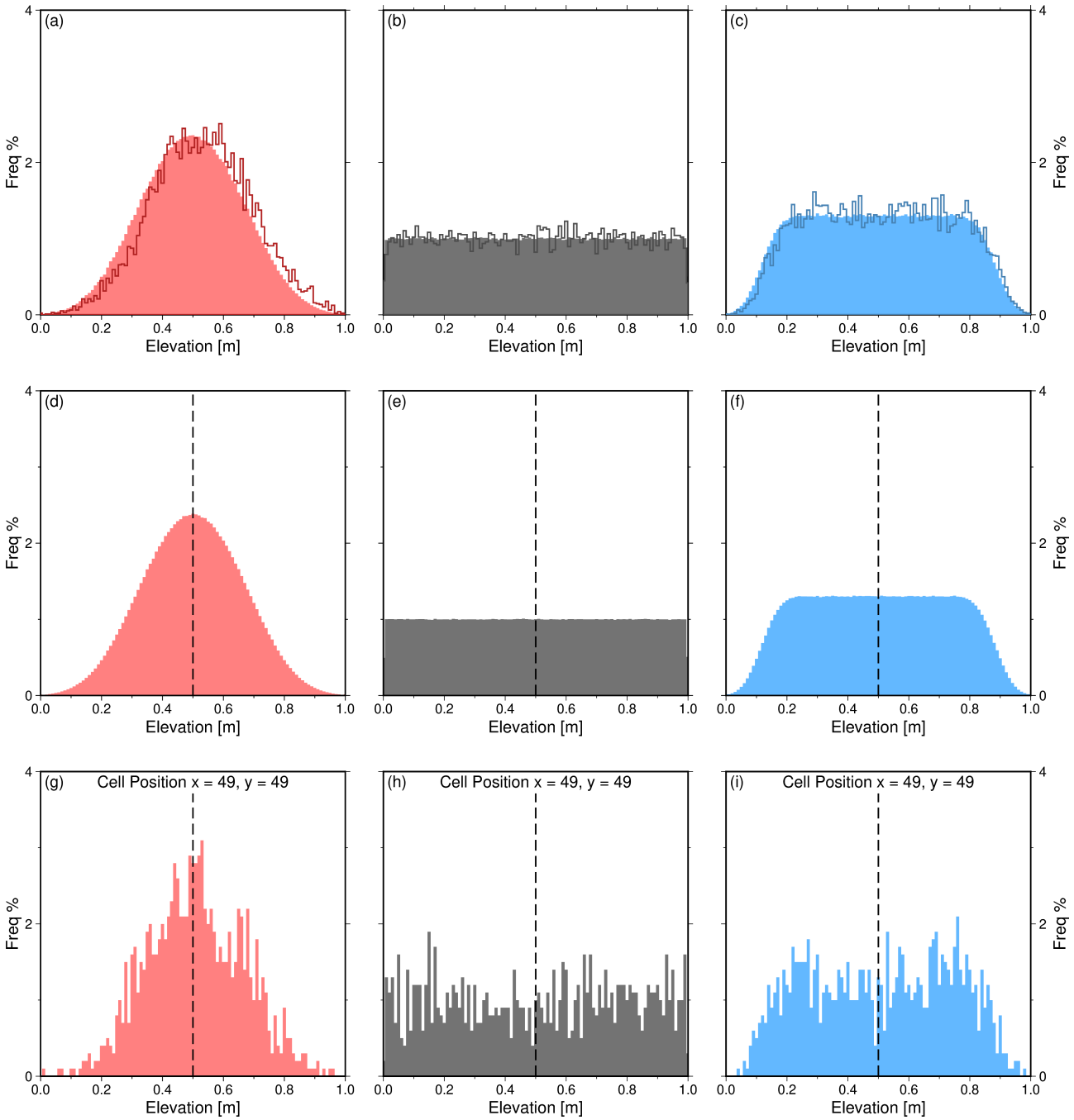


Figure 2.6: **Verifying the distributions of noisy functions added to landscapes** (a–c) Filled histograms = distributions of elevations for 100 different noisy functions of red, white, and blue noise respectively. Solid lines = distributions of elevations for a single simulation. These noisy functions are used as initial conditions in scenarios A–D, as quenched noise in scenario B, and as final noise in scenario D, where they are scaled by $\alpha = 2$, 20, and 200. (d–f) Distributions of red, white, and blue spatio-temporal noise used for a single simulation within scenario C, for all grid cells. (g–i) As above, for a single grid cell within the same simulation.

and distribution of noise, but crucially they all have different specific arrangements of noisy elevations; different 'seeds' were used to generate noise in each model. The resultant M landscape geometries were used to gain statistical insight into the impact of noise on landscape evolution, form and recovery of geomorphic metrics. Figure 2.8 summarises the ensembles tested (scenario A: ensembles 1–18).

In scenario B the impact of quenched (i.e., 'frozen') noise is tested. For an individual model, a noisy function is added to its starting condition (as in scenario A), then the exact same arrangement of noisy elevations is inserted at every subsequent time step (Figure 2.8: ensembles 19–21). A rationale for testing such a scenario arises from the work presented in Birnir et al. (2001) and Wapenhans et al. (2021), which demonstrate the need for landscape evolution models to incorporate additive noise to avoid artificial spectral reddening of landscapes, i.e., unrealistic reductions in topography at short wavelengths (small scales). Incorporating noise in this way is loosely related to modelling studies that seek to assess the impact of substrate on landscape evolution by changing erodibility (see e.g., Sklar and Dietrich, 2001; Haviv et al., 2010; Forte et al., 2016; Campforts et al., 2020b).

Scenario C again includes noise added to the starting condition. However, in contrast with scenario B, different arrangements of the same underlying distribution (colour) of noise are added to each model at every time step. In other words, noise varies as a function of space and time. Arguably, this approach is more realistic than scenarios A and B given that noisy surface processes are likely to vary spatio-temporally, and is also probably more appropriate when specific arrangements of noise are likely to be unknown. Figure 2.8 (ensembles 22–24) summarises this experimentation.

The noise added throughout models within Scenarios B and C has amplitudes of $0 - 1$ m. Incorporating additive noise is chosen for two reasons. First, to maintain consistency with the amplitude of noise added to the starting condition, and second, to avoid cases in which regions of internal drainage may arise, thus potentially requiring additional (*ad hoc*) sink-filling steps. However it is acknowledged that this may not necessarily represent noisy surface processes which act to alter topography. Instead, such processes may also reduce elevations. Whilst it is generally unclear what an appropriate mean elevation might be in order to represent these processes, an additional set of simulations are performed in the style of Scenarios B and C with noise of -0.5 to 0.5 m amplitude (i.e. mean elevation $= 0$). Results for these tests are shown in Figures 2.32 and 2.35.

Scenarios A–C have flow routing and erosion applied in their final time step, after noise has been inserted. Thus, inserted noise is eroded for 10 kyr (i.e., the length of the time step) before metrics are extracted. In actuality, noise could be inserted into a landscape at any time. Thus, I test scenario D

in which noise is inserted into synthetic landscapes at the end of model run time. The steady state landscapes (at 100 Myr) generated by scenario A with 0 – 1 m of noise are taken and noise with the same arrangement is inserted. The impact of inserting final noise with scaled maximum amplitudes of 2, 20 and 200 m is assessed (see Table 2.1). For clarity, metrics are extracted from the noisy landscapes using drainage planforms determined before final noise is added, i.e., no additional flow routing or sink filling is performed. This approach is a generalisation, to two dimensions, of that presented in Roberts et al. (2012a) and Smith et al. (2022), in which noise is added directly to the longitudinal profiles of rivers (Figure 2.8: ensembles 25–27).

2.2.4 Identifying steady state landscapes for experimentation

The assumption of topographic steady state remains widely used in quantitative studies of fluvial geomorphology (see e.g., Snyder et al., 2000; Istanbulluoglu and Bras, 2005; Attal et al., 2008; Perron and Fagherazzi, 2012; Theodoratos et al., 2018; Leonard and Whipple, 2021; Fisher et al., 2022; Clubb et al., 2023; Hoskins et al., 2023; Zhou et al., 2024). It underpins the use of a variety of geomorphic metrics used to generate quantitative estimates of erosional parameter values and uplift rates (see e.g., Wang et al., 2017). Thus, models are run until they are demonstrably at, or get as close as reasonably possible to, steady state and then examine the impact of noise on calculated metrics. A variety of criteria can be used to define steady state topography in both natural (observed) and synthetic landscapes (see e.g., Willett and Brandon, 2002; Gasparini et al., 2024, and references therein). For clarity, here steady state means $\partial z/\partial t = 0$, i.e., rate of change of elevation is invariant everywhere in the landscape due to the balancing of uplift and erosion within a single time step.

As Gasparini et al. (2024) explain, demonstrating that a synthetic landscape is at topographic steady state is not necessarily trivial; that approach is extended here. A useful attribute of landscape evolution modelling is that it is straightforward to extract and visualise distributions of topographic change over consecutive time steps, which can be used to assess topographic (in)transience. Figure 2.9 shows three statistics used to assess topographic steady state. First, following Gasparini et al. (2024), the maximum local change in elevation, Δz, are extracted across the entire model domain between consecutive time steps

$$\Delta z_{\alpha}^{t} = \max(|z_i^t - z_i^{t-\Delta t}|), \tag{2.10}$$

where i here indicates the index of all elevations ($i = 1, \ldots, N_x N_y$), and t is the index of time steps. Similarly, the change in mean elevation of the entire domain, from one time step to the next, is

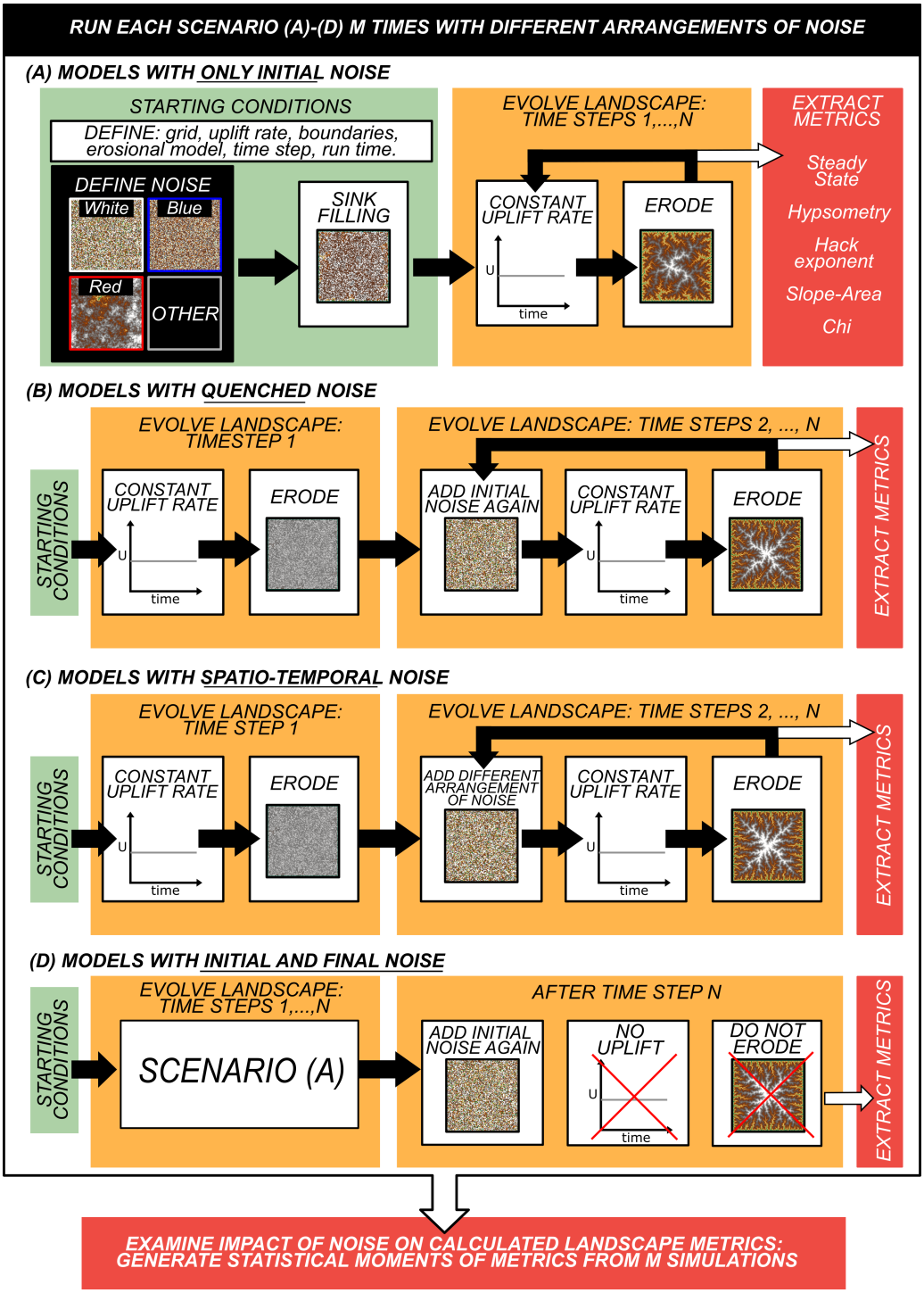

RUN EACH SCENARIO (A)-(D) M TIMES WITH DIFFERENT ARRANGEMENTS OF NOISE
(A) MODELS WITH ONLY INITIAL NOISE
STARTING CONDITIONS
DEFINE: grid, uplift rate, boundaries, erosional model, time step, run time.
DEFINE NOISE
White
Blue
Red
OTHER
SINK FILLING
EVOLVE LANDSCAPE: TIME STEPS 1,...,N
CONSTANT UPLIFT RATE
U
time
ERODE
EXTRACT METRICS
Steady State
Hypsometry
Hack exponent
Slope-Area
Chi
(B) MODELS WITH QUENCHED NOISE
STARTING CONDITIONS
EVOLVE LANDSCAPE: TIMESTEP 1
CONSTANT UPLIFT RATE
ERODE
EVOLVE LANDSCAPE: TIME STEPS 2, ..., N
ADD INITIAL NOISE AGAIN
EXTRACT METRICS
(C) MODELS WITH SPATIO-TEMPORAL NOISE
EVOLVE LANDSCAPE: TIME STEP 1
EVOLVE LANDSCAPE: TIME STEPS 2, ..., N
ADD DIFFERENT ARRANGEMENT OF NOISE
(D) MODELS WITH INITIAL AND FINAL NOISE
EVOLVE LANDSCAPE: TIME STEPS 1,...,N
SCENARIO (A)
AFTER TIME STEP N
NO UPLIFT
DO NOT ERODE
EXAMINE IMPACT OF NOISE ON CALCULATED LANDSCAPE METRICS: GENERATE STATISTICAL MOMENTS OF METRICS FROM M SIMULATIONS

Figure 2.7: **Schematic summarising the scenarios tested and approach to extracting metrics.** In scenarios A–D forward models are initialised with starting conditions that include noise (white, blue or red in this study), they are then run for a specified number of time steps, evolving to steady state. Geomorphic metrics are extracted from steady state topography. Each scenario is run multiple (M) times using different arrangements of noise to generate statistical insights and assess stability of calculated metrics. The example demonstrated here is for the 'square' landscape shown in Figure 1d. Note that I also assess the impact of changing boundary conditions and uplift function, and scenarios when no noise is explicitly incorporated. Scenario A: Noise is only incorporated into the starting condition; the quintessential landscape evolution modelling strategy. Scenario B: Noise used in the starting condition is incorporated at each time step; testing the impact of quenched, 'frozen', noise. Scenario C: Different arrangements (but same distribution) of noise are incorporated at each time step. Scenario D: Uneroded noise is added to the landscape at the end of model run time.

calculated,

$$\Delta z_{\beta}^{t} = |\overline{z^{t}} - \overline{z^{t-\Delta t}}|, \tag{2.11}$$

where $\bar{z}$ is the mean elevation of a landscape. Change in maximum elevation between consecutive time step is also extracted,

$$\Delta z_{\gamma}^{t} = |\max(z^{t}) - \max(z^{t-\Delta t})|. \tag{2.12}$$

Examples of these statistics are shown in Figure 2.9 for three landscapes generated with white noise only in their initial conditions. Figures 2.10 and 2.11 similarly show statistics for typical landscapes generated within scenarios B and C.

In addition to such statistical approaches, it is beneficial to examine how distributions of elevation change evolve as the synthetic landscapes mature. Consequently, Figure 2.9 shows histograms of topographic change between successive time steps for all cells within the three example landscapes. The histograms summarise topographic change for the individual landscapes when they are immature (time steps 0.99 $\rightarrow$ 1 Myr), juvenile (4.99 $\rightarrow$ 5 Myr), and mature (i.e., have reached steady state; 14.99 $\rightarrow$ 15, and 79.99 $\rightarrow$ 80 Myr).

It is noted that a model runtime of 100 Myr is in excess of the time required for models to reach a topographic steady state ($\partial z/\partial t = 0$; or as close to steady state as can be expected). For instance, as the histograms in Figures 2.9, 2.10 and 2.11 show, there is little change in the distribution of elevations of the models between 15 and 80 Myr. Figure 2.14 shows a map of response times for the landscapes shown in Figures 2.12a-f calculated such that $\tau = \int_{\circ}^{x} \mathrm{d}x/KA(x)^{m}$, where x is streamwise distance (also see Chapter 4, Equation 4.3). The longest response times shown are $\lesssim 7$ Myr, further emphasising that 100 Myr is beyond the time taken for fluvial parts of a landscape to reach topographic steady state.

Ensemble	Noise			Landscape Model			Figures
	Red	White	Blue	Square	Escarpment	Domal	
Scenario A: Initial Noise Only							
1		✔		✔			2.1d, 2.9a-e, 2.12b, 2.15a-b, 2.21b, 2.23, 2.24, 2.27, 2.29, 2.30, 2.40
2		✔			✔		2.1e, 2.9f-j, 2.12e, 2.15f-g, 2.21e, 2.26
3		✔				✔	2.1f, 2.9k-o, 2.12h, 2.21h, 2.28
4			✔	✔			2.12c, 2.21c, 2.24, 2.29, 2.30, 2.40
5			✔		✔		2.12f, 2.21f, 2.26
6			✔			✔	2.12i, 2.21i, 2.28
7	✔			✔			2.12a, 2.21a, 2.24, 2.29, 2.30, 2.40
8	✔				✔		2.12d, 2.21d, 2.26
9	✔					✔	2.12g, 2.21g, 2.28
10*	✔			✔			2.16a-b, 2.18a
11*		✔		✔			2.16a-b, 2.18b
12*			✔	✔			2.16a-b, 2.18c
13*	✔				✔		2.18d
14*		✔			✔		2.18e
15*			✔		✔		2.18f
16*	✔					✔	2.18g
17*		✔				✔	2.18h
18*			✔			✔	2.18i
Scenario B: Quenched Noise							
19		✔		✔			2.10, 2.20d-f, 2.31, 2.32, 2.40
20			✔	✔			2.10, 2.20d-f, 2.31, 2.32, 2.40
21	✔			✔			2.10, 2.20d-f, 2.31, 2.32, 2.40
Scenario C: Spatio-Temporal Noise							
22		✔		✔			2.11, 2.20g-i, 2.34, 2.35, 2.40
23			✔	✔			2.11, 2.20g-i, 2.34, 2.35, 2.40
24	✔			✔			2.11, 2.20g-i, 2.34, 2.35, 2.40
Scenario D: Final Noise							
25		✔		✔			2.36 - 2.40
26			✔	✔			2.36 - 2.40
27	✔			✔			2.36 - 2.40

Figure 2.8: **Guide to *scenarios*, *ensembles* and *models* in this study.** Ensembles with asterisk (*) contain $M = 1000$ models, all others contain $M = 100$ models.

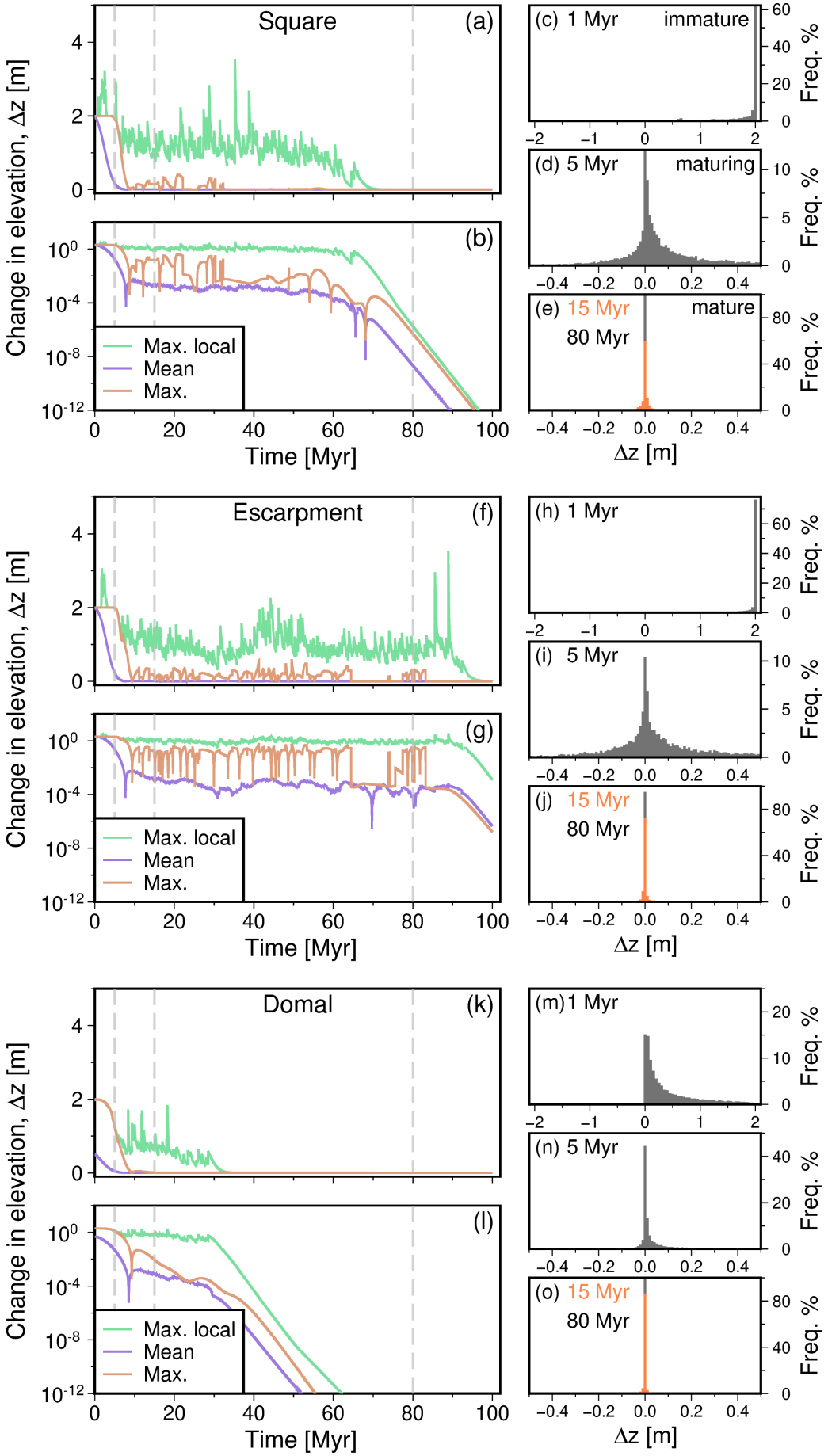

Square
(a)
(b)
(c) 1 Myr
immature
(d) 5 Myr
maturing
(e) 15 Myr
80 Myr
mature
Escarpment
(f)
(g)
(h) 1 Myr
(i) 5 Myr
(j) 15 Myr
80 Myr
Domal
(k)
(l)
(m) 1 Myr
(n) 5 Myr
(o) 15 Myr
80 Myr
Max. local
Mean
Max.
Change in elevation, Δz [m]
Time [Myr]
Δz [m]
Freq. %

Figure 2.9: **Identifying steady state landscapes**. In each of these examples, white noise is only inserted in the starting condition, see scenario A in Figure 2.7. (a) Evolution of changes in elevation between consecutive time steps ($\Delta t = 0.01$ Ma) for the 'square' landscape shown in Figure 2.1d; green = maximum change in local elevation (Δz_α); purple and orange = change in mean elevation (Δz_β) and change in maximum elevation across the entire domain (Δz_γ), respectively (see Equations 2.10–2.12). Grey dashed vertical lines correspond to histograms shown in panels (c)–(e). (b) As (a), on logarithmic scale. (c) Histogram of elevation change, Δz, for all grid cells between 0.99 and 1 Myr. (d) & (e) As per (c), from 4.99 → 5 Myr, 14.99 → 15 Myr and 79.99 → 80 Myr, respectively. (f–j) As above for 'escarpment' landscape shown in Figure 2.1e. (k–o) As above for 'domal' landscape shown in Figure 2.1f.

Response time maps for the domal landscapes are not shown here because of the spatially varying nature of uplift meaning assuming that tectonic signals propagate from the edge of the domain to fluvial headwaters is not reasonable. Nonetheless, it is useful to run the models out to 100 Myr when assessing, for example, the impact of quenched and especially spatio-temporal noise. If a user were looking to optimise computation time, however, a shorter model run time may be more appropriate.

2.2.5 Mapping noise-specific geometries of landscapes

As Kwang and Parker (2019) discuss, planforms generated in simulations with noise inserted into starting conditions tend to be 'burned' into simulated landscapes for the duration of model run time—their structure remains long-lived. This result is intuitive for models in which uplift rates tend not to vary as a function of time, or cannot outpace erosion (cf. O'Malley et al., 2021). This behaviour implies that long-lived planform geometries, at least at some scales, are specific to the distribution and particular arrangement of noise. The consequences of inserting different distributions and specific arrangements of noisy topography on the geometries of emergent landscapes, their planforms and marginals are assessed by running multiple simulations (see e.g., Figures 2.1, 2.12, 2.15).

The model ensembles are also used to assess the impact of different distributions and arrangements of noisy starting conditions on resulting drainage basin sizes. Upstream drainage area is extracted from the outlet positions of the ten largest drainage basins in each 'square' model of scenario A for 1000 simulations (ensembles 10–12). This is shown in Figure 2.16.

Establishing expectations (probabilities) of drainage network and divide geometries

Following Lipp and Roberts (2021), to develop statistical insights into the development of synthetic landscapes, 1000 simulations were run for each landscape configuration within scenario A (i.e., 'square', 'escarpment', 'domal'). The same distribution of noise, but different specific arrangements of topog-

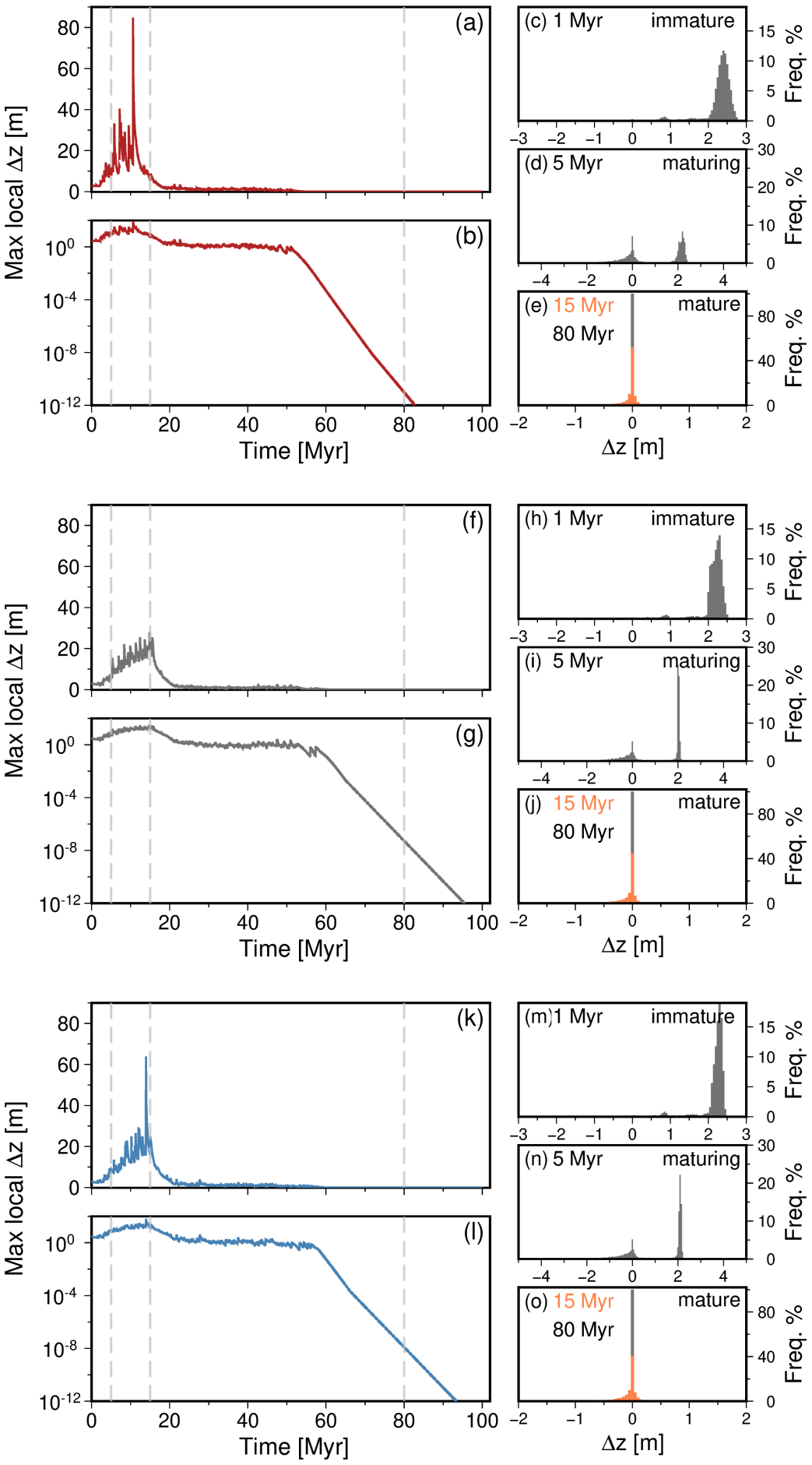

(a)
(b)
(c) 1 Myr immature
(d) 5 Myr maturing
(e) 15 Myr
80 Myr
mature
Max local Δz [m]
Time [Myr]
Δz [m]
Freq. %
(f)
(g)
(h) 1 Myr immature
(i) 5 Myr maturing
(j) 15 Myr
80 Myr
mature
(k)
(l)
(m)1 Myr immature
(n) 5 Myr maturing
(o) 15 Myr
80 Myr
mature

Figure 2.10: **Identifying steady state landscapes with quenched noise.** In each of these examples the same arrangement of red (a–e), white (f–j) or blue (k–o) noise is inserted at each time step into 'square' landscapes. See scenario B in Figure 2.7. (a) Evolution of maximum change in local elevation (Δz_α) between consecutive time steps ($\Delta t = 0.01$ Ma; see Equation 2.10). Grey dashed vertical lines correspond to histograms shown in panels (c)–(e). (c) Histogram of elevation change, Δz, for all grid cells between 0.99 and 1 Myr. (d) & (e) As per (c), from 4.99 $\rightarrow$ 5 Myr, 14.99 $\rightarrow$ 15 Myr and 79.99 $\rightarrow$ 80 Myr, respectively. (f–j) As above for white noise. (k–o) As above for blue noise.

raphy (i.e., 1000 simulations initialised with different 'seed' numbers) with amplitudes 0 to 1 m were used to define the initial conditions (model ensembles 10 – 18). To establish the propensity of cells within landscapes to host rivers, cells with upstream drainage areas $> 5 \times 10^7$ m^2 were extracted from each model. This threshold was chosen in order to exclude very small drainage networks (e.g., minor tributaries). The probability of a river being in a cell is calculated by dividing the number of times a cell met this criteria by the total number of simulations (i.e., $N/1000$), which results in a probabilistic drainage map (Figure 2.18). These maps also help to establish expected locations of drainage divides, i.e., where calculated probability is low. Similar maps are shown for 100 'square' landscapes generated by omitting the initial sink-filling step in Figure 2.19, and for scenarios B and C in Figure 2.20.

The spectral characteristics of the synthetic landscapes can be assessed by transforming them into the frequency domain using Equations 2.4 & 2.8 (see Figure 2.21). It is also straightforward to extract other geometric properties from the landscapes (e.g., longitudinal river profiles, hypsometry, channel length-area relationships) that can be directly compared or used to calculate geomorphic metrics that can be compared in turn (Figure 2.23).

2.2.6 Geomorphic metrics

I now examine the impact of noise on a number of widely used geomorphic metrics. The metrics extracted from landscapes in this chapter include: concavity indices, erosional parameter values and uplift rates from slope-area and χ (chi) analyses. In most landscape evolution models the typical order of a single time step, which is followed here, is add noise (if desired) $\rightarrow$ uplift $\rightarrow$ flow routing $\rightarrow$ erode. For efficiency, slopes and drainage areas are calculated as part of the flow routing step. However, an obvious issue is that metrics calculated for steady state landscapes are sought, which requires knowledge of landscape geometries once erosion has been performed. Therefore, just prior to extracting metrics (i.e., at time step $N = 100$ Myr) a single additional flow routing step is run.

Hack exponents are calculated from channel lengths and basin areas. Hypsometry is calculated using elevations and cell areas. Longitudinal river profiles are extracted from the synthetic landscapes using a

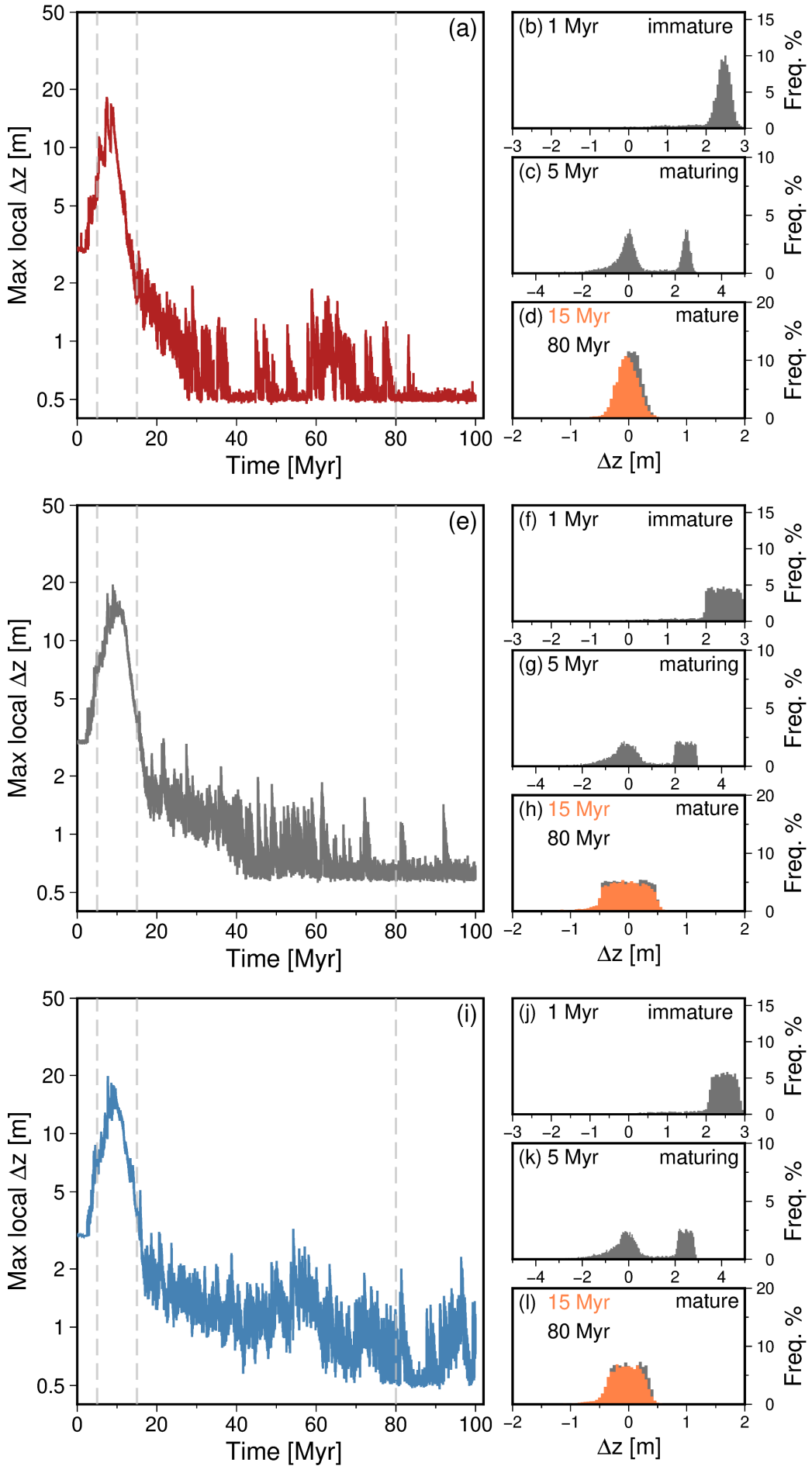

(a)
Max local Δz [m]
Time [Myr]
(b) 1 Myr immature
(c) 5 Myr maturing
(d) 15 Myr mature
80 Myr
Δz [m]
Freq. %
(e)
(f) 1 Myr immature
(g) 5 Myr maturing
(h) 15 Myr mature
80 Myr
(i)
(j) 1 Myr immature
(k) 5 Myr maturing
(l) 15 Myr mature
80 Myr

Figure 2.11: **Identifying steady state landscapes with spatio-temporal noise (scenario C).** In each of these examples the same distribution but different arrangements of red (a–d), white (e–h) or blue (i–l) noise is inserted at each time step into 'square' landscapes. See Figure 2.10 for extended description.

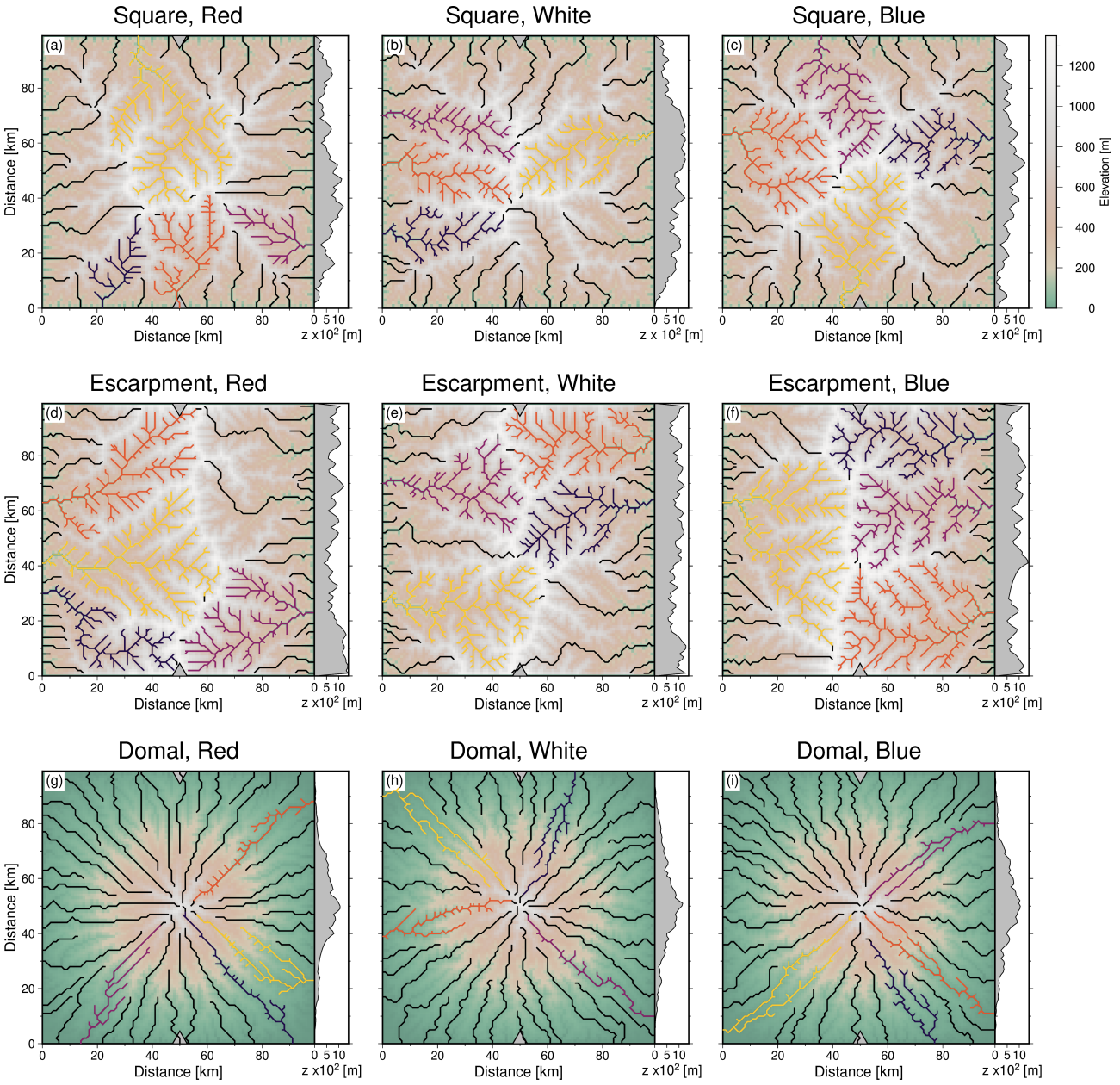


Figure 2.12: **Steady state landscapes generated with different initial conditions.** (a–c) Steady state 'square' landscapes generated with red, white and blue initial conditions, respectively. Planforms of channels in the four largest drainage networks in each landscape are emphasised by the coloured lines. Main (longest) channels of 40 largest basins shown in black lines, plus the four longest coloured lines. Adjacent topographic transects are between grey triangles at $x = 50$ km. (d–f) As above, for 'escarpment' landscapes. (g–i) As above, for 'domal' landscapes.

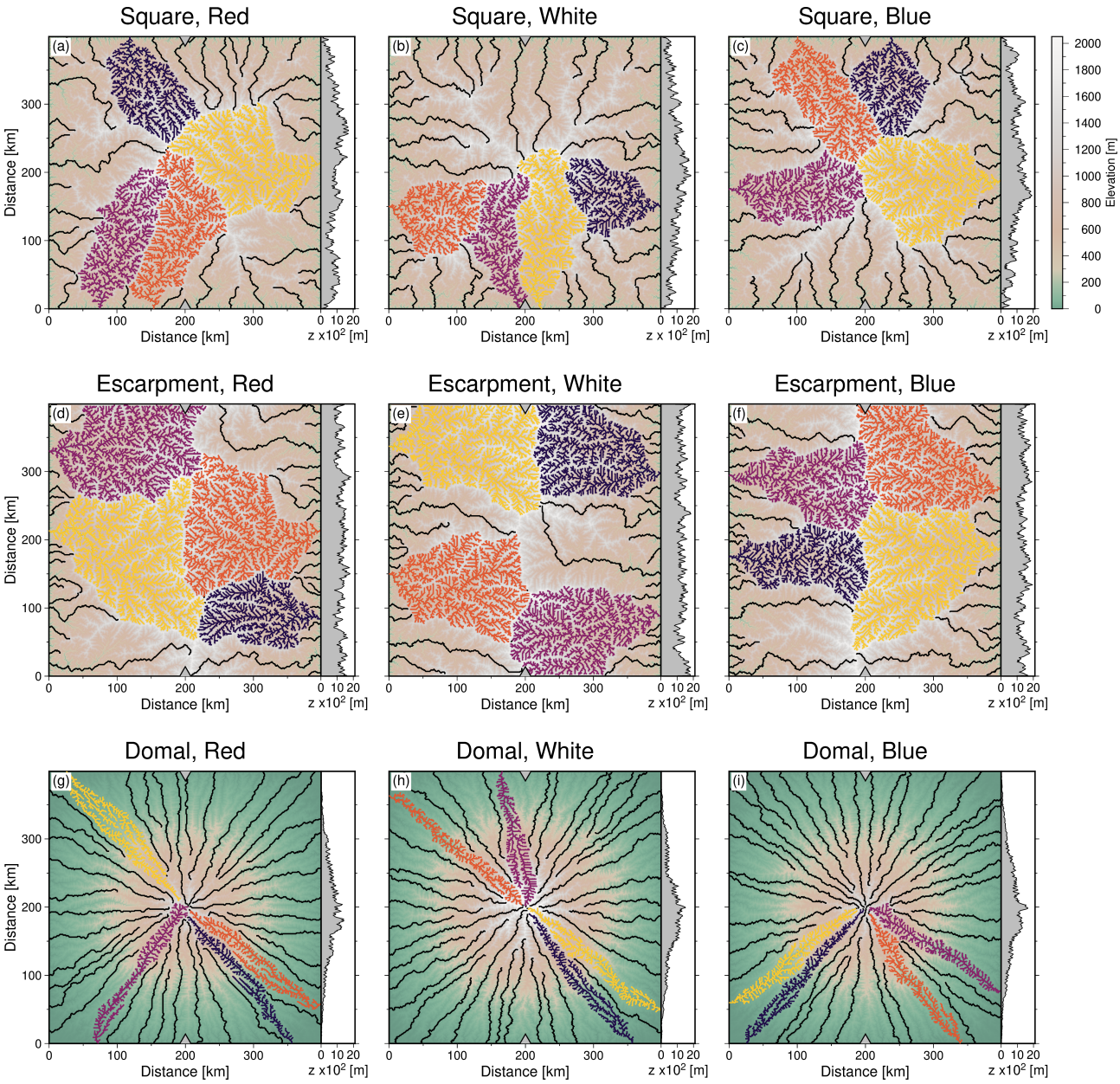


Figure 2.13: **Steady state landscapes generated with different initial conditions using a 400 × 400 km grid.** See Figure 2.12 for extended description.

version of the code within the `ChannelProfiler` component of Landlab (modified for data manipulation and visualisation). It is noted that metrics are often derived, via slope-area or χ analyses for instance, from profiles alone.

Slope-area analysis

Expectations of power law scalings of channel slope and upstream drainage basin areas were discussed by Gilbert (1877), and later quantified in a few settings by Hack (1957), Morisawa (1962) and Flint (1974), and subsequently by many others. Slope-area analysis remains a widely used tool to estimate

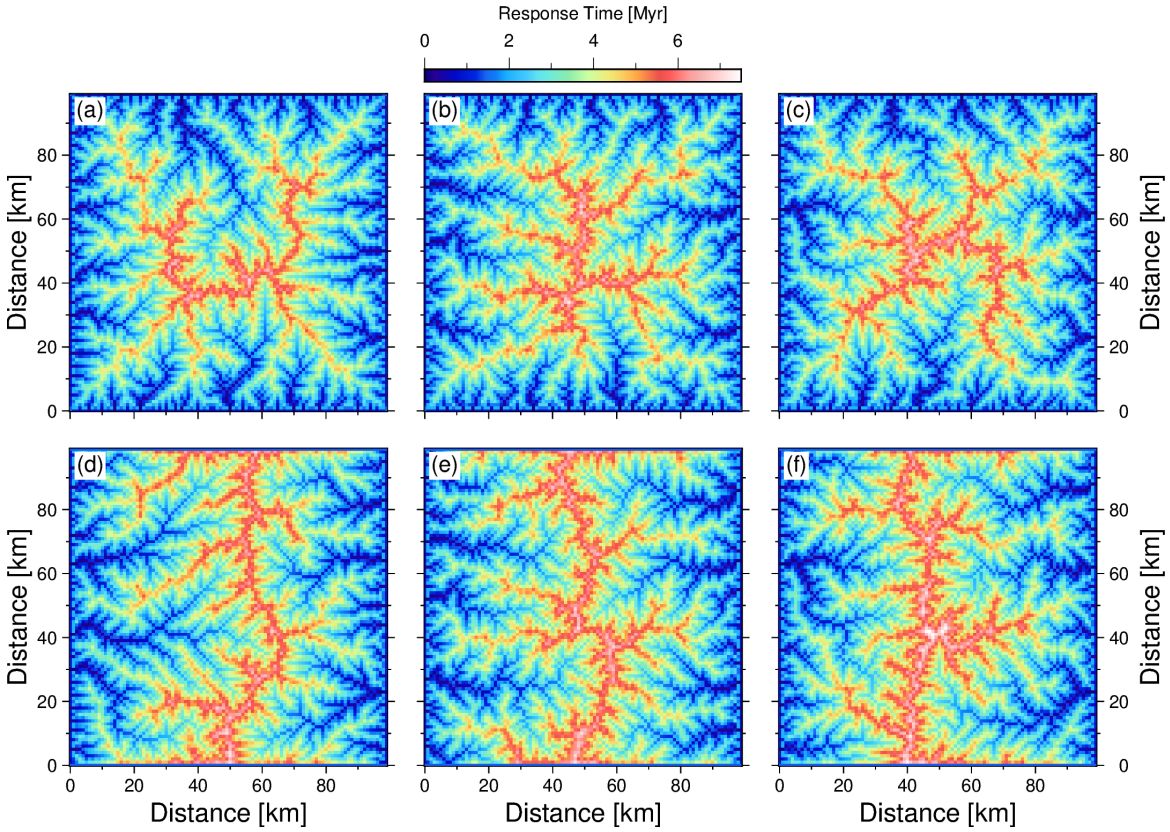


Figure 2.14: **Landscape response times, τ, for typical 'square' (a–c) and 'escarpment' (d–f) landscapes.**

uplift rates and erosional parameter values (e.g., Schoenbohm et al., 2004; Kirby and Whipple, 2012; Adams et al., 2020; Marder and Gallen, 2023). It is typically applied to information about local changes in slope, $\partial z(x)/\partial x$, and upstream drainage areas, $A(x)$, extracted from the longitudinal profiles of individual rivers, where x here indicates streamwise distance. There are many explanations of the approach in previously published work (see e.g., Tarboton et al., 1989; Montgomery and Foufoula-Georgiou, 1993; Kirby and Whipple, 2001). For completeness it is summarised as follows.

If a river is assumed to be at topographic steady state, $\partial z/\partial t = 0$, $\kappa = 0$, and there are no additional sources of elevation (e.g., noise), the one dimensional version of Equation 2.1, predicting evolution of the longitudinal profile of the river,

$$\frac{\partial z(x)}{\partial t} = -KA(x)^m \left(\frac{\partial z}{\partial x}\right)^n + U, \tag{2.13}$$

can be rearranged such that

$$\left|\frac{\mathrm{d}z}{\mathrm{d}x}\right| = \left(\frac{U}{K}\right)^{\frac{1}{n}} A(x)^{-\frac{m}{n}}. \tag{2.14}$$

By substituting k_s (widely referred to as the 'channel steepness index') for $(U/K)^{\frac{1}{n}}$, and θ ('concavity

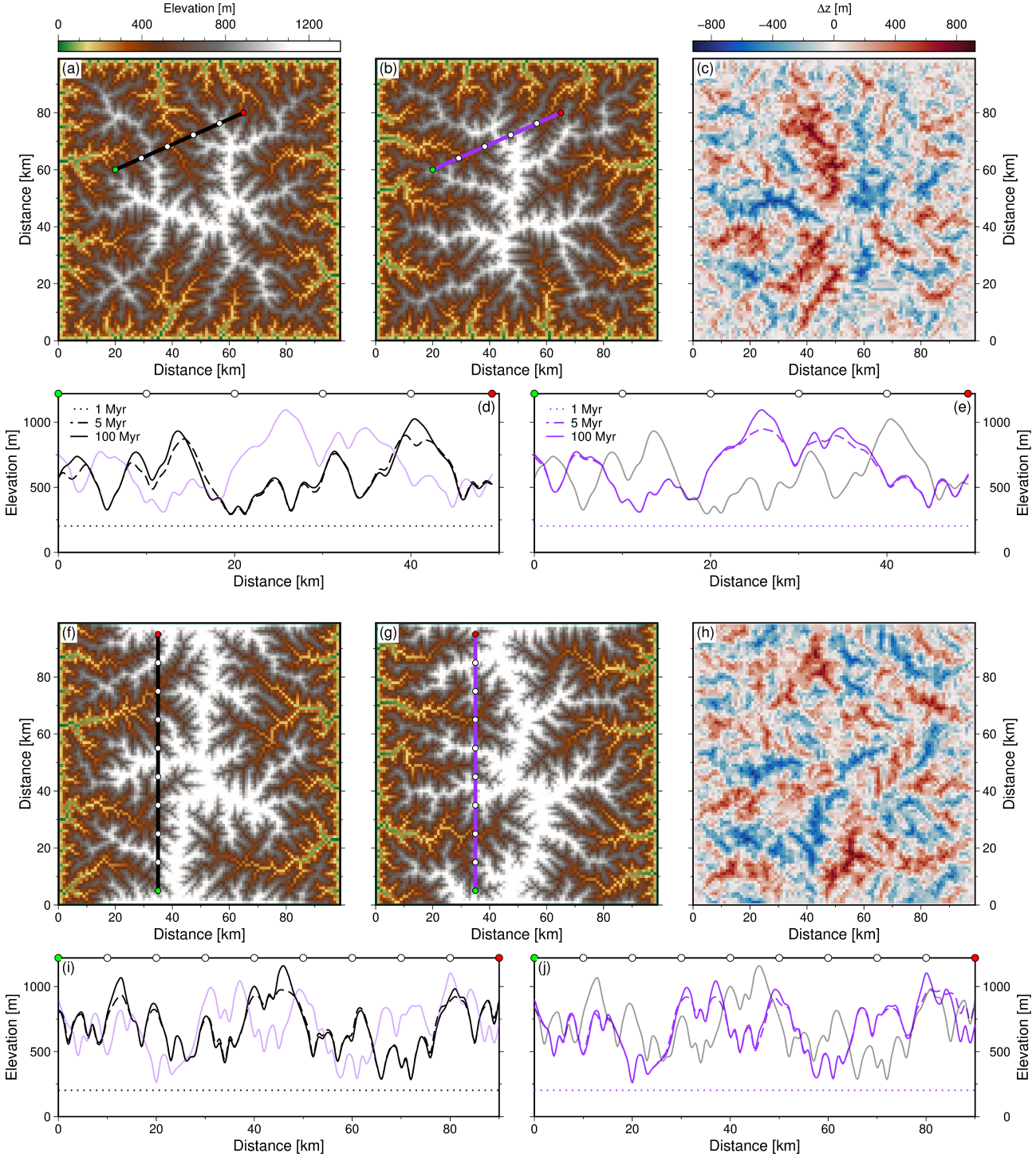


Figure 2.15: **Differences in elevations and drainage network planforms due solely to changing arrangements of initial noise.** (a)–(b) Steady state 'square' landscapes (at 100 Myr) generated with the same uplift rate histories, boundary conditions, and distributions (but different arrangements) of white noise. (c) Landscape in panel (a) subtracted from that in panel (b). (d) Black dotted, dashed, solid lines = elevation along transect indicated in panel (a) at 1, 5 and 100 Myr. Purple line = landscape at 100 Myr along transect indicated in panel (b). (e) as for (d) for transects shown in panels (b) and (a). (f–j) Same as panels (a)–(e) for 'escarpment landscapes.

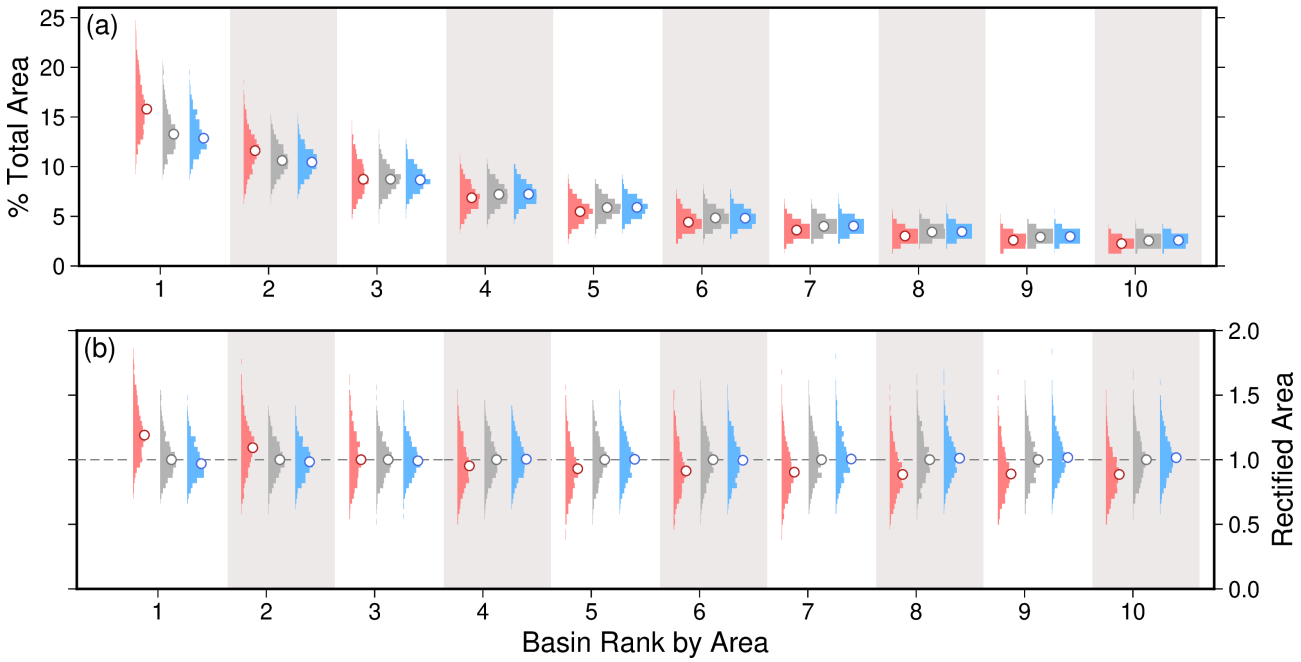


Figure 2.16: **Variability of drainage areas due to noise.** (a) Distributions of maximum upstream drainage area for the 10 largest drainage basins of 1000 simulations for red, white, and blue noise initial conditions (i.e., scenario A, ensembles 10–12). White closed circles show median values of drainage area as a proportion of total landscape area. Cumulative median areas sum to 64.4%, 63.5%, and 63.0% for red, white, and blue noise respectively. (b) Data shown in (a) are divided by the white noise median values of drainage area in each respective basin.

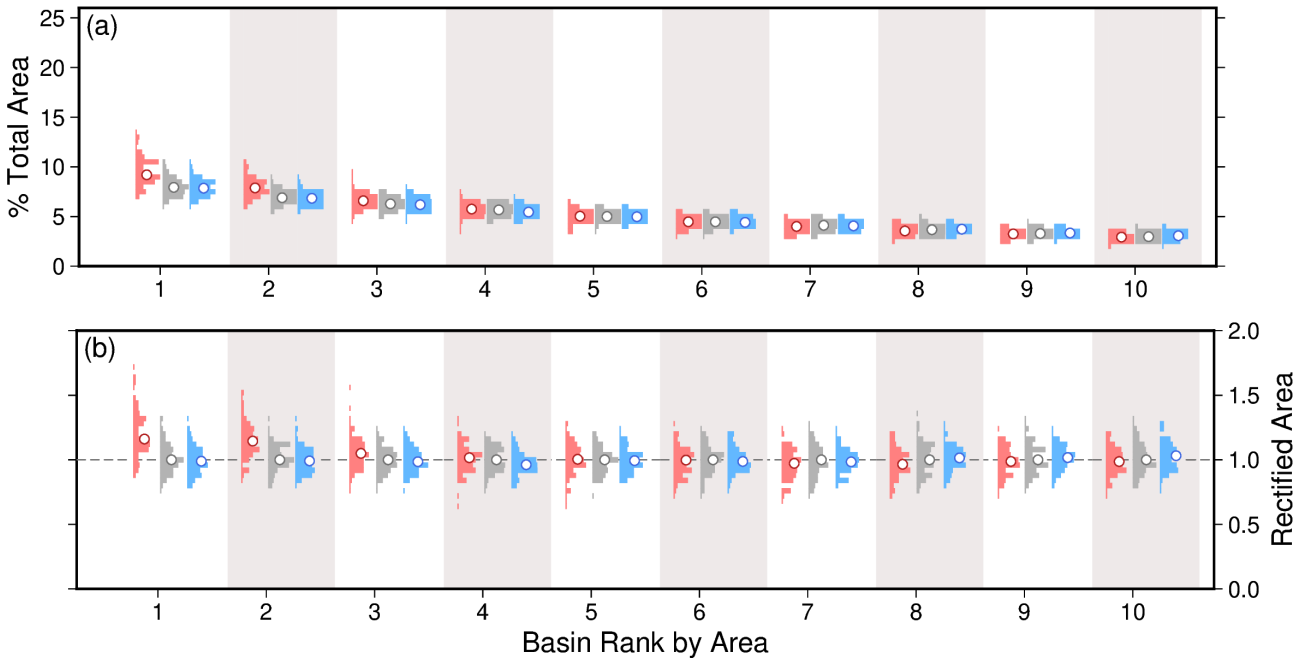


Figure 2.17: **Variability of drainage basin areas due to noise in landscapes without initial sink-filling.** See Figure 2.16 for extended description. Note distributions shown here are for $M = 100$ simulations of landscapes initialised with red, white, or blue noise.

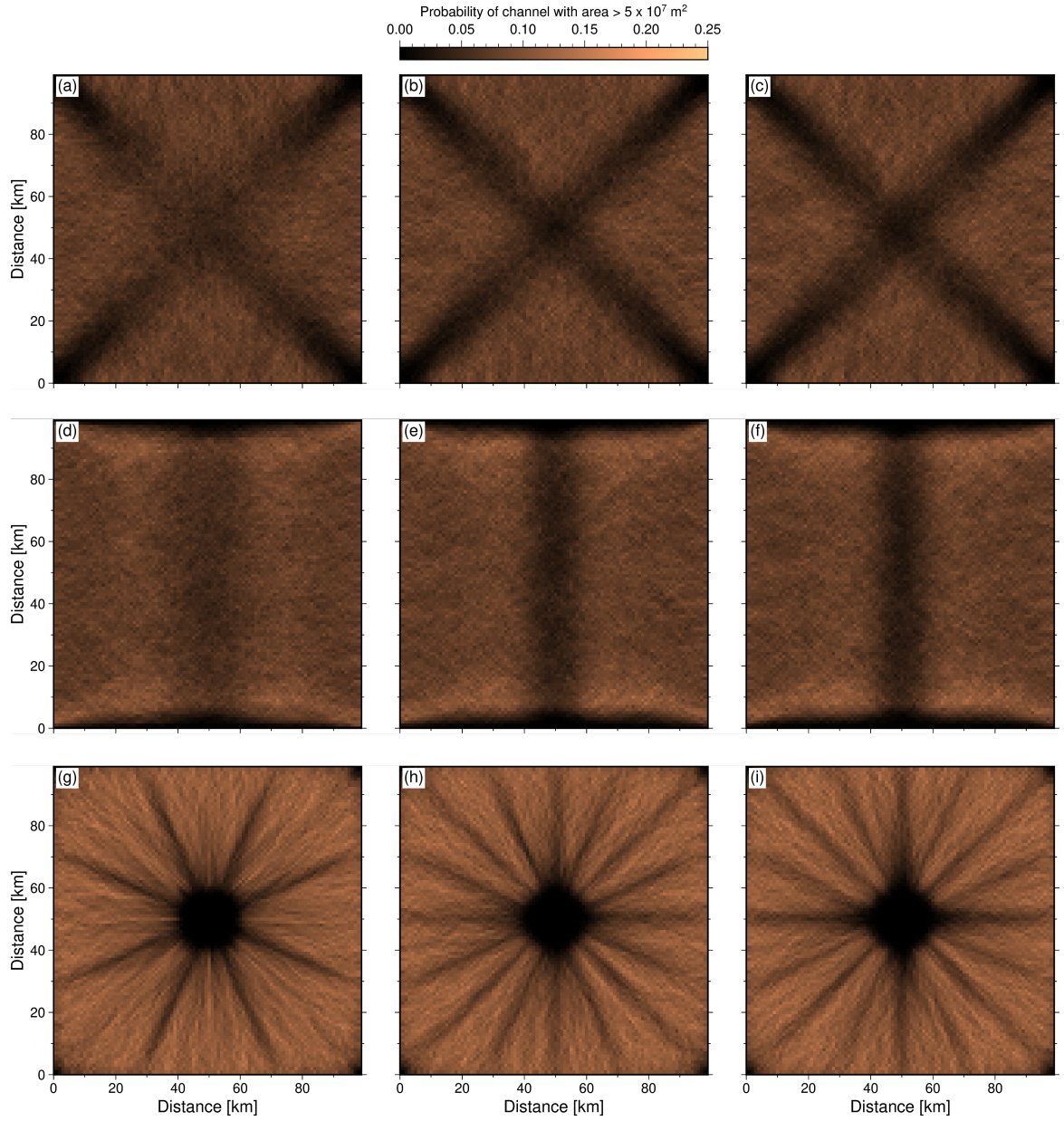


Figure 2.18: **Probability of drainage within landscapes generated by different arrangements of initial noise.** (a–c) Colours indicate probability of a grid cell in 1000 'square' landscapes containing a channel with upstream drainage area $> 5 \times 10^7$ m^2 generated with initial red (a), white (b), or blue (c) noise. (d–f) As above, for 'escarpment' landscapes, and (g–i) for 'domal' landscapes. Examples of individual landscapes that feature in this suite are shown in Figure 2.12. Associated power spectra are shown in Figure 2.21.

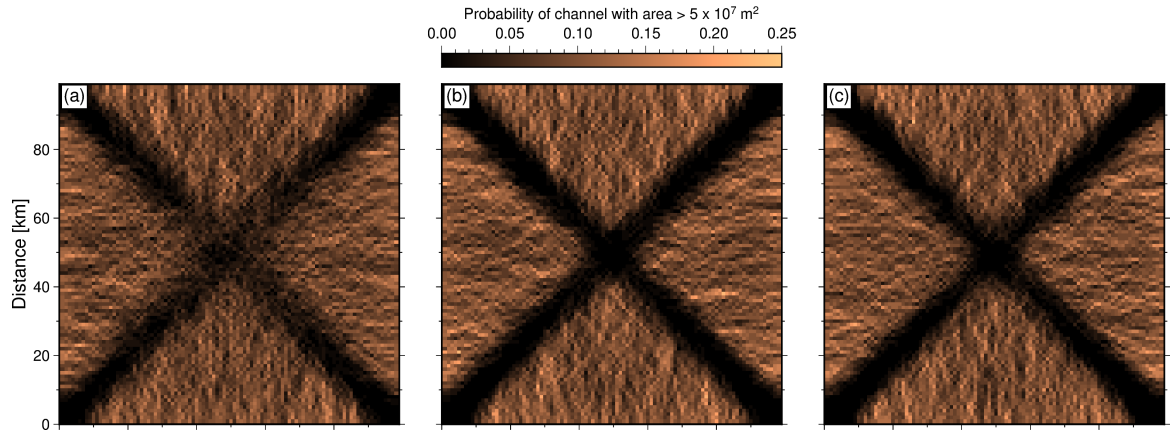


Figure 2.19: **Drainage probability maps for 'square' landscapes with no initial sink-filling.** See Figure 2.18 for extended description. Note distributions shown here are for $M = 100$ simulations of landscapes initialised with red, white, or blue noise.

index') for the exponent ratio m/n, Equation 2.14 can be rewritten as

$$\log(S) = \log(k_s) - \theta \log(A). \tag{2.15}$$

Equation 2.15 takes the form of a straight line in a plot of log(S) against log(A), with gradient θ, and $\log(k_s)$ at the y-intercept. In turn, because the values of n and K in the experiments of this chapter are known, one can, in principle, recover the values of uplift rate and erosional parameter m,

$$U = {k_s}^n K, \quad m = \theta n. \tag{2.16}$$

The black line in Figure 2.23e shows the analytical relationship (from Equation 2.15) between slope and area expected for all rivers within steady state landscapes generated with 'block' uplift (see Figure 2.8: 'square', 'escarpment') in this chapter given the values of erosional parameters and uplift rate used. Slope-area analysis of river profiles extracted from the two-dimensional landscapes is restricted to cells with upstream drainage areas >4 km^2, a value often used in studies of real landscapes as indicative of overland flow (e.g., Whipple and Tucker, 1999; Roberts and White, 2010). Slope is calculated between adjacent cells in the streamwise distance downstream.

Chi analyses

Metrics estimated from slope-area analysis can be extremely sensitive to noise and thus calculated parameter values can be highly unstable (see e.g., Roberts et al., 2012a; Smith et al., 2022). This result is unsurprising because even small amounts of noise can dramatically change local slopes. Fortunately,

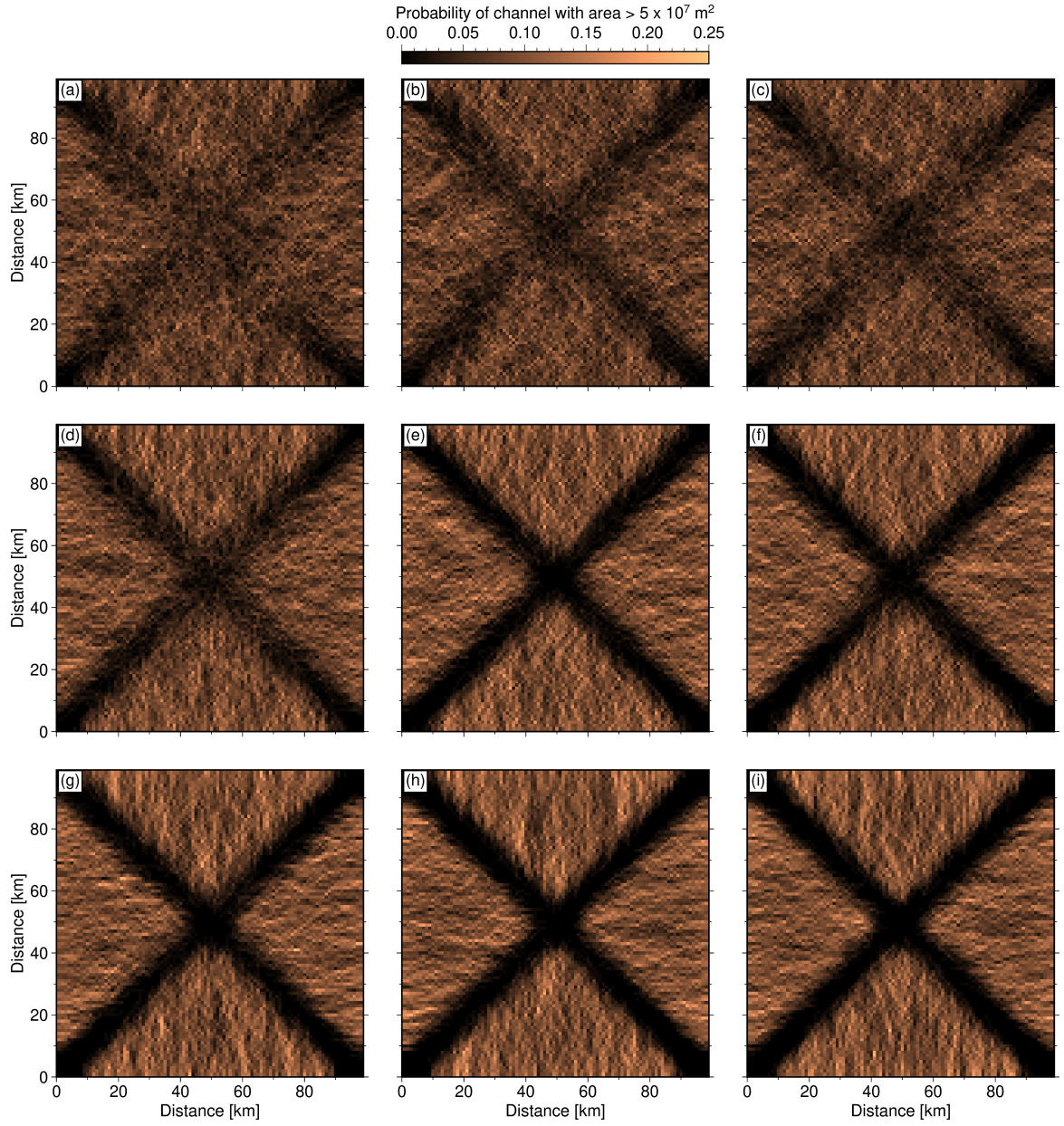


Figure 2.20: **Probability of drainage within landscapes generated by 100 different arrangements of initial, quenched, and spatio-temporal noise.** (a–c) Colours indicate probability of a grid cell in 100 'square' landscapes containing a channel with upstream drainage area $> 5 \times 10^7$ m^2 generated with initial red (a), white (b), or blue (c) noise. Compare to the equivalent panels in Figure 2.18a–c for 1000 simulations, demonstrating convergence from 100 simulations. (d–f) As above, for landscapes containing quenched noise, and (g–i) for landscapes with spatio-temporal noise added. Examples of landscapes with white quenched or spatio-temporal noise added are shown in Figures 2.31a and 2.34a.

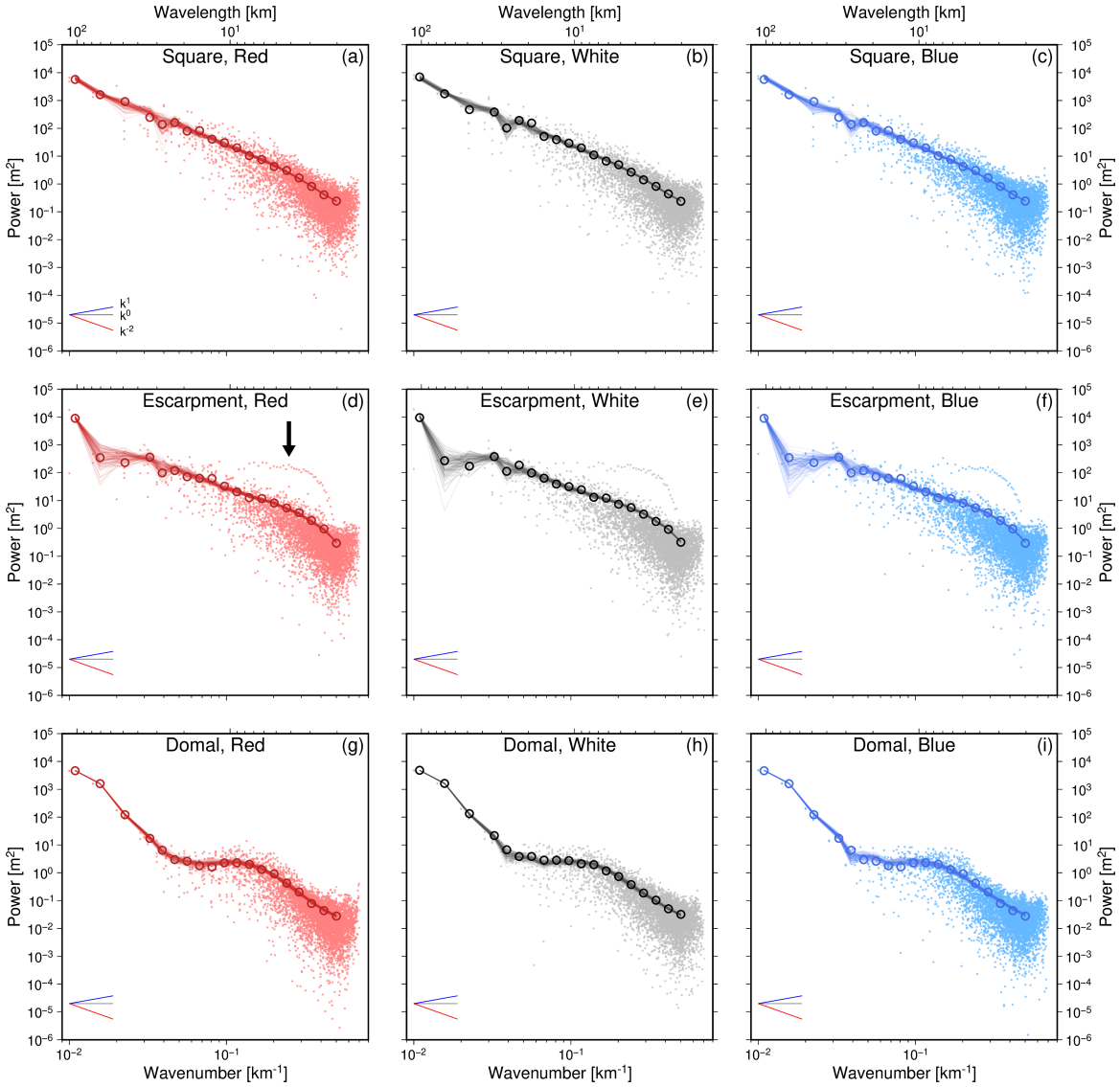


Figure 2.21: **Spectral (two-dimensional Fourier) analysis of steady state landscapes generated with noise in the initial condition.** (a) Small red dots = power at positive frequencies from the two-dimensional Fourier transform collapsed into one dimension for a single 'square' landscape generated with a red noise initial condition (see body text for details). Open circles = mean power within logarithmically equalled spaced bins (see Equation 2.9). Thin lines show the mean values for the other 99 models with same distribution but different arrangement of initial noise. (b–c) As per (a), for a steady state landscape generated with a white noise (b), and blue noise (c) initial condition. (d–f) As per (a–c) for the 'escarpment' landscapes such as that shown in Figure 2.1d. Arrow indicates power for regions on north and south boundaries. (g–i) Power spectra for 'domal' landscapes (e.g., Figure 2.1e).

a variety of integral-based techniques exist that avoid the need for differentiation of elevations when attempting to recover information from fluvial landscapes (e.g., erosional parameter values, uplift rates; see e.g., Harkins et al., 2007; Pritchard et al., 2009; Roberts and White, 2010; Roberts et al., 2012b; Perron and Royden, 2013).

Here, I focus on examining impact of noise on geomorphic metrics calculated using the widely used 'χ' (chi) analysis (Royden et al., 2000; Harkins et al., 2007; Perron and Royden, 2013). Like slope-area analysis, χ-analysis can, in principle, be used to estimate uplift rates and values of erosional parameters from the geometries of longitudinal river profiles providing certain assumptions hold. There are many published explanations of the approach available (see e.g., Perron and Royden, 2013; Mudd et al., 2014; Mudd et al., 2018; Smith et al., 2022; Marder et al., 2023). For completeness, it is summarised as follows. First, Equation 2.14 is rearranged and integrated in the upstream direction such that

$$z(x) = z_b + \int_{x_b}^{x} \frac{k_s}{A(x)^{\frac{m}{n}}} \mathrm{d}x, \tag{2.17}$$

where z is elevation, x_b is a downstream position on the channel often assumed to be base level (though not always), with elevation z_b. A reference drainage area $A_\circ$ (here $= 1$ m^2) is often incorporated, such that

$$z(x) = z_b + \frac{k_s}{A_\circ^{\frac{m}{n}}} \int_{x_b}^{x} \frac{A_\circ^{\frac{m}{n}}}{A(x)^{\frac{m}{n}}} \mathrm{d}x. \tag{2.18}$$

Thus χ is defined as the integral from downstream channel position x_b to the position x of the ratio between the reference drainage area and upstream drainage area, raised to the fractional power m/n,

$$\chi(x) = \int_{x_b}^{x} \left(\frac{A_\circ}{A(x)} \right)^{\frac{m}{n}} \mathrm{d}x. \tag{2.19}$$

Making use of Equation 2.16,

$$z(x) = z_b + \frac{k_s}{A_\circ^{\frac{m}{n}}} \chi(x) = z_b + \left(\frac{U}{K A_\circ^m} \right)^{1/n} \chi(x). \tag{2.20}$$

Various techniques exist to find the optimal values of m/n from the construction of $z(\chi)$ profiles (e.g., Perron and Royden, 2013; Mudd et al., 2014; Hergarten et al., 2016; Mudd et al., 2018; Gailleton et al., 2021). If the landscape is at steady state then elevation is expected to be a linear function of χ. By systematically sweeping $0 < m/n \leq 1$, the optimal value can be identified, i.e., as one that results in the $z(\chi)$ profile with the highest linear correlation coefficient, R^2 (see e.g., Perron and Royden, 2013).

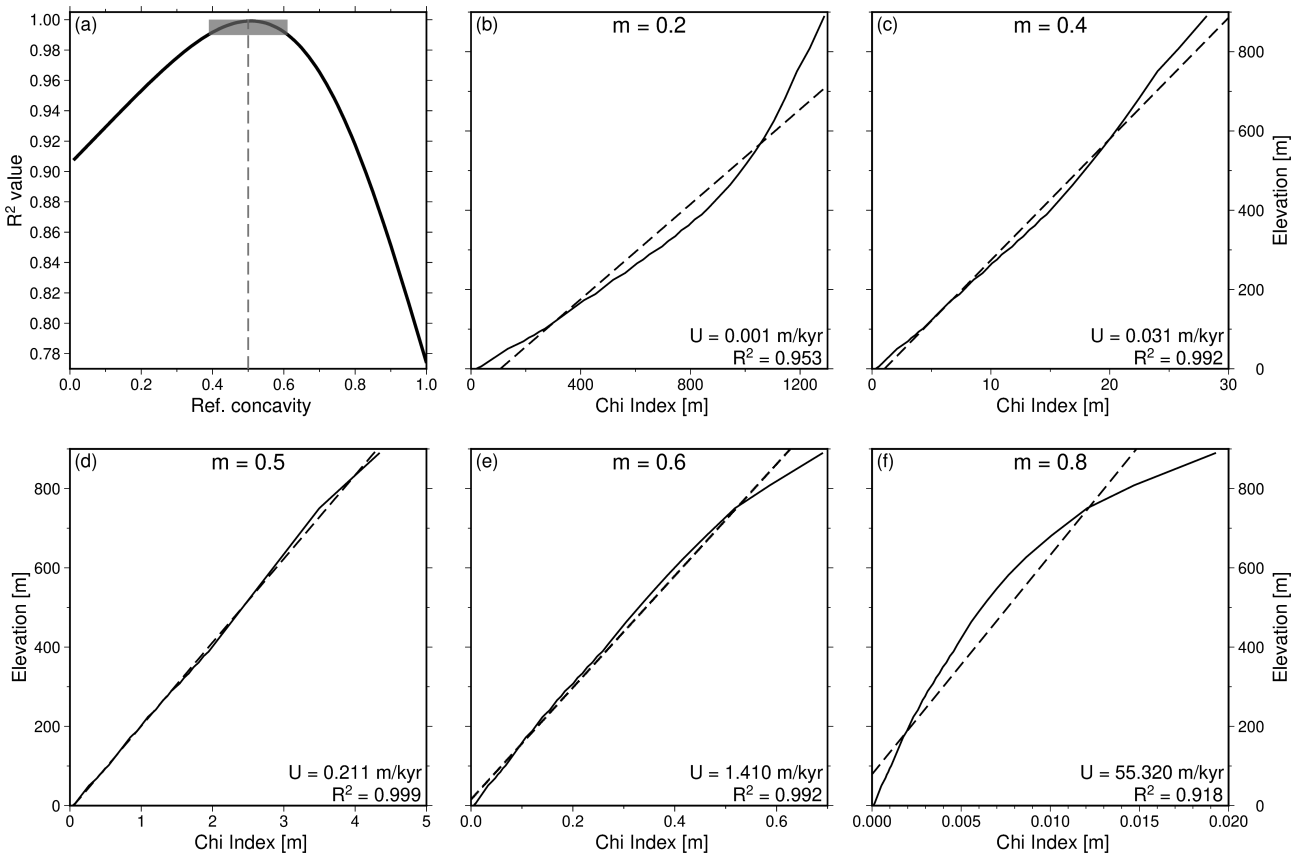


Figure 2.22: **Impact of assumed value of concavity index on recovery of uplift rates from chi-analyses.** Chi-analysis of longest river extracted from a steady state landscape (at 100 Myr) generated with white noise only in the initial condition (from catchment coloured yellow in Figures 2.12b and 2.23d). (a) Black curve = results from linear regression of chi-elevation data generated with annotated values of concavity index ($\theta = m/n$); dashed line = true value used to generate the synthetic landscape; grey band = values where $R^2 > 0.99$. (b–f) Examples of chi-elevation profiles (solid line) used to generate the solid curve in panel (a) with annotated values of m (note, $n = 1$, hence $\theta = m$). Dashed line = linear regression; note annotated R^2 values and recovered uplift rates (see Equation 2.20).

In the experiments run in this study, the true values of m and n are known. As Figure 2.22 shows, if an incorrect value of m/n is assumed, $z(\chi)$ profiles are not linear. Correlation coefficients are calculated for the main channel in each simulation to identify the 'optimal' value of m/n as if a real landscape for which no independent information about the erosional parameter values exists was being studied. Once armed with an optimal value for m/n it is straightforward to estimate the uplift rate from the slope of the $z(\chi)$ profile (because the values of $n = 1$ and K are known here),

$$U = K A_{\circ}^{m} \frac{\mathrm{d}z}{\mathrm{d}\chi}. \tag{2.21}$$

Figure 2.23f shows an example of a relationship between χ and elevation for the main channel and tributaries of the largest drainage network in a single simulation.

Hack exponent

Hack's law is an empirical relationship between the length of rivers and their upstream drainage areas, both of which are straightforward to extract from synthetic landscapes and digital elevation data. It has been used to relate changes in channel sinuosity to basin shapes, to develop an understanding of fractal (scale-dependent) characteristics of basins, and of energy expenditure in drainage basins, for example (Langbein, 1947; Hack, 1957; Robert and Roy, 1990; Ijjasz-Vasquez et al., 1993; Rigon et al., 1996; Turcotte, 1997; Willemin, 2000). The law can be expressed as

$$L = CA^h \quad \text{thus} \quad \log(L) = \log(C) + h\log(A), \tag{2.22}$$

where L is the length of the longest river in a basin, A is upstream drainage area, and C and h are known as the Hack coefficient and exponent, respectively. Their values can be estimated from the respective intercept and slope of regressed log(L) and log(A) data. It is shown how noise impacts the values of Hack exponents calculated from the maximum lengths and upstream drainage areas of the longest channels in the forty largest drainage basins (by area) in each model run.

Hypsometry

Hypsometry summarises area-elevation relationships of a landscape, including topography not necessarily incorporated into the other geomorphic metrics examined (see e.g., Langbein, 1947; Strahler, 1952; Strahler, 1957; Harrison et al., 1983; Lifton and Chase, 1992; Willgoose and Hancock, 1998; Hurtrez et al., 1999; Montgomery et al., 2001). Hypsometry is calculated for the entire domain of each steady state landscape by generating normalised cumulative density functions (the simple algorithm used is available; see Code statement at the beginning of this chapter). Hypsometry is also produced for select landscapes during their evolution (e.g., Figure 2.23g).

Each of the geomorphic metrics extracted from synthetic landscapes in this chapter have now been introduced. The primary aim is to assess how changing the colour, amplitude, timing, and arrangement of noise affects these metrics. Results are synthesised for each scenario as follows.

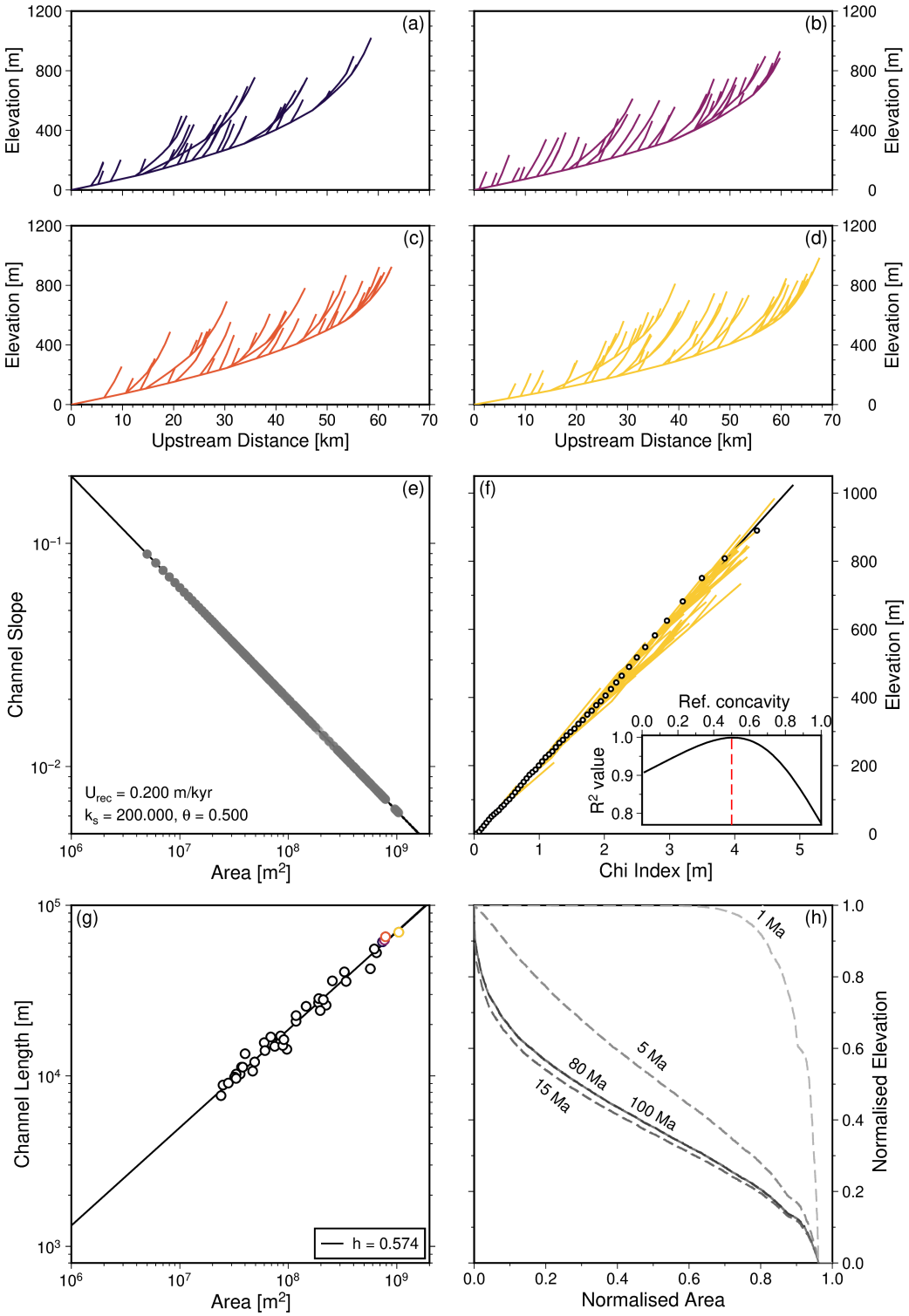

(a)
(b)
(c)
(d)
Elevation [m]
Upstream Distance [km]
(e)
Channel Slope
Area [m²]
U_rec = 0.200 m/kyr
k_s = 200.000, θ = 0.500
(f)
Chi Index [m]
Ref. concavity
R² value
(g)
Channel Length [m]
h = 0.574
(h)
Normalised Elevation
Normalised Area
1 Ma
5 Ma
80 Ma
15 Ma
100 Ma

Figure 2.23: **Geomorphic metrics for an example 'square' landscape generated with white noise only in the initial condition.** All metrics are for the steady state landscape (at 100 Myr) shown in Figure 2.12b unless otherwise indicated. (a–d) Longitudinal profiles of rivers, including tributaries, within four largest drainage basins shown in Figure 2.12b. (e) Grey points show slope-area relationship for grid nodes of rivers in four largest basins with drainage areas exceeding 4 km^2. Black line = linear regression: calculated intercept = k_s (*steepness index*); U_{rec} = recovered uplift rate; slope = $\theta = m/n$ (*concavity index*). True values, used to generate LEM: $U = 0.2$ m /kyr, $\theta = 0.5$. See body text for details. (f) Yellow = χ-elevation profiles for the main channel and tributaries of the largest drainage basin (panel d); open circles = main channel. Inset shows R^2 values for different assumed *concavity indices* for main channel; red dashed line = true value. Black solid line in main panel illustrates linear relationship for $\theta = 0.5$. (g) Coloured/black circles show maximum length-drainage area relationships for longest rivers from four/forty largest drainage basins, respectively. h = Hack exponent. (h) Hypsometry (i.e., landscape area-elevation relationships) at 1, 5, 15, 80 and 100 Ma.

2.3 Results

2.3.1 Scenario A: Noise only inserted into the initial condition

Verification of Topographic Steady State

The boundary conditions and uplift rates—producing 'square', 'escarpment', or 'domal' landscapes in this study—influence the precise time taken to reach steady state. Histograms shown in Figure 2.9 illustrate that, for the erosional model used in this study, with noise only inserted into initial conditions, landscapes are immature and topographic change is driven by the imposed uplift until ca. 1 Myr. By 5 Myr, the landscapes are maturing as drainage networks develop; topographic change is largely centred around zero by this time. By 15 Myr drainage networks have matured such that erosion rates balance the imposed uplift rates across most of the domain. For most intents and purposes these landscapes can be regarded as being at steady state at this time. However, it is noted that true numerical steady state is achieved where topographic change within a single time-step across all cells is zero within computer precision, which is typically achieved by 40–90 Myr.

Spectral power of initial, sink-filled, and steady state landscapes

Figure 2.1c shows examples of the spectral content of single models. It demonstrates how landscapes with initial white noise ($\phi \propto k^0$) quickly 'redden' due to sink-filling, which reduces local roughness, resulting in such sink-filled landscapes having pink noise ($\phi \propto k^{-1}$) characteristics. Figure 2.5d shows the spectral content of 100 initial conditions for each distribution of noise (red, white, blue) used in this study.

Examination of the power spectra of evolving landscapes shows that the spectral signature of all (red,

white, blue) initial noise conditions with amplitude 0 – 1 m evolve to have red noise characteristics within 2 Myr of model run time ($\phi \propto k^{-2}$). Spectral reddening of topography in these landscape evolution models is attributed to the smoothing effects of sink-filling and erosion, and the imposed uplift. Figure 2.21 shows radially-averaged power spectra for typical steady state landscapes in ensembles 1 – 9. The escarpment landscapes (ensembles 2, 5, 8) contain above-average spectral power at a few intermediate to high wavenumbers ($10^{-1} \leq k \leq 5 \times 10^{-1}$ km^{-1}), highlighted with the black arrow in Figure 2.21d. This pattern is attributed to the high elevations at the closed north and south boundaries of these landscapes. The domal landscapes exhibit a flattening in the power spectrum at intermediate wavenumbers ($5 \times 10^{-2} \leq k \leq 1 \times 10^{-1}$ km^{-1}). The flattening corresponds to a white noise signal at these wavenumbers. This spectral power is attributed to the areas of low elevation (few meters) between the uplifted dome and the edge of the domain.

Overall, Figure 2.21 shows that whilst landscape configuration can influence the details of the power spectrum, the steady state landscapes produced in this study tend to exhibit red noise characteristics and are insensitive to the colour of noise used to generate the initial condition.

Impact of noise on geometries and planforms

In contrast, Figure 2.12 illustrates how those initial conditions can lead to very different drainage planforms. This result emerges even for landscapes that are generated with the same erosional model parametrisations and uplift histories. Figure 2.15 extends this demonstration by showing how different arrangements of the same distribution of noise (e.g., white) in the initial condition results in formation of very different drainage planforms. Inevitably, the dissimilarity of planform arrangements is consistent with elevations being very different locally, resulting in substantial differences in the positions of valleys and interfluves. These differences are illustrated using topographic transects from identical locations in the two landscape models shown in Figure 2.15.

As a further demonstration of the impact of noisy initial conditions on the geometries of landscapes, Figure 2.16 shows drainage area of each of the 10 largest fluvial networks in the 3000 simulations generated with either red, white, or blue noise as a percentage of the total area of the model domain. The are ordered by rank: largest to smallest drainage area. Landscapes initialised with red noise tend to create, on average, fewer, larger drainage basins. The upstream area of the largest drainage basin in a landscape initialised with red noise can be up to 2 times that of the median white noise equivalent, and on average is approximately 20% larger. A consequence is that smaller drainage basins (rank 4 and

below) in landscapes initialised with red noise are smaller than their white and blue noise counterparts. Drainage basins in landscapes generated by white and blue noise conditions are similar in size to each other.

Figure 2.18 shows calculated probabilities of channel locations for steady state landscapes generated with different distributions of initial noise. Three features of interest in the probability maps of 'square' landscapes are emphasised (Figure 2.18a–c). First, all three distributions of noisy initial conditions have regions of low probability within a 'cross' that extends from the four corners of the domain to its centre. Secondly, in between those regions the probability of drainage is broadly equal, and relatively high. Thirdly, landscapes with red noise initial conditions (panel a) have a more uniform probability of drainage across the domain. The escarpment landscapes initialised with red noise also have a higher probability of drainage across the domain than those initialised with white or blue noise (Figures 2.18d-f).

The domal landscapes exhibit probabilistic drainage patterns with a radial 'spoke' pattern for all three colours of noise. This pattern is interpreted as being a consequence of the interaction of D8 flow routing on a square Cartesian raster grid and the distribution of inserted uplift. In other words, the pattern is a numerical artefact, and similar patterns have appeared in other landscape studies that utilise different numerical setups (e.g., Perron and Fagherazzi, 2012; Borse and Biswal, 2025). It is suggested that the lower number of spokes for landscapes generated with red noise initial conditions are a result of longer wavelength topographic roughness reducing the propensity for a flowpath to be diverted locally as frequently as they are for white or blue noise. In other words, channels in a landscape initialised with red noise are more likely to drain along a continuous azimuth without being interrupted by local topographic roughness. It is noted that the structure of probability in these maps is similar to drainage networks produced in models with no added noise (see Figure 2.3).

Slope-Area Analysis

Slope-area data shown in Figures 2.23e, 2.24a and 2.26a are clustered around a single line with a slope and intercept that permit reliable uplift rates, U_{SA}, and m/n ratios (θ_{SA}) to be recovered (Equation 2.16). These results demonstrate the utility of slope-area analysis for landscapes that are demonstrably at topographic steady state and subject to spatially invariant uplift; the 'square' and 'escarpment' landscapes studied here. Lines of best fit are shown in Figures 2.24a and 2.26a for each of the 3 $\times$ 100 simulations generated with 0 – 1 m of red, white or blue noise. They are largely indistinguishable

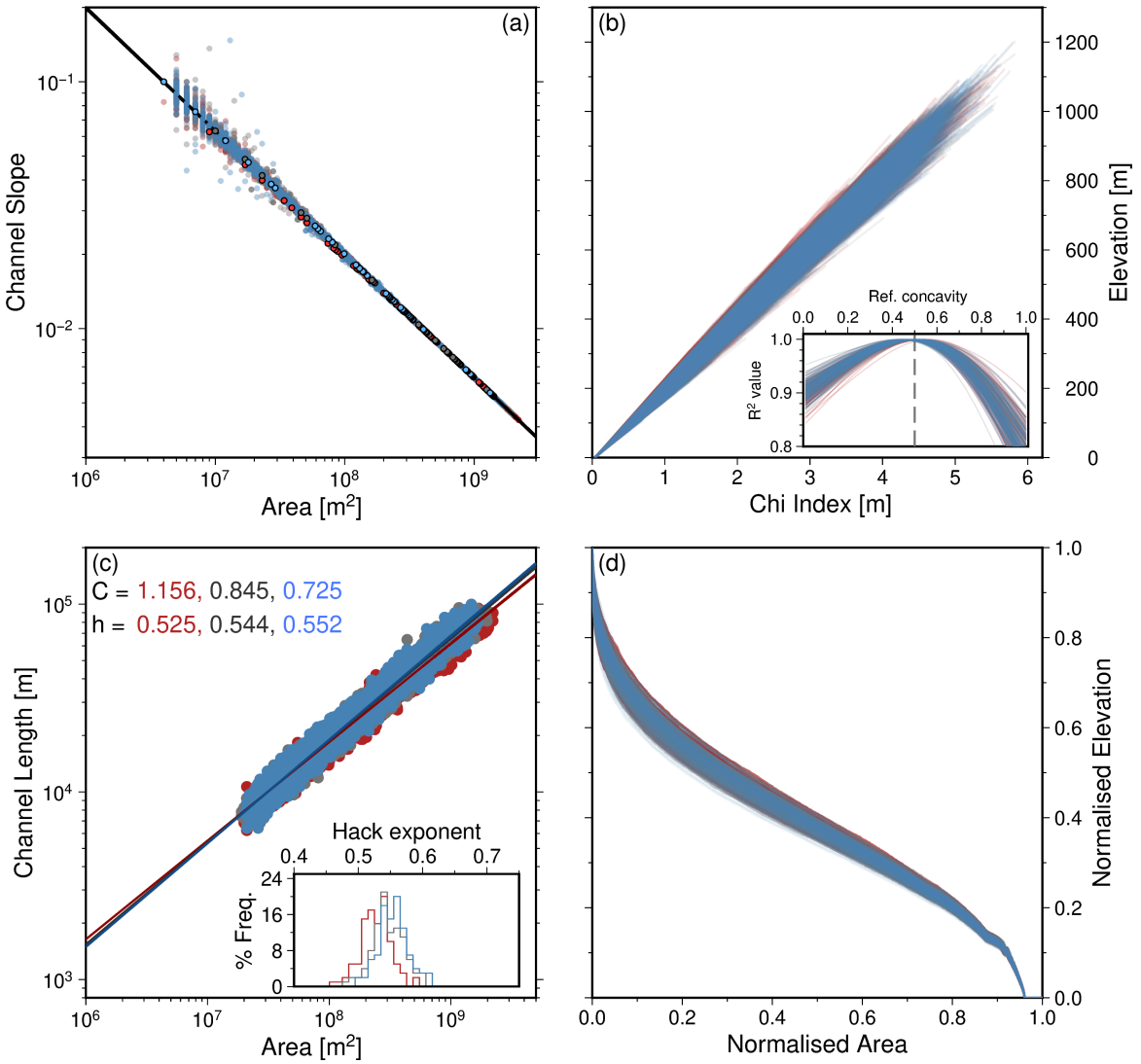


Figure 2.24: **Comparing geomorphic metrics from 'square' steady state landscapes initialised with red, white or blue noise.** Each panel shows metrics from 100 landscapes initialised with red, white or blue noise. (a) Upstream drainage area vs. channel slope for all grid cells in rivers of four largest drainage basins with drainage area > 4 km^2; black line = linear regression. Outlined circles show examples of relationships for the main channel in the largest drainage network in single, typical, simulation for each colour of noise. (b) Elevation as a function of χ for the main channel and tributaries of the largest drainage basin in each simulation, produced using $\theta = 0.5$. Inset shows the R^2 value of different reference concavities. Dashed line marks true value of 0.5 used to parametrise models. (c) Maximum upstream drainage area vs. maximum channel length for the longest (trunk) channels in the forty largest drainage networks in each landscape. Inset histogram shows Hack exponent for the 4000 rivers generated for each colour of noise. (d) Hypsometries of the 300 landscapes.

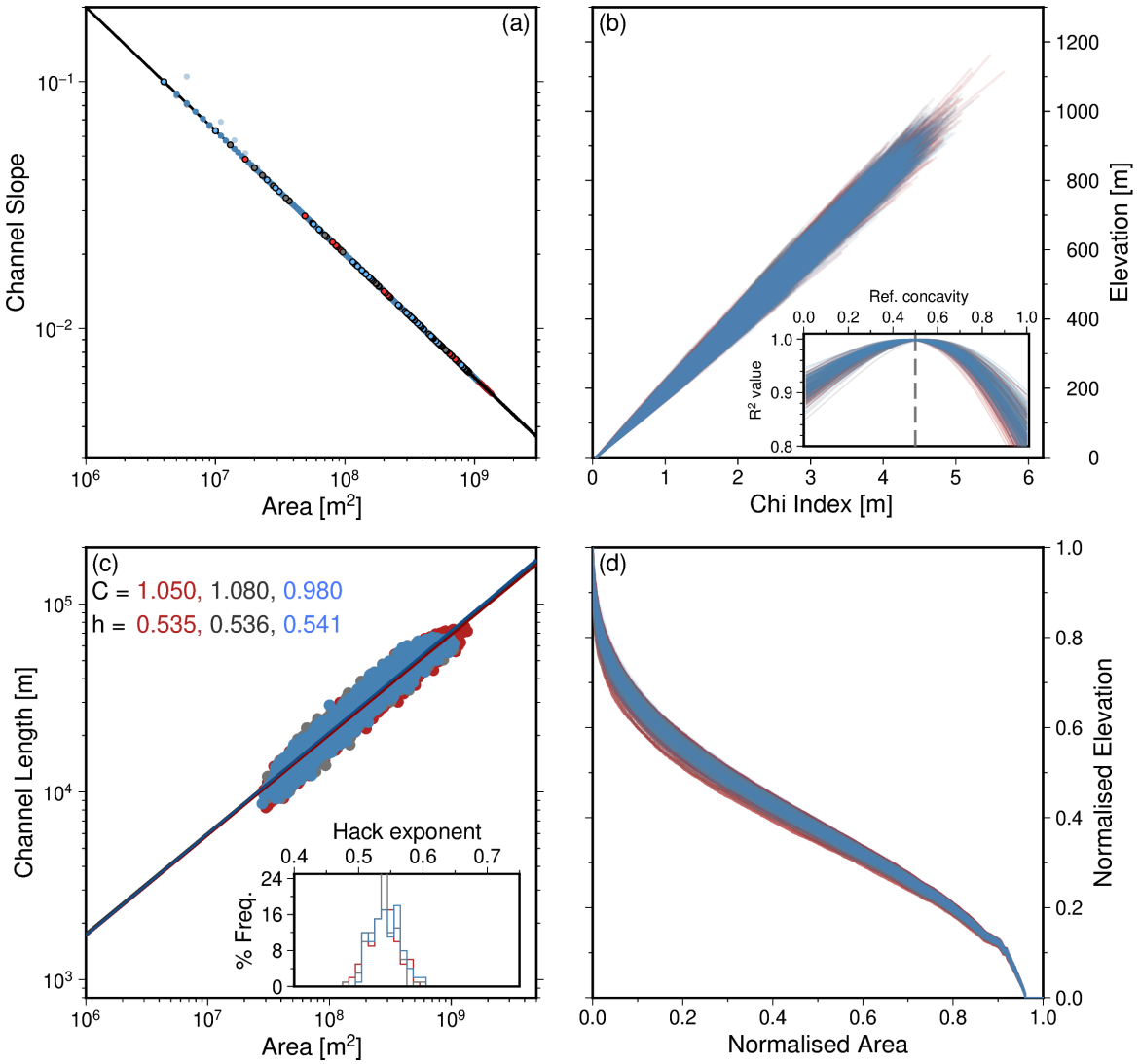


Figure 2.25: **Geomorphic metrics for 'square' landscapes with no initial sink-filling.** See Figure 2.24 for extended description.

from each other, demonstrating the insensitivity of slope-area relations to the colour of noise in the initial conditions. It is noted that changing the amplitude of noise increases the spread of calculated U_{SA} and θ_{SA} (Figure 2.30). However, changing the amplitudes of initial noise, even by many orders of magnitude, has a small impact (few percent compared to true values) on the recovered values of U_{SA} and θ_{SA}.

χ analysis

Figures 2.23f, 2.24b and 2.26b show $z(\chi)$ profiles for the main channel and tributaries of the single largest drainage basin for simulations in which uplift rate is spatially invariant ('square' and 'escarpment'). Results are shown for each of the 100 simulations generated with red, white or blue noise initial conditions. In theory, $z(\chi)$ profiles in such steady state landscapes should be straight and collinear,

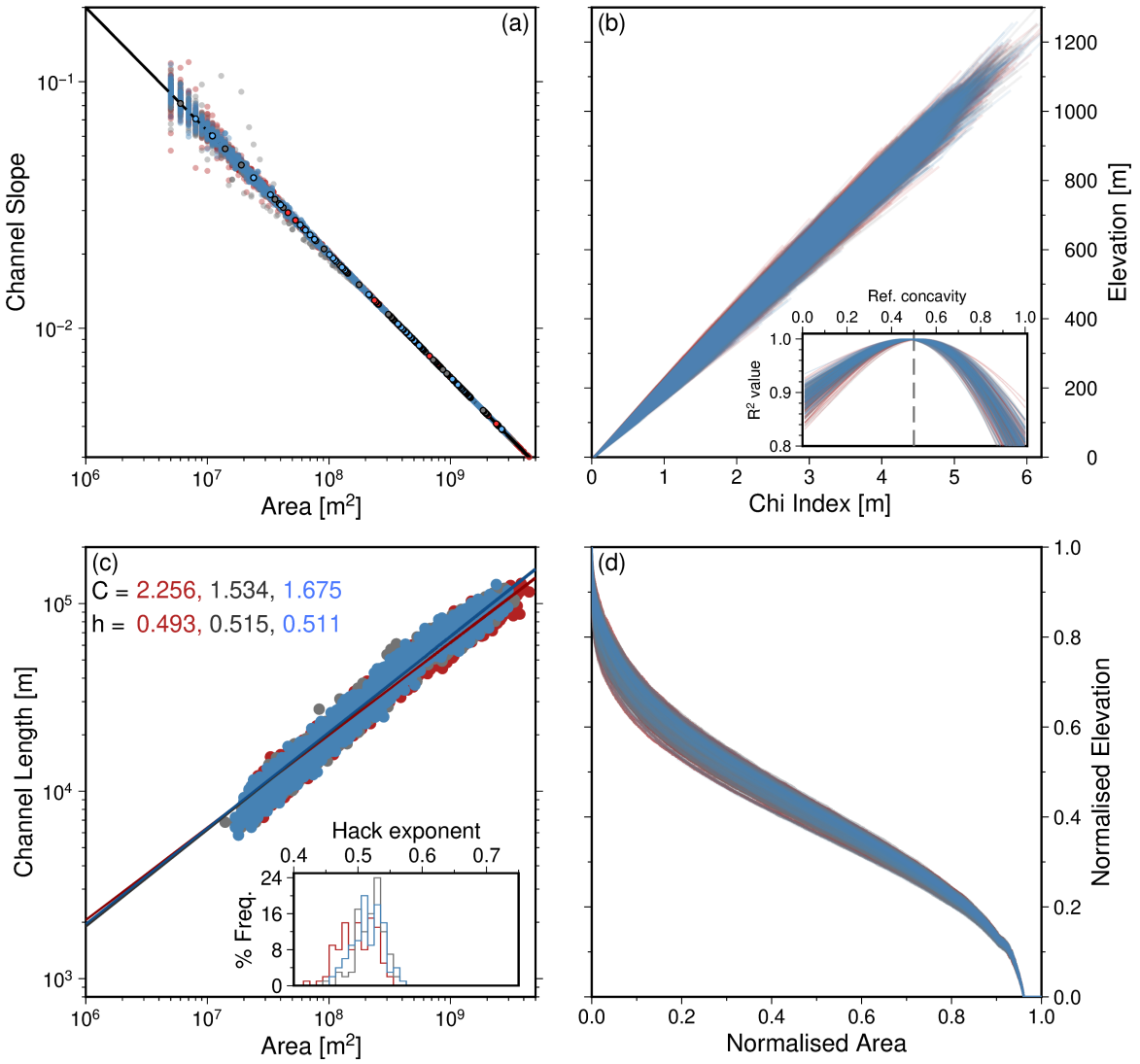


Figure 2.26: **Geomorphic metrics of steady state 'escarpment' landscapes initialised with red, white or blue noise.** See Figure 2.24 for extended notation.

i.e., collapse to a single line (see Section 2.2.6). Whilst individual profiles are linear, it is demonstrated that when the models are initialised with noisy conditions, families of profiles do not collapse to a single line, even when they have the same distribution of noise in their initial conditions.

The inset panels in Figures 2.23f, 2.24b and 2.26b show R^2 values for the suite of $z(\chi)$ profiles generated by systematically testing different concavity values (θ_χ; see Section 2.2.6). Highest R^2 values are generated when $0.4 \leq \theta_\chi \leq 0.6$ (note: actual value used to produce the landscapes is 0.5). These results highlight the variability in best-fitting χ transformations introduced by different noisy initial conditions.

Having established that different colours and arrangements of noise in initial conditions contribute to uncertainty in calculated best-fitting concavity, Figure 2.27 demonstrates the impact of using the best-

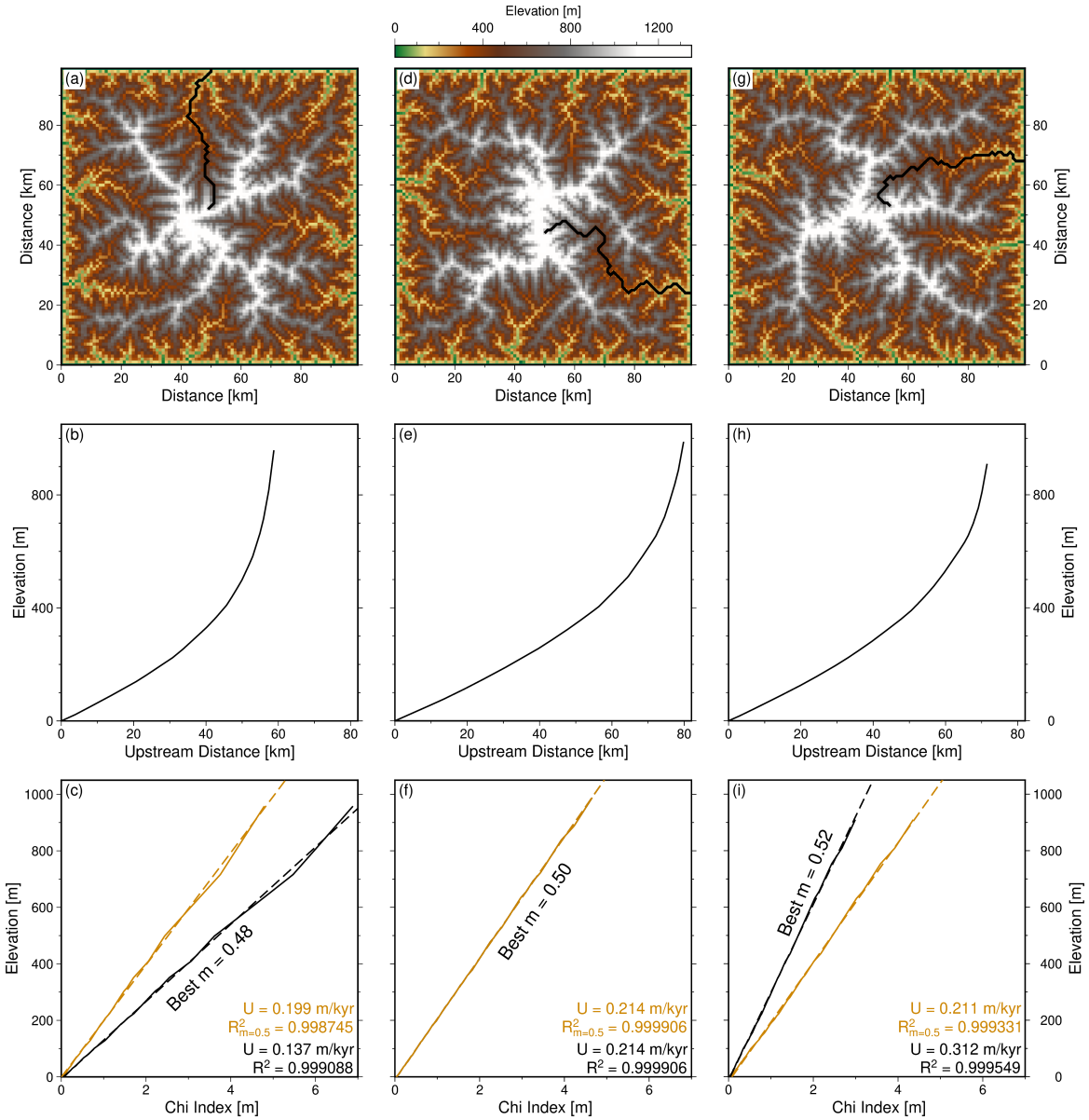


Figure 2.27: **Impact of noise on recovered uplift rates from** $z(\chi)$. (a) Topography and planform of longest single river channel for a steady state landscape initialised with 0–1 m white noise (scenario A). (b) Longitudinal profile of largest river channel. (c) Longitudinal profile transformed into χ space (see Equations 2.17–2.20) using a best-fitting (highest R^2) reference concavity value of 0.48 (black solid line) and the true m/n value of 0.5 (orange solid line). Dashed black and orange lines show linear regressions. The slope of these lines, $dz/d\chi$ is used to calculate an uplift rate (see Equation 2.21). (d–f) and (g–i) show two additional landscapes, longitudinal profiles, and $z(\chi)$ profiles for models in scenario A with different arrangements of white noise and different best-fitting reference concavity values.

fitting values on calculated uplift rates. This test mimics calculation of θ and U from χ-transformation of rivers in the real world. In this demonstration the rivers with the largest upstream drainage area were extracted from three typical landscapes initialised with different arrangements of white noise (scenario A: ensemble 1). Each longitudinal river profile is transformed into a $z(\chi)$ profile using the best-fitting value of concavity. R^2 values for each θ_χ value are shown. In the cases where the best-fitting reference concavity $\neq 0.5$ (i.e., the true value), uplift rates recovered from the slope of the regression line (see Eq. 2.21) significantly differ—by more than 50% when amplitudes of initial noise are $0 - 1$ m—from the true value of 0.2 m/kyr. These results demonstrate that even though chosen values of θ_χ may result in $z(\chi)$ profiles with high R^2 values (> 0.99), they can yield inaccurate and misleading estimates of uplift rates. The instability of calculated U_χ arises because of its sensitivity to the derivative, $\mathrm{d}z/\mathrm{d}\chi$ (see Equation 2.21), and the sensitivity of $\mathrm{d}z/\mathrm{d}\chi$ to noise and the way in which it impacts the geometries of landscapes.

Length-Area relationships

Relationships between maximum channel lengths and upstream drainage areas are shown in Figure 2.23g (black circles) for the main channels within the forty largest basins extracted from a typical 'square' landscape initialised with white noise. A best-fitting non-linear regression, generated using Equation 2.22, is shown, and yields a Hack exponent value, h (slope of regression in log-log space), of 0.574.

Figures 2.24c, 2.26c and 2.28c collate lengths and areas for the main channels in the forty largest drainage basins for each ensemble in scenario A. The non-linear regression is shown for each ensemble. The regressions are similar for landscapes initialised with white and blue noise, However, a shallower gradient (and hence lower h) is required for landscapes initialised with red noise. Each inset panel in these figures show histograms of Hack exponent values calculated for each model from its forty longest rivers. They demonstrate the variability in Hack exponent values: $0.4 \leq h \leq 0.75$, with h values in the landscapes generated with red noise initial conditions tending to be slightly lower than those for the white and blue noise initial conditions.

Figures 2.29a-c demonstrates that the amplitude of initial noise has limited influence on the distributions of Hack exponents at the range of amplitudes tested (0.002 to 200 m). Landscapes initialised with different amplitudes of red, white or blue noise have broadly consistent trends. For instance, the 25th and 75th percentile, and median show little variation between ensembles 1, 4 and 7 (Figure 2.29).

These results demonstrate that the distribution of Hack exponent values largely do not depend on the amplitude of initial noise. They all show considerable variance arising from noisy initial conditions.

Hypsometry

The history of hypsometry for a single landscape is shown in Figure 2.23h. A large proportion of the landscape has relatively high elevations early in its evolution, whilst fluvial networks are forming. As the landscape matures, an increasing proportion of its area is at lower elevations. Figures 2.24d, 2.26d and 2.28d show the hypsometries of steady state landscapes within scenario A. Two features are emphasised. First, changing the arrangement of specific distributions of noise (i.e., red, white, blue) generates up to approximately 5% variability in the hypsometry, but the shape of the hypsometric curves remain similar. This result is expected as hypsometry is largely insensitive to the age or maturity of landscapes once they approach steady state. Secondly, there is little difference between the hypsometries of the landscapes initialised with red, white or blue noise once they reach steady state. Figures 2.29d-f show the hypsometries for ensembles 1, 4 and 7 in which amplitudes of noise in the initial conditions is systematically varied between 0.002 and 200 m. These results show that hypsometries of steady state landscapes are largely insensitive to the amplitudes of initial noise.

Spatially variable uplift

I now draw attention to the results for domal landscapes (Figure 2.28). As expected, given there is less cumulative uplift overall across the domain, they tend to reach steady state earlier than 'escarpment' or 'square' landscapes generated with the same erosional model (Figure 2.9k-o). Given that a fundamental assumption in slope-area and χ analyses (i.e., that uplift is spatially invariant) no longer holds, it is also unsurprising that the results shown in Figure 2.28a-b have considerably more scatter than the equivalent panels in Figures 2.24 and 2.26. Decreases in slope as a function of upstream area are not linear, clearly departing from the analytical solutions expected when uplift is spatially invariant. $z(\chi)$ profiles are not (col)linear when produced using the true concavity value of 0.5. Instead, the value of θ_χ that best linearised these profiles is close to 1. Therefore, it is also unsurprising that calculated values of uplift rate and concavity indices are wrong when uplift varies spatially. Alternative approaches to recovery of uplift histories and erosional parameter values are discussed in Section 2.4.

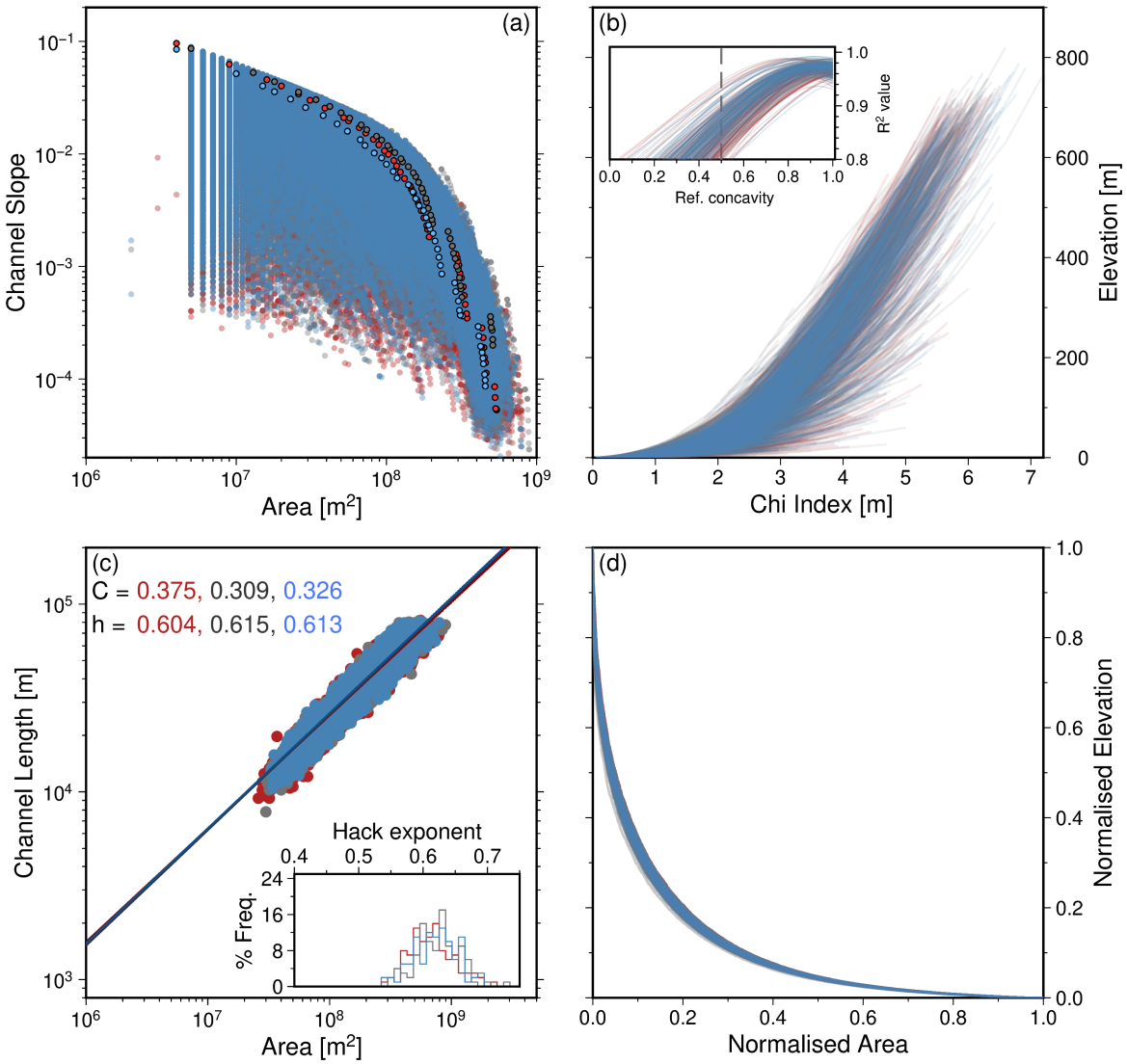


Figure 2.28: **Geomorphic metrics of steady state 'domal' landscapes initialised with red, white or blue noise.** (a) Coloured circles with black outline show slope-area relationships for the main channel in the largest drainage network in single, typical, simulations initialised with red, blue or white noise. (b–d) See Figure 2.24 for notation.

Impact of initial sink-filling

To assess the role of initial sink-filling in generating variability in drainage planforms and geomorphic metrics, the models in ensembles 1, 4, and 7 are rerun with the initial sink-filling step excluded. Figure 2.19 shows drainage probabilities, identical to Figure 2.20a-c, of course with the modification that the landscapes have been generated without an initial sink-filling step. Comparing the two demonstrates that neglecting this step produces, in general, drainage networks which are more direct (less sinuous) than those which have been produced after an initial filling of sinks. However, the remaining patterns of drainage probability (i.e., broadly equal probabilities to four edges, low probabilities within a central cross) are consistent with those in Figure 2.20 and Figure 2.18.

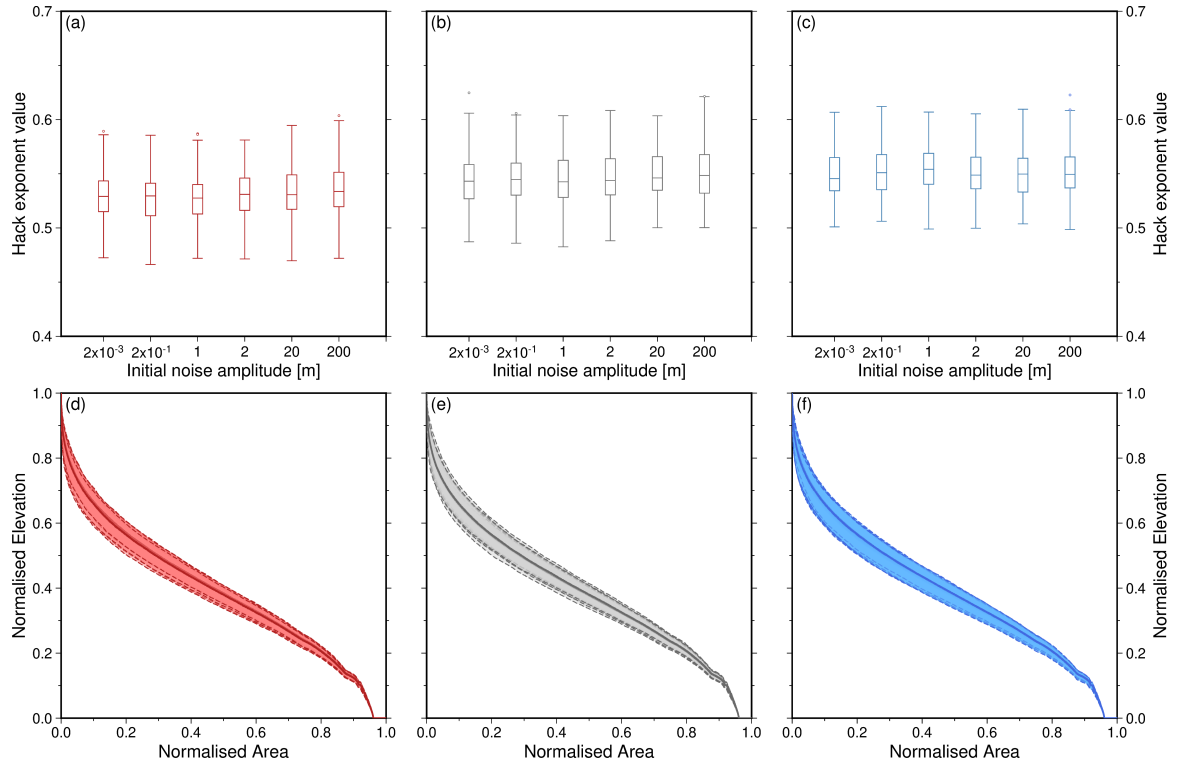


Figure 2.29: **Impact of amplitude of initial red, white or blue noise on geomorphic metrics recovered from steady state 'square' landscapes.** Each box-and-whiskers plot shows results for $M = 100$ landscapes generated with annotated initial noise of indicated colour. Whiskers = 1.5×IQR, or maxima/minima if higher/lower; dots = fliers. (a–c) Range in Hack exponent. (d–f) Solid lines = median hypsometries; filled areas shows range for $M = 100$ landscapes of each amplitude of initial noise, bounded by dashed lines.

Figure 2.17 summarises the variability of drainage basins areas, akin to Figure 2.16 (though for 300 simulations, rather than 3000). Again, both results are similar. The same is true of Figure 2.25, which summarises metrics for the 'square' landscapes generated with no initial sink-filling (cf. Figure 2.24).

2.3.2 Scenario B: Quenched noise

Drainage Planforms and Steady State

The impact of adding quenched noise to the morphometry of a single simulated landscape is shown in Figures 2.31a-b. In this typical example, both landscapes are initialised with identical noisy starting conditions and evolve under the same forcing except for the identical (quenched) noise that is added at each time step to the model shown in panel a. The landscape with quenched noise contains a larger proportion of higher elevations, as expected due to the additional noise. The mean elevation of added noise is 0.5 m per time step (10 kyr). In essence, the addition of quenched noise in this way may be considered as a noisy but spatially constant uplift rate of 0.2 – 0.3 m/kyr, with a mean uplift rate of 0.25 m/kyr. Thus, added noise contributes mean cumulative uplift of 5 km by 100 Myr. In

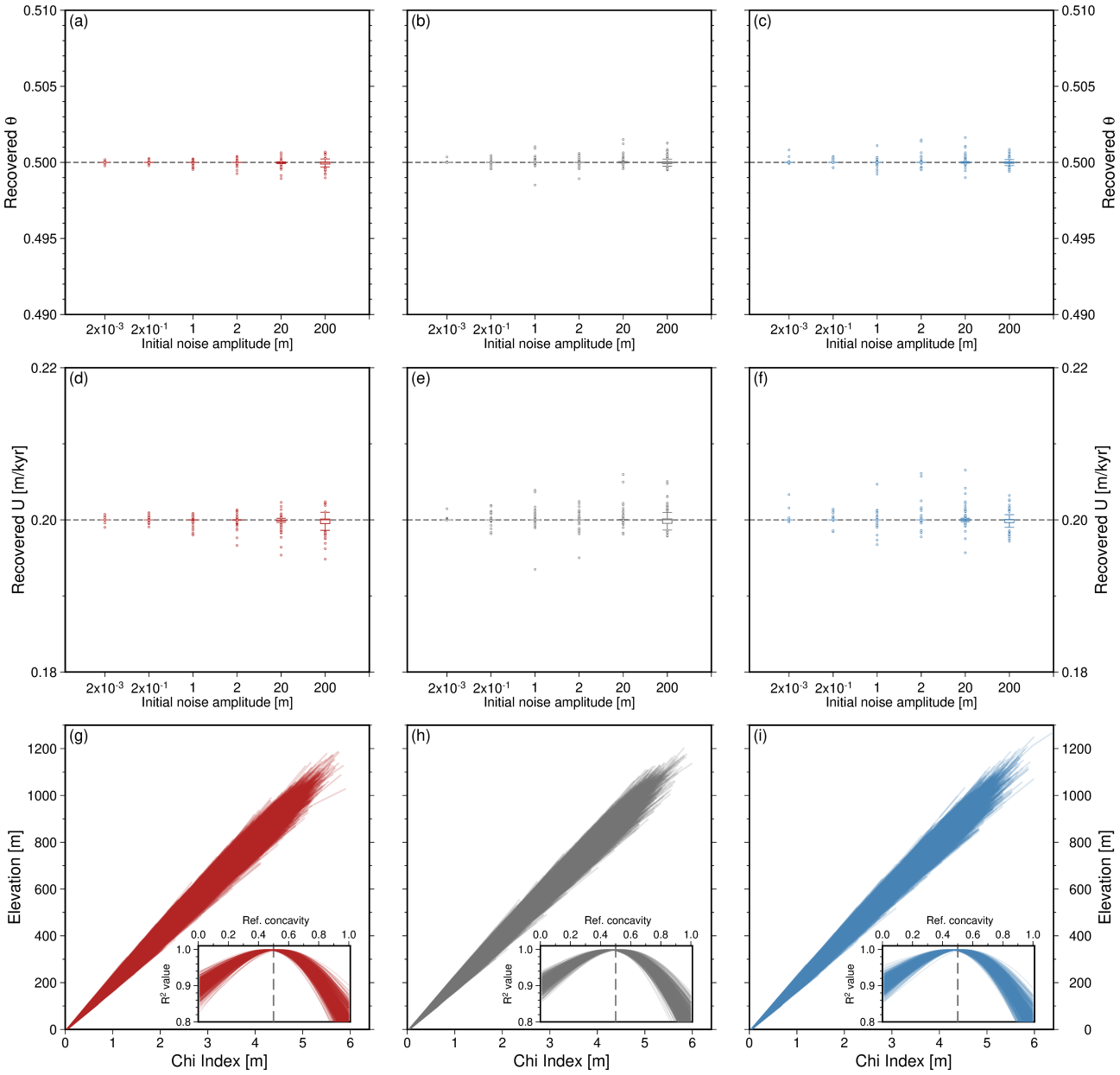


Figure 2.30: **Impact of amplitude of initial red, white or blue noise on geomorphic metrics recovered from steady state 'square' landscapes.** (a–f) Each box-and-whiskers plot shows results for $M = 100$ landscapes generated with annotated initial noise of indicated colour. Whiskers = 1.5×IQR, or maxima/minima if higher/lower; dots = fliers. (a–c) Range of θ values recovered from slope-area analysis. Dashed black line shows 'true' θ value used to parametrise LEM. (d–f) Range of uplift rates recovered from slope-area analysis. (g–i) χ-elevation profiles and associated reference concavities for all channels in the largest basin in each simulation with the different amplitudes of noise indicated in panels (a–f).

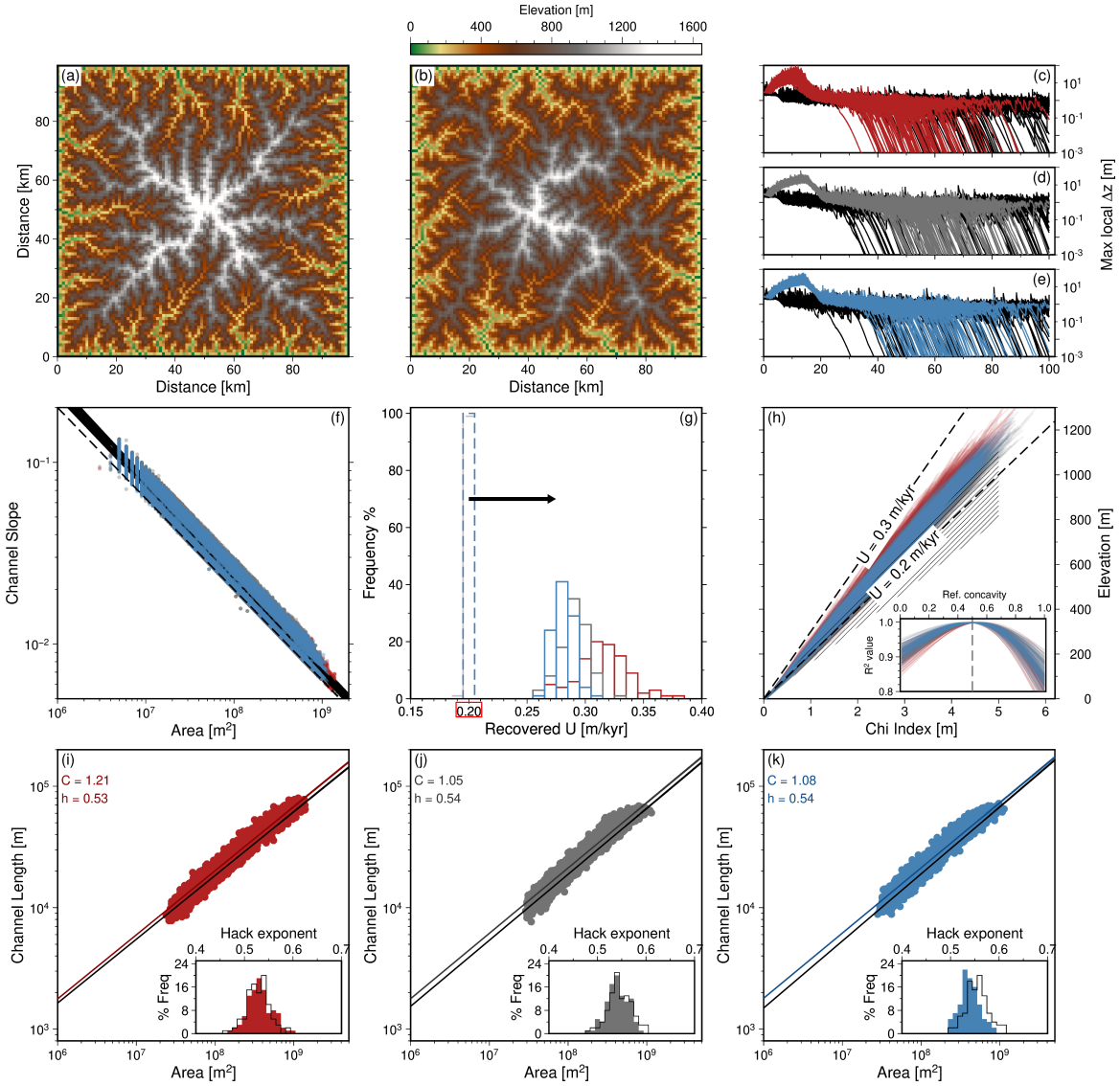


Figure 2.31: **Comparison of geomorphic metrics for steady state 'square' landscapes evolving with initial or quenched noise.** (a) Topography (at 100 Myr) generated with 0 – 1 m of identical (i.e., quenched) white noise added at every time step, i.e., scenario B in Figure 2.7. (b) Landscape at 100 Myr generated with identical initial condition to (a) but with no additional noise, i.e., scenario A in Figure 2.7. (c–e) Changes in maximum local relief in $M = 100$ landscapes generated with only initial noise (black lines), and red, white or blue quenched noise (coloured lines). (f–k) Geomorphic metrics for $M = 100$ red, white or blue landscapes generated with quenched noise unless otherwise indicated. (f) Slope-area relationship for grid nodes with drainage area exceeding 4 km^2. Black lines = linear regression. (g) Solid lines = histograms of uplift rate recovered from each of the 100 red, white, and blue quenched noise landscapes from slope-area analysis. Dashed lines = results for landscapes with only initial noise. Red rectangle = 'true' uplift rate used to parametrise the LEMs. (h) $z(\chi)$ profiles for the main channel and its tributaries of the largest drainage basin in each simulation, produced using $\theta = 0.5$. Black hashed region shows range of equivalent $z(\chi)$ profiles when quenched noise with elevations -0.5 to 0.5 m is added (see Section 2.3.2 for details). Inset shows the R^2 value of different reference concavities. (i–k) Upstream drainage area vs. channel length for main trunks of the forty largest drainage networks in the red (i), white (j), and blue (k) quenched noise landscapes. Black line = non-linear least squares best-fit. Filled/black histograms show the range in Hack exponent for each simulations from quenched noise/initial noise landscapes.

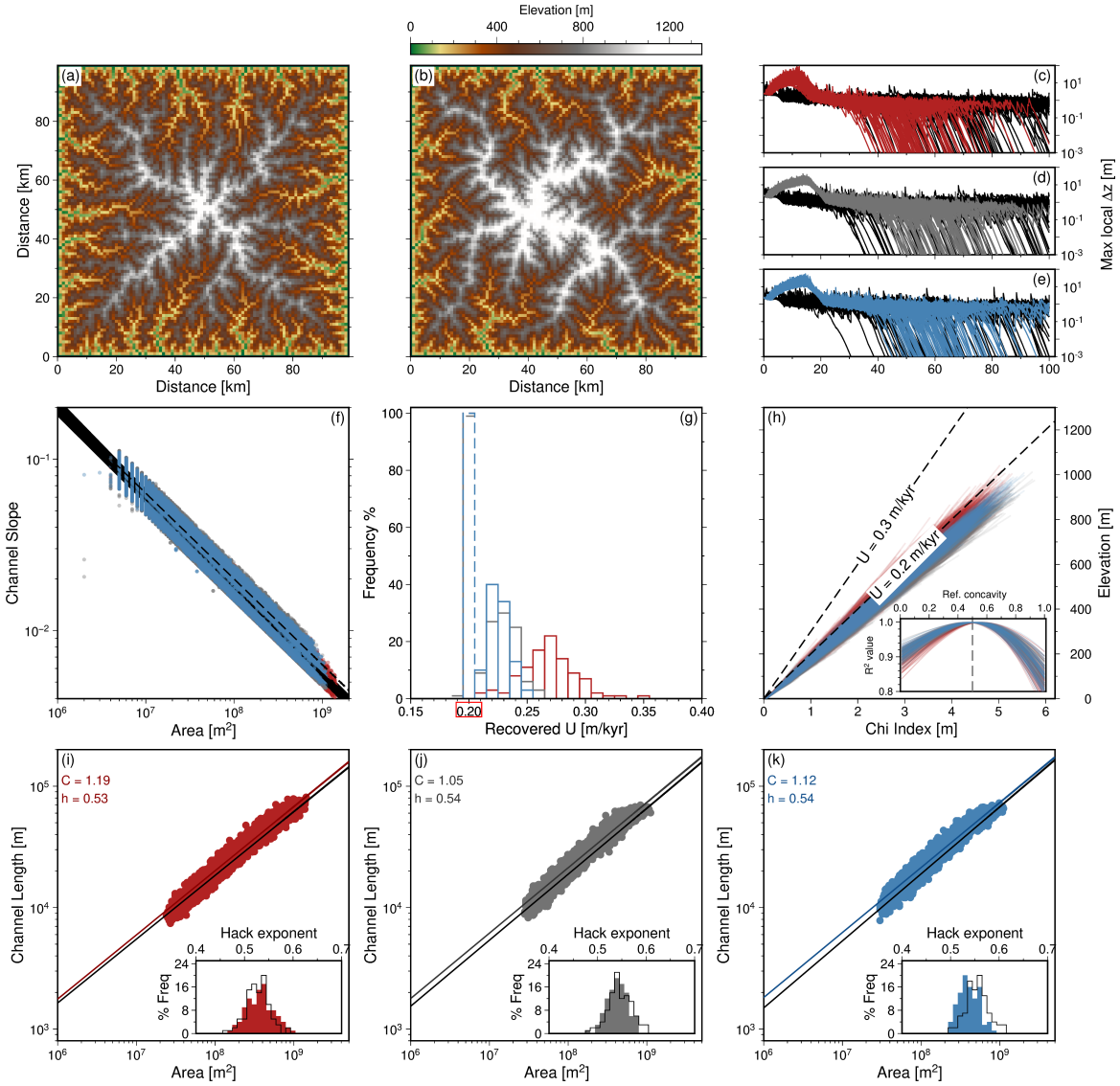


Figure 2.32: **Comparison of geomorphic metrics for steady state 'square' landscapes evolving with initial or quenched zero-mean noise.** (a) Topography (at 100 Myr) generated with −0.5 to 0.5 m of identical (i.e., quenched) white noise added at every time step. (b) Landscape at 100 Myr generated with identical initial condition to (a) but with no additional noise, i.e., scenario A in Figure 2. (c–e) Changes in maximum local relief in $M = 100$ landscapes generated with only initial noise (black lines), and red, white or blue quenched noise (coloured lines). (f–k) Geomorphic metrics for $M = 100$ for red, white or blue landscapes generated with quenched noise unless otherwise indicated. (f) Slope-area relationship for grid nodes with drainage area exceeding 4 km^2. Black lines = linear regression. (g) Solid lines = histograms of uplift rate recovered from each of the 100 red, white, and blue quenched noise landscapes from slope-area analysis. Dashed lines = results for landscapes with only initial noise. Red rectangle = 'true' uplift rate used to parametrise the LEMs ($U = 0.2$ m/kyr). (h) $z(\chi)$ profiles for the main channel and its tributaries of the largest drainage basin in each simulation, produced using $\theta = 0.5$. Inset shows the R^2 value of different reference concavities. (i–k) Upstream drainage area vs. channel length for main trunks of the forty largest drainage networks in the red (i), white (j), and blue (k) quenched noise landscapes. Black line = non-linear least squares best-fit. Filled/black histograms show the range in Hack exponent for each simulations from quenched noise/initial noise landscapes.

comparison, when added noise has a mean elevation of 0 m per time step, the quenched noise landscape has elevations which are similar to that of the landscape in Scenario A (see Figure 2.32).

This figure demonstrates that the geometry of the drainage network in a landscape generated with quenched noise can differ from that in a landscape generated with the same arrangement of noise only in its initial condition. Landscapes generated with the same distributions (but different arrangements) of quenched noise tend to have drainage patterns that are more similar to each other than those generated with different arrangements of initial noise (cf. Figures 2.7 and 2.20). These results are attributed to the enhanced role noise plays in determining the location of drainage networks when it is quenched.

Figure 2.31c–e illustrates that landscapes with quenched noise tend to have an early phase during which they tend to move away from equilibrium (see increasing Δz between 0–15 Myr) before moving towards equilibrium ($\Delta z \rightarrow 0$ at $T > 15$ Myr). Such trajectories have not been observed in models in which noise is only inserted into initial conditions (see black curves in Figure 2.31c–e).

Slope-Area, χ, and Length-Area Analyses

Figures 2.31f-g show that slope-area data becomes more scattered when noise is quenched compared to when it is only inserted into initial conditions. A consequence of this scatter is that there is more variability in the lines of best fit (shown in Figure 2.31f), including their slopes and intercepts, which positively trade off against each other (Figure 2.33). Consequently, recovery of the true uplift rate becomes more unreliable, even when elevation added by quenched noise is corrected (average: 0.05 m/kyr; see arrow in Figure 2.31g), or when quenched noise has a mean elevation of 0 m (Figure 2.32g). Recovered rates are 25% to 85% higher than the true value of 0.2 m/kyr. Uplift rates recovered from landscapes with quenched red noise have greater variance than those generated with quenched white or blue noise. The reasons why distributions of recovered values of U are not centred at 0.25 m/kyr is explored in the Discussion section.

To test the impact of quenched noise on uplift rates extracted from χ analyses I examine the consequences of fixing θ to its true value (0.5; Equation 2.21). Figure 2.31h shows that $z(\chi)$ profiles generated in this way are linear with some scatter. Landscapes with quenched red noise tend to have higher elevations as a function of χ than those with quenched white or blue noise. It is noted that, in contrast, noise inserted only into initial conditions results in more similarly distributed $z(\chi)$ profiles (ensembles 1, 4, 7; cf. Figures 2.24b & 2.31h). The best-fitting concavity values are centred on the

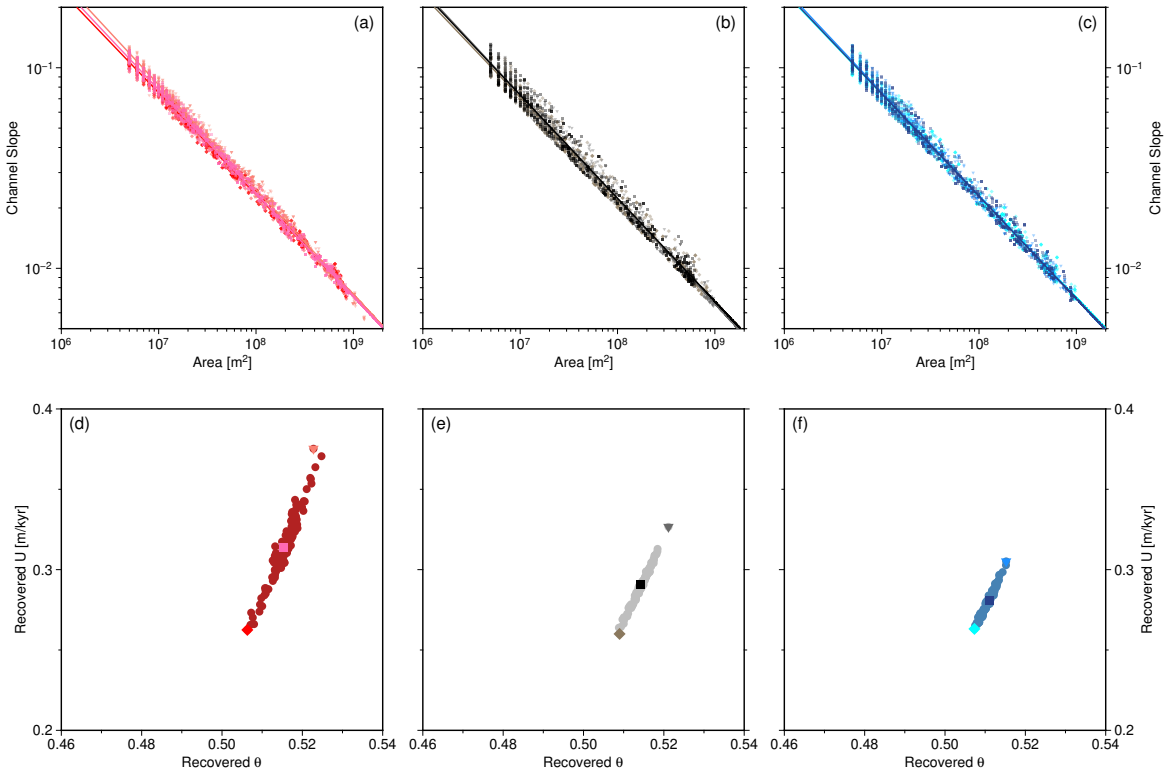


Figure 2.33: **Trade off between recovered parameters from slope-area data.** (a–c) Slope-area data from three selected simulations containing quenched ('frozen') red, white, or blue noise, respectively, where recovered uplift rate is low, intermediate, or high within the distribution of recovered rates. (d–f) Each panel shows the relationship between the value of θ and uplift rate, U, calculated from the best-fitting regression line of the 100 models containing quenched ('frozen') red, white, or blue noise respectively within Scenario B; i.e., the regressions shown within Figure 2.31f. Data from selected models within panels (a)–(c) is highlighted with respective colours/symbology.

true value of 0.5 in both cases (see inset panels in Figures 2.24b & 2.31h). The black hashed region in Figure 2.31h shows that scatter in $z(\chi)$ profiles is also present when quenched noise has elevations of -0.5 to 0.5 m (and mean elevation of 0).

Figure 2.31i-k illustrates that there can be large variability in Hack exponent, h, values when noise is quenched. The distributions of h are broadly similar in simulations with quenched noise and noise inserted only into the starting condition (cf. coloured and black histograms in Figure 2.31i-k).

2.3.3 Scenario C: Spatio-temporal noise

There are two main differences in the results obtained from landscapes generated with quenched or spatio-temporal noise. The first (expected) result is that landscapes with spatio-temporal noise never reach true steady state (Figure 2.34c). Time series of maximum local Δz show that, similar to models in scenario B, simulations with spatio-temporal noise take up to 20 Myr to stabilise around a gradually decreasing mean value. However, they do not reach true numerical steady state (i.e., $\Delta z = 0$) as a result

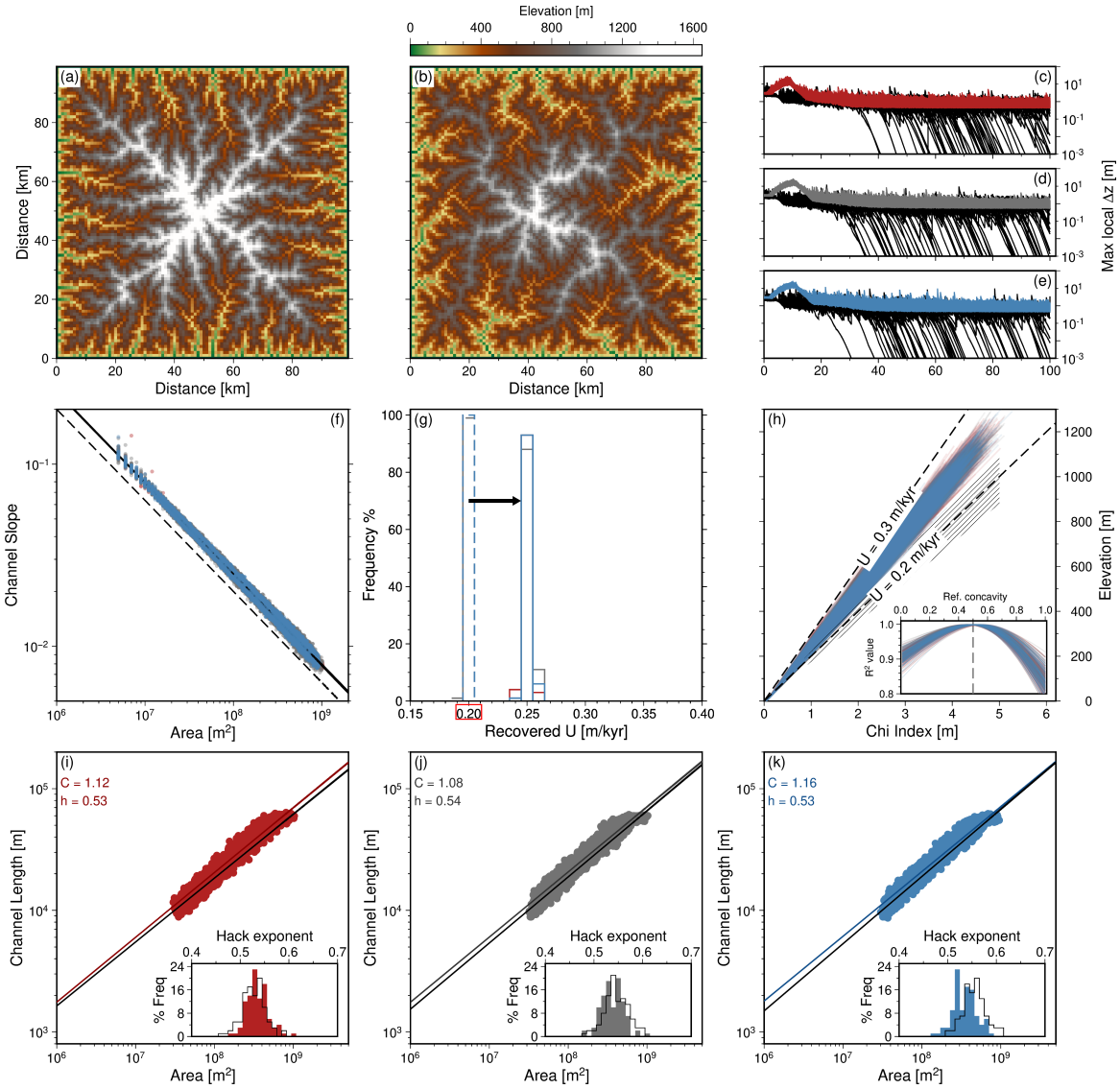


Figure 2.34: **Comparison of geomorphic metrics for 'steady state' 'square' landscapes evolving with initial or spatio-temporal noise.** (a) Example of a 'steady state' landscape (at 100 Myr) generated with different (spatio-temporal) arrangements of white noise added at each time step. (b) 'Steady state' landscape (at 100 Myr) generated with identical initial condition to (a). (c–k) Same annotation as for Figure 2.31 for models with spatio-temporal red, white or blue noise, or noise added only to the initial condition.

of the arrangements of added noise changing at each time step. The absence of spatial consistency in added noise can prevent erosion from balancing the added elevations within a single time step. The second main difference is that, unlike quenched noise, adding spatio-temporal noise produces less scattered slope-area relationships (Figure 2.34f). Consequently, uplift rates recovered via linear regression are more tightly clustered than those generated in scenario B. However, they are offset from the true value by the added noise (see arrow in Figure 2.34g). This offset is not present when spatio-temporal noise has a mean elevation of 0 m (Figure 2.35g). A corollary is that recovering true tectonic uplift rates requires information about the amplitude and distribution of noise in a landscape. In

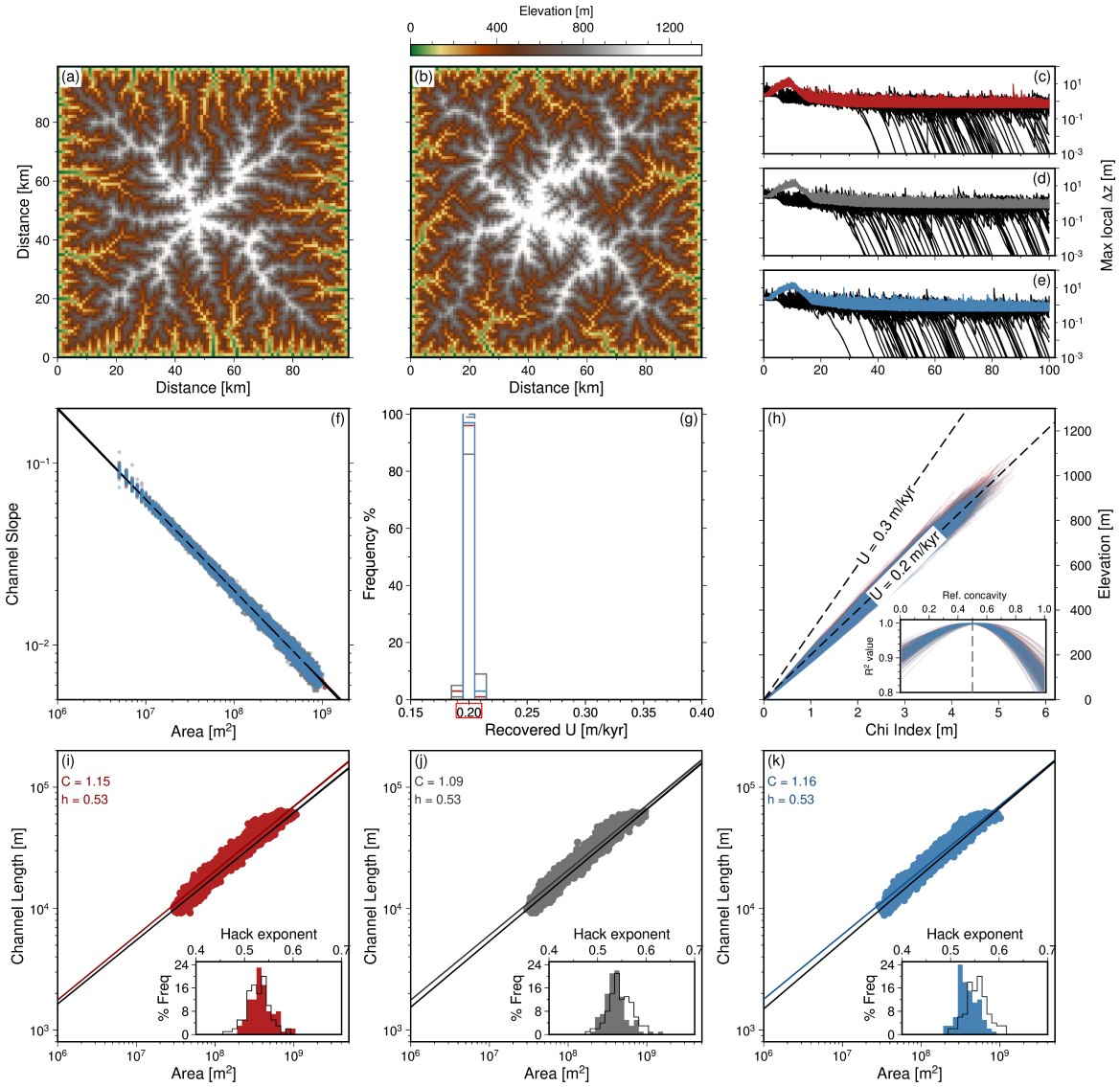


Figure 2.35: **Comparison of geomorphic metrics for 'steady state' 'square' landscapes evolving with initial or spatio-temporal zero-mean noise.** (a) Example of a 'steady state' landscape (at 100 Myr) generated with different (spatio-temporal) arrangements of white noise of amplitudes −0.5 to 0.5 m added at each time step. (b) 'Steady state' landscape (at 100 Myr) generated with identical initial condition to (a). (c–k) Same annotation as for Figure 2.32 for models with spatio-temporal red, white or blue noise, or noise added only to the initial condition.

contrast, the results from $z(\chi)$ analyses, drainage probabilities, and channel length-area relationships are all broadly similar to those obtained for scenario B (Figures 2.34h, i–k, & 2.20g–i).

2.3.4 Scenario D: Addition of un-eroded noise

The impact on geomorphic metrics of adding noise to a steady state landscape such that the noise remains un-eroded is shown in Figures 2.36 and 2.40. Adding noise in this way acts to 'blur' topography, and increases the proportion of elevations which are between 20–50% of the maximum height, shown in Figure 2.36c. Whilst the impact of adding 0–20 m of noise is subtle on the longitudinal profiles shown

in Figure 2.36d, this noise generates scatter in the slope-area data such that recovered uplift rates are 50% larger than the steady state case. $z(\chi)$ profiles are less affected by 0–20 m of un-eroded noise, but become highly scattered when 0-200 m of un-eroded noise is added to the landscape. Slope-area analysis is demonstrably an inappropriate technique to use for recovering U and θ from steady state landscapes containing, say, 200 m of un-eroded noise. In fact, even 20 m of added noise can result in calculated uplift rates being unreliable (Figures 2.40b, 2.37 to 2.39).

2.4 Discussion

2.4.1 Distributions of geomorphic metrics and determinism

Results obtained from scenarios A – D are synthesised in Figure 2.40 and this is used as a framework to discuss key findings regarding geomorphic metrics.

Across almost all scenarios distributions of results are obtained from model ensembles. In other words, slope-area relationships, χ analysis, and length-area relationships are sensitive to noise inserted into the models. These results emphasise the benefits of using model ensembles or probabilistic approaches to landscape evolution modelling (rather than relying on interpretation of singular, or small-batch, runs of stream power-based models). An ensemble-based approach permits characterisation of, for instance, uncertainty and dependence on noisy (starting) conditions, model assumptions or model parameter values. These results clearly indicate that caution is required to avoid over-interpretation of results from single models (and the real world) which may be outliers with geometries that depend on an arbitrary noisy starting condition, which in reality represents (largely) unknowable palaeo-conditions (topography, weather, climate, biota, etc.) It emphasises the importance of embracing the fundamental unknowability inherent to landscapes and thus the importance of quantifying the impact of noise (and especially its distributions) on geometric predictions (e.g., of topography, sedimentary flux) and calculated metrics (see e.g., Perron and Fagherazzi, 2012; Gray et al., 2017; Lyons et al., 2020; Roberts and Wani, 2024; Thompson Jobe and Reitman, 2025).

Uplift Rates and Concavity Indices Recovered from Slope-Area and χ Analyses

The sensitivity of slope data to added noise has previously been discussed, for example in Roberts et al. (2012a) and Mudd et al. (2018). In this chapter, it is shown that, when operating in a numerical steady state under spatially invariant uplift, slope-area analysis can be used to recover input values of erosional parameters and uplift rates (see e.g., Figures 2.23, 2.40a-b). However, it is also shown

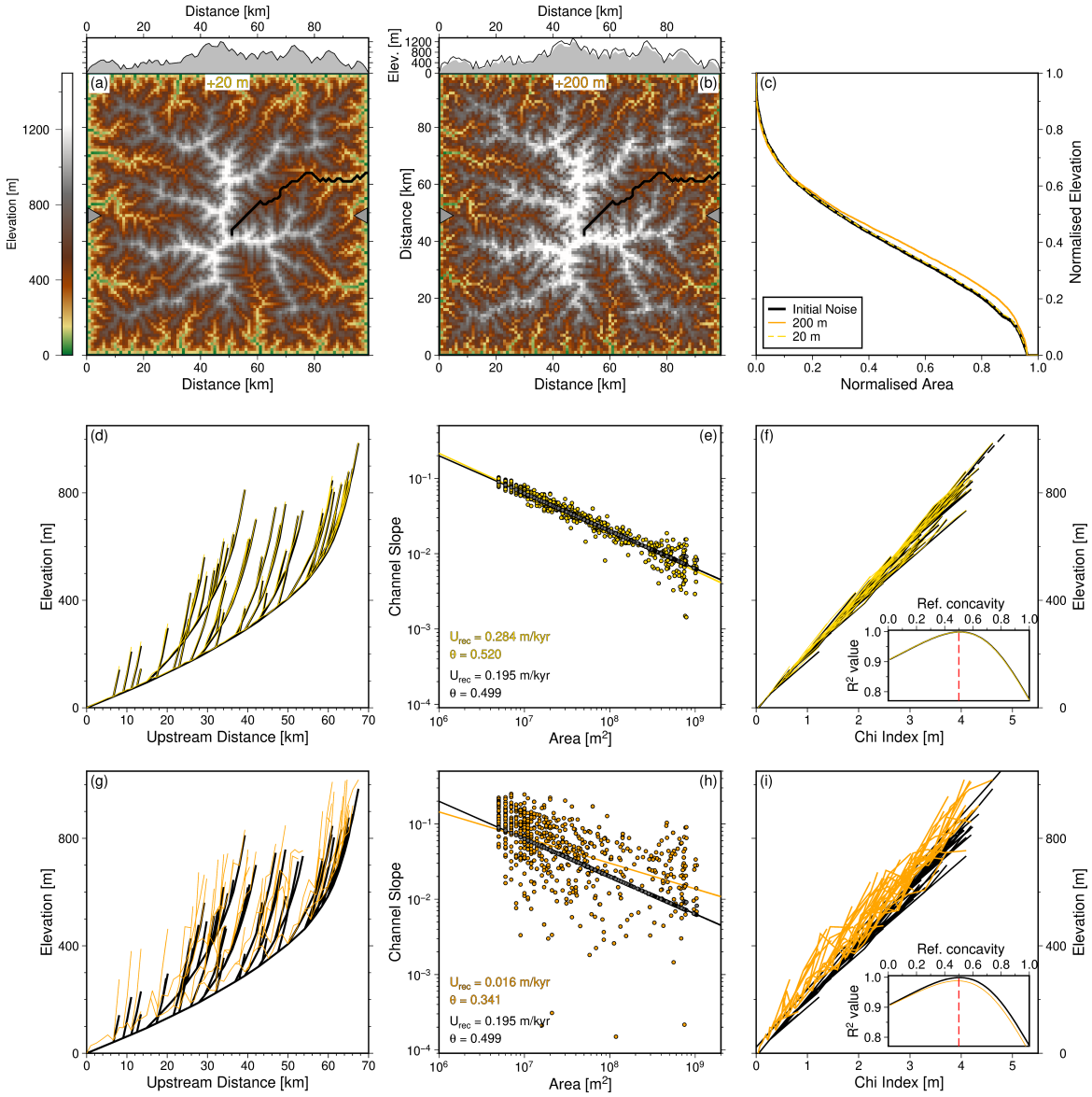


Figure 2.36: **Impact of un-eroded noise on metrics: An example.** (a) Steady state 'square' landscape generated with up to 1 m of white noise in its initial condition (Figure 2.8: ensemble 1), and with up to 20 m of white noise added after the final model time step. Filled grey transect shows topographic profile of steady state landscape (without final noise). (b) Same landscape as in panel (a), but with up to 200 m of un-eroded noise. Black outline shows location of the same (longest) river in landscapes with final noise added. (c–i) Yellow/orange = geometries and metrics extracted from landscapes with up to 20 and 200 m of un-eroded noise. (c) Black dashed curve = hypsometry of landscape shown in panel (a); colours = hypsometries of landscapes with un-eroded noise. (d–f) Longitudinal profiles of rivers in largest drainage basin (see panel a), slope-area and χ analyses of rivers shown in panel (d) respectively, for steady state landscape and landscape with 0–20 m noise added. (g–i) As above, for landscape with 0–200 m noise added. Metrics for un-eroded red and blue noise are shown in Figures 2.38 and 2.39

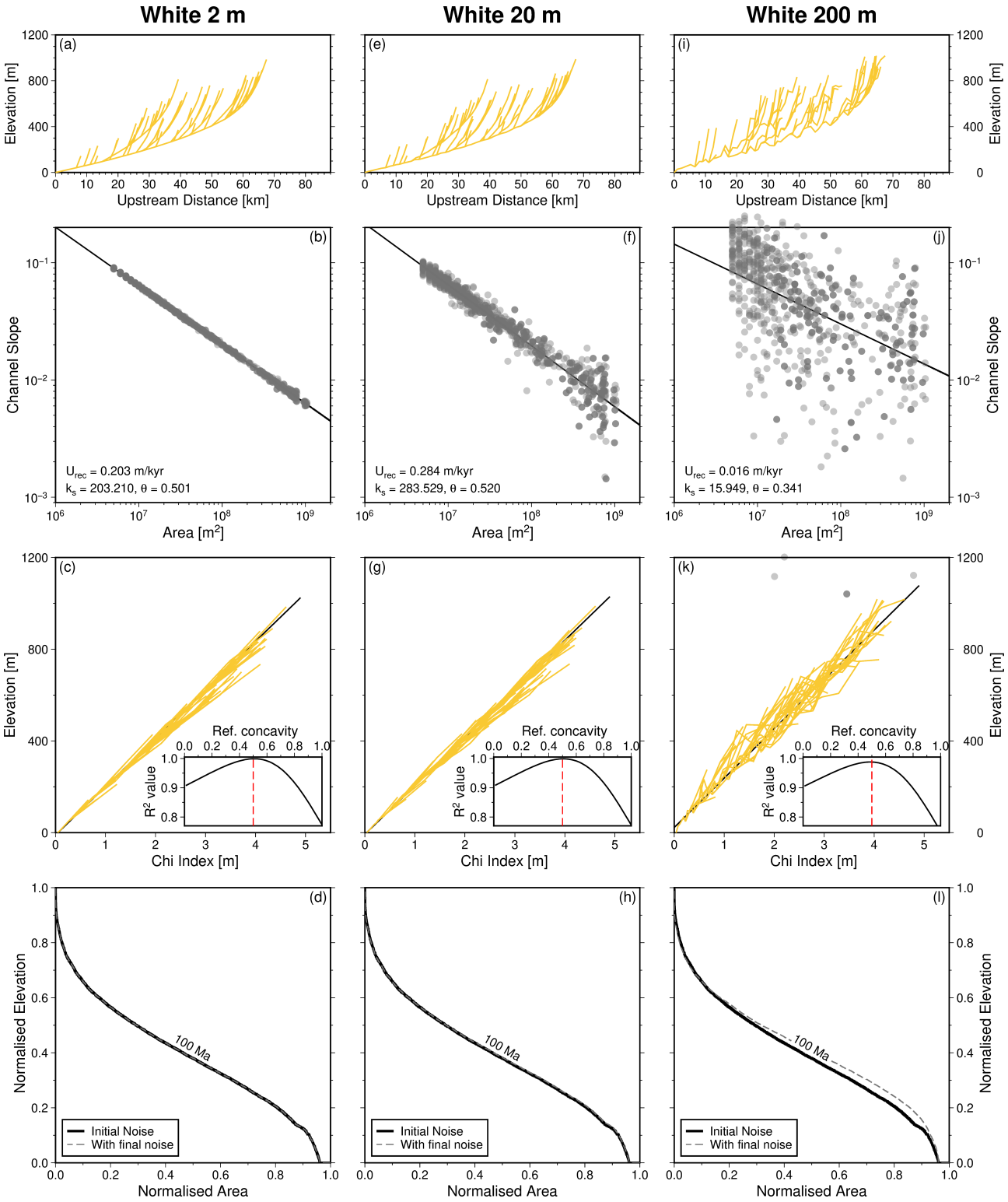

White 2 m
White 20 m
White 200 m
(a)
(e)
(i)
Elevation [m]
Upstream Distance [km]
(b)
(f)
(j)
Channel Slope
Area [m^2]
U_{rec} = 0.203 m/kyr
k_s = 203.210, θ = 0.501
U_{rec} = 0.284 m/kyr
k_s = 283.529, θ = 0.520
U_{rec} = 0.016 m/kyr
k_s = 15.949, θ = 0.341
(c)
(g)
(k)
Chi Index [m]
Ref. concavity
R^2 value
(d)
(h)
(l)
Normalised Elevation
Normalised Area
100 Ma
Initial Noise
With final noise

Figure 2.37: **Examples of geometries of river profiles and associated metrics in landscapes with un-eroded white noise.** (a–d) Results when up to 2 m of un-eroded noise is added to steady state landscape shown in Figure 2.12e (see Figure 2.36). (a) Longitudinal profiles of rivers extracted from largest basin. (b) Grey circles = slope-area analysis and associated metrics of the longest river. Note: some measurements extend beyond panel bounds in later examples with higher amplitude noise. Black line = linear regression; associated values of θ, k_s and U_{rec} are annotated. True uplift rate = 0.2 m/kyr, and $\theta = 0.5$. (c) Chi-elevation profiles of rivers shown in panel (a). Black line = linear regression. Inset shows R^2 values for different concavity indices used to linearise river profiles; red dashed line = true value used to produce the landscape. (d) Hypsometry of steady state landscapes with only initial noise (solid) and with additional (un-eroded) noise (dashed; cf. Figures 2.36a and 2.36b). (e–h) and (i–l) Results when up to 20 and 200 m of un-eroded noise are incorporated, respectively.

that this technique does not yield accurate results under conditions of spatially variable uplift (Figure 2.28), or when noise is added during or at the end of a simulation (Figures 2.36, 2.40a-b). This finding is also true of χ analysis, which is impacted by noise in a different way.

The specific arrangement and distribution of noise used as a starting condition can change the value of the reference concavity which best linearises $z(\chi)$ profiles. The sensitivity of χ to reference concavity values has also been shown by Gailleton et al. (2021). Best-fitting reference concavity values are shown in Figure 2.40c, and can vary from the true value of 0.5 (in this study). The colour of noise has a minor impact on the variance of the distributions. The distributions become less centred on 0.5 when the amplitude of initial or final noise increases, or when quenched noise is present. Figure 2.27 shows the impact of using different values of θ_{ref} to generate $z(\chi)$ plots, and the resulting distributions of uplift rate calculated from the slopes of these profile are shown in Figure 2.40e. Several clusters of distributions exist because of the different best-fitting values of θ_{ref}, with calculated uplift rates varying between 0.5 and 1.5× the true uplift rate for scenario A, and up to 2× the true uplift rate for scenarios B-D. Even in the case of $z(\chi)$ profiles calculated using the true value of $\theta = 0.5$, rather than the best-fitting θ, recovered uplift rates are distributed around the true uplift rate of 0.2 m/kyr (Figure 2.40d). This result highlights the uncertainties generated from noisy conditions in landscape evolution models and thus the challenges associated with interpreting outputs from single models.

A further complication in recovering tectonic information from slope-area and $z(\chi)$ analyses arises in cases where uplift is spatially variable, e.g., for domal landscapes. In general, Figures 2.28a-b demonstrate that slope-area analysis is an inappropriate tool for recovering uplift rates and erosional parameter values from domal landscapes, or more broadly landscapes with spatially variable uplift. This comment is extended to also encompass χ analysis when used in this way, given the absence of (col)linearity of $z(\chi)$ profiles in Figure 2.28b and the best-fitting reference concavity being close

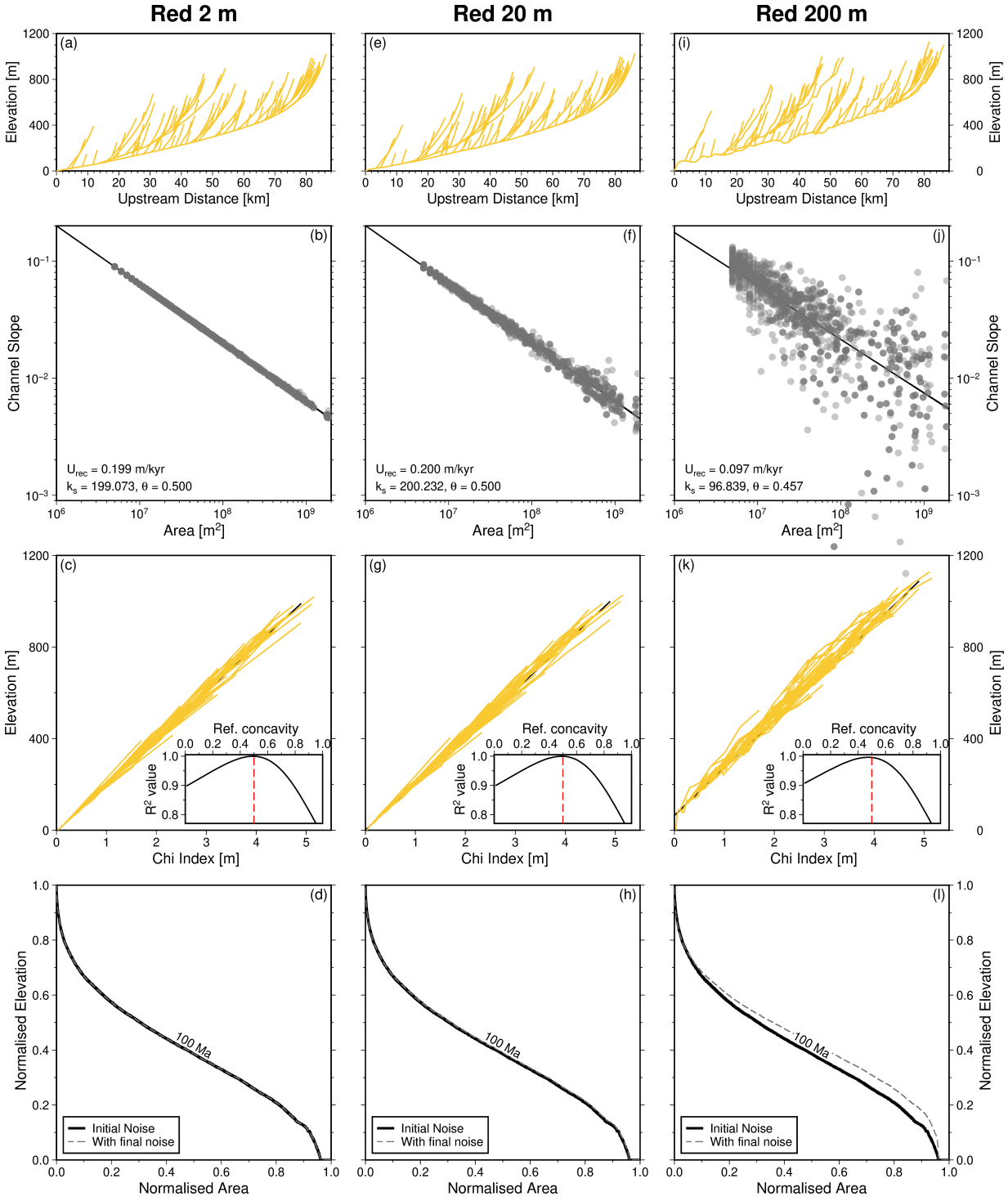


Figure 2.38: **Geometries of river profiles and associated metrics generated with un-eroded red noise.** (a–j) See caption to Figure 2.37 for extended description.

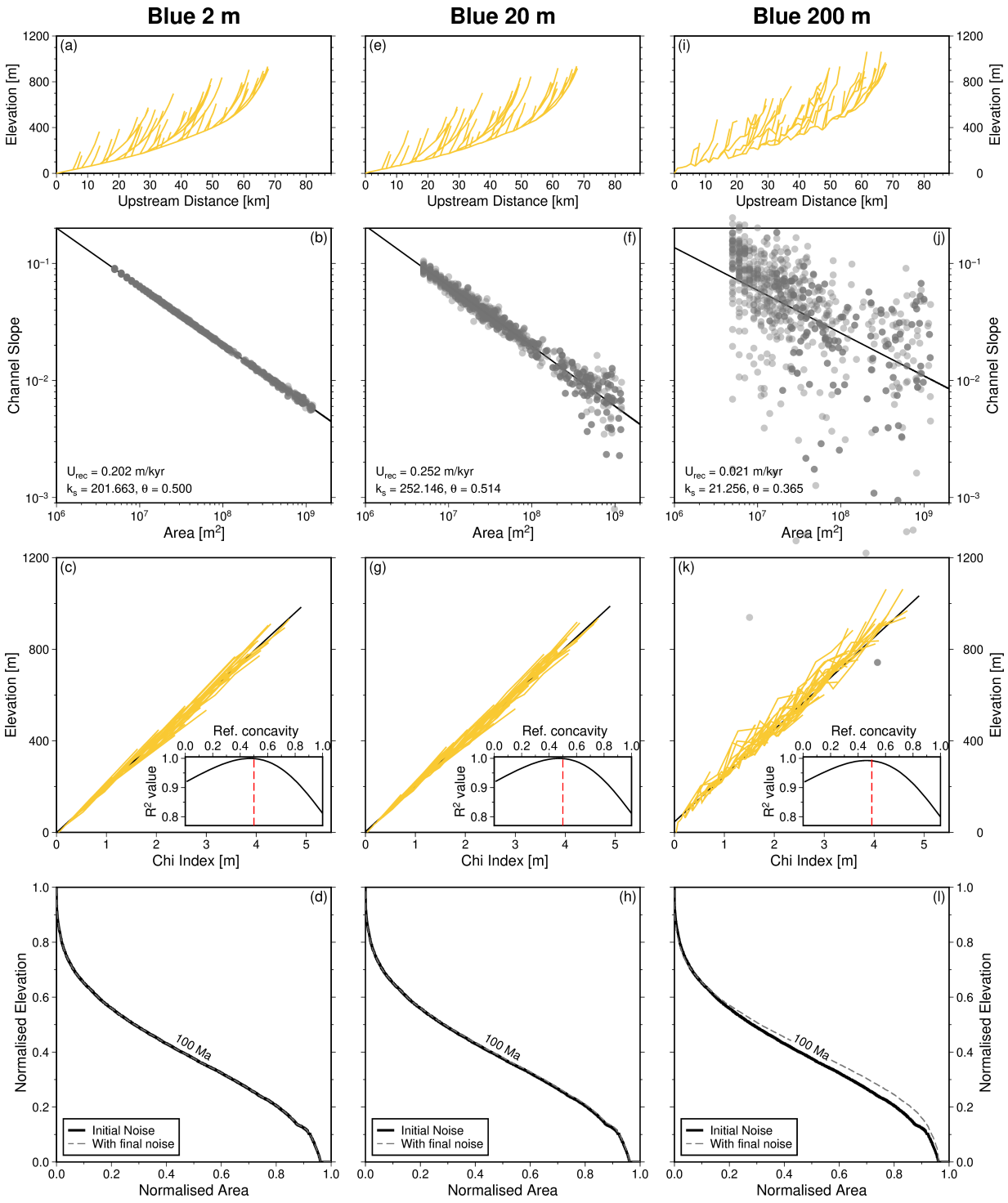


Figure 2.39: **Geometries of river profiles and associated metrics generated with un-eroded blue noise.** (a–j) See caption to Figure 2.37 for extended description.

to 1, rather than the true value of 0.5. It is acknowledged that modifications to χ analysis exist to account for spatially variable uplift (see e.g., Mudd et al., 2014; Hergarten et al., 2016; Mudd et al., 2018). In practice, both slope-area analysis and χ analysis rely on an assumption of steady state, which are discussed in section 2.4.2. This result, generated under steady state conditions and different arrangements, distributions, or implementations of noise, extends those of Mudd et al. (2018), who generate examples of transient synthetic landscapes with spatially variable erodibility or uplift rate, and calculate distributions of best-fitting reference concavities from different basins, across a range of calculation methods.

One could also argue that the uplift applied to the 'square' landscapes in scenario B is spatially variable, due to the presence of quenched noise. A consequence of quenched noise is to add scatter to slope-area data such that recovered uplift rates are distributed between 0.26 and 0.37 m/kyr (Figures 2.31g, 2.40b). Given that the mean elevation of noise added per time step is 0.5 m, and the maximum elevation added is 1 m, it might be expected that quenched noise contributes an additional mean and maximum uplift rate of 0.05 and 0.1 m/kyr, leading to mean and maximum calculated uplift rates of 0.25 and 0.3 m/kyr respectively. Recovered uplift rates being up to 0.37 m/kyr is interpreted as the result of scattered data and trade-offs between the slope and intercept (from which uplift rates are calculated) of the best-fitting linear regression (see Figure 2.33). The presence of quenched noise in models tends to generate considerable spread in slope-area data, and thus in calculated intercepts (and thus uplift rates). In contrast, uplift rates recovered from slope-area data in scenario C are offset from the true uplift rate by 0.05 m/kyr, i.e., the mean amplitude of uplift added from noise. It is noted that it is unlikely that the true amplitudes of noise are known for real landscapes, meaning that it is not trivial and perhaps impossible in some circumstances to correct uplift rates calculated in this way for noise.

Variability in Hack exponent value

A consistent result across all model scenarios and ensembles is the variability in Hack exponent value, h, due to different arrangements and distributions of noise. Hack exponent values vary between 0.45 and 0.75, generally a larger range than previous studies which calculate h based on data from natural landscapes across regional and global scales (Hack, 1957; Mueller, 1972; Montgomery and Dietrich, 1992; O'Malley, 2020; He et al., 2024; Singer et al., 2024). Many of these studies find $0.45 \leq h \leq 0.7$, whilst dimensional analysis predicts $h = 0.5$. It has been suggested that Hack exponent values < 0.5 imply that drainage basins are widening and values > 0.5 imply elongating basins (Mueller, 1972).

Many of the distributions of h calculated from the models have values > 0.5, indicating that, if this reasoning is accepted, basins are elongating more than they are widening. Figure 2.40f demonstrates that on average, landscapes initialised with red noise in Scenarios A–D produce lower Hack exponent values than their white and blue noise counterparts, implying that their catchments are elongating at a slower rate. However, it is unclear that the temporal evolution of drainage basins can be related to length-area relationships obtained at a single model time step, and in many cases the topography is at a numerical steady state (i.e., $\partial z/\partial t = 0$ everywhere), indicating no change in basin geometry. Prior studies have recognised the potential for drainage basin scale to influence the calculation of h (Mandelbrot and Wheeler, 1983; Robert and Roy, 1990). The drainage basins in the models used to calculate Hack exponents range in size from 10^7–10^9 m^2. These sizes fall within the range of basin areas from which Hack exponents have been calculated in previous studies, though are closer in size to those originally examined by Hack (1957), who found $h > 0.5$. Extraction of channel lengths and upstream areas from synthetic landscapes also circumvents measurement errors encountered when calculating these metrics from field data or digital elevation models.

Climatic conditions have also been suggested to influence Hack exponent values. For example, Yi et al. (2018) categorise drainage basins in the contiguous United States by aridity index and find that $h \simeq 0.49$ for basins in arid regions, and $h \simeq 0.59$ for basins in humid regions. Conversely, Singer et al. (2024) find from a global drainage dataset that h increases with increasing aridity. Findings from this chapter suggest that different arrangements and distributions of noise within landscape evolution models produce at least as much variance in Hack exponent values as climatic variables. This result is similar to that of Sassolas-Serrayet et al. (2018) and O'Malley (2020), who found a limited influence of (modern day) mean annual precipitation (and lithology) on Hack exponent values calculated from observational data.

2.4.2 An assumption of steady state

A fundamental assumption underlying the recovery of uplift rates and erosional parameter values from widely used techniques such as slope-area or χ analyses is that uplift rates are balanced by erosion, i.e., there exists a topographic steady state. When operating with synthetic landscapes it is straightforward to numerically verify that this condition is true (e.g., Figure 2.9). The results of this chapter demonstrate that, even under conditions of steady state, recovery of uplift rates and erosional information is complicated by the choice of how noise is included within models, which leads to distributions of recovered values, shown in Figure 2.40.

Notwithstanding inconsistencies in how steady state topography is defined, as outlined by Gasparini et al. (2024), in general, observational evidence to confirm that landscapes in the real-world are at topographic steady state is scant. In fact, most continental topography appears to refute the steady state assumption, which in general must be wrong because geological observations (e.g., uplifted marine rock; sedimentary isopachs indicating punctuated sedimentary flux; incision rates from radiometrically dated rocks) demonstrate that topography increases and decreases in elevation on a variety of spatial and temporal scales, and may horizontally advect (e.g., Rust and Summerfield, 1990; Young and McDougall, 1993; Roberts and Kirschbaum, 1995; Willett and Brandon, 2002; Karlstrom et al., 2007; Stephenson et al., 2019; Racano et al., 2020; Malatesta et al., 2022). These observations, alongside the findings from synthetic landscapes in this chapter, and results from some analogue models, call into question the utility of geomorphic techniques which rely on assumptions of steady state (see e.g., Hasbargen and Paola, 2000).

2.4.3 Drainage planform variability and maximum drainage sizes

Figures 2.15 and 2.18 demonstrate how different arrangements and colours of noise can lead to different drainage planform structures. This result extends that of Kwang and Parker (2019), who interpret the lasting influence of initial conditions in landscape evolution models as an absence of other mechanisms that can remove initial network structure (e.g., lateral erosion and migration of channels present in natural environments; Kwang et al., 2021). Figure 2.15 emphasises how landscapes that evolve with identical tectonic histories can have different geometries due to noise. It is clear that in such cases using Euclidean-based approaches to compare modelled and observed elevations of entire landscapes may lead to undesirable high misfit when tectonic histories are in fact similar. Instead, minimising misfits (via inverse modelling for instance) to recover tectonic (uplift) rates probably requires techniques that can 'see through' the local complexity of precise planform arrangements introduced by specific arrangements of noise (e.g., Morris et al., 2023). More generally, broadly equal probabilities of channel locations under the uplift and erosional conditions modelled (Figure 2.18) indicates that caution should be taken when interpreting drainage planform structures, or related metrics, from single models, or observations. It is noted that the drainage planform patterns of 'square' landscapes containing quenched or spatio-temporal noise (scenarios B, C) more closely resemble the general structure of probabilistic drainage maps than landscapes containing only initial noise (scenario A). For instance, landscapes generated with spatio-temporal or quenched noise tend to have interfluves and high topography with low drainage probability extending in a 'cross' from the centre of the domain to each corner; cf. Figures 2.31a-b,

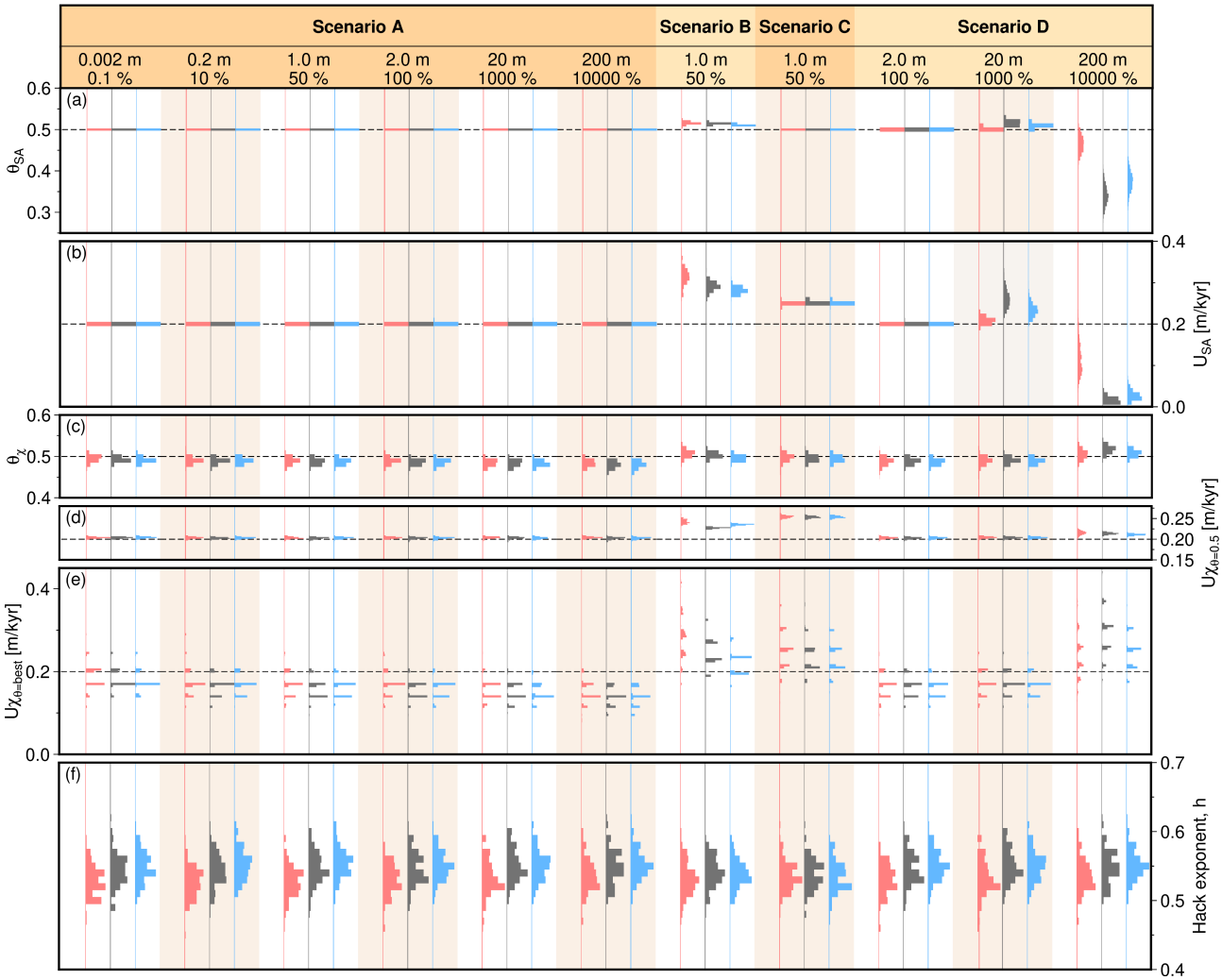


Figure 2.40: **Impact of noise on variance of geomorphic metrics from steady state landscapes.** Series of histograms showing the distribution of different geomorphic metrics under different noisy conditions for the 'square' landscape (Scenarios A–D; see Figures 2.7–2.8). Black dashed lines = true values, used to produce the LEMs. For the quenched and spatio-temporal examples, up to 1 m of noise was added at every time step. (a–b) *Concavity index* and uplift rate recovered from slope-area analysis. (c) Value of *concavity index* that best linearises χ-elevation plots. (d) Corresponding uplift rate associated with the slope of the best-fitting line of χ-elevation data, from the rivers of the four largest basins transformed using $\theta = 0.5$. (e) As per (d), for a slope of the best-fitting line of χ-elevation data from the rivers of the four largest basins, transformed using the respective best-fitting values of θ. (f) Values of Hack exponent calculated from river length-upstream area relationships.

2.34a-b, 2.20. Perhaps surprisingly, even landscapes with quenched noise display this pattern. These results indicate that repeated insertion of noise (i.e. at each time step), reduces the influence of noisy initial conditions on the geometries of landscapes at large scales.

Similarly, the position of drainage divides can also depend on noisy starting conditions, for example the areas of low probability in the 'escarpment' landscapes shown in Figures 2.18d-f. In particular, models initialised with red noise have less well-defined regions of low drainage probability. This result is interpreted as a consequence of long wavelength changes in topography permitting initial flow-lines to span across more than half of the domain, even after sink-filling. Conversely, the shorter wavelength topographic roughness present in landscapes initialised with white or blue noise means that the largest drainage basins usually terminate at the centre of the domain, leading to consistent regions of low drainage probability (see Figures 2.18b-c). This is also interpreted as a mechanism for why the largest drainage basins in 'square' landscapes initialised with red noise are, on average, larger than those from landscapes initialised with white or blue noise (Figure 2.16).

2.4.4 Comparison to natural landscapes

The relevance of initial, quenched, and spatio-temporal noise

The result that distributions in geomorphic metrics arise from different arrangements, colours, and implementations of noise within landscape evolution models is a finding similar to that of Perron and Fagherazzi (2012), and emphasises that the application of noise is not an arbitrary model choice. Whilst noisy initial topography enables the generation of realistic drainage planforms within models, it can also be representative of natural processes or features. For example, noisy starting conditions may be considered to represent a palaeotopography. In some studies, it may be inappropriate to solely implement random noise as a starting condition, for example where it may be possible to guess palaeotopography prior to volcanic eruption or ice cover, for instance (e.g., Paxman et al., 2019; Barnhart et al., 2020d; O'Hara et al., 2024). Yet in many other studies and at different scales, palaeotopography is unknowable and therefore assessing uncertainties using ensembles of models with variable starting conditions is probably a sensible, perhaps necessary, strategy.

However, it is questionable whether the application of noise exclusively as an initial condition is a reasonable assumption. Perhaps incorporating noise throughout model run time is closer to reality. For instance, erosion of substrate with constant (in time) erodibilities, or landsliding occurring repeatedly in the same place, could be regarded as sources of quenched (i.e., fixed for all time) noise. In general

however, geomorphic noise in natural landscapes must vary as a function of space and time. For instance, as lithologies with different erodibilities are exposed. Thus, in scenarios B–C the consequences of adding quenched and spatio-temporal red, white, or blue noise with amplitudes 0 to 1 m and −0.5 to 0.5 m throughout model run time are explored. Figures 2.31g and 2.34g show that noise generates uncertainty in recovered uplift rates, which can be considerable (see also Figures 2.32 & 2.35).

Colour, scale, and metrics

The spectral content of synthetic steady state landscapes generated in scenario A is characteristic of red noise ($\phi \propto k^{-2}$). Similar spectral characteristics have been identified in natural landscapes, across scales from centimetres to thousands of kilometres (e.g., Balmino, 1993; Birnir et al., 2001; Perron et al., 2008; Booth et al., 2009; Roberts et al., 2019). Wavelet spectral analysis of longitudinal profiles for large African rivers shows that their power spectra can be characterised as pink noise ($\phi \propto k^{-1}$) at wavelengths $\lesssim$ 100 km and as red noise ($\phi \propto k^{-2}$) at longer wavelengths (Roberts et al., 2019). The transition from complexity at local scales to relative predictability at large scales emphasises why some geomorphic metrics are more sensitive to noise than others. For example, it is unsurprising that the recovery of uplift rates or erosional parameter values from derivatives (i.e., topographic slopes, $\mathrm{d}z/\mathrm{d}x$, or gradients of $z(\chi)$ profiles, $\mathrm{d}z/\mathrm{d}\chi$) is hampered by the addition of noise; Figure 2.36. In these examples, metrics which incorporate topographic information from restricted spatial scales are likely to have lower signal to noise ratios, and differentiation of noisy data accentuates uncertainties. In comparison, geomorphic metrics which consider the entire shapes of landscapes, such as hypsometry, appear less sensitive to noise.

2.4.5 Limitations and recommendations

Obvious ways in which the work presented could be extended include assessing the impact of noise using other landscape modelling software packages (e.g., Badlands, CHILD, FastScape) or by randomising flow directions (Tucker et al., 2001; Salles, 2016; Salles and Hardiman, 2016; Bovy, 2021). Secondly, it is noted that alternative approaches to defining noise could be examined. I briefly explored the use of simplex noise (related to Perlin noise) but found it to generate linear artefacts (Perlin, 2002). Third, there are a host of additional geomorphic properties that have not been examined that may be impacted by noise, such as sedimentary flux.

The first recommendation concerns the application of noise within landscape evolution models. Noise should be expected to always be present, even if it is difficult to quantify, in real landscapes (Birnir

et al., 2001). I therefore consider the application of noise as an important, and not arbitrary, choice within models that seek to represent natural landscapes and underlying mechanisms which govern their evolution. It is shown that two widely used techniques (namely slope-area and χ analyses) for recovering uplift rates or erosional parameter values from topography can give results that are wrong but look correct, even when a landscape is demonstrably at topographic steady state. If such methodologies are used, it is suggested to, first, do more, for instance re-run models many times to test the impact of uncertainties (noise), and to explicitly communicate the distributions (colours) and amplitudes of noise used within model configurations. Second, do it better, i.e., find ways to ensure that fundamental assumptions, such as topographic steady state, are appropriate. One pragmatic way of doing so is to use independent evidence (e.g., geologic evidence of uplift or erosion) to test results. Third, above all else, acknowledge and communicate uncertainties, e.g., in calculated uplift rates or concavity indices from metrics-based approaches.

The second recommendation is to use or develop other methodologies that allow assumptions about topographic steady state to be relaxed, and explicitly incorporate uncertainties. Inverse modelling of landscapes for uplift rate histories, for instance, allows one to avoid many of the pitfalls associated with metrics-based approaches, in particular when probabilistic approaches are taken (e.g., Willgoose et al., 2003; Croissant and Braun, 2014; Rudge et al., 2015).

2.5 Conclusions

Landscapes with the same uplift and erosional forcings evolved to equilibrium conditions using the SPM can have very variable geometries as a result of noise inserted into their starting conditions or as models evolve. Extraction of geomorphic information from such landscapes using common metrics-based approaches (slope-area, χ), and subsequent recovery of uplift rates, erosional parameters values, and Hack exponents, show that varying the arrangement, distribution, and implementation of even small amplitudes ($< 1\%$ of cumulative uplift) of noise can produce results with broad distributions. Adding quenched noise to models produces more uncertainty in recovered uplift rates than when noise varies spatio-temporally. Observations of the spectral content in natural landscapes indicates that features with red noise are prevalent. The largest drainage basins produced in modelled landscapes initialised with red noise tend to be larger than those in landscapes initialised with white or blue noise. Positions of drainage divides in landscapes initialised with red noise are less predictable than those generated with white or blue noise. All introduce considerable uncertainties in the position of

drainage divides and basin geometries. The production of distributions in results arising from noisy conditions illustrates the benefits of probabilistic or ensemble approaches to modelling, and the peril of interpreting predictions from single models. It is suggested that assessing the impact of noise on SPM predictions benefits from two considerations. First, utilising ensembles of models. Secondly, assessment of the distributions of geometries including elevations, planforms, drainage divides, length-area relationships, and metrics, e.g., concavity and steepness indices. Doing so provides insight into the uncertainties that arise solely through the incorporation of noise, which can be considerable.

A general goal of geomorphology is to understand and quantify the vertical motions of continental topography through geologic time. Inverse modelling provides an attractive approach to do so, in particular because it does not necessarily require assumptions around topographic steady state. However, it is clear that variable landscape geometries arising due to noise, rather than tectonics, can pose problems for inverse methods that seek to compare landscapes using pixel-wise (Euclidean) approaches. It is therefore likely that other techniques for comparing landscapes are required in order to identify their tectonic histories. This topic is explored in the next chapter.

Chapter 3

Introducing the Wasserstein distance as a tool for inverting landscapes

Abstract

Extricating histories of uplift and erosion from landscapes is crucial for many branches of the Earth sciences. An objective way to calculate such histories is to identify calibrated models that minimise misfit between observations (e.g., topography) and predictions (e.g., synthetic landscapes). In the presence of natural or computational noise, widely used Euclidean measures of similarity can have complicated objective functions, obscuring the search for optimal models. Instead, the Wasserstein distance is introduced as a means to measure misfit between observed and theoretical landscapes. Results in this chapter come in two parts. First, it is shown that this approach can generate much smoother objective functions than Euclidean measures when realistic landscapes are compared, simplifying the search for optimal models. Second, it is shown how locations and amplitudes of uplift can be accurately recovered from synthetic landscapes even when seeded with different noisy initial conditions. Results suggest that this approach holds promise for inverting real landscapes for their histories, which will be explored in Chapter 4.

Publication Note

Part of the work presented in this chapter has been published as:

> **Morris, M. J.**, A. G. Lipp, and G. G. Roberts (2023). 'Towards Inverse Modelling of Landscapes using the Wasserstein Distance'. *Geophysical Research Letters* 50, e2023GL103880, DOI: 10.1029/2023GL103880

For reproducibility purposes, code and data relevant to this chapter can be found at

https://github.com/MatthewJMorris/landscape-wasserstein.

3.1 Introduction

Planetary surface topography is shaped by geologic and geomorphic processes operating on a broad range of spatial and temporal scales (e.g., Davis, 1899; Bishop, 2007; Anderson and Anderson, 2010; Wapenhans et al., 2021). A general goal is to identify geologic and geomorphic models that can accurately predict observed landscapes. For example, a suite of inverse models have been developed to identify uplift rate histories that yield low residual misfits to longitudinal river profiles (e.g., Pritchard et al., 2009; Roberts and White, 2010; Goren et al., 2014a; Gallen and Fernández-Blanco, 2021). Despite increased computational expense, forward and inverse modelling of two dimensional landscapes can incorporate geomorphic information that is not captured by river profiles (e.g., Croissant and Braun, 2014; Barnhart et al., 2020d; O'Malley et al., 2021). They can also be used to relax assumptions about drainage planform stability and include other erosional processes (e.g., hillslope erosion).

An important development in this field has been the application of methodologies to efficiently search the parameter space of landscape evolution models for those that yield low residual misfit, e.g., conjugate direction, linear least squares, neighbourhood algorithm and Bayesian minimisations (e.g., Roberts and White, 2010; Croissant and Braun, 2014; Fox et al., 2014; Glotzbach, 2015; Rudge et al., 2015). Fundamental to these approaches is deciding how observed and synthetic landscapes should be compared. An obvious and commonly used approach is to measure similarities using Euclidean distances such as root mean squared misfit (e.g., Roberts and White, 2010; Croissant and Braun, 2014). In special cases the objective functions used to search for optimal models can vary smoothly and have single minima when calculated using Euclidean distances. For example, if the landscapes being compared vary smoothly (e.g., approximating Gaussian domes). However, most landscapes have complicated shapes (e.g., ridges and valleys, drainage networks), which can produce complex objective functions with many local minima. It is challenging to automate the search for optimal landscape evolution models when objective functions are complex and contain local minima.

As is well known, a related and important issue is that, the location of drainage networks in landscape evolution models are sensitive to inserted noise (see e.g., Perron and Fagherazzi, 2012; Kwang and Parker, 2019; Lipp and Roberts, 2021, and Chapter 2). Noise is often inserted into the starting conditions of landscape evolution models to promote realistic channelisation, but may also be considered as representing a palaeotopographic surface, or local variations in elevation that arise from geomorphic processes, as is discussed in Chapter 2. Models with slightly different distributions or arrangements of noise can produce landscapes with ridges and valleys in different locations, even when inserted uplift

histories and erosional parameters are the same (e.g., Kwang and Parker, 2019). Consequently, Euclidean measures of misfit, which typically calculate pixel-wise differences in elevation, are sensitive to noise. As such, automating the search for optimal ('true') uplift or erosional histories again becomes challenging.

In this chapter I introduce a methodology using the Wasserstein distance, a metric from the field of Optimal Transport, which resolves many of these issues due to its ability to consider both the amplitude and location of mass. I first demonstrate the calculation of Wasserstein distances using one dimensional topographic transects. I then demonstrate how it can be used to identify optimal two dimensional synthetic landscapes even in the presence of added noise.

3.2 Euclidean statistics

As far as I am aware, all studies that have formally inverted landscapes have made use of Euclidean statistics, e.g., root-mean-squared (RMS) or the l^2-norm, to assess misfit (Croissant and Braun, 2014; Barnhart et al., 2020d,e; O'Malley et al., 2021; Curry and van der Beek, 2025; Petit et al., 2025; van der Meij, 2025). This approach compares elevations on a pixel by pixel basis, i.e., $z^o(x, y)$ vs. $z^c(x, y)$, where z^o and z^c indicate observed and calculated elevations, and x and y are spatial co-ordinates. The RMS and l^2-norm can be defined as

$$\left[\frac{1}{N}\sum_{i=1}^{N}(z_i^o - z_i^c)^2\right]^{1/2} \quad \text{and} \quad \left[\sum_{i=1}^{N}(z_i^o - z_i^c)^2\right]^{1/2}, \tag{3.1}$$

respectively, where z_i^o and z_i^c are the respective elevations of the observed and calculated landscapes. N is the number of measurements of elevation, e.g., along a transect.

It is acknowledged that some existing inverse models incorporate other observations into their assessment of goodness of fit, which are not discussed further in this chapter (e.g., thermochronometric or cosmogenic derived estimates of denudation, radiometric estimates of incision rates; Glotzbach, 2015; Pedersen et al., 2018; Gallen et al., 2023; Curry and van der Beek, 2025).

The use of Euclidean statistics in inverse modelling of entire landscapes can introduce a serious problem for recovery of tectonics from topography. The central issue, akin to cycle-skipping problems in seismology (see e.g., Sambridge et al., 2022), is that noise at small scales plays a considerable role in determining landscape geometries at larger scales, leading to topographic valleys and ridges 'misaligning' in landscapes with similar, or identical, tectonic histories. Consequently, maps of misfit have

local minima, which can easily lead to undesirable outcomes (such as solutions with the incorrect uplift history) or too broad a suite of acceptable solutions to be useful. With regards to the real world, spectral analyses of flow directions indicate that it is highly likely that the geometries of landscapes (and consequently drainage planforms) at some scales is largely arbitrary with regards to tectonics (e.g., Lipp and Roberts, 2021). Instead they are determined by the essentially unknown (and probably unknowable) history of processes introducing noise at smaller scales. These reasons mount to why Euclidean measures of misfit, which are sensitive to local noise, are unlikely to be well suited for identifying optimal models and for recovery of tectonics from topography. The Wasserstein distance is introduced in the next section as an alternative method to compare landscapes.

3.3 Wasserstein statistics: theory

Also known as the Earth-mover's distance, the Wasserstein distance is a statistical measure of the work required to map or transform one probability distribution to another given a specified metric space (e.g., Euclidean space). An intuitive understanding of the Wasserstein distance can come from considering the movement of one pile of material (such as sand) into another pile, with no loss or gain of material. The optimal transport plan is the one which transports material the least amount of distance, where 'distance' can be arbitrarily defined. The Wasserstein distance is the total cost associated with this optimal transport plan. Originating from the work of Monge (1781) on Optimal Transport, calculation of Wasserstein distances have been developed by Kantorovich (1942) and Villani (2003). The Wasserstein distance has been applied to a range of problems in computing (Arjovsky et al., 2017), chemistry (Seifert et al., 2022), oceanography (Nooteboom et al., 2020; Hyun et al., 2022), climate science (Chang et al., 2015; Vissio et al., 2020), geophysics (Engquist and Froese, 2014; Métivier et al., 2016a,b; Sambridge et al., 2022), sedimentology (Lipp and Vermeesch, 2023), and hydrology (Magyar and Sambridge, 2023). As far as I am aware it has not been used to invert landscapes for their properties (e.g., uplift histories, erosion rates, sedimentary fluxes).

For one dimensional distributions along the real line, the Wasserstein distance can be calculated analytically. Consider two 1D distributions p and q where $\int_{-\infty}^{\infty} p(x)\mathrm{d}x = \int_{-\infty}^{\infty} q(y)\mathrm{d}y = 1$. The p^{th} Wasserstein distance between p and q is given by

$$W_p(p,q) = \left[\int_0^1 |P^{-1} - Q^{-1}|^p \mathrm{d}t\right]^{1/p}, \tag{3.2}$$

where P and Q represent cumulative density functions (CDFs) of $p(x)$ and $q(x)$; $P(x) = \int_{-\infty}^{x} p \, \mathrm{d}x$ and $Q(y) = \int_{-\infty}^{y} p \, \mathrm{d}y$. In one dimension, when $p = 1$, Equation 3.2 decomposes to represent the area between the two inverse CDFs and is equivalent to the area between the two CDFs.

An illustrative example is shown in Figure 3.1. Two probability density functions $p(x)$ and $q(y)$ are shown in the top left panel. In this case, $p(x)$ and $q(y)$ are normal distributions with different mean values and standard deviations. In general, a variable X that exists in a metric space (e.g., distance, time) m can be described with a probability density function $f_X(m)$. A quantified similarity between $p(x)$ and $q(y)$ is sought by calculating a Wasserstein distance, representing the minimum 'cost' required to transform $p(x)$ to $q(y)$. An efficient approach to do so, following Sambridge et al. (2022), represents $p(x)$ and $q(y)$ as weighted sums of Dirac delta functions. These can be defined as

$$p(x) = \sum_{i=1}^{n_p} p_i \delta(x - x_i), \text{ and } q(y) = \sum_{j=1}^{n_q} q_j \delta(y - y_j), \tag{3.3}$$

where the delta function $\delta(x - x_i)$ represents a unit point mass at position x_i, weighted by the value of $p(x)$ at that position, p_i. Eight example delta functions for both $p(x)$ and $q(y)$ are shown in Figure 3.1a, represented by the vertical dotted lines that terminate at white circles. In general a larger number of individual delta functions are required in order to adequately represent $f(m)$. Note that the number or location of delta functions does not have to be identical for the two probability densities (i.e., $n_p \neq n_q$, $x_i \neq y_j$), though in this example, both are. The probability density functions, and their delta function representations, must both integrate to 1.

The delta function approximations of $p(x)$ and $q(y)$ are converted to cumulative density functions, $P(x)$ and $Q(y)$. The delta function CDFs are piecewise functions that have the appearance of staircases when the number of delta functions representing $p(x)$ and $q(y)$ is small, and closely approximate the true CDFs when the number of delta functions is large. Note that Figure 3.1b shows CDFs of $p(x)$ and $q(y)$ using a large number of delta functions and not using the eight delta function representations. In general, an advantage of transforming $f(m)$ to $F(m)$ is to ensure both functions are defined on the interval $[0, 1]$. $P^{-1}(t)$ and $Q^{-1}(t)$, the inverse cumulative density functions (also known as quantile functions), are calculated from $P(x)$ and $Q(y)$ and are shown in the Figure 3.1c with the cumulative density (i.e. in general terms, $F(m)$) represented by the variable t. The difference between the two quantile functions is shown by the hashed region, and in Figure 3.1d as a function of cumulative density. Integrating these differences (Equation 3.2) gives the Wasserstein distance. When $p = 1$, the Wasserstein distance is the area between the two quantile functions.

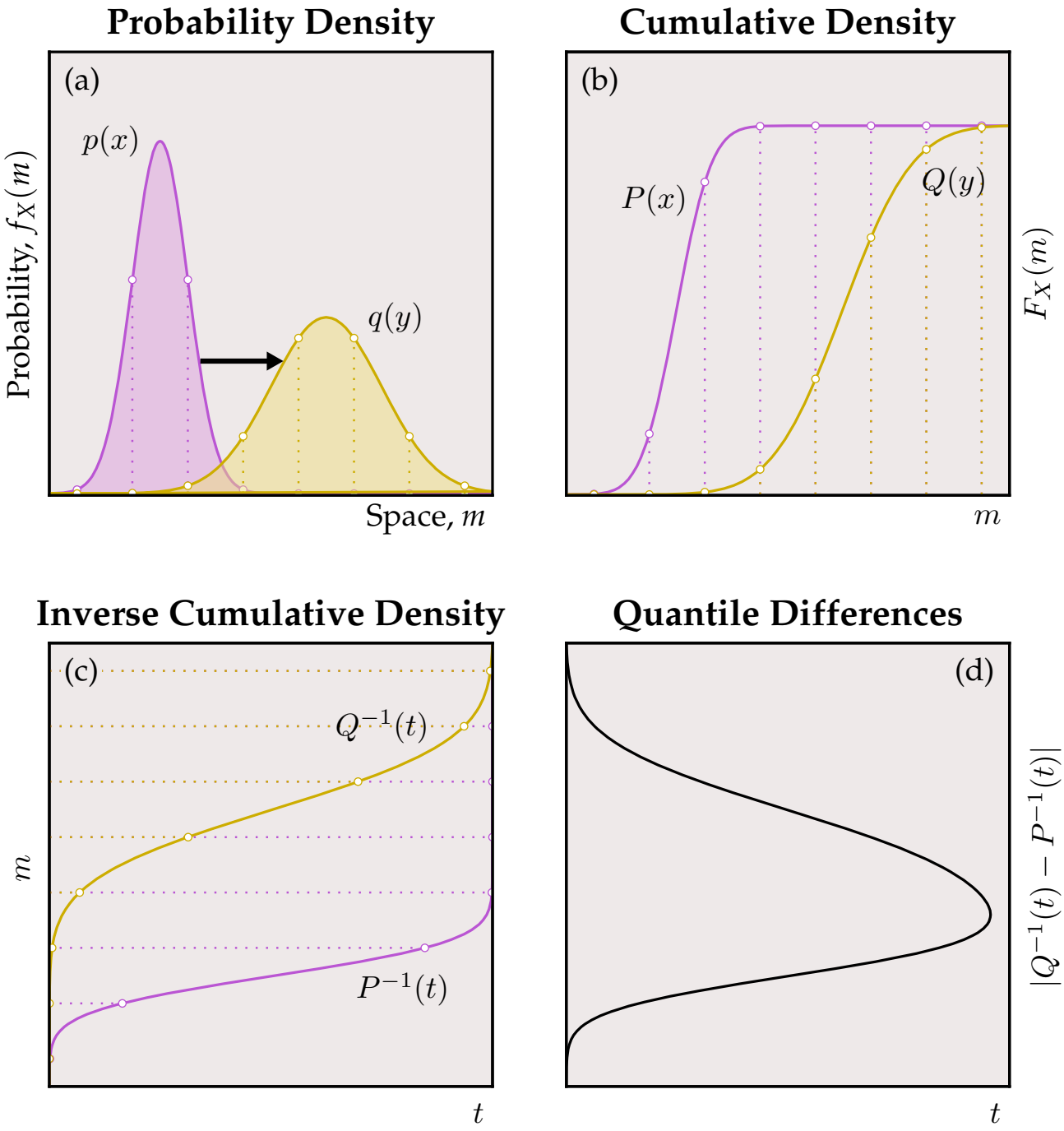


Figure 3.1: **Schematic illustrating how a Wasserstein distance is calculated between two probability density functions** (a) Pink and yellow curves show two probability density functions, $p(x)$ and $q(y)$, defined on an arbitrary metric space, Both $p(x)$ and $q(y)$ are normal distributions, with $q(y)$ having a standard deviation twice as large as $p(x)$. Dotted vertical lines terminating at white circles show examples of delta functions; see body text for details. Black arrow indicates the transformation of $p(x)$ to $q(y)$. (b) $P(x)$ and $Q(y)$ are cumulative density functions calculated from $p(x)$ and $q(y)$ respectively. (c) Inverse cumulative density functions, defined as a function of t, where t represents cumulative probability. (d) Black line shows the absolute difference between $Q^{-1}(t)$ and $P^{-1}(t)$.

Whilst straightforward to visualise W_1, there are two advantages of using a squared Wasserstein distance ($p = 2, W_2^2$). The first is that mathematical functions that use the Wasserstein distance as a measure of (dis)similarity between two distributions, for instance objective functions that are developed in this chapter, are more likely to have favourable structures (e.g., steeper gradients, see Sambridge et al. (2022) Figures 1 & 7 for examples) which can benefit automated techniques in finding optimal solutions. Additionally, as shown by Irpino and Romano (2007), under certain conditions the squared 2-Wasserstein distance between two density functions decomposes in terms of the differences between the two distributions' location, spread and shape. This result is useful because these terms could intuitively describe how functions differ from each other.

3.4 Calculating Wasserstein distances in one dimension

A simple demonstration of how Wasserstein distances can be calculated and used to locate best-fitting theoretical distributions is shown in Figure 3.2. A suite of normalised synthetic functions are shown in black, termed here as 'target' distributions. An equivalent function, shown in red and termed as the 'source' distribution, has been translated in the negative x direction. The normalisation transforms the functions into probability distributions; for a function $f(x)$ evaluated on N pixels, the normalised function $f^*(x)$ is

$$f^*(x) = \frac{f_i(x)}{\sum_i f_i(x)}, \tag{3.4}$$

where $i \in \{1, 2 \dots N\}$. Each source function is progressively translated across the abscissa, overlapping with the target, and continuing until there is no overlap. The l^2-norm (dark red; Equation 3.1) and squared Wasserstein (light blue; Equation 3.2) misfit are shown in the right panels, calculated at each translation step. In all cases, the Wasserstein misfit is quadratic, whereas the Euclidean misfit contains local minima.

It is instructive to demonstrate the relevance of this experiment for geomorphology by extending it to an observed landscape. Figure 3.3 shows how Wasserstein distances can be used to identify an optimal topographic transect. This transect was chosen to demonstrate how an optimal source (e.g., theoretical landscape) can be identified even for quasi-periodic topography, analogous to 'cycle-skipping' problems in seismology. The transect was extracted from the SRTM 1 arc second dataset across the Appalachian mountains, USA (Figure 3.3a: A—A′; horizontal resolution $\sim$ 30 m). The resultant target profile is shown in Figure 3.3b (black polygon). Source transects (e.g., red polygon in Figure 3.3b) are generated by translating the target transect in the same style as Figure 3.2. Initially the source transect does not

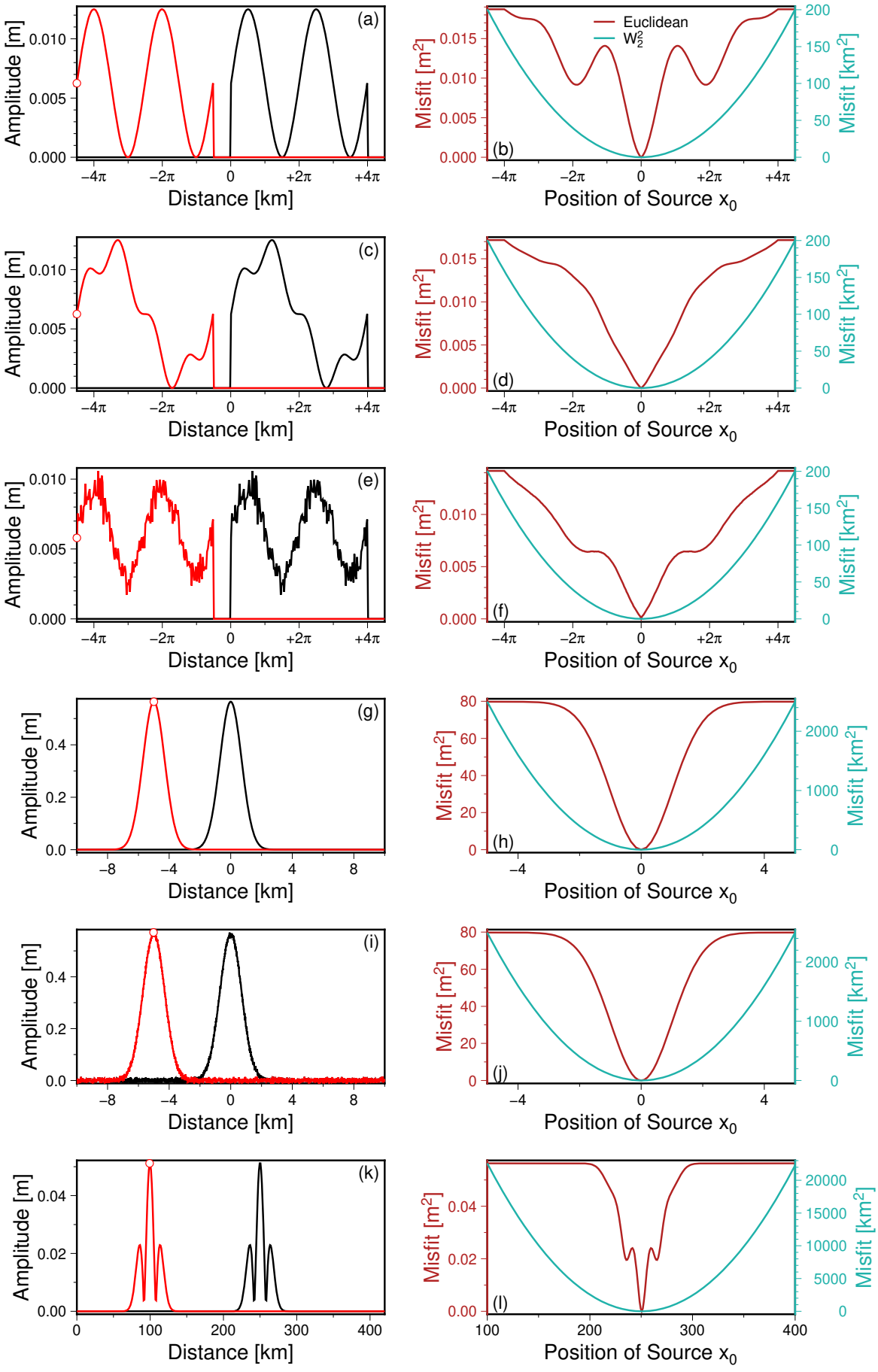

(a)
Amplitude [m]
Distance [km]
(b)
Euclidean
W_2^2
Misfit [m²]
Misfit [km²]
Position of Source x_0
(c)
(d)
(e)
(f)
(g)
(h)
(i)
(j)
(k)
(l)

Figure 3.2: **Comparison of Euclidean and Wasserstein misfit for synthetic one-dimensional functions** (a) Black line (target) = $y = 2\pi \sin(x) + 1$, normalised to unit mass and discretised to range $\frac{\pi}{2}$ to $\frac{9\pi}{2}$. Red line (source) = same function, translated by -4.5π units. Red circle marks starting position over which the source is translated across the target. (b) Euclidean (dark red) and Wasserstein (light blue) calculated as source function is translated across target. Panels (c) to (l) show the same process for different functions. (c) $y = 2\sin(\frac{x}{2}) + \frac{sin(2x)}{2}$, (e) $y = \sin(x + \frac{\pi}{2}) + 2 + \mu$, where μ is random Gaussian noise with a standard deviation of 0.2. (g) Gaussian distribution with a mean = 0 and variance = 0.5. (i) Noisy Gaussian. As per (g), except random Gaussian noise added with standard deviation of 0.005, (k) Ricker wavelet with un-normalised amplitude of 8 and mean of 100.

overlap with the target, it is progressively shifted until it fully overlaps, before continuing translating until, again, there is no overlap. Euclidean misfit and a Wasserstein distance are calculated for each translated (source) transect. These transects have identical absolute elevations. Thus, in this scenario I define the Wasserstein misfit simply as the squared one dimensional Wasserstein distance between the two normalised elevation profiles (Equation 3.2).

The Euclidean misfit function in Figure 3.3c is complicated and contains several local minima, highlighted by the arrows. However, the associated Wasserstein misfit function (Figure 3.3d) is smooth and quadratic, with a single minimum located where the two transects are aligned. The simple one dimensional examples presented in Figures 3.2 and 3.3 suggest that the Wasserstein distance holds promise for comparing real topographic data. In particular, that automated techniques for efficient locating of minima (e.g., Brent's method) within misfit functions are more likely to be successful if similarity between topography is measured using Wasserstein, rather than Euclidean, statistics.

3.5 Wasserstein distance in two dimensions

The Wasserstein distance is, in general, applicable to distributions of N dimensions. When $N > 1$ this problem has no known analytical solution and can be solved via linear programming (e.g., Peyré and Cuturi, 2019). This approach can be computationally expensive (calculation cost scales $O(n^3 + \log n)$ where n is the number of data (grid) points), which is undesirable for inverse problems. However it is important to recognise the existence of such solutions, and an explanation of calculating the Wasserstein distance using a linear programming approach is provided here for $N = 2$, as landscapes have two dimensions in addition to their elevations.

For a pair of two dimensional density functions $f(x, y)$ and $g(x, y)$, a Wasserstein distance can be calculated with the following approach: First, a cost matrix is calculated, representing the distance from each coordinate point in the source function (f) to every coordinate point in the target function

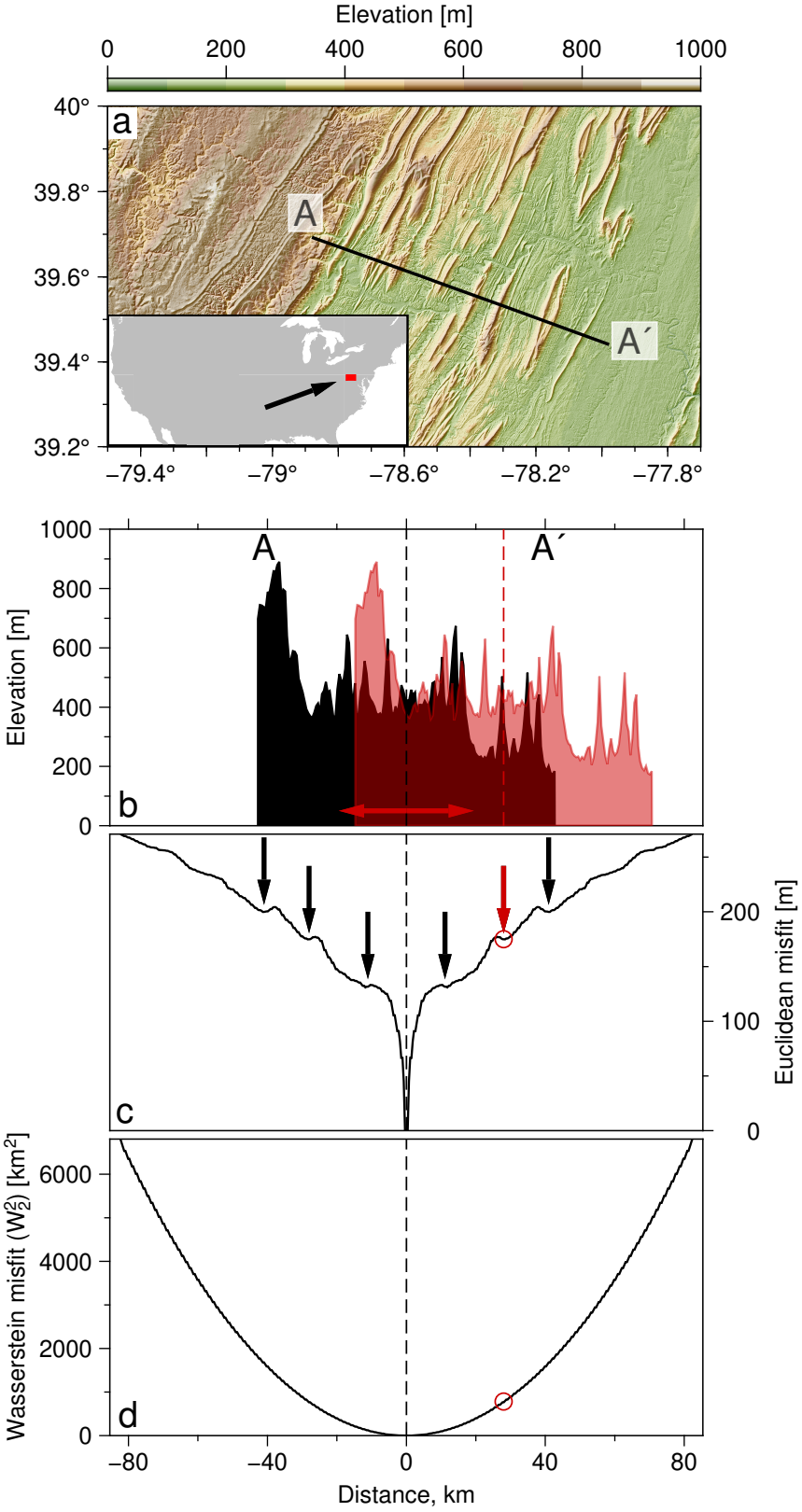

Elevation [m]
0
200
400
600
800
1000
a
A
A´
40°
39.8°
39.6°
39.4°
39.2°
−79.4°
−79°
−78.6°
−78.2°
−77.8°
b
Elevation [m]
c
Euclidean misfit [m]
d
Wasserstein misfit (W_2^2) [km^2]
Distance, km
−80
−40
0
40
80

Figure 3.3: **Wasserstein and Euclidean (RMS) misfit between observed (target) and theoretical (source) topographic transects.** (a) Transect A—A′ across the Appalachian mountains, USA. Red box on inset map indicates region shown in panel (a). Topography extracted from SRTM 1 arc second dataset. (b) Black polygon shows observed elevation along transect A—A′; dashed black line = profile mid-point. Theoretical transects were generated by translating the observed transect left and right (red arrows); red dashed line = mid-point of example theoretical transect (red translucent polygon). (c) Euclidean (RMS) misfit between observed and theoretical transects. Distance = distance between mid-points of observed and theoretical transects. Arrows = local minima. Black dashed line = global minima; centre of observed transect. Red arrow and circle = misfit of theoretical transect shown in panel (a). (d) Wasserstein misfit (Equation 3.2) between observed and translated transects. Red circle = mid-point of theoretical transect shown in panel (b). Black dashed line = global minima at mid-point of observed transect shown in (a).

(g). A choice must be made about the method used to transform these points, known as the cost function. Several approaches exist including the squared Euclidean distance, Manhattan distance, and Jaccard similarity. A squared Euclidean distance is an intuitive and very commonly used type of cost function, and I therefore proceed with in this example. The cost c_{ij} to transport point i to point j using a squared Euclidean distance is given by

$$c_{ij} = (x_i - x_j)^2 + (y_i - y_j)^2, \tag{3.5}$$

where x_i and y_j are the x and y coordinates of the ith and jth discrete points in the distributions. A map of transport cost, known as the cost matrix may be constructed by computing the cost function for all pairs of coordinates.

There are a number of ways to transport f to g, however some are more efficient than others. Any chosen method of transport is given by a transport plan, π_{ij}, defined as the mapping of the source distribution onto the target distribution. i.e., entry i, j corresponds to how much of the source distribution f is translated from point i onto point j. Thus the total cost, C, of any given transport plan is

$$C = \sum_{i=1,j=1}^{n_f,n_g} \pi_{ij} c_{ij}. \tag{3.6}$$

The most efficient, or optimal, transport plan is sought, which results in the least cost to transport f to g (i.e. minimises C). This transport plan can be given generally, as per Kantorovich (1942), by the linear programming problem

$$W = \min_{\pi_{ij}} \sum_{i,j} \pi_{ij} c_{ij}. \tag{3.7}$$

Equation 3.7 is subject to three constraints. First and second, the row and column sums of the

transport plan are equal to the number of elements in f and g respectively, and third that the optimal transport plan is greater than or equal to zero. I note that linear programs have unique and well defined solutions, which are therefore always feasible to find (even if it may require a large number of iterations to do so).

To illustrate, an example of calculating a Wasserstein distance using two dimensional density functions is demonstrated in Figure 3.4. Two simplistic 'landscapes' are created. Figure 3.4a shows the target landscape with concentric stepped uplift blocks of 25 m, 50 m, and 100 m elevation. Figure 3.4b shows the source landscape. This landscape is identical except it has been translated five units horizontally left ('west') and two vertically downwards ('south'), resulting in the landscape being split across the grid domain. The cost matrix is calculated following Equation 3.5 and is shown in Figure 3.4c . The optimal transport matrix, representing the most efficient way to transport the source to the target, is shown in the lower right panel, and corresponds to the arrows drawn on the upper right panel. The white arrows illustrate the transport for a single example grid cell: cell 12 in the source is transported to cell 34 in the target as part of the optimal transport plan. It is important to note that the linear programming approach permits mass to be split and combined during transport, as demonstrated with certain cells.

Methods for calculating Wasserstein distances between datasets with two or more dimensions are not only limited to linear programming approaches. Engquist and Froese (2014) calculated Wasserstein distances between synthetic examples of seismic waveforms using a numerical approach that is based on solving the Monge-Ampère equation (i.e., a partial differential equation), building on previous numerical approaches (e.g., Brenier, 1991; Benamou and Brenier, 2000; Benamou et al., 2014). Such numerical techniques are reliant on a squared Euclidean distance being used as the cost function (i.e., Equation 3.5). This may not always be the case, and the linear programming approach is more generally applicable. Efforts within the medical and machine learning communities have generated a family of computational methods alternative to linear programming that achieve greater computational efficiency by relaxing the requirement for an exact solution (e.g., Solomon et al., 2015; Genevay et al., 2016; Seguy et al., 2018). These stem from the entropic regularisation approach of Cuturi (2013), which involves the incorporation of an additional term to Equation 3.7 that penalises transport plans with low Shannon entropy. When this penalty term is high, the optimal transport plan becomes less exact but the computational cost becomes increasingly linear with respect to the number of data points (Altschuler et al., 2018).

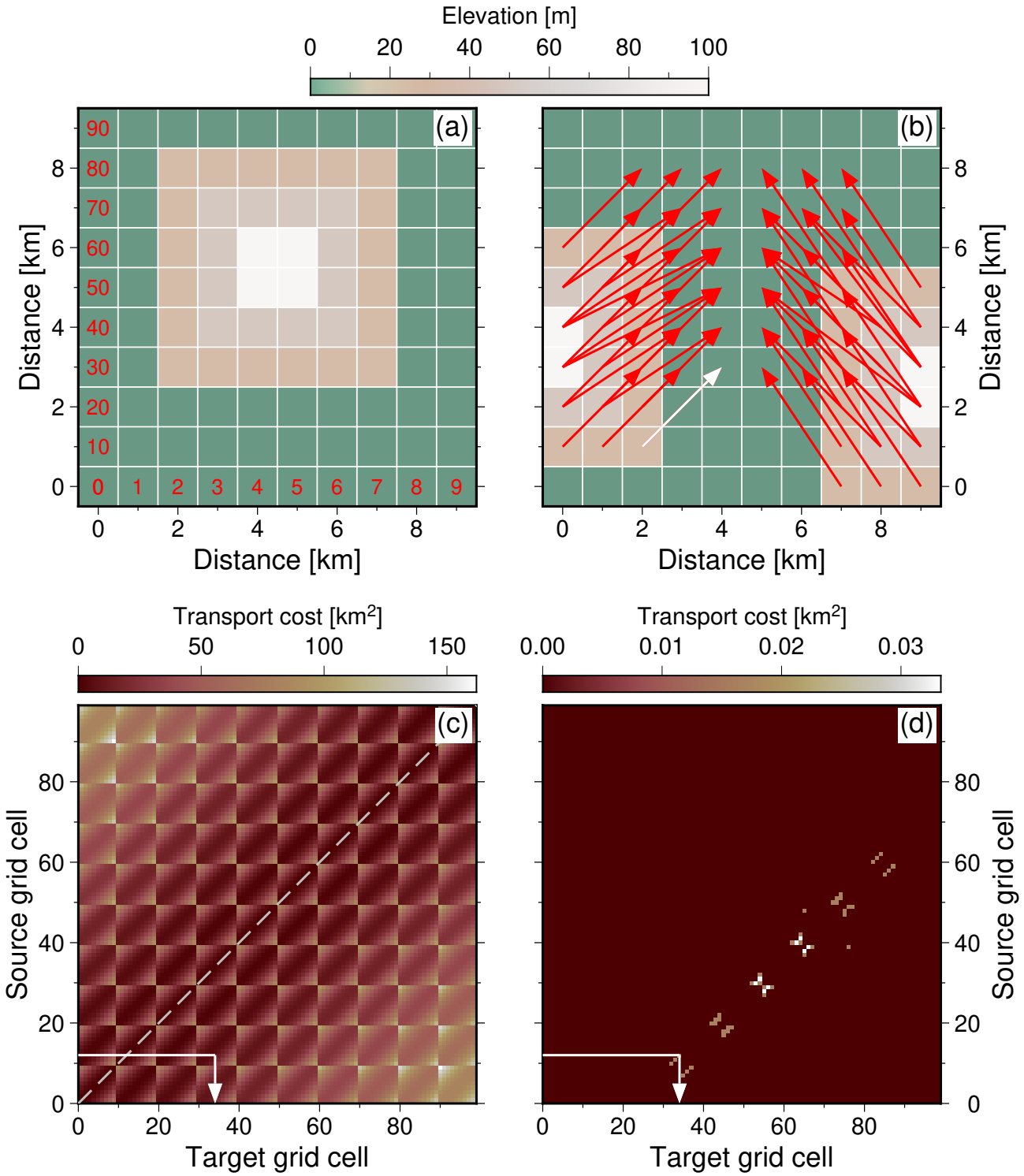


Figure 3.4: **A simple example of calculating a Wasserstein distance for a 2D density function** (a) A target blocky pyramid 'landscape', with concentrically stepped uplifted blocks of 25 m, 50 m, and 100 m. Red numbering identifies each grid cell; see body text. (b) A source landscape, identical to the target landscape except that it has been translated five units horizontally left and two units vertically downwards. Arrows illustrate the optimal transport of this source landscape to the target landscape. (c) The cost matrix, illustrating the squared Euclidean distance between corresponding points in the target and source. Grey dashed diagonal line marks equality, cost = 0. White arrow shows the cost of transporting grid cell 12 in the source to cell 34 in the target. (d) Optimal transport matrix, illustrating the most efficient transport plan for transforming the source to the target. White arrow highlights the transport for the same grid cell as in (c), which corresponds to white arrow on (b).

3.5.1 Marginal distributions

Whilst algorithms to efficiently calculate approximate multidimensional Wasserstein distances have been developed, such as those described above, an alternative approach is to decompose a two dimensional problem such as a landscape into subsidiary one dimensional problems, such as that demonstrated by Sambridge et al. (2022) and described as follows.

For each landscape, two marginal profiles, $z(x)$ and $z(y)$ are generated by summing elevations z along the x and y axes. These are transformed into probability distributions $z^*(x)$ and $z^*(y)$ by normalisation as per Equation 3.4. A consequence of this normalisation that is relevant for landscapes is that information about absolute elevation is lost. Fortunately, additional misfit term(s), which incorporate information about absolute elevations, can be straightforwardly incorporated into the objective function. Choosing an appropriate term will likely depend on the specific problem, for example inverse modelling of two dimensional landscapes may benefit from incorporating hypsometry, which has the added benefit of also being a cumulative density function. In this chapter, a simple scheme is used in which squared and scaled differences in mean elevation are incorporated, $P(z_1, z_2) = \bar{z}_1 - \bar{z}_2$, where $\bar{z}_1$ and $\bar{z}_2$ are mean elevations of two landscapes (e.g., Figure 3.3). Combining the above steps a misfit function, H, is defined, utilising the Wasserstein distance between a 'target' landscape, t, and a 'source' landscape s,

$$H(t,s) = W_2^x(t,s)^2 + W_2^y(t,s)^2 + \mu P(t,s)^2, \tag{3.8}$$

where $W_2^x(t,s)$ and $W_2^y(t,s)$ are the 2$^{\text{nd}}$ one dimensional Wasserstein distances ($p = 2$; Equation 3.2) between the normalised elevation marginals calculated by summing along the x and y axes, respectively. The scaling factor μ is a hyper-parameter which is adjusted systematically to test its impact on calculated misfit values. A python script which implements Equation 3.8 is provided at github.com/MatthewJMorris/landscape-wasserstein.

The above approach is demonstrated in the next section using two simple examples. The first example undertakes a search for the optimal location of a two dimensional, noisy, theoretical landscape, $z(x, y)$, using the misfit function defined above (Equation 3.8). In the second example, this search is extended to identify the optimal initial elevation of the landscape.

3.6 Exploring Wasserstein statistics with synthetic landscapes

The use of Wasserstein distances is demonstrated for inverse modelling of two dimensional synthetic landscapes. The calculated landscapes are produced using the surface process computing package Landlab (Hobley et al., 2017). Landscape geometry is governed by the history of uplift, the erosional model, inserted additional noise and time. An advective-diffusive formulation of erosion is assumed, such that,

$$\frac{\partial z}{\partial t} = -vA^m \nabla z^n + \kappa \nabla^2 z + U(x, y, t) + \eta(x, y, t), \tag{3.9}$$

where z is elevation, t is time, v, m, n and κ are erosional constants. A is upstream drainage area, x is distance upstream and U is uplift rate. The model is parametrised using a uniform grid with dimensions of 300 × 100 km, and cell size of 1 × 1 km. Each starting condition is generated by the following three steps. First, a central rectangular block is assigned an initial uniform elevation, u. Secondly, uniform (white) noise, η, with amplitudes 0–4% of initial elevation is added. Finally, sink-filling is performed once to permit continuous flowlines to the model boundaries (Barnes et al., 2014). m and n are set to = 0.5 and 1, respectively, $v = 10^{-3}$ kyr^{-1}, erosional 'diffusivity' $\kappa = 100$ m^2/kyr. The FastScape erosion scheme is used to solve Equation 3.9 (Braun and Willett, 2013). Flow-routing is performed with the 'D8' algorithm (O'Callaghan and Mark, 1984). The landscape model is run forwards in time for 10 Myr, with flow-routing, and advective and diffusive erosion calculated at each timestep. In all models $U = 0$, i.e., no uplift is added beyond the initial elevation. The timestep is set to 8 kyr, such that the Courant-Friedrichs-Lewy condition for numerical stability is satisfied.

The marginal approach is now demonstrated in two dimensions. In this simple example first the location of uplift that was used to generate a synthetic (target) landscape is sought. It is desirable to identify optimal theoretical landscapes even in the presence of additional noise inserted into the model (as is common in landscape evolution models when channelisation is required). Figure 3.5b shows the target landscape generated following the procedure described above (Equation 3.9). The marginals are shown in Figure 3.5a and 3.5c. A separate source landscape is generated by changing the arrangement of added noise, η, by using a different random seed integer, all other parameters are held constant. This source landscape is translated along the x axis of the model domain (midpoints from 50 to 250 km; 200 translations), illustrated by the red arrows in Figure 3.5d-e. An example of a translated landscape and its marginals are shown in Figure 3.5d-f. Figure 3.5g shows the difference in cell elevations between the target and source landscapes when fully aligned. This map shows the changes in landscape geometry (including elevations and fluvial planform) that are governed by changing the

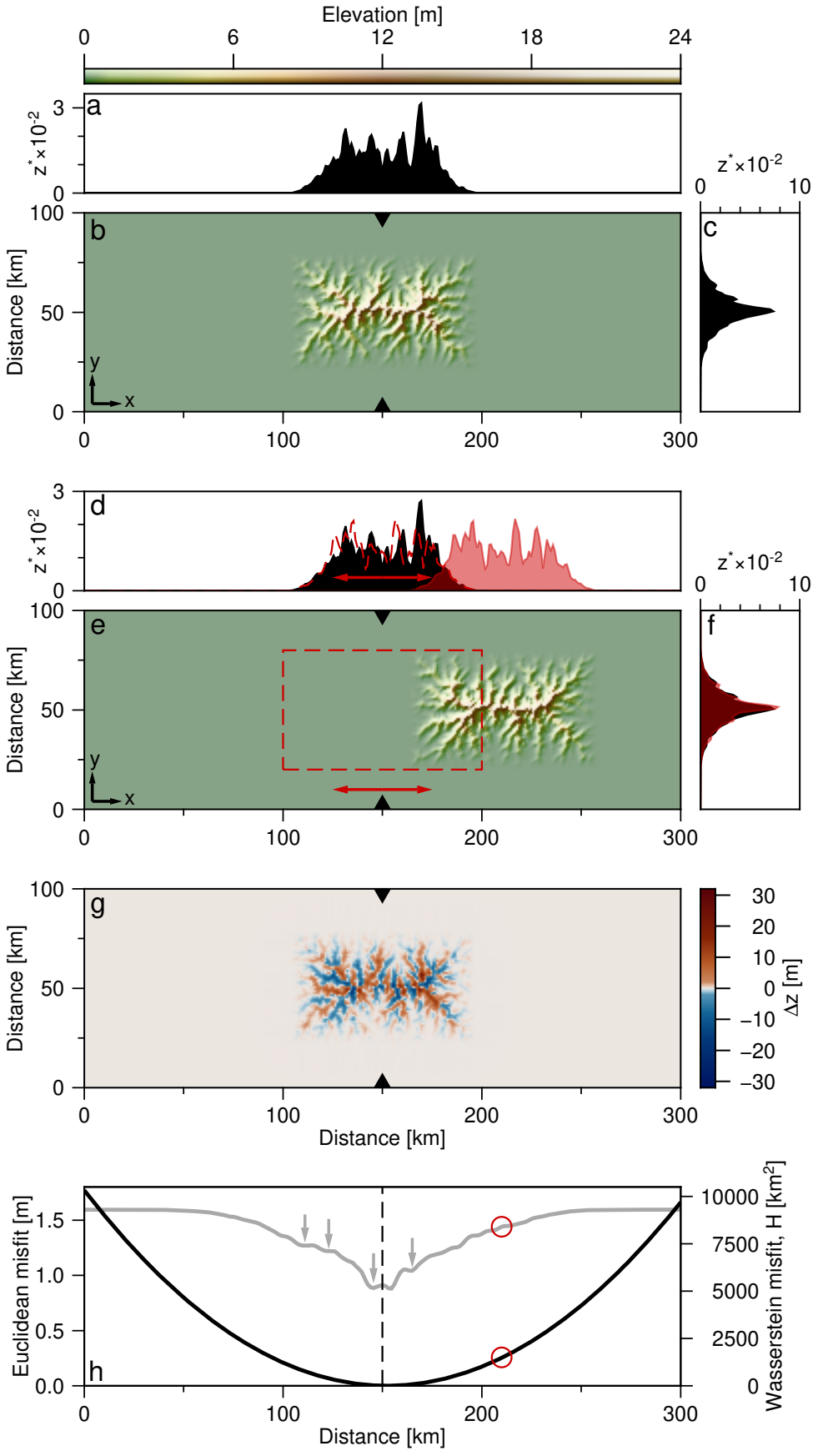

Elevation [m]
0
6
12
18
24
a
b
c
d
e
f
g
h
z*×10-2
Distance [km]
x
y
Δz [m]
Euclidean misfit [m]
Wasserstein misfit, H [km2]

Figure 3.5: **Misfit between two dimensional, $z(x, y)$, theoretical landscapes.** (a) Marginal elevations (z_x^*) of the landscape shown in panel (b). (b) Synthetic, 'target', landscape (see body text for construction). Filled black triangles point to centre of the domain. (c) Marginal elevations (z_y^*) of the landscape shown in panel (b). (d) Black profile is as per panel (a). Red dashed profile = marginal generated from synthetic landscape that has different initial noise but same distribution of uplift used to generate landscape shown in panel (b): red-dashed rectangle shown in panel (e). Red translucent marginal was generated from the translated, 'source', landscape shown in panel (e). (e) Red arrows indicate translation directions. Topography = example translated landscape. (f) As per panel (c); red translucent profile = marginal from landscape shown in panel (e). (g) Elevation differences, Δz, between the target and source landscapes when all conditions bar initial noise are constant. (h) Grey curve = RMS misfit (Equation 3.1) between synthetic landscape shown in panel (b) and translated landscapes (e.g., panel e). Grey arrows = local minima. Red circle = misfit between target and source landscapes shown in panels (b) and (e), respectively. Black solid curve = Wasserstein misfit (Equation 3.8, $p = 2$). Black dashed line = target and source landscapes with common mid-points indicated by black triangles on panels (b), (e) and (g).

initial noise inserted into the landscapes at their inception. Figure 3.5h illustrates that despite different initial noise conditions generating different drainage networks (Figure 3.5g), the Wasserstein distance successfully identifies a global minimum misfit where the landscapes are fully aligned. In comparison, the Euclidean misfit contains local minima and the position of the global minimum is offset from the target. This marginal experiment took 0.1 seconds on an Intel i7-6700 desktop computer with 64 gigabytes of RAM. Calculating Euclidean distances took 0.03 seconds.

Examples of Wasserstein distances calculated using two dimensional density functions (i.e., Equation 3.7, not using the marginals approach) are shown in Figure 3.6. This figure shows the results of an experiment similar to that shown in Figure 3.5. Due to the computational expense involved with this approach, only 7 translations of the source landscape are presented, rather than the 200 translations used for the marginals approach. Nonetheless, Figure 3.6c shows that the calculated misfit function correctly identifies the optimal location of the source landscape. However, calculating Wasserstein distances using two dimensional density functions for 7 translations of the source landscape took approximately 45 minutes (Figure 3.6). This highlights the difference in computational efficiency between the marginals approach and calculating Wasserstein distances using two dimension density functions.

The marginals experiment is now extended by changing the amplitude of initial uplift, U, used to generate the target landscape. Wasserstein and Euclidean statistics are calculated for each source landscape. The amplitude of uplift was systematically varied by $\Delta U = 25$ m between 25 to 250 m. For each of these ten landscapes, 100 random distributions of white noise with amplitudes 0–4% of uplift were added prior to the initial sink-filling and flow routing steps, generating the starting condition for

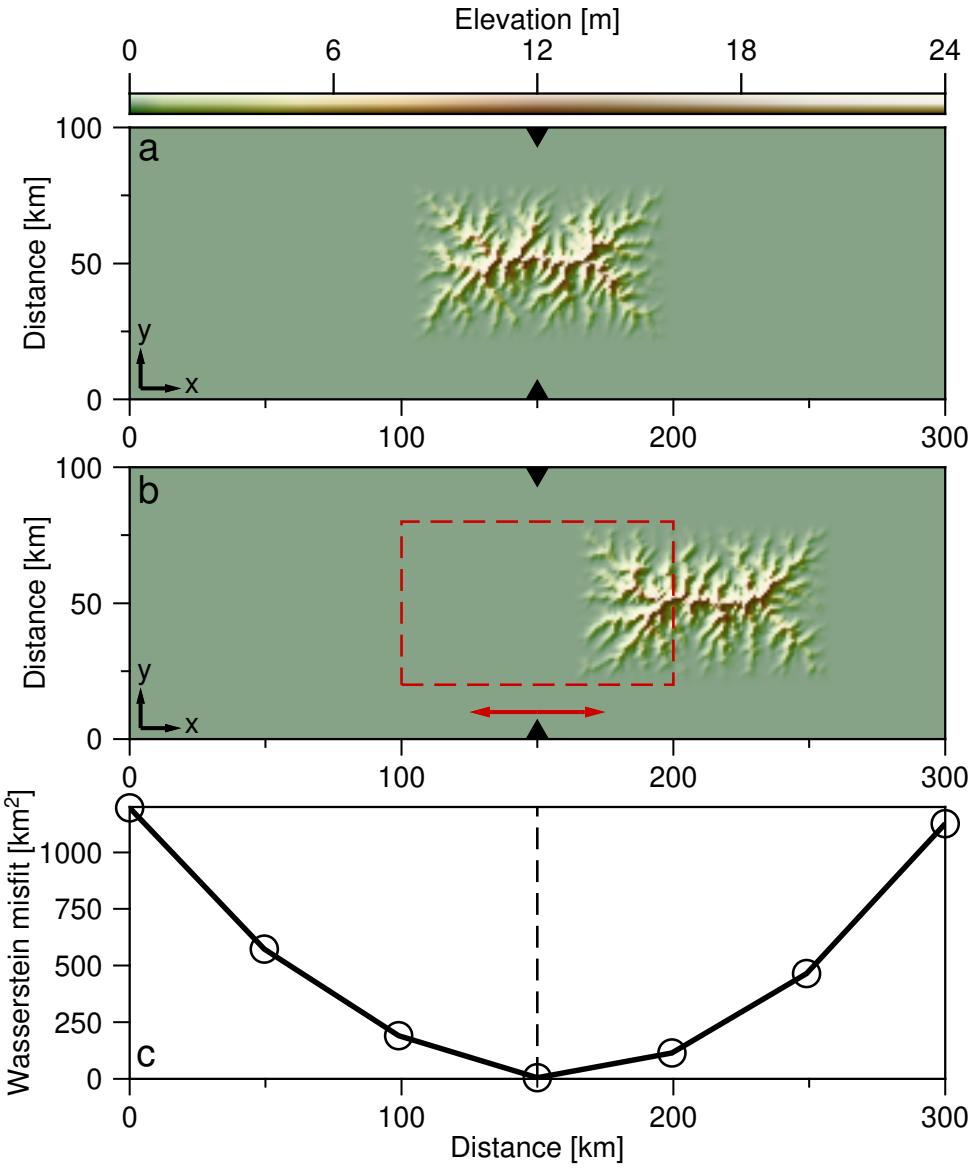


Figure 3.6: **Two-dimensional Wasserstein distances for synthetic landscapes.** (a) Target landscape, as per Figure 3.5a. (b) Source landscape, as per Figure 3.5b. (c) Two dimensional Wasserstein distance calculated between the target and the source landscapes for 7 translations (circles) of the source landscape across the domain using the two dimensional approach (Equation 3.7).

each model. As in the previous example, these source landscapes are translated along the x axis. This Monte Carlo style experiment is designed to test the impact of noisy initial conditions on identifying optimal theoretical landscape evolution models. In short, 100 brute force inversions are performed to identify two parameters: the location and magnitude of initial uplift, each with a different initial distribution of noise in the starting condition.

Figure 3.7a shows Euclidean (RMS) misfit as a function of initial elevation (uplift) and position for a more general and granular ($\Delta U = 3$ m) version of the test shown in Figure 3.5. The black curves in Figure 3.7b-c show slices through the Euclidean misfit function centred on the target landscape

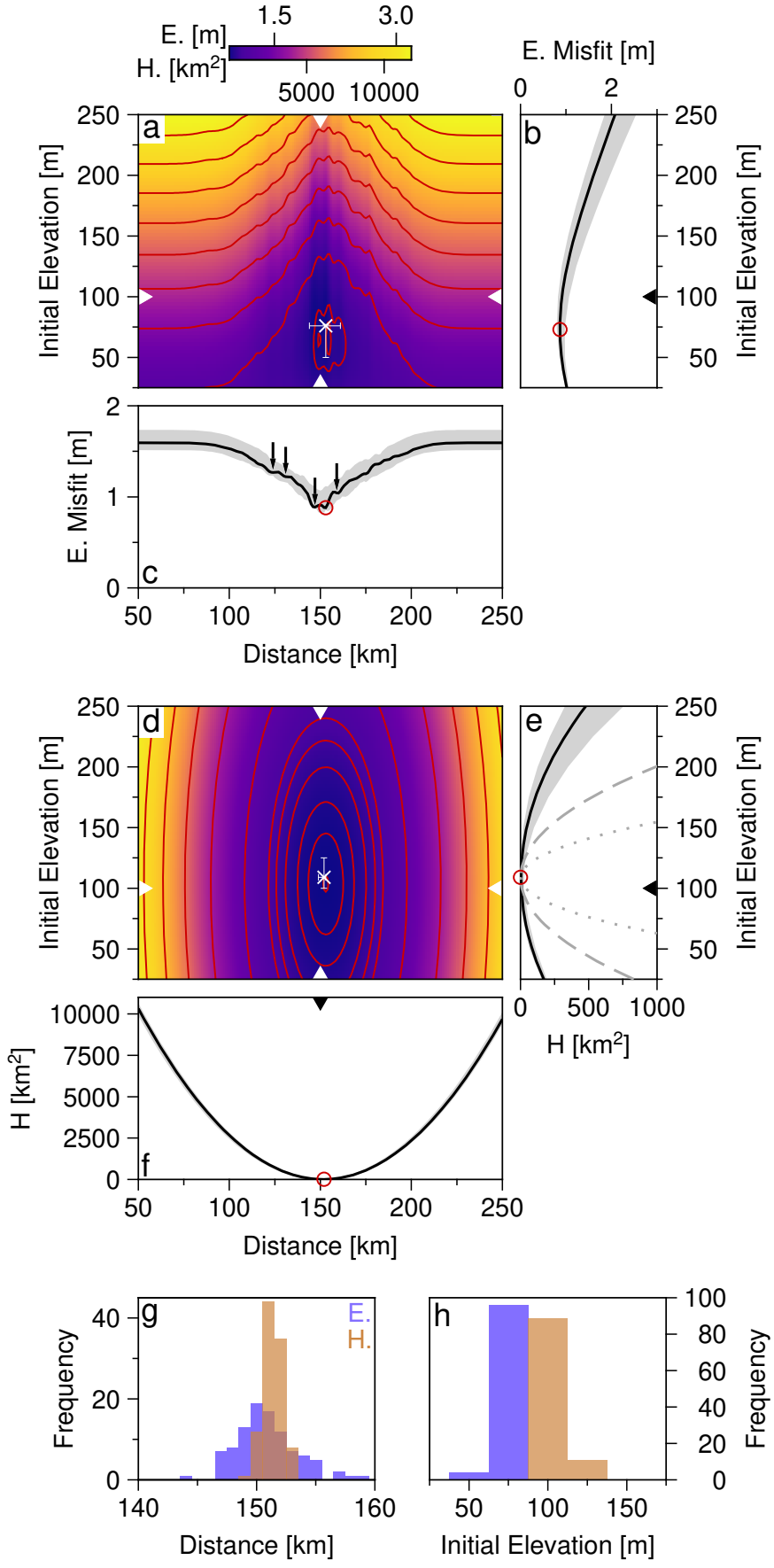

E. [m]
1.5
3.0
H. [km²]
5000
10000
E. Misfit [m]
0
2
a
b
c
d
e
f
g
h
Initial Elevation [m]
E. Misfit [m]
H [km²]
Distance [km]
Frequency
E.
H.
250
200
150
100
50
2
1
0
10000
7500
5000
2500
500
1000
140
160

Figure 3.7: **Inverse modelling of noisy synthetic landscapes: Euclidean and Wasserstein statistics.** (a) Euclidean (RMS) misfit (Equation 3.1) between target landscape (Figure 2b) and source landscapes as a function of noise and uplift. Uplift was translated as demonstrated in Figure 2; initial elevations (amplitude of uplift) were systematically varied between 25–250 m. Amplitudes of initial added white noise were scaled to be 0–4% of initial elevation. White cross = minimum misfit; error bars = range of misfit minima for 100 different parameterisations of noise. Outer white triangles point to initial elevation and mid-point of target landscape (100 m, 150 km). (b-c) Black curves = transects through misfit function between white triangles in panel (a). Shaded grey regions = minimum and maximum misfit for the 100 different distributions of noise. Black arrows = local minima of the 1D transect; circles = global minimum. (d-f) Wasserstein (H) misfit (Equation 3.8). (e) Black curve and grey envelope: $\mu = 10^4$; dashed and dotted grey curves: $\mu = 2.5 \times 10^5$ and 10^6, respectively. (g-h) Loci of misfit minima for the 100 different distributions of initial noise; E/H = Euclidean/Wasserstein misfit.

parameterisation (indicated by the white arrowheads in panel a). Local minima are indicated by the black arrows in Figure 3.7c. The error bars in Figure 3.7a show the range of global minima for the models examined. These results are summarised in the histograms shown in Figure 3.7g-h. The grey envelope in Figure 3.7b-c indicates the range of misfit values for all initial noise conditions. The global minima from all models is shown by the red circles. The Wasserstein-based misfit functions for the same models are shown in Figure 3d-h. The shape of the objective function with respect to initial elevation is governed by the value of the scaling parameter, μ. Increasing μ increases the contribution of the penalty term, P. A value of $\mu = 10^4$ was used to generate the results shown in Figure 3.7d-h (e.g., thin black curve and grey envelope in panel e). For comparison, the dashed and dotted grey curves in panel e show the shape of the objective function as a function of initial elevation when $\mu = 2.5 \times 10^5$ and 10^6, respectively.

Euclidean minima are broadly distributed around a point offset from the expected parameter values (Figure 3.7a). In contrast, minima calculated using Wasserstein distances have a smaller spread around the expected value (Figure 3.7d). These results indicate that Wasserstein distances provide means to identify optimal landscape evolution models even in the presence of noisy initial conditions that hinder Euclidean-based approaches.

3.7 Conclusions

Histories of uplift and erosion can be extracted from features within a landscape, such as longitudinal river profiles, relationships between their slopes and upstream drainage areas, or data extracted from eroded sediment. It is desirable to use the entire geometry of landscapes to do so, but widely used existing Euclidean measures of misfit struggle to consistently and reliably identify best-fitting param-

eters (e.g., uplift rates) due to the presence of local minima in objective functions. The Wasserstein distance offers a promising alternative measure of misfit to quantify similarity between observed and theoretical landscapes. This promise is due to the smoothly varying objective functions produced, which contain a single, global, minimum. Even in the presence of noise (which could be computational or real) Wasserstein statistics identify optimal landscape evolution models when equivalent Euclidean statistics (RMS, l^2-norm) are complex, with global minima offset from the expected value. A logical next step to build on this result is to explore whether the Wasserstein distance can reliably reproduce uplift histories that vary over space and time, and incorporate this into a formalised inverse modelling framework. This next step is investigated in the following chapter.

Chapter 4

Seeing through geomorphic complexity to recover tectonics from topography: Inverting landscapes for uplift histories using the Wasserstein distance

Publication Note

Part of the work presented in this chapter has been published as:

> **Morris, M. J.**, G. G. Roberts, F. D. Richards, A. G. Lipp, E. R. Siddle. 'Seeing through geomorphic complexity to recover tectonics from topography: Inverting landscapes for uplift histories using the Wasserstein distance'. *Journal of Geophysical Research: Earth Surface* 131, e2025JF008966, DOI: 10.1029/2025JF008966

For reproducibility purposes, code and data can be found at 10.5281/zenodo.17454726.

Abstract

An important problem in the Earth sciences is extracting information about tectonic and other processes from topography. A general challenge is that geomorphic activity that we typically have little information about during the lifetime of a landscape can introduce geomorphic 'noise'. Such noise, producing changes in elevation at scales typically $\ll 100$ m, could be introduced by variations in lithology, biology, climate, and sedimentology, for instance. It can dramatically impact the way in which landscapes evolve and their form, including shapes and positions of drainage networks. I seek to establish how information about uplift rate histories can be extracted from entire landscapes despite the presence of noise. The sensitivity of single landscape simulations to noise suggests that statistical and inverse modeling approaches utilizing model ensembles may be required. I establish the use of Wasser-

stein distances in an inverse modeling framework to recover uplift rate histories. I test optimization techniques that automate the search for optimal models (i.e., uplift rate histories) including direction-based and amoeba-simplex algorithms, confirming that the Neighbourhood algorithm is well suited to the task. This approach works even when noise demonstrably plays an important role in determining landscape form but is poorly constrained. I develop and test the approach using synthetic landscapes generated with the stream power erosional model and increasingly complex uplift and noise scenarios. The results indicate that it is possible to recover the history of uplift from natural landscapes in which the origin of the specific arrangements of channels, valleys, interfluves, etc. are poorly understood.

4.1 Introduction

Recovering 'tectonics from topography' remains an important problem in geomorphology partly because of the information that topography and its evolution provide to understand diverse geological, environmental and biological processes. For instance, histories of topographic evolution play a role in understanding mantle convection and lithospheric evolution including mountain building and basin formation, glacio-eustasy and climate, natural resources and hazards, sedimentary and biogeochemical fluxes, and speciation (e.g., Kirby et al., 2008; Cawood and Hawkesworth, 2015; Antonelli et al., 2018; Garefalakis and Schlunegger, 2018; Hoggard et al., 2020; Mitrovica et al., 2020; Igea and Tanentzap, 2021). It also remains an important problem because of the ongoing lack of understanding of how landscapes are generated and evolve across the scales of interest, e.g., metres to continents, seconds to millions of years. Some direct observations exist that provide information about histories of topographic evolution. For instance, stratigraphy, in particular the elevations of rock formed in shallow marine conditions, provides perhaps the most robust direct constraints on net vertical motions (e.g., Ziegler et al., 1985; Sahagian, 1988; Rowley et al., 2013; Fernandes and Roberts, 2020). Radiometrically dated fluvial terraces and palaeo-thalwegs can be used to estimate rates of erosion (e.g., Wellman and McDougall, 1974; Stock and Montgomery, 1999; Karlstrom et al., 2008; Stucky de Quay et al., 2019), and other chemical measurements such as U-Th/He thermochronology provide indirect information about exhumation (e.g., Braun, 2002; Stockli et al., 2002; Reiners et al., 2005; Flowers et al., 2008; Kent-Corson et al., 2009). A general challenge, which geomorphology can help to address, is 'filling in' the spatio-temporal gaps between such observational constraints.

The approach to extracting tectonics from topography presented in this chapter focuses on developing a methodology to calculate histories of uplift using quantitative information about landscape geometries that are likely to be sensitive to uplift. Such information could include observations of elevation, for instance, SRTM, TanDEM-X, MOLA or lidar data, and predictions from analytical, numerical, or flume tank experiments (Bonnet and Crave, 2003; Farr et al., 2007; Krieger et al., 2013; Zink et al., 2014;

Salles, 2016; Hobley et al., 2017). Central to this approach is the concept that landscapes respond to changes in uplift by eroding, which takes time, producing a record of past uplift in the geometry of landscapes (e.g., in the shape of longitudinal river profiles, hill slopes and hypsometry; e.g. Davis, 1899; King, 1953; Penck, 1953; Hack, 1960; Howard, 1994; Rosenbloom and Anderson, 1994). Unfortunately recovering tectonics from topography is hampered by the sculpting of uplifted landscapes by diverse physical, chemical and biological modification. These processes, which can operate across a very large range of scales (seconds to millions of years, < 1 m to continents), introduce complexity and 'noise' obscuring the link between tectonics and resultant topography (e.g., Anderson and Anderson, 2010; Roberts and Wani, 2024). All of which makes the extraction of uplift histories from the geometries of landscapes using existing approaches fraught. In this chapter a new approach is demonstrated that makes use of statistical methodologies arising from the theory of optimal transport to demonstrate how uplift histories can be recovered from landscapes that contain such noise (Figure 4.2).

Geomorphic 'noise' is considered in two forms. These have been introduced in Chapter 2, and I briefly revisit them here. First, noise introduced by processes in the real world is considered, which could take the form of changes in elevation generated by, for instance, lithologic, climatic, or biotic variability. Typically, these sources of variability shape topography across scales that are smaller (e.g., amplitudes $\ll 100$ m) than the tectonic signals (amplitudes > 100 m) that are of interest when recovering on geological timescales ($O(10^4 - 10^7$ years); see e.g., Willgoose et al., 2003; Anderson and Anderson, 2010; Willgoose, 2018; Wapenhans et al., 2021; Morris and Roberts, 2025). Such geomorphic 'noise' may have no direct, obvious or measurable relationship to uplift or tectonic processes actively generating topography. Nonetheless it may play an important role in determining landscape geometries, e.g., shapes and positions of valleys, channels, interfluves and drainage divides. Obtaining information about the arrangement of such 'noise' during the lifetime of a landscape is likely to be impossible for most landscapes because erosion has removed the information needed, e.g., spacing of joints and fractures, lithologic strength and heterogeneity, vegetation. Additionally, information about the specific processes (such as precipitation and its contributions to discharge, temperature, small scale geometries) that govern the physics of erosion is unlikely to be available for the majority of a landscape's lifetime (see Lamb et al. (2015) and Stucky de Quay et al. (2019) for examples of physics-based models parameterised when specific information required was available). It seems reasonable then to consider how uplift rate histories might be recovered from landscapes when processes that are (or at least appear to be) deterministic at small scales must be treated as being random at larger temporal, and perhaps spatial, scales. Despite the unknowability of precise contributions of erosional processes to landscape

evolution across the scales of interest, it is likely that their (spectral or probabilistic) characteristics of such features and processes can be at least bracketed from, for instance, modern observations and and physics-based insights operating in systems and at scales that we can measure (see e.g., Perron et al., 2008; Perron and Fagherazzi, 2012; Lague, 2014; Campforts et al., 2020b; Roberts and Wani, 2024). Noise attributed to measurement or observational uncertainties is also included in this category.

The second type of noise considered is computational, which usually takes the form of small-amplitude random elevations or flow directions introduced into the starting conditions of numerical simulations of landscape evolution to facilitate the development of realistic topography and drainage patterns (see e.g. Tucker et al., 2001; Salles, 2016; Hobley et al., 2017). As established in Chapters 2 and 3, it is well known that the locations of drainage networks within landscape simulations can be extremely sensitive to the choice of starting condition (Ijjász-Vásquez et al., 1992; Willgoose et al., 2003; Perron and Fagherazzi, 2012; Kwang and Parker, 2019). A variety of landscape simulator studies have demonstrated that incorporation of small-amplitude noise, introduced arbitrarily or caused by, for instance, changes in erodibility related to lithology, biological or chemical processes, can have dramatic and long-lasting impacts on the geometries of theoretical landscapes (e.g., Kwang and Parker, 2019; Kwang et al., 2021; Morris and Roberts, 2025). Treating the addition of computational noise as a proxy for natural noise can be thought of as a way to replicate processes that alter topography that we typically have little information about during the lifetime of a landscape, e.g., climate or lithologic variation and its impact on erosion.

By far the most popular approach to extracting tectonics from topography makes use of topographic metrics, which tend not to explicitly consider the role of noise in generating landscape geometries (e.g., 'slope-area', 'χ' analyses; see Anderson and Anderson (2010) and Morris and Roberts (2025) for summaries of these approaches). One issue with such approaches from a geological perspective is that they require questionable (certainly largely untested) assumptions about the form of uplift and the relationship between erosion and uplift (e.g., topographic steady state; where uplift is inserted into a landscape). A second, technical, issue is that they rely on differentiation of discrete and often noisy information (e.g., channel slopes and areas, elevation-chi profiles), which can lead to considerable uncertainty in calculated uplift rates—even when landscapes are demonstrably at steady state (e.g., Roberts et al., 2012a; Smith et al., 2022, Chapter 2).

An advance in the last 15 years with regards to extraction of tectonics from topography, addressing some of the shortcomings of metrics-based approaches, has been the introduction of inverse method-

ologies to geomorphology. The inverse methodology seeks to objectively identify uplift histories that minimise misfit between observed and theoretical landscape geometries (e.g., longitudinal river profiles; Pritchard et al., 2009; Roberts and White, 2010; Roberts et al., 2012a; Fox et al., 2014; Glotzbach, 2015). They do not require steady state assumptions and can solve for spatio-temporal histories of uplift without differentiation of noisy or discrete data. Inverse modelling studies of drainage patterns in most continents have indicated that commonalities in the geometries of landscapes, for instance longitudinal river profiles at scales $> 10^2$ km, exist and that they were likely generated by tectonic processes with recoverable histories (see e.g. Roberts et al., 2019; O'Malley et al., 2021; Wapenhans et al., 2021). Parameter values in erosional models have also been recovered from inverse modelling of entire landscapes (e.g., Croissant and Braun, 2014; Barnhart et al., 2020d). A crucial component of this approach is the quantitative assessment of misfit between observed and theoretical landscape geometries. As far as I am aware, all studies that have formally inverted landscapes have made use of Euclidean statistics, e.g., root-mean-squared (RMS) or the l^2-norm, to assess misfit. This approach compares elevations on a pixel by pixel basis, i.e., $z^o(x, y)$ vs. $z^c(x, y)$, where z^o and z^c indicate observed and calculated elevations, and x and y are spatial co-ordinates. It is acknowledged that some existing inverse models incorporate other observations into their assessment of goodness of fit, which are not discussed further in this chapter (e.g., thermochronometric or cosmogenic derived estimates of denudation, radiometric estimates of incision rates; Glotzbach, 2015; Pedersen et al., 2018; Gallen et al., 2023; Curry and van der Beek, 2025).

As demonstrated in Chapter 3, the use of Euclidean statistics in inverse modelling of entire landscapes can introduce a serious problem for recovery of tectonics from topography. The central issue, akin to cycle-skipping problems in seismology (see e.g., Sambridge et al., 2022), is that noise at small scales plays a considerable role in determining landscape geometries at larger scales. Consequently, maps of misfit have local minima, which can easily lead to undesirable outcomes (e.g., solutions with the incorrect uplift history) or too broad a suite of acceptable solutions to be useful. Consider the example shown in Figure 4.1 in which landscapes generated with different arrangements of the same distribution of noise in the initial condition but otherwise identically parameterised (same uplift history, erosional model and boundary conditions) have very different topographies at the scale of drainage basins. With regards to the real world, spectral analyses of flow directions indicate that it is highly likely that the geometries of landscapes (and consequently drainage planforms) at some scales is largely arbitrary with regards to tectonics (e.g., Lipp and Roberts, 2021). Instead they are determined by the essentially unknown (and probably unknowable) history of processes introducing noise at smaller

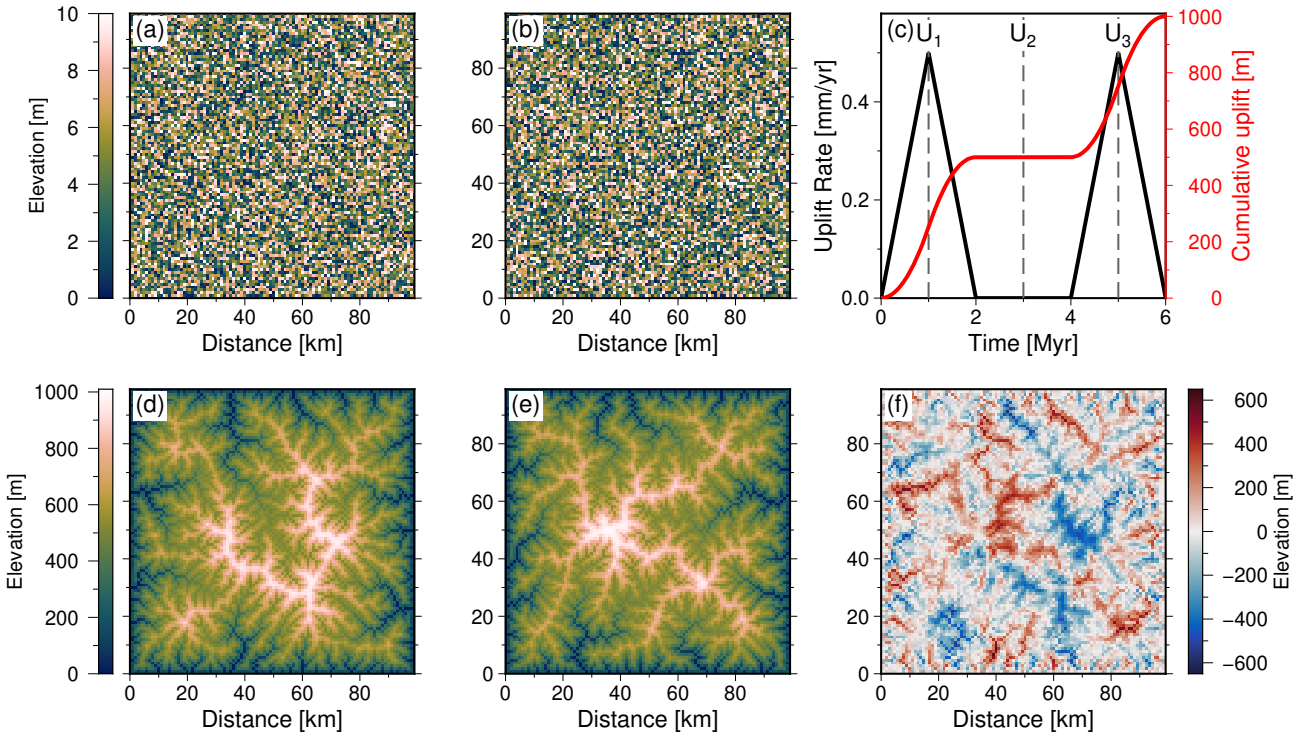


Figure 4.1: **Noisy starting conditions and their impact on landscape geometries: Generation of target 'observed' landscapes.** (a) An example of initial random uniform (white) noise used as a starting condition in a simulation of landscape evolution—used to generate the landscape shown in panel (d). (b) A different arrangement of the same white noise distribution, used to generate the landscape in panel (e). (c) Uplift history used to generate the landscapes shown in panels (d) and (e). Black line = uplift rate as a function of time; red line shows cumulative uplift. Dashed grey lines labelled U_n = free parameters (times at which uplift rates can vary) in the inverse models. (d–e) Target 'observed' landscapes generated using the noisy initial conditions shown in panels (a) and (b), the uplift history shown in panel (c) and the stream power erosional model (see body text for details). These 'observed' landscapes will be inverted in attempts to recover their uplift rate history, which from now is assumed as unknown. (f) Pixel-wise difference in elevation between the landscapes shown in panels (e) and (d).

scales. A consequence is that Euclidean measures of misfit, which are sensitive to local noise, are unlikely to be well suited for identifying optimal models and for recovery of tectonics from topography.

In this chapter a new approach is presented that makes use of methodologies arising from the theory of optimal transport to demonstrate how uplift histories can be recovered from landscapes with geometries impacted by noise. I adapt the Wasserstein marginals-based approach recently introduced for seismological problems by Sambridge et al. (2022), building on work presented in Chapter 3. The approach is developed using synthetic landscapes, in which there is complete control and knowledge of their uplift, erosion and noise properties. The methodology explicitly incorporates the reality that many landscape geometries are possible for a given uplift rate history because noise exists.

A variety of approaches exist to generate synthetic landscapes, including landscape evolution models

(LEMs; Tucker et al., 2001; Salles, 2016; Yuan et al., 2019a). An advantage of using LEMs that incorporate landscape evolution in three-dimensions (two spatial and one temporal) is that assumptions regarding temporal stability of drainage planforms, implicit in approaches that invert suites of longitudinal river profiles, can be relaxed. LEMs require parameterisation of initial and boundary conditions, which are often not especially well constrained by observations in the real world. The specific arrangement and the distribution of noise in the initial condition inserted into LEMs is often arbitrary—more often than not they are determined using convenient random number generators, which tend to produce noisy initial conditions with a uniform (white) noise distribution by default (Ijjász-Vásquez et al., 1992; Perron and Fagherazzi, 2012). In the absence of independent constraints, which are scant, there is no obvious scientific justification for using a specific arrangement of noise. Thus, the consequences of using different arrangements of noise are examined, by generating ensembles of models building on forward modelling work presented in Chapter 2 (Morris and Roberts, 2025). It is noted that a subset of previous studies seeking to understand the evolution of topography also make use of ensemble approaches (see e.g., Willgoose et al., 2003; Chandra et al., 2019a,b; Barnhart et al., 2020c; Gallen and Fernández-Blanco, 2021).

In the following section each component of the methodology, including the inversion strategy is described. The framework is summarised in Figure 4.2. I first describe the forward model used to predict landscape evolution once initial conditions, the erosional model, and uplift histories have been parameterised. The inversion strategy is then described, including the creation of objective functions used in the search for optimal models. The challenge of 'valley-skipping' is addressed by making use of Wasserstein distances, extending the approach developed in Chapter 3. Finally the methodology for searching for adequately fitting models and recovery of uplift rate histories is described. The recovery of tectonic information from synthetic landscapes with Euclidean and Wasserstein measures of misfit are compared and the efficacy of a variety of optimisation algorithms is assessed. Such algorithms aim to efficiently search parameter space in order to reduce computational burden. Uncertainties are quantified using model ensembles and probabilistic techniques.

4.2 Methodology

4.2.1 Forward model

The forward model in this chapter simulates the evolution of topography by implementing a widely used partial differential equation (PDE) within the open-source Python package Landlab (Hobley et al.,

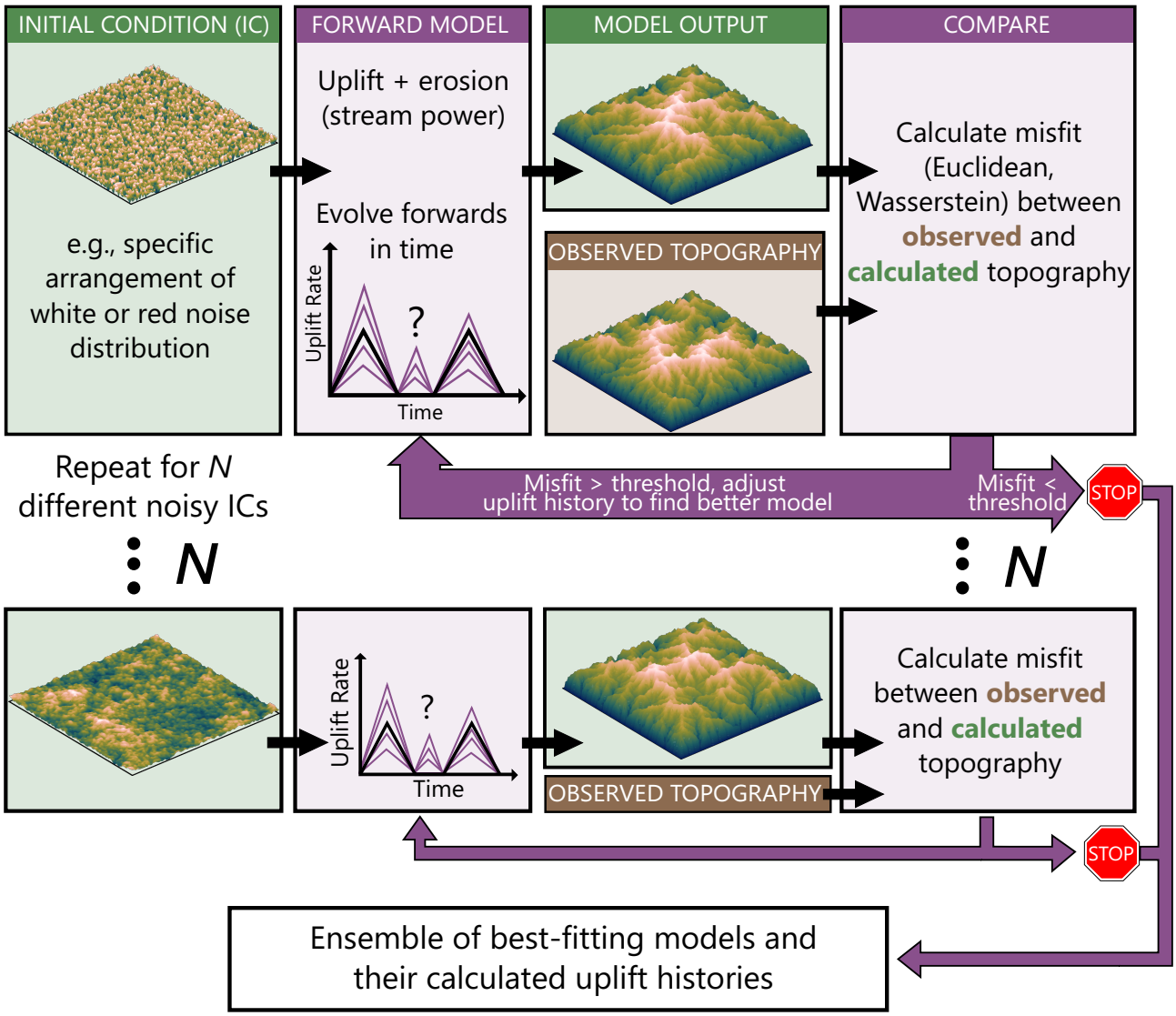


Figure 4.2: **Schematic summarising approach to inverting landscapes for uplift histories in the presence of noise.** In a single inverse model (top row), a forward model is first initialised with a given arrangement of noisy elevations, the landscape then evolves forward in time with erosion governed by the stream power model and a prescribed uplift rate history. Model output (a theoretical landscape) at a predefined time, T, is compared to observed topography using Euclidean or Wasserstein-based metrics. The forward model is then re-run with an uplift rate history adjusted to provide a better fit to the observed landscape. This loop continues until misfit between observed and calculated landscapes is below a defined threshold. The entire process is repeated for N different initial topographies (middle to bottom rows) producing an ensemble of best-fitting models. The ensemble of corresponding calculated uplift rate histories can then be examined.

2017; Barnhart et al., 2020d). Elevations, z, evolve as a function of time, t, determined by uplift rate, U, and a stream power erosional model, plus noise, η:

$$\frac{\partial z}{\partial t} = -vA^m \nabla z^n + U + \eta. \tag{4.1}$$

Here v, m, and n are erosional constants that are fixed to values of $v = 10^{-3}$ /kyr, $m = 0.5$, $n = 1$. This model is again consistent with those introduced and applied in previous chapters, and presented again here for clarity. The erosional parameter values are chosen to be within the range of those used within many existing studies of observed and numerically modelled landscapes, and are considered to be representative of fluvial systems in which erosion rate is controlled by the ability to detach substrate material (see e.g., Howard, 1994; Whipple and Tucker, 1999; Kirby and Whipple, 2001; Pritchard et al., 2009; Lague, 2014; Kwang and Parker, 2019; Barnhart et al., 2020d; Thompson Jobe and Reitman, 2025). In essence the erosional model advects (moves) slopes upstream at a rate that depends on upstream drainage area (i.e., they slow down as they move because A decreases upstream) and the values of the erosional parameters. Other mathematical formulations of erosion exist, for example hillslope and transport-limited processes are often predicted using diffusive models, other more complex erosional models including erosional thresholds and stochastic discharge have also been developed (e.g., Culling, 1960; DiBiase and Whipple, 2011; Scherler et al., 2017; Shobe et al., 2017; Campforts et al., 2020b; Forte and Rossi, 2024a,b; Roberts and Wani, 2024; Wang et al., 2024).

It is recognised that some debate exists surrounding parameterisation of n in stream power models (see e.g., Lague, 2014). The simple (linear, $n = 1$) stream power model is adopted because it is widely used to understand landscape evolution at a variety of spatio-temporal scales, it is relatively simple to solve numerically, straightforward to reproduce results with, and can generate realistic landscapes (e.g., Fernandes et al., 2019; Roberts et al., 2019; O'Malley et al., 2021; Wapenhans et al., 2021).

In this chapter synthetic landscapes are generated using a Cartesian grid with dimensions 100 × 100 km, with each grid pixel having dimensions 1 × 1 km. All four sides of the model domain are fixed at zero elevation and permit flux of material, i.e 'open' boundary conditions of the Dirichlet type. An initial noisy surface with elevations 0 to 10 m is inserted. This initial noise is constructed following the approach described in Chapter 2 (Morris and Roberts, 2025). Examples of two different arrangements of white noise initial conditions are shown in Figure 4.1. Topographic depressions are filled to permit continuous flowlines and minimise the chance of internally draining regions forming (Barnes et al., 2014). The synthetic landscape is evolved forwards in time for T million years. Uplift, flow-routing,

and erosion occur at each time step of the model, $\Delta t = 10$ kyr, which ensures that the models always satisfy the Courant-Friedrichs-Lewy condition for numerical stability, and are large enough to permit a reasonable computational runtime. Advection of slopes is calculated using the FastScape erosional scheme, and flow routing is performed with the 'D8' algorithm (O'Callaghan and Mark, 1984; Braun and Willett, 2013). Each forward model takes ~ 5 seconds of computational time using an Intel Xeon Platinum 8358 processor with 16 GB of RAM.

In this chapter, three categories of synthetic landscape are generated by implementing three simple uplift functions. In the first category, a single phase of uplift is inserted at all non-boundary (core) grid nodes in order to generate a 'block-style' landscape, i.e., uplift is spatially invariant. In the second category, staged spatially-invariant uplift is applied. In the third category, uplift varies spatially as a two-dimensional Gaussian function with the form

$$U(x,y) = U_{max} \exp\left\{-\left[\frac{(x-x_0)^2}{2\sigma_x^2} + \frac{(y-y_0)^2}{2\sigma_y^2}\right]\right\}, \tag{4.2}$$

where $U(x,y)$ is uplift rate, $x_0 = y_0 = 50$ km are the central coordinates of the dome, and $\sigma_x = \sigma_y = 20$ km are the standard deviations (spreads) in the x and y directions. The function is scaled by maximum uplift rate, U_{max}. This category produces 'domal' landscapes. All three categories of synthetic landscape are designed to represent natural systems, such as the evolution of orogenic plateaux, domal swells, or volcanic regions (e.g., Pritchard et al., 2009; O'Hara et al., 2024, 2025). The uplift rate histories that are solved for in this chapter are shown in Figures 4.3b and 4.4h .

It is useful to consider the amount of information about uplift a landscape might contain. To avoid designing experiments where tectonic information has been completely removed from topography, the choice of uplift history is guided by the erosional response time. The response time determines how long an erosional signal will take to propagate from the boundary of the map upstream. For the linear ($n = 1$) stream power model, the erosional response time, τ can be expressed as

$$\tau = \int_0^{x^*} \frac{\mathrm{d}x^*}{vA(x^*)^m} \tag{4.3}$$

(Roberts et al., 2012a). Here, x^* is distance in the upstream direction. A map of response time is shown in Figure 4.3c, illustrating that the time taken for a knickzone to propagate from base level (i.e., 0 m, the lower bound of the integral) to the headwater regions of the longest rivers exceeds 6 Myr. These results are also illustrated with the longitudinal profiles shown in Figure 4.3d. The associated

model coverage, i.e., number of grid cells in the landscape sensitive to uplift at a given time, is shown by the histogram in Figure 4.3b.

Figure 4.1 shows landscapes generated in two simulations initialised with different arrangements of the same distribution of white (uniform) noise with the uplift rate history shown in panel (c). The resulting topographies have broadly similar characteristics (e.g., distributions of elevations), however, differences in the locations of river valleys and interfluves can be substantial resulting in pixelwise differences in elevation > 600 m. This figure demonstrates the first of two key necessities for the inverse model. First, the need to develop quantitative methods that can objectively compare observed and calculated topographies whilst 'seeing through' local complexity. The second is a strategy to efficiently explore model parameter space and find better-fitting calculated topographies.

4.2.2 Inversion strategy

The inverse modelling framework developed in this chapter is shown in Figure 4.2. The goal of a single inversion is to determine the unknown uplift rate history (i.e., the values of uplift rate) used to generate an 'observed' target landscape. An automated and objective (quantitative) optimisation approach is used to perform the search for the unknown history. The search seeks the minimum value of an objective function that quantifies misfit between the 'observed' and theoretical landscapes. This strategy closely follows that of existing inverse modelling approaches stemming from Roberts and White (2010). However, in contrast with previous studies, I construct objective functions using Wasserstein-based metrics, which, having been introduced in Chapter 3, are described again below. For clarity, I also note that the maximum uplift rate is sought for the domal landscapes (U_{max} in Equation 4.2).

The theoretical landscapes are generated using a landscape evolution model incorporating stream power erosion, uplift and noise (Equation 4.1). The inverse models start with either a raster grid of uplift rates supplied by the user (e.g., an initial guess of appropriate values or zero) or random values chosen by the optimisation algorithm. In subsequent iterations of the model new theoretical landscapes are generated by adjusting the uplift rate history, with each iteration seeking to identify an uplift rate history that produces an updated theoretical landscape that better matches the 'observed' one. The model terminates when the misfit between the 'observed' and theoretical landscape is less than a predetermined threshold or a predefined number of forward models have been run. Termination criteria for the experiments in this chapter are provided in Section 4.2.2. The presence of multiple

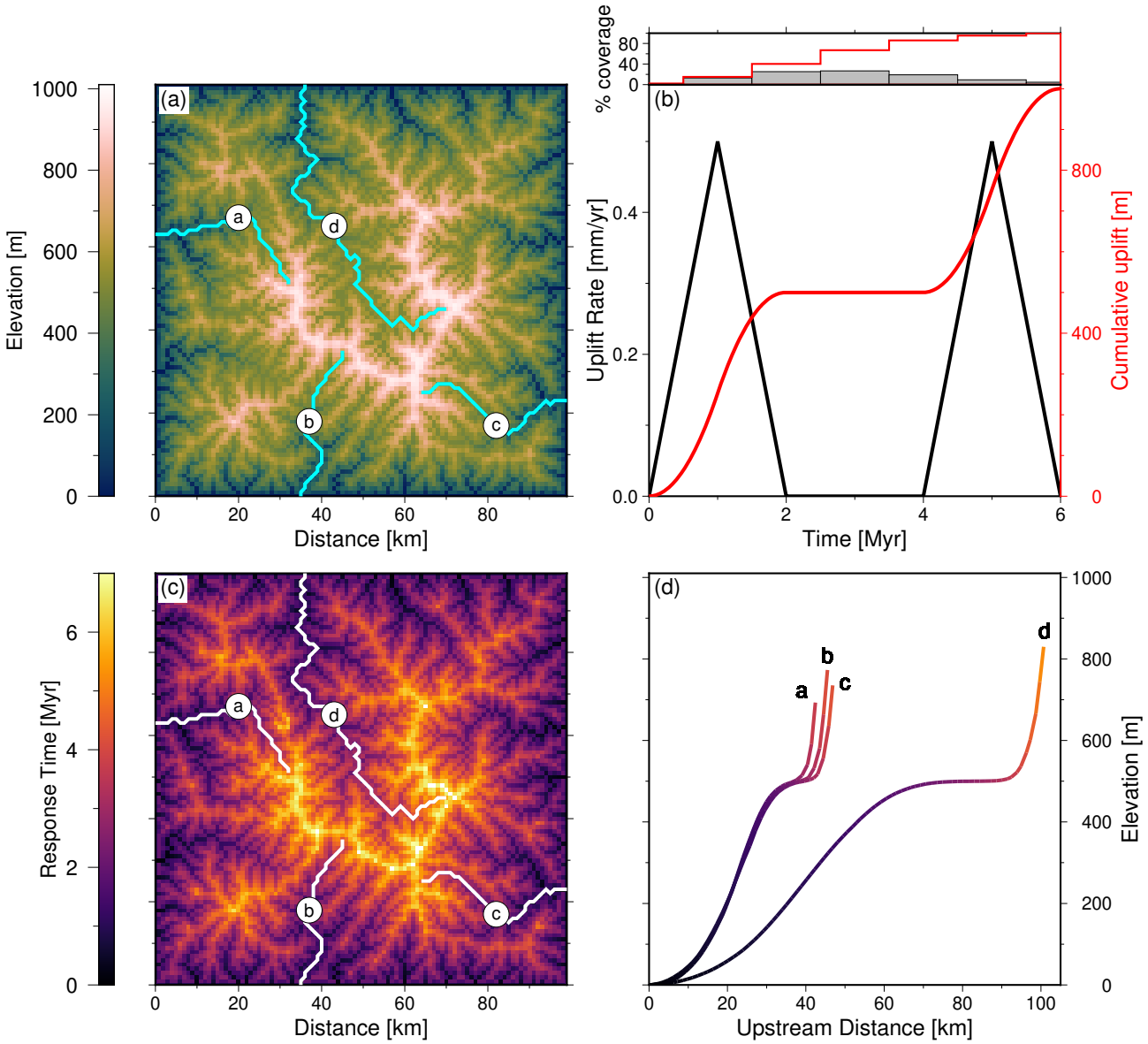


Figure 4.3: **Tectonic information—landscape response times—within a fluvial landscape.** (a) An 'observed' landscape (see Figure 4.1). Turquoise lines = positions of main channels in the four largest drainage basins. (b) Black and red lines = uplift rate and cumulative uplift history used to generate the landscape in panel (a). Filled histogram shows proportion of grid cells sensitive to uplift at that time, governed by response time: $\tau = \int 1/vA(x^*)^m \mathrm{d}x^*$ (see body text for details). Red line shows the cumulative histogram. (c) Map of landscape response times—note erosional signals propagate from the map boundary. (d) Longitudinal profiles of four rivers shown in panels (a) and (c). colours correspond to the response times shown in panel (c).

misfit minima, due to the role of noise, means that the model may terminate when the uplift history between the best-fitting landscape does not resemble that used to produce the 'observed' landscape. However, if the inverse model is working well, the uplift rate history used to produce that *optimal* theoretical landscape should closely resemble the history of uplift used to produce the 'observed' landscape. Here, the 'observed' landscape is a synthetic one generated with a known uplift rate history, which means that one has the information needed to assess the accuracy of calculated uplift rates. I use the nomenclature 'observed' throughout this chapter to refer to the target landscapes that theoretical landscapes, generated during inverse modelling, are compared to. Of course, the inversions are done blindly without any priors related to the actual uplift parameters used to generate the real topography. In other words, it is pretended that the true uplift history used to generate the 'observed' landscapes is unknown when they are inverted.

An ensemble of inverse models is produced in which an 'observed' landscape, generated with a specific arrangement of noise, uplift history and stream power model, is compared to a series of theoretical landscapes each generated with a different noisy starting topography.

Constructing Euclidean-based objective functions

The first objective function that is tested is generated using 'standard' Euclidean statistics (see e.g., Roberts and White, 2010; Croissant and Braun, 2014; Barnhart et al., 2020d; O'Malley et al., 2021; Petit et al., 2025; van der Meij, 2025). The objective function to be minimised includes only root mean squared (RMS) misfit, H_e, which is calculated such that

$$H_e = \left[\frac{1}{N} \sum_{i=1}^{N} (z_i^o - z_i^c)^2 \right]^{1/2} \tag{4.4}$$

where z_i^o and z_i^c are the respective elevations of the 'observed' and calculated theoretical landscapes. i is the index of cells on the grid, and N is the number of measurements of elevation, i.e., total number of cells on the grid.

Constructing Wasserstein-based objective functions

The second objective function that is constructed extends the approach in Chapter 3, where Wasserstein (sometimes called 'Earth-mover') distances are calculated between pairs of topographic marginals, by making use of landscape hypsometries and maximum elevations. The approach stems from Optimal Transport theory (Monge, 1781; Kantorovich, 1942; Sambridge et al., 2022). Examples of topographic

marginals are shown in Figure 4.4. In this chapter, as in Chapter 3, they are constructed for each cardinal direction (i.e. along the x and y axes) such that

$$z^*_{x,y}(x,y) = \frac{z_i(x,y)}{\Delta \sum_i z_i(x,y)}, \tag{4.5}$$

where z^* is elevation normalised by the sum of elevations in the landscape and i refers to the index of grid cells. Δ is the grid resolution.

Here, the Wasserstein distance, W_2, is defined as a measure of the minimum cost associated with transforming a topographic marginal from a theoretical landscape to its associated marginal from the 'observed' landscape. Conversion to cumulative density functions makes it straightforward to compare marginals (Sambridge et al., 2022; Morris et al., 2023). Pairs of cumulative density functions generated from the topographic marginals of the 'observed' and calculated landscapes (indicated by the suffixes 'o' and 'c', respectively) are compared, such that

$$W_2^{x,y}(o,c) = \left[\int_0^1 |O^{-1}_{x,y} - C^{-1}_{x,y}| \right]^{1/2} \tag{4.6}$$

where $O_{x,y}$ and $C_{x,y}$ represent the cumulative density functions of the 'observed' and calculated elevation marginals in the x or y directions normalised such that $\int_{-\infty}^{\infty} z^o(x)\mathrm{d}x = \int_{-\infty}^{\infty} z^o(y)\mathrm{d}y = \int_{-\infty}^{\infty} z^c(x)\mathrm{d}x = \int_{-\infty}^{\infty} z^c(y)\mathrm{d}y = 1$. The cumulative density functions for the 'observed' topography in, for instance, the x direction is $O_x(x) = \int_{-\infty}^{x} z^o(x)\mathrm{d}x$. Similarly, $O_y(y) = \int_{-\infty}^{y} z^o(y)\mathrm{d}y$, $C_y(y) = \int_{-\infty}^{y} z^c(y)\mathrm{d}y$, and $C_x(x) = \int_{-\infty}^{x} z^c(x)\mathrm{d}x$. It is noted that it is possible to choose other (e.g., non-orthogonal) directions to calculate and compare marginals. Wasserstein distances can also be calculated in two dimensions, rather than using a marginals approach, however, doing so tends to be very computationally expensive (see Figure 3.6 for an example).

The methodology used to compare landscapes is adapted from the Wasserstein-based 'fingerprint' approach introduced by Sambridge et al. (2022) for seismological problems. Here, misfit between 'observed' and calculated landscapes, H_w, with units of square kilometres, is calculated such that

$$H_w(o,c) = W_2^x(o,c)^2 + W_2^y(o,c)^2 + \mu_1 W_2^h(o,c) + \mu_2 \left[z_{max}(o) - z_{max}(c) \right]^2, \tag{4.7}$$

where $W_2^x(o,c)$ and $W_2^y(o,c)$ are the 2$^{\text{nd}}$ one dimensional Wasserstein distances between the normalised elevation marginals of the 'observed' and theoretical (calculated) landscapes.

W_2^h is the Wasserstein distance between the hypsometries of the two landscapes (which are also cumulative density functions), and z_{max} is the maximum elevation of a landscape (in kilometres). These two terms are incorporated into the objective function to improve its sensitivity to uplift timing and rate. For instance, Strahler (1952) demonstrated that landscapes of different maturities have different hypsometries. Incorporating information about maximum elevation differences can be diagnostic of total (cumulative) uplift. It also provides information about absolute elevations lost when topographic marginals are made dimensionless. The two dimensionless weighting terms, μ_1 and μ_2, control the influence of hypsometric and maximum elevation differences within the objective function. By systematically varying $10^{-6} \leq \mu_1 \leq 10^2$ and $10^0 \leq \mu_2 \leq 10^8$, values that produce objective functions with well defined global minima were identified (Figures 4.8 and 4.10). In this chapter, $\mu_1 = 1$ and $\mu_2 = 10^6$.

Searching for true uplift rate histories

It is usually impractical from the perspective of computational burden to search the parameter space by brute force, e.g., by systematically changing values of uplift rate parameters with sufficient resolution that true or sufficiently accurate uplift rate histories can be identified. Instead, I seek to reduce computational burden by minimising the number of forward models run and iterations of the inverse model required to yield a desirable solution. A variety of optimisation algorithms exist that aim to efficiently search parameter space and are suitable for tackling non-linear problems without the need for calculation of derivatives of the objective function, which can be a time-consuming step. I test algorithms commonly used in geophysics and other disciplines: Powell's method of conjugate directions, the Nelder-Mead 'amoeba'/simplex approach, and the Neighbourhood Algorithm (Powell, 1964; Nelder and Mead, 1965; Press et al., 1992; Sambridge, 1999a,b).

Powell's algorithm is a direction-based method used to find the minimum (or maximum) of a function. The algorithm operates by searching for the minimum misfit in conjugate directions within the parameter spaces $H_e(U_n)$ or $H_w(U_n)$. Multiple iterations of this process are performed with potential new conjugate directions being constructed at each iteration. The algorithm continues until successive iterations yield no significant improvement in misfit reduction. Powell's algorithm has previously been used in studies of landscape evolution (e.g., Roberts and White, 2010; Roberts et al., 2012a; Rudge et al., 2015). In this chapter I use a version of Powell's algorithm implemented within the SciPy python package, modified to return additional information about intermediate stages of the inversion (Press et al., 1992).

The Nelder-Mead algorithm is also implemented using the SciPy package (Gao and Han, 2012). This algorithm makes use of a simplex, that can be described as a shape with N dimensions and $N + 1$ points where each point is connected by a line segment. For instance in two dimensions, the simplex is a triangle, and is a tetrahedron in three dimensions. The number of dimensions of the simplex is equal to the number of parameters. The algorithm iteratively proceeds 'downhill' through the parameter space (towards a minimum) by evaluating the objective function at each vertex of the simplex and adjusting the simplex shape to move away from this point by making use of geometric transformations (extending or contracting a side length, for instance). As the algorithm progresses, the simplex should, in theory, move towards and contract upon the minimum of the objective function. As with Powell's algorithm, the Nelder-Mead algorithm terminates when function evaluations at successive iterations yield no significant improvement.

For Powell's and the Nelder-Mead algorithms, the Euclidean-based inverse models were terminated when the absolute difference between H_e in adjacent iterations was less than the predefined tolerance, $T_e = 10^{-4}$ m. The Wasserstein-based models were terminated when relative differences between values of $H_w \leq T_w = 10^{-4}$ km^2, respectively (see Figure 4.2). The values of the tolerances were chosen to ensure that there is a balance between computational efficiency and the convergence of solutions. It is found that tolerances $< 10^{-4}$ make little difference to the accuracy of solutions.

The Neighbourhood Algorithm (NA) is a derivative-free method used to explore parameter space, and has been applied across various geophysical and geological non-linear problems (e.g., Sambridge, 1999a,b; Moschetti et al., 2010; Ariyanto et al., 2017; Attanayake et al., 2017; Berbellini et al., 2017; Yudistira et al., 2017; Pedersen et al., 2018; Yuan et al., 2019b; Ferreira et al., 2020; Jones et al., 2021; Stanley et al., 2021; Stephenson et al., 2021a; Gallen et al., 2023; Sturgeon et al., 2023; Curry and van der Beek, 2025). Croissant and Braun (2014) used the algorithm to invert for values of erosional parameters in the stream power model. The algorithm consists of two phases. In the first phase, the algorithm searches the parameter space by running a number of forward models and evaluating misfit for each model. A Voronoi cell is constructed in the parameter space around each model, and assigned the corresponding value of misfit. A Voronoi cell is defined as a region in the parameter space surrounding a point (representing parameter values of a specific model), where every location inside that region is closer to the point than any other point (model). The searching phase is guided by four user-supplied variables: the initial number of models (N_i), the number of models generated at each iteration (N_s), the number of Voronoi cells to be resampled during each iteration (N_r), and the number

of iterations (N). The total number of forward models evaluated during the search phase is defined by

$$N_{total} = N_i + N_s \times N. \tag{4.8}$$

In this respect, the NA has two advantages over Powell's algorithm. First, the total time for a single inversion can be estimated with reasonable accuracy, assuming the time for one forward model to run is known, simplifying the allocation of computational resources. Secondly, by varying the values of N_i and N_r, a user can control the style in which the algorithm explores the parameter space. High values of N_i and N_r result in a wide exploration of parameter space, which may be useful when several minima exist or little is known about the expected values of best-fitting parameters. Lower values of N_i and N_r lead to a more focused search in fewer regions of the parameter space. I note that the initial sampling N_i, represents the model prior, which is drawn from a uniform probability distribution.

The output of the search phase is an ensemble of models that have varying degrees of fit to the 'observed' landscape. Whilst this ensemble could be interrogated for its statistical properties, or used to identify a best-fitting model, doing so can be misleading because ensemble results can be irregularly distributed. Instead, greater statistical insight can be gained by completing an additional *appraisal* phase (Sambridge, 1999b). The appraisal phase, which operates within a Bayesian framework, is designed to resample the model ensemble generated by the search phase. It can be used to construct posterior probability distributions (PPDs) for each parameter via Monte Carlo integration techniques. The PPDs can be used to quantify uncertainties in parameters (in this case, calculated uplift rates) and their covariance. In this chapter I use the neighpy implementation of the Neighbourhood Algorithm within Python.

4.2.3 Experimentation strategy

In order to test whether two dimensional noisy topography, $z(x, y)$, can be inverted for its uplift rate history, four experiments that have increasing complexity are conducted.

In **Experiment 1** I explore whether the timing of a single phase of uplift can be recovered from a landscape when noise is present (Figure 4.4). To do so, only the timing of uplift is permitted to vary—all other model parameters are fixed. The landscapes are generated with a single, symmetric phase of uniform uplift lasting 2 Myr with a peak uplift rate of 1 mm/yr. Several examples are shown in Figure 4.4a-c; the example with late uplift (peak rate at 8 Myr) is treated as the 'observed' topography. A suite of theoretical landscapes are generated by initialising each landscape evolution model with a

different arrangement of the same white noise distribution as the 'observed' landscape, and shifting the timing of peak uplift rate systematically every 0.01 Ma between 1 and 9 Myr. Misfit between the 'observed' and each of the 8×10^4 (800 periods of uplift $\times$ 100 initial noise configurations) theoretical landscapes is calculated. The experiment is repeated for a domal uplift scenario and for when the initial noise applied to theoretical landscapes is 0 – 400 m, i.e., of a much greater amplitude than in the 'observed' topography. The results of all three experiments are used to assess sensitivity of misfit statistics to uplift timing when noise is present in landscapes.

In **Experiment 2** a more complex 'observed' landscape generated with two phases of uplift is inverted to recover its uplift history (Figures 4.3a-b). The two-stage uplift history was chosen for three reasons. First, uplift within 6 Myr ensures that tectonic information from the first phase of uplift is still contained within the landscape, for the chosen erosional parameter values. Secondly, a two-peaked uplift history is obviously more complex than one containing a single phase of uplift. Thirdly, uplift rates of up to 0.5 mm/yr are comparable to those calculated from observational constraints (e.g., uplifted marine rock) and previous inverse modelling (Wellman and McDougall, 1974; Karlstrom et al., 2007; Czarnota et al., 2013, 2014; Adams et al., 2015; Fernandes et al., 2019; Fernandes and Roberts, 2020; Racano et al., 2020; O'Malley et al., 2021).

The theoretical landscapes are generated with starting conditions identical to the 'observed' landscape—the same arrangement of white noise. In the inverse model, uplift rate is permitted to vary at three times: 1, 3, and 5 Myr between 0–1 mm/yr. Theoretical landscapes are compared to the 'observed' landscape using Euclidean and Wasserstein-based objective functions. The parameterisation of the Neighbourhood Algorithm search phase is shown in Table 4.1. During the appraisal phase, the best 50% of models in the ensemble are resampled 50,000 times. An advantage of a three parameter inversion is that it remains computationally tractable to perform a systematic search of parameter space and generate maps of misfit space that can be compared to the trajectories and results of the optimisation algorithms. Results of the brute force searches and optimisation algorithms are presented in Figures 4.8 and 4.13.

In **Experiment 3** I again invert the topography shown in Figure 4.3a for its uplift history. In this experiment, however, each of the 100 inverse models have theoretical landscapes that are initialised with an arrangement of white (uniform) noise that is different to that used to generate the 'observed' landscape and to each other. This model is designed to mimic the procedures that are likely to be necessary when inverting real landscapes for which one usually has no information about the specific

Experiment	N_i	N_s	N_r	N
2	50	50	5	5
3	128	256	64	16

Table 4.1: **Parameter values for Neighbourhood Algorithm.** N_i = number of initial models, N_s = number of models generated at each iteration, N_r = number of Voronoi cells resampled during each iteration, N = number of iterations (see body text for details).

arrangement of noise. The inverse model in this experiment uses the Neighbourhood Algorithm. Results are presented in Figures 4.16–4.19.

Finally, in **Experiment 4** I demonstrate how uplift rate histories can be recovered from landscapes in which uplift rates vary as a function of space as well as time. As with Experiment 3, 'observed' and theoretical landscapes are generated with different arrangements of white noise in their initial conditions. Results are presented in Figure 4.21.

4.2.4 Comparisons with existing approaches

The uplift rate histories calculated by inverting entire landscapes using Wasserstein-based objective functions are compared with solutions from established methods that invert single or multiple longitudinal river profiles for a history of uplift. To do so I extract the longitudinal profiles, $z(x^*)$ and upstream areas, $A(x^*)$, of the longest river in five landscapes chosen randomly from the 100 optimal landscapes generated in Experiment 3. They are then inverted using the optimisation techniques introduced in Roberts and White (2010). The erosional model in this case is the one-dimensional version of the stream power model:

$$\frac{\partial z}{\partial t} = -vA(x^*)^m \frac{\partial z}{\partial x^*} + U(t). \tag{4.9}$$

Note that no additional noise is included. x^* is the streamwise distance. Erosional parameter values within Equation 4.9 are the same as those used to produce the synthetic landscapes in this chapter.

The optimisation uses Powell's algorithm to search for the uplift rate parameter values that minimise misfit between the 'observed' longitudinal river profile(s) and those predicted by Equation 4.9, whilst also minimising penalty functions that penalise roughness of the solution (calculated uplift rate history) and negative uplift rates. Misfit is calculated using Euclidean (RMS) statistics (Equation 4.4). Two types of experiment are run. In the first, each river is inverted individually with the objective function given by Equation 3 in Roberts and White (2010) with weightings to penalise the first and second derivative of the uplift rate history $W_1 = W_2 = 10^{-5}$ and the positivity penalty $W_3 = 10$. In practice, setting these values to zero has little impact on solutions obtained. As is typical in previous studies,

uplift rates are permitted to vary every 1 Myr between 0–6 Myr, i.e., there are seven free parameters in total (four more than in Experiment 3), which is a useful test of the impact of different approaches to solving the inverse problem. The second experiment follows the same strategy but jointly inverts the five river profiles to identify the single optimal uplift rate history. In this experiment the objective function is simply generated by summing the misfit calculated for each river individually and keeping the same penalty function parameterisation used in the inversion of single profiles.

4.3 Results

4.3.1 Experiment 1: Recovering timing of a single uplift event from landscapes with different noisy starting conditions

Figure 4.4 demonstrates the sensitivity of both Euclidean and Wasserstein misfit metrics to the timing of a single phase of uplift when 'observed' and theoretical landscapes have different noisy initial conditions. Euclidean misfit (Figure 4.4i; Equation 4.4) is highest when timing of uplift differs considerably from the true history (peak at 8 Myr) because the geometries of the associated theoretical landscapes differ considerably from the 'observed' landscape (compare the landscapes, uplift rates and misfit function in Figure 4.4a-h). Misfit decreases as the timing of peak uplift approaches the true value (e.g., Figure 4.4e). A summary of results is shown in Table 4.2. The timing of mean minimum misfit (i.e., the mean of the best-fitting results from the different initial noises) is shown by the black arrow, and occurs at 8.21 Myr. The 0.21 Myr discrepancy is attributed to noise and the role it has in producing theoretical landscapes that are extremely unlikely to match to the 'observed' landscapes with high accuracy.

A similar pattern is observed when comparing landscapes using only the Wasserstein marginals $W_2^x(o,c)^2 + W_2^y(o,c)^2$ in Equation 4.7 ($\mu_1 = \mu_2 = 0$; Figure 4.4i). Mean misfit decreases as the timing of uplift peak becomes more similar to that of the true landscape. The timing of mean minimum misfit occurs at 8.02 Myr. This improved accuracy is attributed to the way in which the Wasserstein marginals 'see through' local variability in landscape geometries introduced by noise (consider the comparison of the marginals shown in Figure 4.4 panels a–f). The variability of the absolute values of misfit across the ensemble of models is greater for more mature landscapes (i.e., those with early uplift), shown by the shaded region in Figure 4.4i. This result is attributed to two factors. First, the oldest landscapes (earliest uplift) are almost entirely eroded, which has removed the signal of uplift from nearly all parts of the 'present-day' landscape (i.e., $T > \tau$, Equation 4.3). Secondly, removing more topography results

in landscapes with marginals that increasingly differ from those of the 'observed' landscape. In such cases the Wasserstein metric, in particular the marginals, are increasingly sensitive to noise at small scales and the different arrangements of drainage planforms caused by the noise.

Figure 4.5 shows values of the three components that contribute to the full Wasserstein metric in this experiment (Equation 4.7: $\mu_1 = 1$, $\mu_2 = 10^6$). It demonstrates the sensitivity of hypsometry and Δz_{max} to uplift timing. However, Δz_{max} is largely insensitive to youthful uplift occurring at times > 6 Myr. In such juvenile landscapes erosion has not yet had time to erode the highest elevations determined by cumulative uplift. Figure 4.5d shows the objective function used to search for the true uplift history, combining the three components. It illustrates the sensitivity of the objective function to uplift timing, and the precision with which the timing of peak uplift can be recovered using a Wasserstein-based metric.

Figures 4.6 and 4.7 demonstrates that Euclidean and Wasserstein misfit are also sensitive to the timing of a single peak of uplift when the uplift style is domal and when the amplitude of the initial noise added to theoretical landscapes is different to that of the 'observed' landscape. The global minima of Euclidean and Wasserstein misfit are 8.13 and 7.97 Myr respectively in the domal uplift experiment (black arrows in Figure 4.6i), and 8.16 and 8.04 Myr when the amplitude of initial noise is 0–400 m (Figure 4.7i).

4.3.2 Experiment 2: Recovering a more complex uplift history when noise is known

Having established that Euclidean and Wasserstein-based objective functions are sensitive to uplift timing, Figure 4.8 presents the results of Experiment 2, a three-parameter inversion where uplift rate can vary at three time intervals. In this experiment each theoretical landscape is initialised with a specific arrangement of white noise identical to that used to generate the 'observed' landscape (shown in Figure 4.1a).

Figure 4.8a-c shows maps of Euclidean (RMS) misfit for a systematic sweep of parameter combinations. Misfit is low in regions proximal to the true solution, shown by the red cross. The red circle marks the global minimum of the brute force search. Unsurprisingly it is located at the same parameter values as the true solution; the 'observed' and theoretical landscapes are identical (within machine precision). Each map is overlain by a white network of Voronoi cells that illustrate the search locations of the Neighbourhood Algorithm. It is encouraging that the density of resampling is densest close to

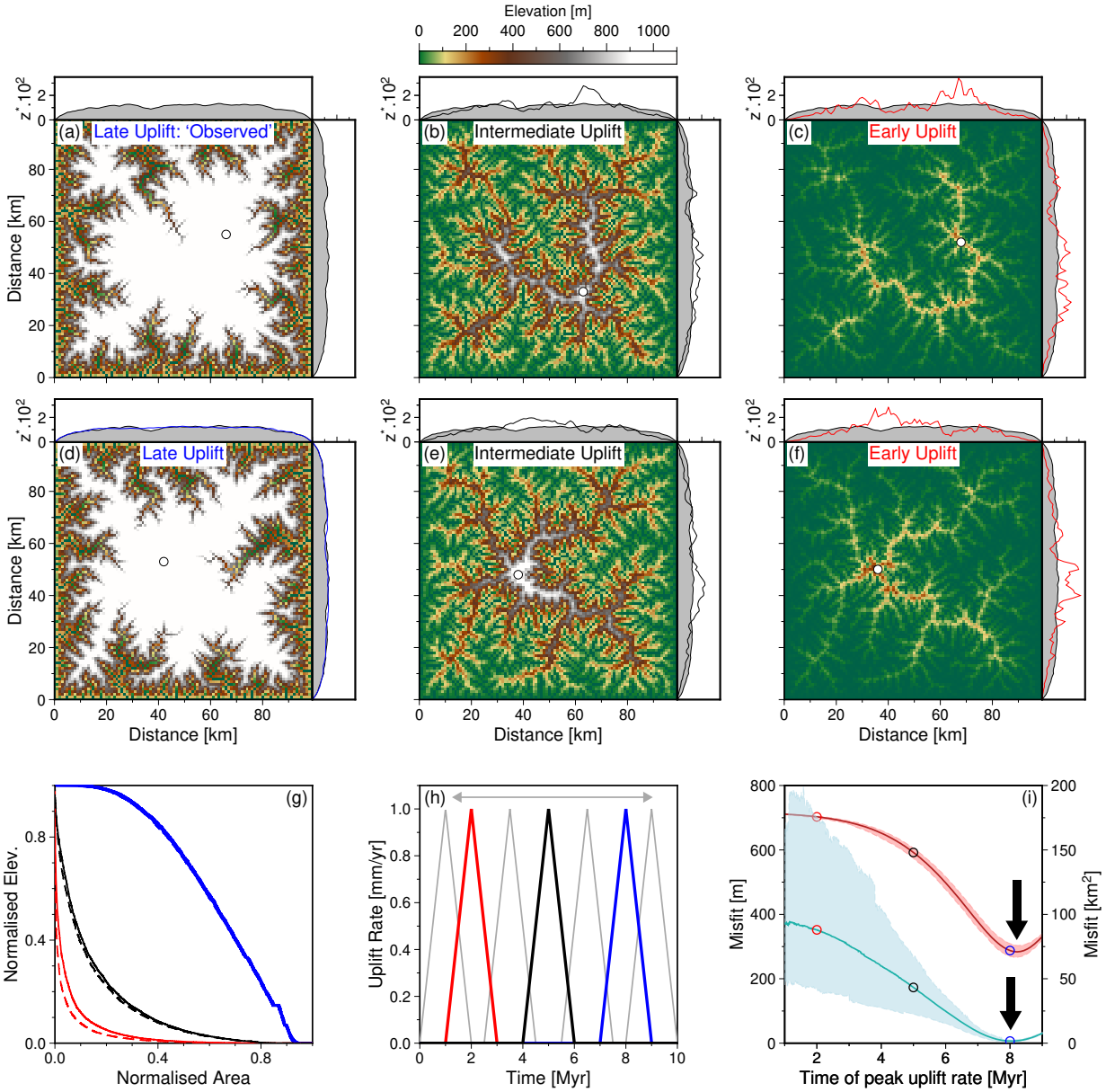


Figure 4.4: **Comparing 'observed' and theoretical landscapes with Euclidean and Wasserstein metrics.** (a–c) Examples of landscapes and topographic marginals generated with the same white noise initial condition and the red/black/blue uplift histories shown in panel (h). Location of maximum elevation, z_{max}, is marked with a white circle. Filled grey marginals correspond to 'observed' landscape shown in panel (a). coloured lines show marginals of adjacent landscapes. (d–f) As per (a–c), generated with a different arrangement of white noise as the initial condition. (g) Hypsometries of landscapes shown in (a–f), coloured by timing of peak uplift. Solid lines correspond to landscapes in (a–c), dashed (d–f). (h) Uplift rate histories, coloured by timing that corresponds to landscapes shown in panels (a–f). grey lines and arrow illustrate how timing of uplift peak is varied to generate statistics shown in panel (i). (i) Euclidean (red) and Wasserstein (blue) metrics generated by comparing the landscape in panel (a) to 8×10^4 landscapes generated with different timings of peak uplift and initial (white noise) conditions. Timing of peak uplift was systematically varied between 1–9 Myr (see panel g), every 0.01 Myr; for each model (i.e., different peak uplift) 100 different initial conditions were tested. Dark line = mean; shaded polygon encloses all results. Red/black/blue circles mark misfit when uplift peak occurs at 2/5/8 Myr (see panel g). Black arrow = minimum misfit. Timing of peak uplift rate for the 'observed' landscape = 8 Myr (panel a).

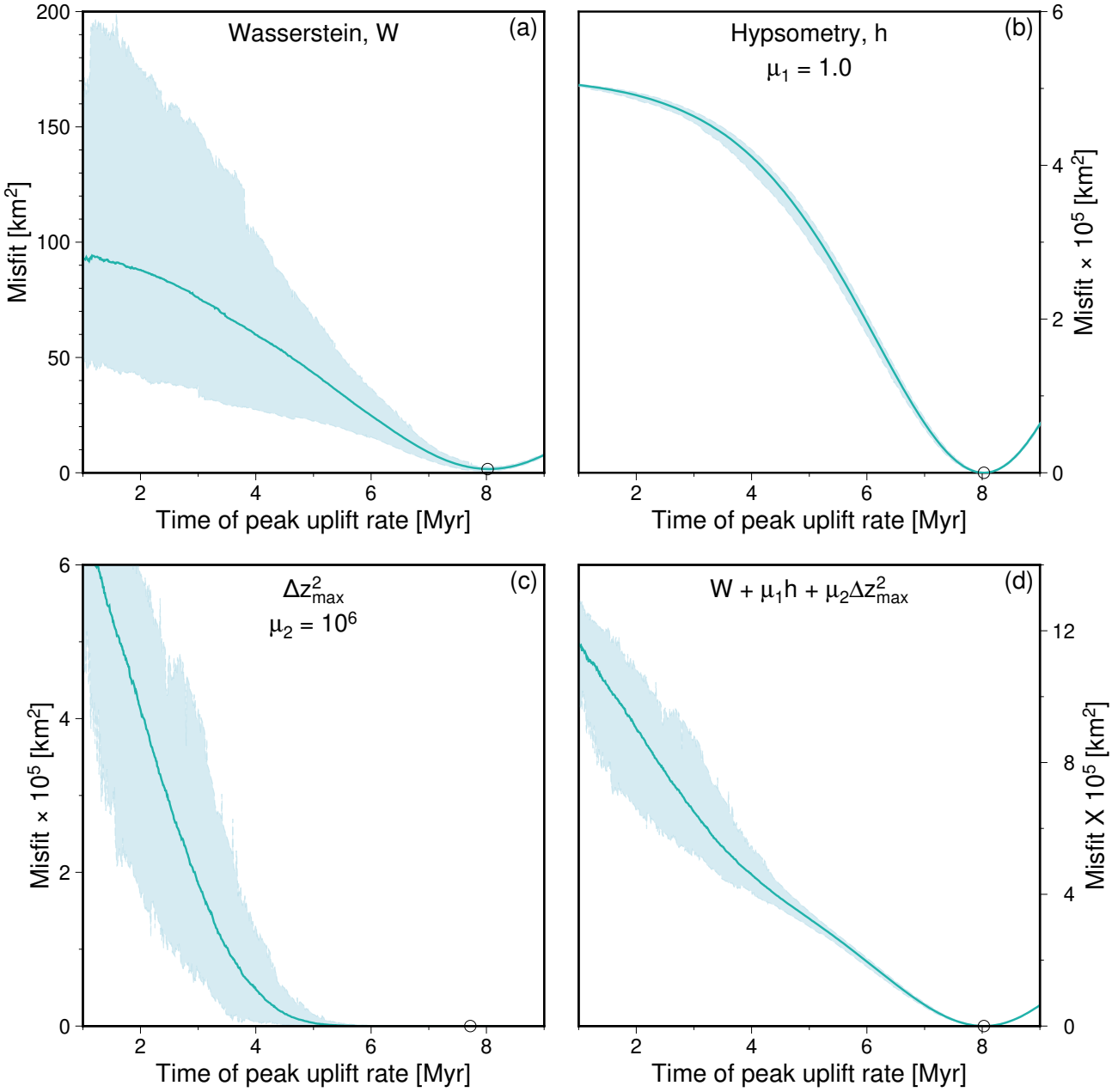


Figure 4.5: **Constructing a Wasserstein-based objective function in one dimension to support the search for true uplift histories.** (a) Wasserstein misfit for the experiment illustrated in Figure 4.4i. Dark blue line shows mean misfit; shaded light blue region encloses all results; note that this example incorporates 8×10^4 models with 800 different timings of peak uplift each with 100 individual simulations initialised with different arrangements of white noise. Open circle shows location of global minimum misfit; note timing of peak uplift for 'observed' landscape = 8 Myr, which is accurately recovered in this experiment. (b) As per (a), for hypsometric misfit scaled by a weighting of $\mu_1 = 1$ (see body text for details). (c) As per (a), for squared difference in maximum elevation, scaled by weighting of $\mu_2 = 10^6$. (d) The summed misfit of (a) + (b) + (c)—an example of an objective function used to identify an optimal uplift rate history in this chapter.

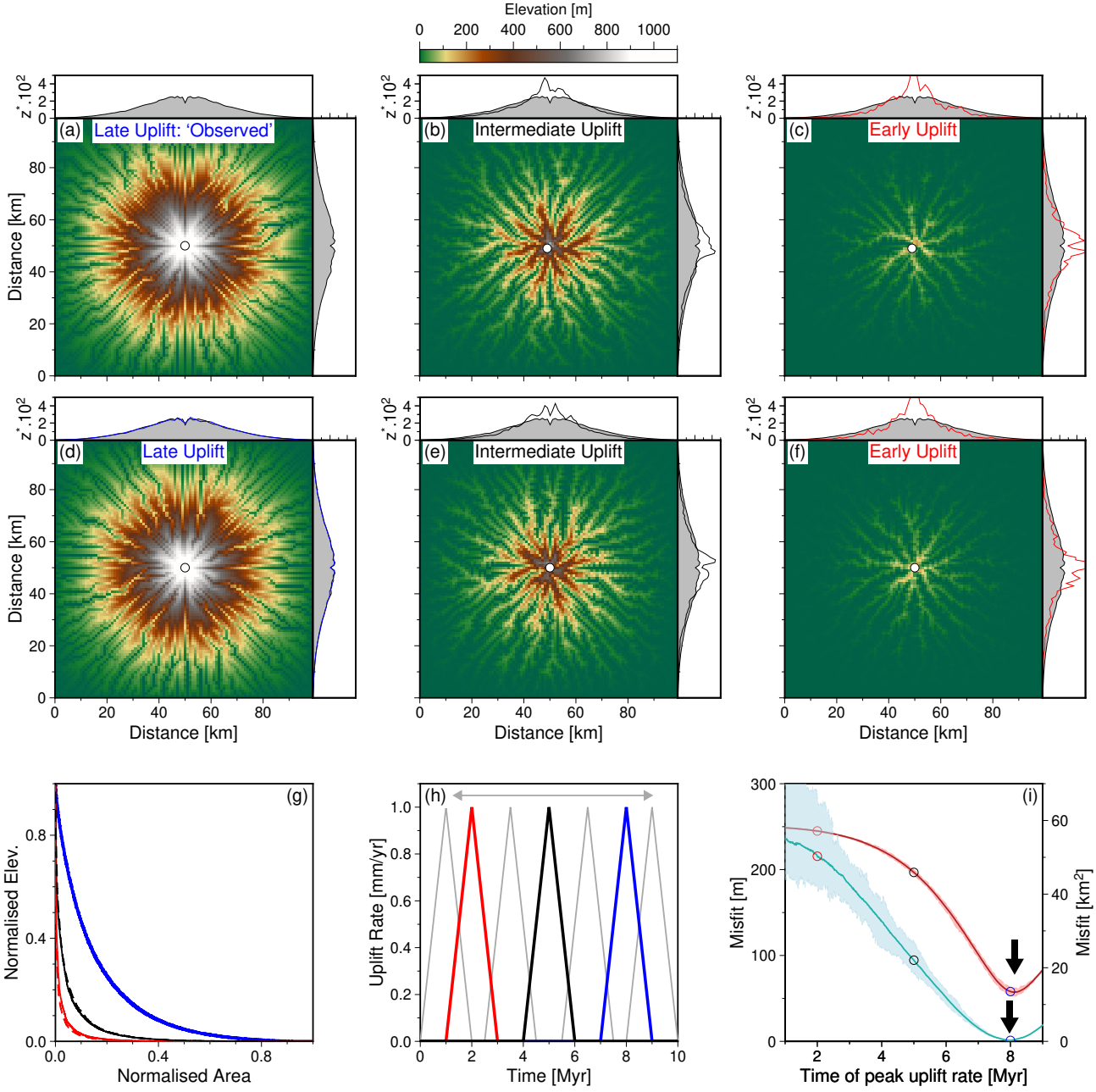


Figure 4.6: **Comparing 'observed' and theoretical domal landscapes with Euclidean and Wasserstein metrics.** Panels as per Figure 4.4, where uplift is applied in a domal style, using Equation 4.2 with $U_{max} = 1$ mm/yr.

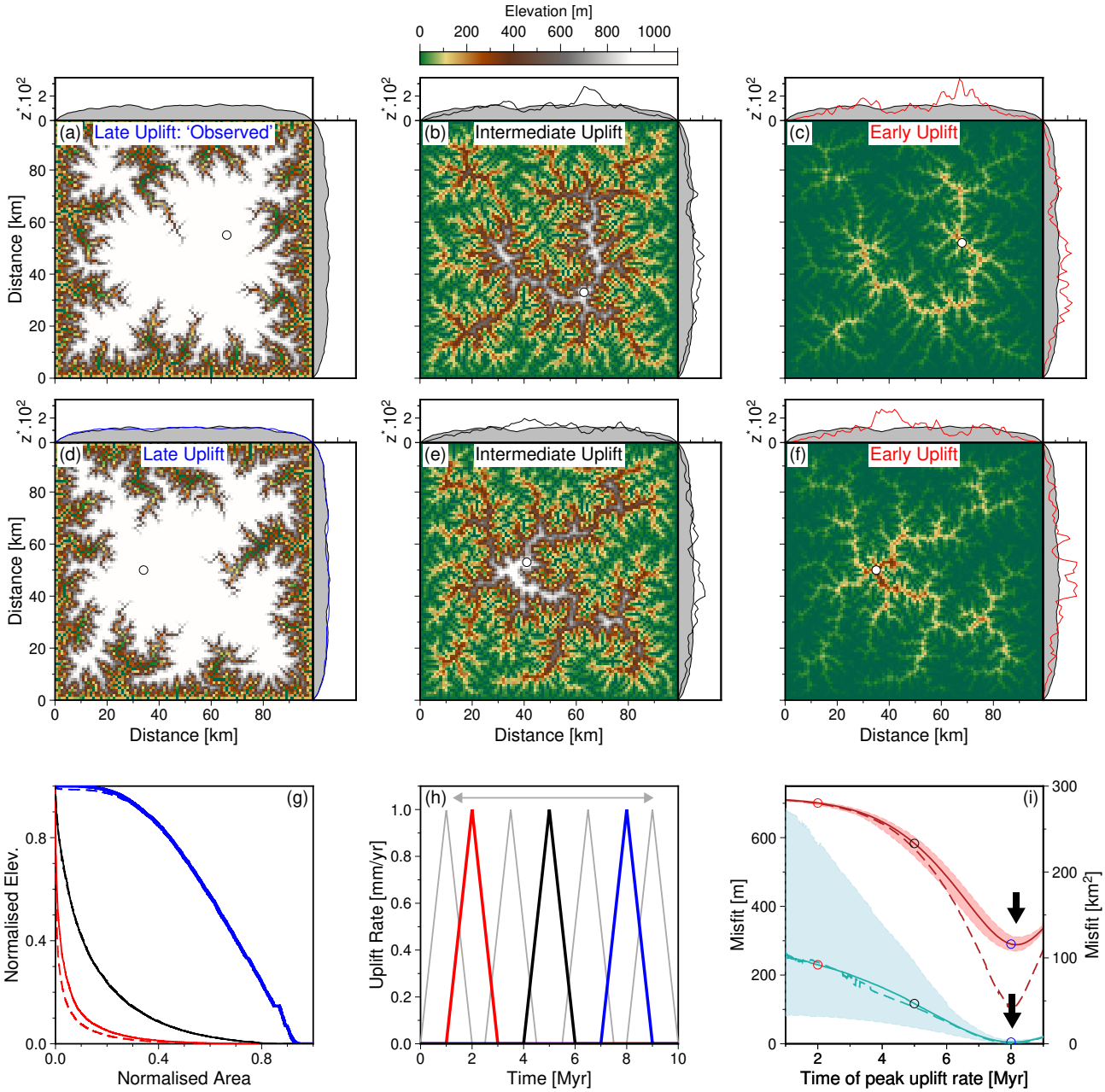


Figure 4.7: **Comparing 'observed' and theoretical landscapes with Euclidean and Wasserstein metrics with different maximum amplitudes of initial noise.** Panels as per Figure 4.4. Here the amplitude of initial noise in the theoretical landscapes is 0–400 m. The dashed lines in (i) show Euclidean (red) and Wasserstein (blue) misfit when the initial noise added to the 'observed' and theoretical landscapes is identical in its arrangement (i.e., the same random seed is used); only its amplitudes differ.

the parameter values used to generate the true uplift history. The trajectory of Powell's algorithm is shown by the blue line. Proceeding from an initial guess of zero uplift rate ($U_1 = U_2 = U_3 = 0$), the algorithm converges towards the true values, however it terminates some distance away from the those values (see small red circles in panels a–c). Note that equivalent misfit maps are shown in Figure 4.9 without results from Powell's and Neighbourhood algorithms.

Scenarios in which Powell's algorithm was initialised with different values of U_n (not shown) were also tested and it was found that they also did not reliably home in on the true solution with much accuracy. These results are attributed to the presence of local minima caused by the 'observed' and theoretical landscapes having different geometries introduced by the impact that even subtle changes in the history of uplift can have on flow routing and landscape form. From the perspective of recovering tectonics from topography, it is concerning that these differences, and local minima arise, even when 'observed' and theoretical landscapes have the same starting conditions and erosional model, and under conditions of spatially invariant uplift. Such local minima hamper the search for optimal solutions when using automated direction-based approaches, such as Powell's algorithm.

Figure 4.8d-f show misfit maps for the Wasserstein-based objective function. The global minimum is located at the same parameter values as the true solution. The parameter values clearly trade-off, illustrated by the 'valleys' of low misfit values. It is noted that the exact shape of the misfit function can be changed by adjusting the values of the scaling factors μ_1 and μ_2 in Equation 4.7 (Figure 4.10). The Neighbourhood Algorithm densely samples regions of the parameter space close to the true solution. Powell's algorithm progresses towards the true solution but does not accurately locate it. These results are attributed to the presence of local minima in the objective function, which Powell's algorithm 'gets stuck in'.

Figure 4.13 shows the uplift histories associated with the best-fitting (minimum misfit) theoretical landscapes from Powell's (dashed) and the Neighbourhood (solid) algorithms, using Euclidean (red) and Wasserstein-based (blue) approaches. The results from inverting with the Nelder-Mead algorithm are indicated by the dotted lines. Powell's and the Nelder-Mead algorithms parameterised with the Wasserstein-based objective function ran 322 and 370 forward models, respectively, to converge on their solutions. 388 and 49,582 forward model runs were required for Powell's and the Nelder-Mead algorithms to converge when the Euclidean objective function is used. The Neighbourhood Algorithm ran 300 forward models (see Table 4.1 for model parameterisation). Convergence metrics for each algorithm are shown in Figures 4.11 and 4.12. The uplift history calculated using Powell's algorithm and

Euclidean statistics overpredicts the first uplift phase, leading to an overall overprediction in cumulative uplift. In comparison, the true uplift history is accurately recovered when using the Neighbourhood Algorithm. The true history is also recovered when using a Wasserstein-based objective function to search for solutions with Powell's or the Neighbourhood algorithm. The Nelder-Mead algorithm performs relatively poorly, underpredicting the first and overpredicting the second uplift phases.

I now extend this experiment to test whether the uplift history is recoverable in the presence of noise. I do so using the Neighbourhood Algorithm, for two reasons. First, its success relative to Powell's and the Nelder-Mead algorithms in recovering uplift information when noise in starting conditions is identical, and secondly the algorithm provides additional information beyond the single best-fitting result, such as posterior distributions, which can be used to quantify uncertainties or parameter trade-off. Note that posterior distributions are shown for Experiment 2 in Figures 4.14 and 4.15.

4.3.3 Experiment 3: Recovering a complex uplift history when noisy starting conditions differ

Figure 4.16 shows examples of brute force parameter sweeps for two typical inversions generated with Euclidean- (panels a-c and d-f) and Wasserstein-based objective functions (g-i, j-l). These maps of misfit are overlain with the search phases of the Neighbourhood Algorithm. Each of the 100 inversions run during Experiment 3 produced 4224 individual forward models (see Table 4.1). In each inversion, the Neighbourhood Algorithm densely samples regions close to the global minimum of the brute force parameter sweep, shown by the red circle. This result verifies that the algorithm can successfully identify regions of low misfit. However, the misfit maps generated with Euclidean statistics demonstrate that the global minimum of the parameter sweep in these scenarios can be located far from the parameter values of the true solution (red cross). These results are attributed to the fact that Euclidean misfit is sensitive to differences in drainage planform geometries that, in this case, originate from differences in arrangements of starting topography.

In contrast, Wasserstein-based objective functions tend to have global minima that cluster tighter around the true values. The success of the Wasserstein objective function in identifying the true uplift history is illustrated for the full ensemble of 100 inversions in the histograms shown in Figure 4.16m-o. These panels illustrate the parameter values at which the global minima occur for the 100 inversions. Euclidean statistics consistently underpredict the true uplift rate of parameter U_1, shown by the black arrow. In comparison, these panels emphasise the ability of the Wasserstein-based approach to identify

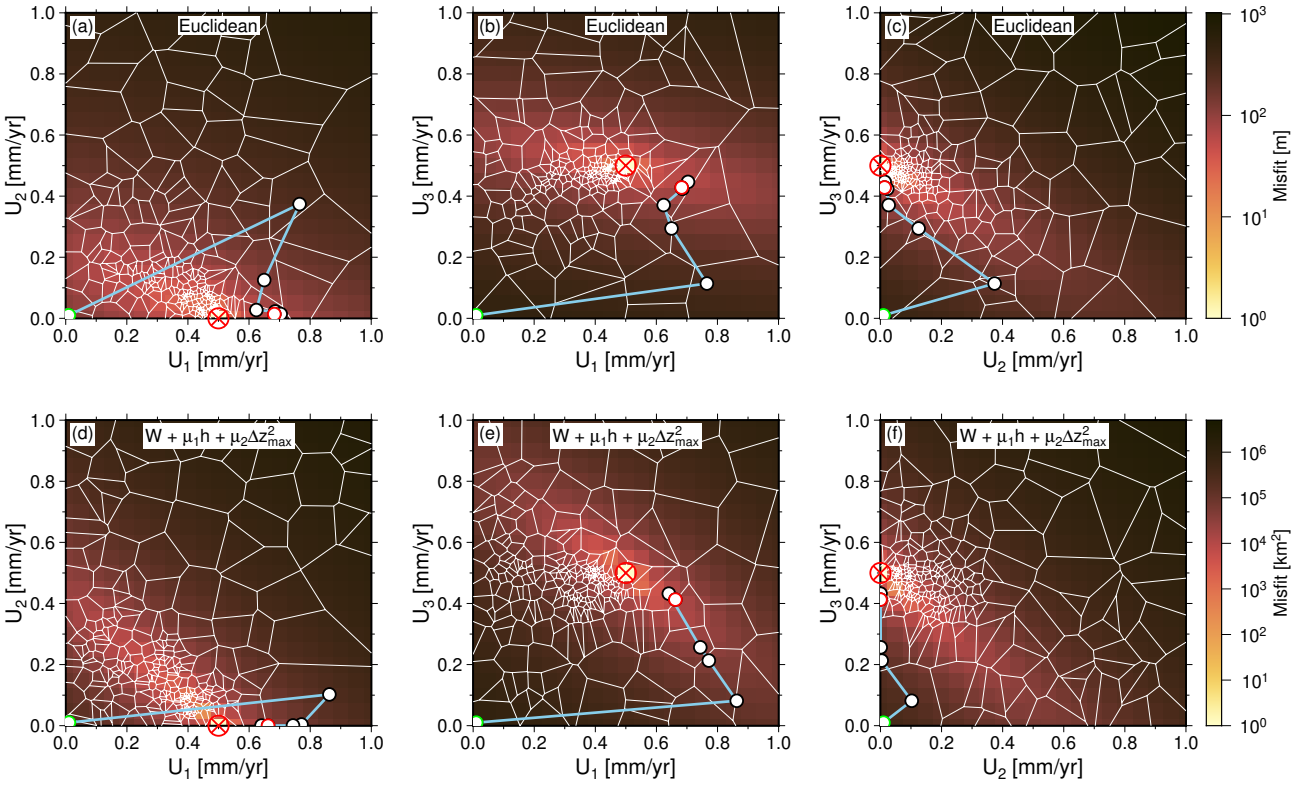


Figure 4.8: **Examples of multi-dimensional Euclidean and Wasserstein-based search spaces for models with same initial noise—objective functions when uplift rate is allowed to vary in time.** (a–c) Slices through Euclidean misfit space for three uplift rate parameters: U_1, U_2, U_3 (see Figure 4.1c for their timings). The 'observed' landscape is shown in Figures 4.1d and 4.3a, which was generated with the uplift rates indicated by the red crosses in panels (a–c). Red-white colour scale = Euclidean (RMS) misfit as a function of uplift rates generated by brute force, systematic, adjustment of parameter values ($\Delta U = 0.05$ mm/yr). White lines = Voronoi cells showing Neighbourhood Algorithm (NA) search; sampling frequency is inversely proportional to cell density. Large red circles = best-fitting uplift rates identified by the brute force search. Blue line = trajectory of Powell's algorithm—another inversion methodology; black outlined circles = iterations of the algorithm, green/red = first/last iteration. (d–f) Slices through Wasserstein-based objective function (see body text for details) for the three uplift parameters (red-white colouring = results from brute force analysis) and associated NA (white lines) and Powell's algorithm search histories. Note trade-offs in the objective function.

true uplift rates for all three parameters, irrespective of the arrangement of noise.

Figure 4.17 compares examples of typical best-fitting landscapes generated using the Euclidean and Wasserstein-based inverse approaches to the 'observed' landscape. The landscape generated using a Euclidean approach has similar drainage patterns to the 'observed' landscape, such as a roughly north-south ridge on the right hand side of the domain, but the topography tends to be lower. In contrast, the landscape generated using a Wasserstein-based approach has a different planform structure, but the topography characteristics (e.g., the distribution of elevations, marginals) are more similar to the 'observed' landscape.

Figure 4.17e shows the mean uplift rate history plus one standard deviation calculated using the 100

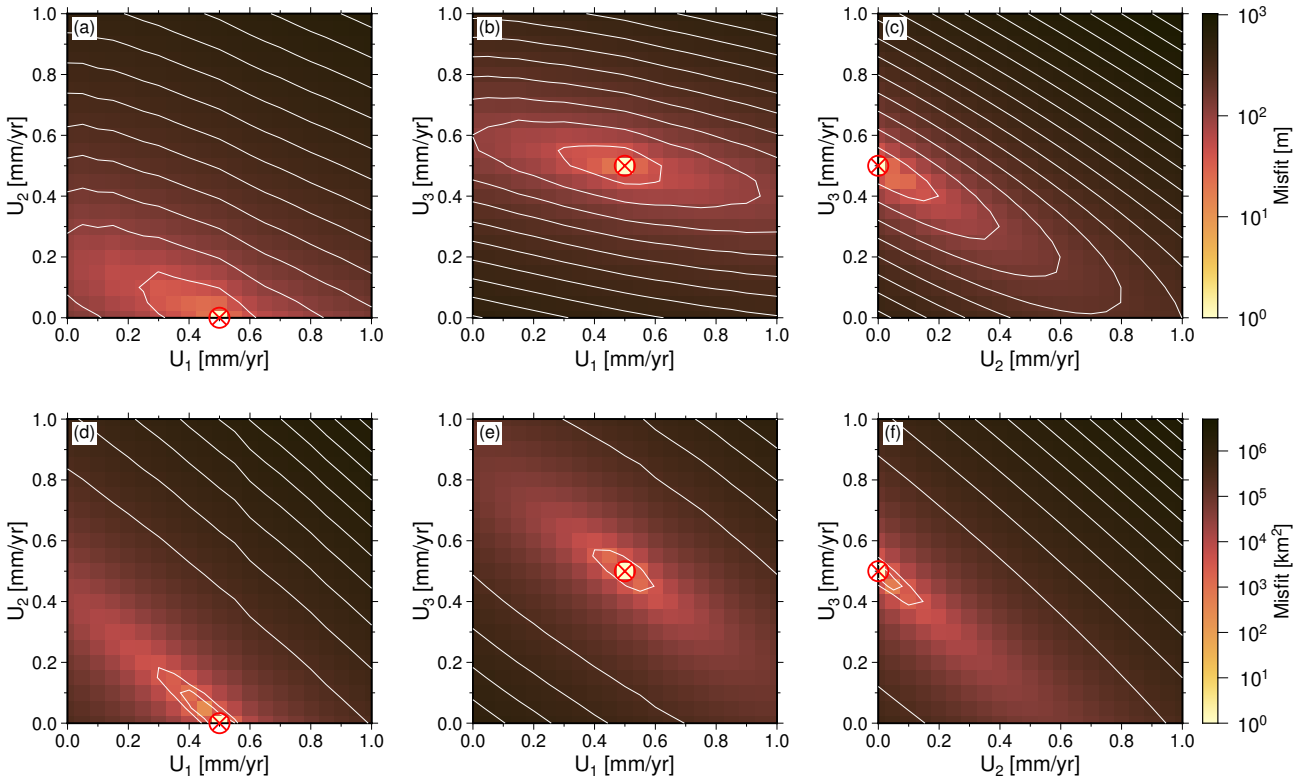


Figure 4.9: **Examples of multi-dimensional Euclidean and Wasserstein-based search spaces for models with same initial noise—objective functions when uplift rate is allowed to vary in time.** This figure reproduces Figure 4.8 with contours of the objective functions. (a-c) Slices through Euclidean misfit space for three parameters. Red cross shows location of true solution. Red circle shows location of global minimum. (d-f) As above, for Wasserstein-based misfit.

best-fitting results of the ensemble of models with noisy starting conditions that are different to the 'observed' landscape and to each other. These results confirm that uplift rate histories recovered using Euclidean statistics consistently underpredict the oldest phase of uplift and accurately recover the second and third parameter values. A consequence is that the cumulative uplift is 30 to 45% less than that of the true solution (e.g., Figure 4.17b). In contrast, the mean uplift history calculated using a Wasserstein-based objective function accurately recovers the true solution. There is a small overprediction in the uplift rate at 3 Myr that is attributed to the true solution of 0 mm/yr being at the boundary of the parameter space.

Posterior probability distributions and sample density plots of the ensemble of Euclidean results are shown in Figure 4.18. These are constructed by aggregating the posterior distributions from each of the 100 inversions within the ensemble. It is noted that the posterior distributions of individual inversions are broadly similar (see grey histograms in Figure 4.18). Convergence of individual posterior distributions is assessed by calculating a potential scale reduction factor, which is explained below.

The ensemble of models produced from the search phase of the Neighbourhood Algorithm can produce

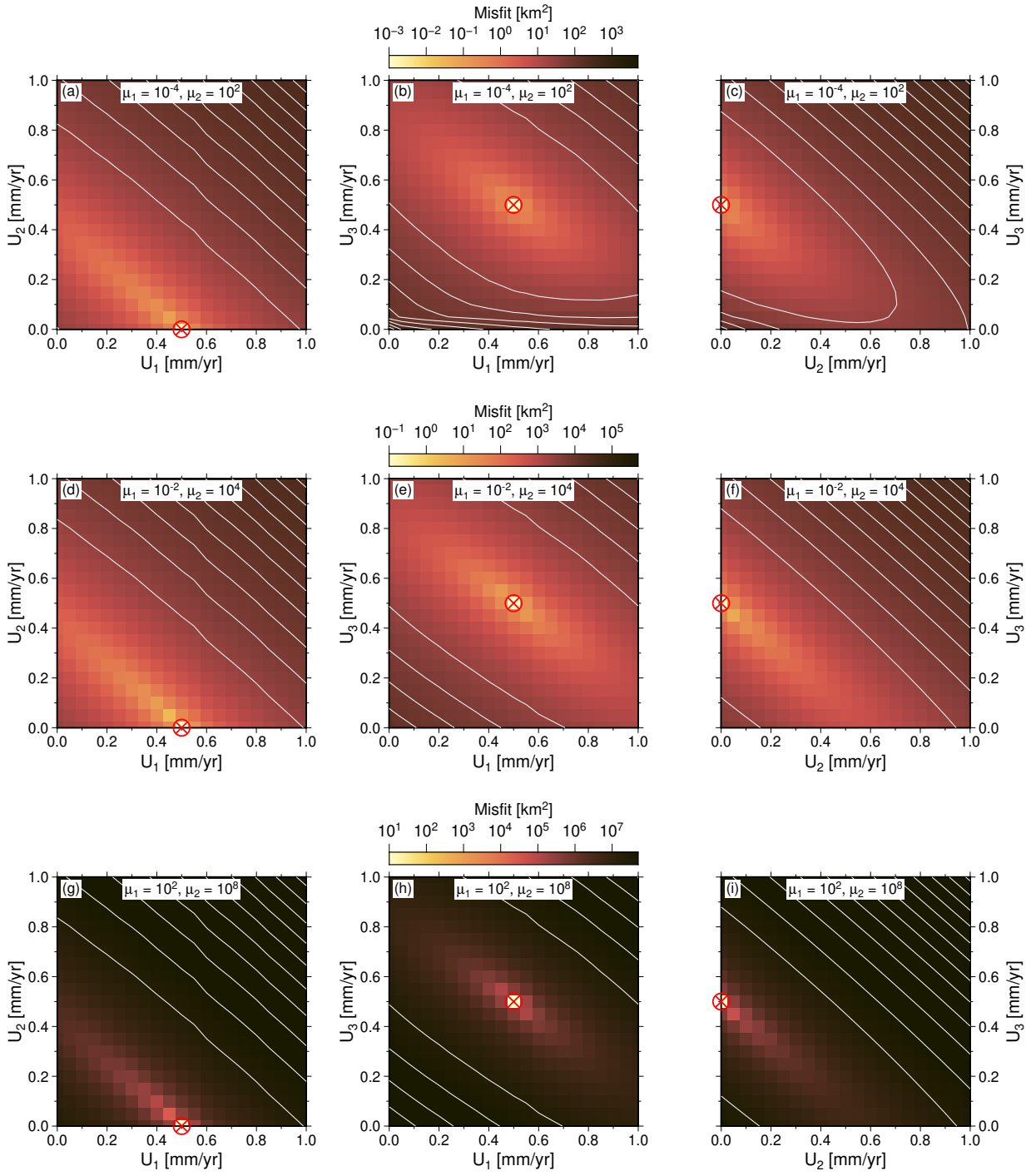


Figure 4.10: **Testing Wasserstein-based parameter spaces for models with same initial noise by varying values of weighting parameters μ_1 and μ_2.** This figure reproduces the experiments shown in Figure 4.8 in the main manuscript and Figure 4.9 (with $\mu_1 = 10^0$ and $\mu_2 = 10^6$) for different values μ_1 and μ_2. (a-c) Slices through Wasserstein-based misfit when $\mu_1 = 10^{-4}$ and $\mu_2 = 10^2$. (d-f) As above, for $\mu_1 = 10^{-2}$ and $\mu_2 = 10^4$. (g-i) As above, for $\mu_1 = 10^{-4}$ and $\mu_2 = 10^8$.

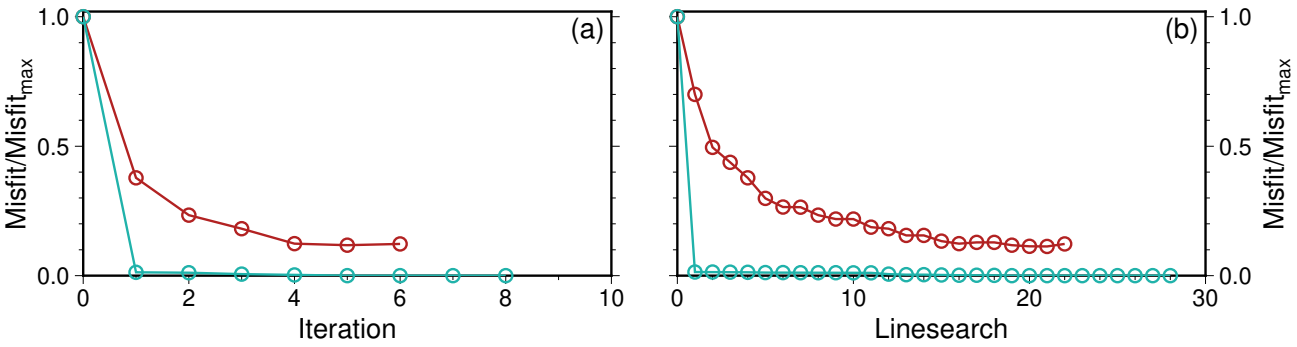


Figure 4.11: **Misfit convergence for Powell's Algorithm.** These results extend those shown in Figure 4.8 (Experiment 2). (a) normalised misfit as a function of iteration for RMS (red) and Wasserstein-based (blue) misfit. (b) As per (a), for linesearch.

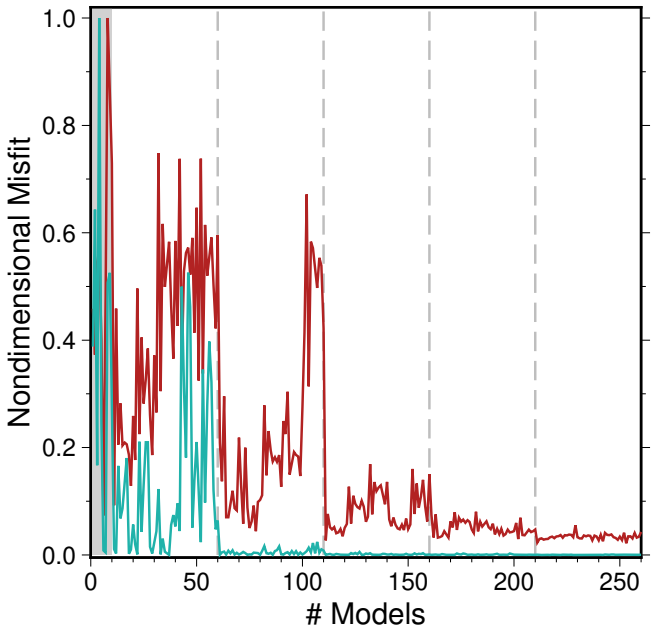


Figure 4.12: **Misfit convergence for Neighbourhood Algorithm.** Misfit as a function of forward model number within the Neighbourhood Algorithm search phase for RMS (red) and Wasserstein-based (blue) misfit extending the results shown in Figure 4.8 (Experiment 2). Misfit is normalised by respective maximum misfit values. grey shaded region shows duration of initial random sampling stage. grey dashed lines show positions at which new iterations begin (i.e., the best N_r subset of models are selected for resampling).

results with sparsely sampled distributions. Therefore, the appraisal phase of the Neighbourhood algorithm is often required in order to resample the search ensemble and produce posterior probability distributions that are statistically robust (Sambridge, 1999b). The resampling strategy of the appraisal phase makes use of Monte Carlo integration that involves a series of random walks through the sampled parameter space. It is possible to test whether the random walks converge using various statistical tests. A failure to converge may indicate that the information inferred from the posterior distributions is unreliable. I verify convergence by calculating a potential scale reduction factor (PSRF, also known as $\hat{R}$ or the Gelman-Rubin statistic; Gelman and Rubin, 1992). The PSRF is a diagnostic measure of

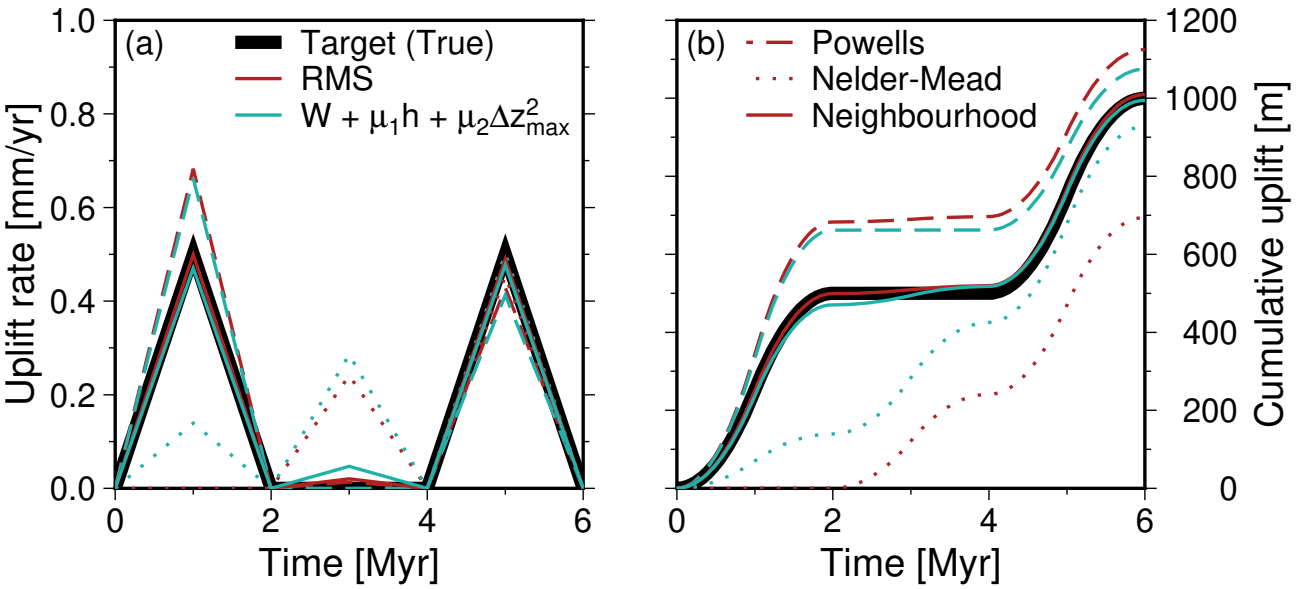


Figure 4.13: **Best-fitting uplift histories recovered from inverse modelling of landscapes with initial noise conditions identical to the 'observed' landscape, generated using different optimisation techniques.** (a) Black line = true uplift rate history used to generate the 'observed' landscape (i.e., what I aim to recover from inverse modelling; Figures 4.1d and 4.3a). Best-fitting calculated uplift rate histories: red = histories generated with Euclidean-based approaches; blue = solutions from Wasserstein-based approaches; solid lines = Neighbourhood Algorithm; dashed lines = Powell's algorithm; dotted lines = Nelder-Mead algorithm. Figure 4.8 shows the trajectories of the associated inverse models. (b) Associated cumulative uplift histories.

convergence and is calculated as a ratio of sample variance between-different and within-each random walk. For a formal definition, see Gelman and Rubin (1992) or Sambridge (1999b). A PSRF greater than 1.1 suggests further resampling is required to achieve convergence. As the number of samples tends to infinity, the PSRF tends to 1. PSRF values calculated for each parameter from a typical inversion chosen at random in Experiment 3 are all < 1.1, suggesting convergence.

The heat map and posterior distribution for U_1 demonstrates how low values of this parameter are preferentially sampled by the Neighbourhood Algorithm. The single best-fitting result, shown by the green arrowhead, is close to the mean value, shown in blue, but both are far from the true value of 0.5 mm/yr. The posterior distributions for parameters U_2 and U_3 are closer to the true solution. In contrast, posterior distributions and heat maps for the Wasserstein-based objective function, shown in Figure 4.19, are tightly arranged close to the true solution for all three parameters.

Comparisons with results from inverting longitudinal river profiles

Results from inverse modelling of river profiles extracted from a random selection of the best-fitting landscapes produced in this experiment are shown in Figure 4.20. The most youthful phase of uplift is

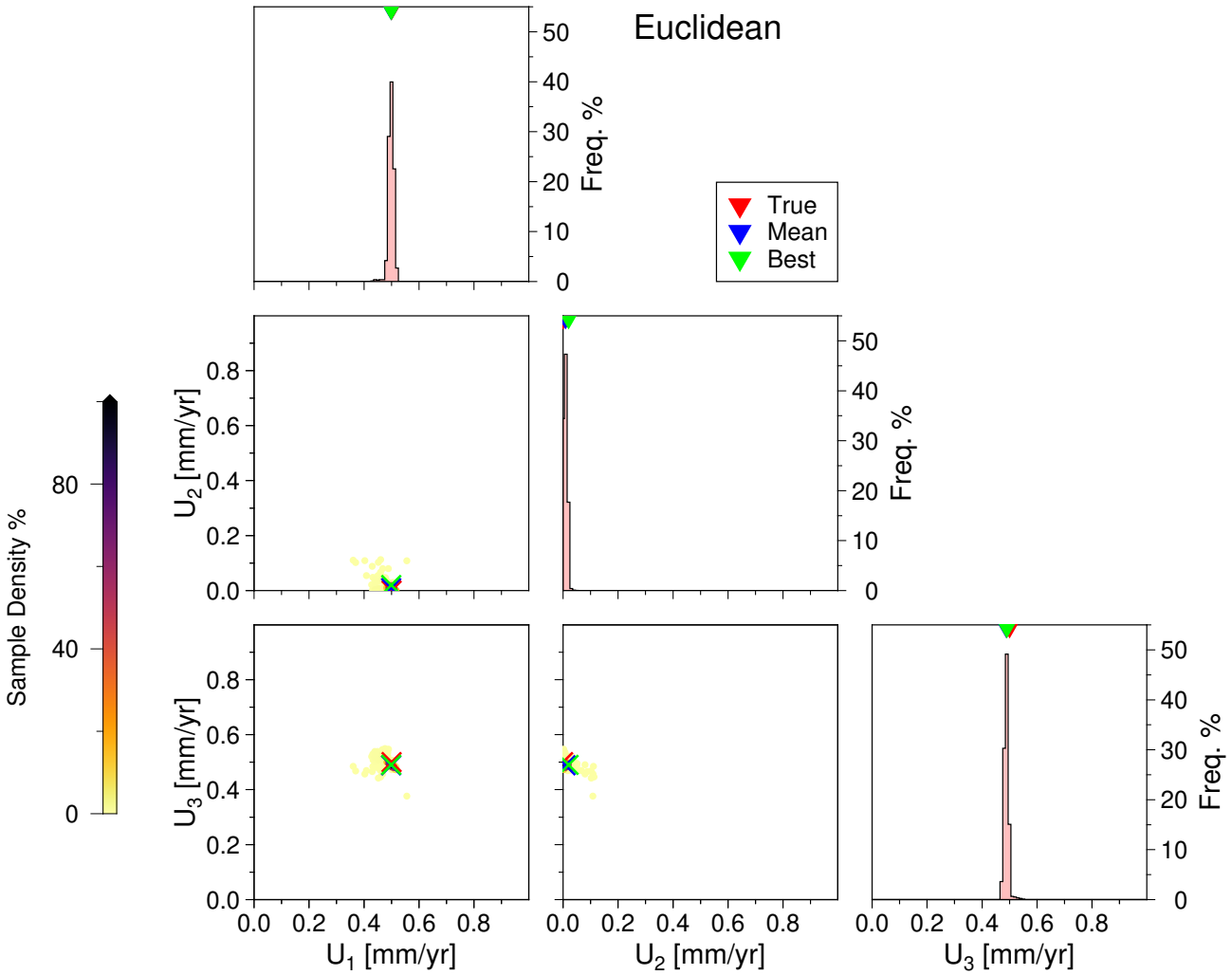


Figure 4.14: **Posterior distributions of RMS misfit for Experiment 2.** Posterior sampling density of each parameter combination, and respective marginal distributions extending the results shown in Figure 4.13. Red/blue/green crosses and arrows show true/mean/best recovered solutions.

accurately recovered by inverting each river individually or by joint-inversion of the five rivers. That the oldest (earliest) phase of uplift is not as accurately recovered is not surprising for two reasons. First, the way in which I have extracted the river profiles follows standard procedures, which assumes overland flow initiates at a defined upstream area (here 4 km^2), and hence the upper few tens of meters of cumulative uplift are 'missing' from the longitudinal profiles (see filled black circle and double-headed arrows). Secondly, the number of measurements that constrain uplift at times < 4 Myr is small (see e.g., response times and model coverage in Figures 4.3c and 4.20a). The inversion took < 1 minute to complete.

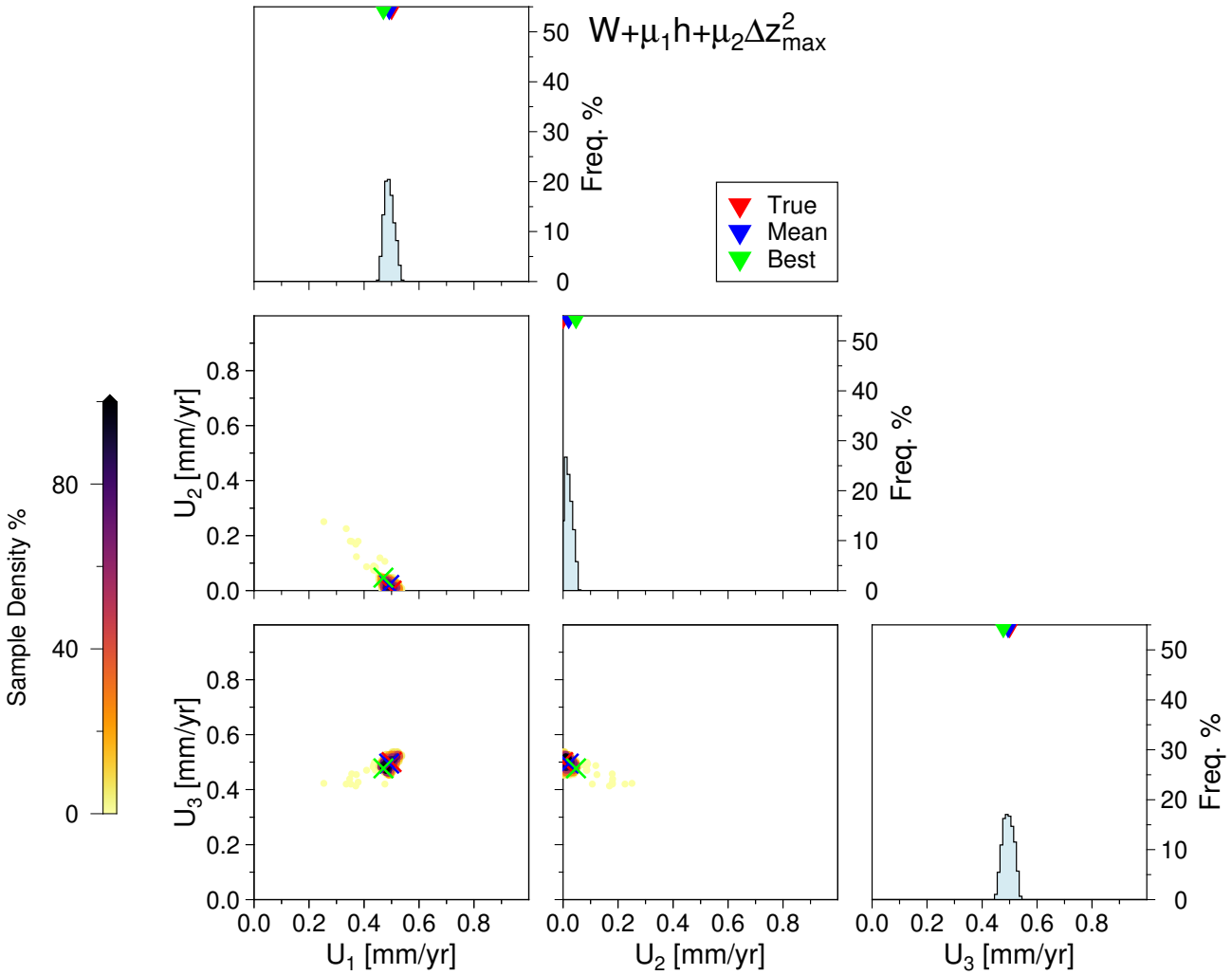


Figure 4.15: **Posterior distributions of Wasserstein-based misfit for Experiment 2.** The results extend those shown in Figure 4.13. Annotations as per Figure 4.14.

4.3.4 Experiment 4: Recovering a complex uplift history from a landscape with spatio-temporal changes in uplift

Posterior distributions and associated uplift histories calculated for a domal uplift style, shown in Figure 4.21, are similar to those calculated from landscapes evolving with a block uplift style. The calculated uplift rate for parameter U_1 using Euclidean statistics is less than the true uplift rate of 0.5 mm/yr, generating calculated topographies with maximum elevations less than that of the 'observed' landscape. In comparison, posterior distributions of uplift rates calculated using Wasserstein metrics are clustered close to the values of the true solution.

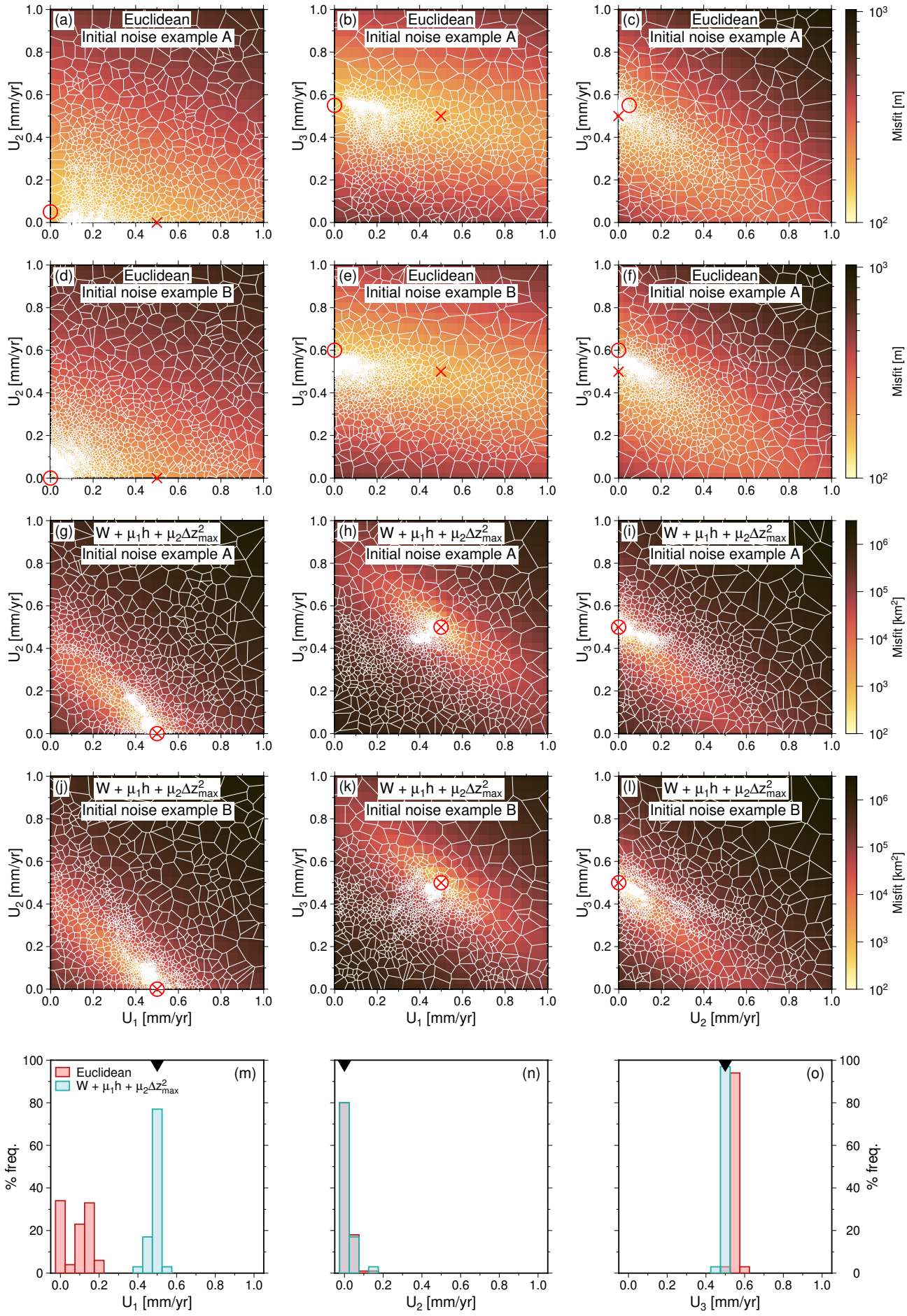

(a) Euclidean
Initial noise example A
(b) Euclidean
Initial noise example A
(c) Euclidean
Initial noise example A
(d) Euclidean
Initial noise example B
(e) Euclidean
Initial noise example B
(f) Euclidean
Initial noise example A
(g) W + μ1h + μ2Δz2max
Initial noise example A
(h) W + μ1h + μ2Δz2max
Initial noise example A
(i) W + μ1h + μ2Δz2max
Initial noise example A
(j) W + μ1h + μ2Δz2max
Initial noise example B
(k) W + μ1h + μ2Δz2max
Initial noise example B
(l) W + μ1h + μ2Δz2max
Initial noise example B
U1 [mm/yr]
U2 [mm/yr]
U3 [mm/yr]
Misfit [m]
Misfit [km2]
(m)
(n)
(o)
Euclidean
W + μ1h + μ2Δz2max
% freq.

Figure 4.16: **Examples of misfit spaces (objective functions) and Neighbourhood Algorithm search for uplift rate history for models with initial conditions different to the 'observed' landscape.** (a–c) Slices through a typical Euclidean misfit space for a landscape generated with an arrangement of initial (white) noise that is different to that used to generate the 'observed' landscape (see Figure 4.1d). Red crosses = values of true uplift rates (used to generate the 'observed' landscape). Red-white colour scale = misfit between 'observed' and theoretical landscapes generated by brute force, systematic, sweep of uplift rates: $\Delta U_n = 0.05$ mm/yr; red circle = global minimum misfit from brute-force parameter sweep. White lines = Voronoi cells of the Neighbourhood Algorithm (NA) search; note sampling density of NA in proximity to global minimum. (d–f) As above, for a different arrangement of white noise in the initial condition. (g–i) As (a–c), generated with Wasserstein-based metrics. (j–l) As (d–f), for Wasserstein-based metrics. (m–o) Histograms of uplift rates at global minima for 100 brute force searches of misfit space between landscapes initialised with different noisy starting conditions (see e.g., Figure 4.1a–b). Red = results from Euclidean-based approach; blue = Wasserstein-based approach. Black arrows = values of true solution, i.e., uplift rates used to generate 'observed' landscape.

Experiment	'True' uplift rate	Euclidean single-best	Wasserstein-based single-best	Euclidean mean + 1σ	Wasserstein-based mean + 1σ
1	8.00 Myr	8.18 Myr	8.00 Myr	$8.21^{+0.31}_{-0.3}$ Myr	$8.02^{+0.25}_{-0.2}$ Myr
2 (NM)	[0.5, 0, 0.5]	[0, 0.24, 0.45]	[0.14, 0.29, 0.50]	N/A	N/A
2 (P)	[0.5, 0, 0.5]	[0.68, 0.01, 0.43]	[0.66, 0, 0.41]	N/A	N/A
2 (NA)	[0.5, 0, 0.5]	[0.50, 0.02, 0.49]	[0.47, 0.05, 0.48]	[0.5±0.01, 0.±0.006, 0.49±0.008]	[0.49±0.02, 0.02±0.01, 0.49±0.02]
3	[0.5, 0, 0.5]	[0.24, 0, 0.53]	[0.47, 0.02, 0.49]	[0.09±0.05, 0.016±0.025, 0.55±0.012]	[0.47±0.015, 0.04±0.016, 0.49±0.003]
4	[0.5, 0, 0.5]	[0, 0.13, 0.52]	[0.45, 0.05, 0.49]	[0.12±0.07, 0.08±0.04, 0.53±0.02]	[0.45±0.045, 0.06±0.04, 0.48±0.01]

Table 4.2: **Summary of results for Experiments 1–4.** NM = Nelder-Mead, P = Powell's, NA = Neighbourhood Algorithm. $[\cdot, \cdot, \cdot] = [U_1, U_2, U_3]$ uplift rates (mm/yr) being searched for in experiments 2–4 (see Figure 4.1c.)

4.4 Discussion

4.4.1 Recovering tectonic information from noisy landscapes

The approach to inverting landscapes for their uplift rate histories developed this chapter was first demonstrated with simple models in which 'observed' and theoretical landscapes are parameterised to be as similar as possible (e.g., same noisy initial conditions, erosional model, boundary conditions). The results from Experiments 1 and 2 show that both Euclidean- and Wasserstein-based objective functions can be used with the Neighbourhood Algorithm to accurately locate true uplift rate histories in such scenarios (Figure 4.13). True uplift rate histories are more challenging to recover when using Powell's algorithm even under identical noise conditions due to the sensitivity of drainage planform

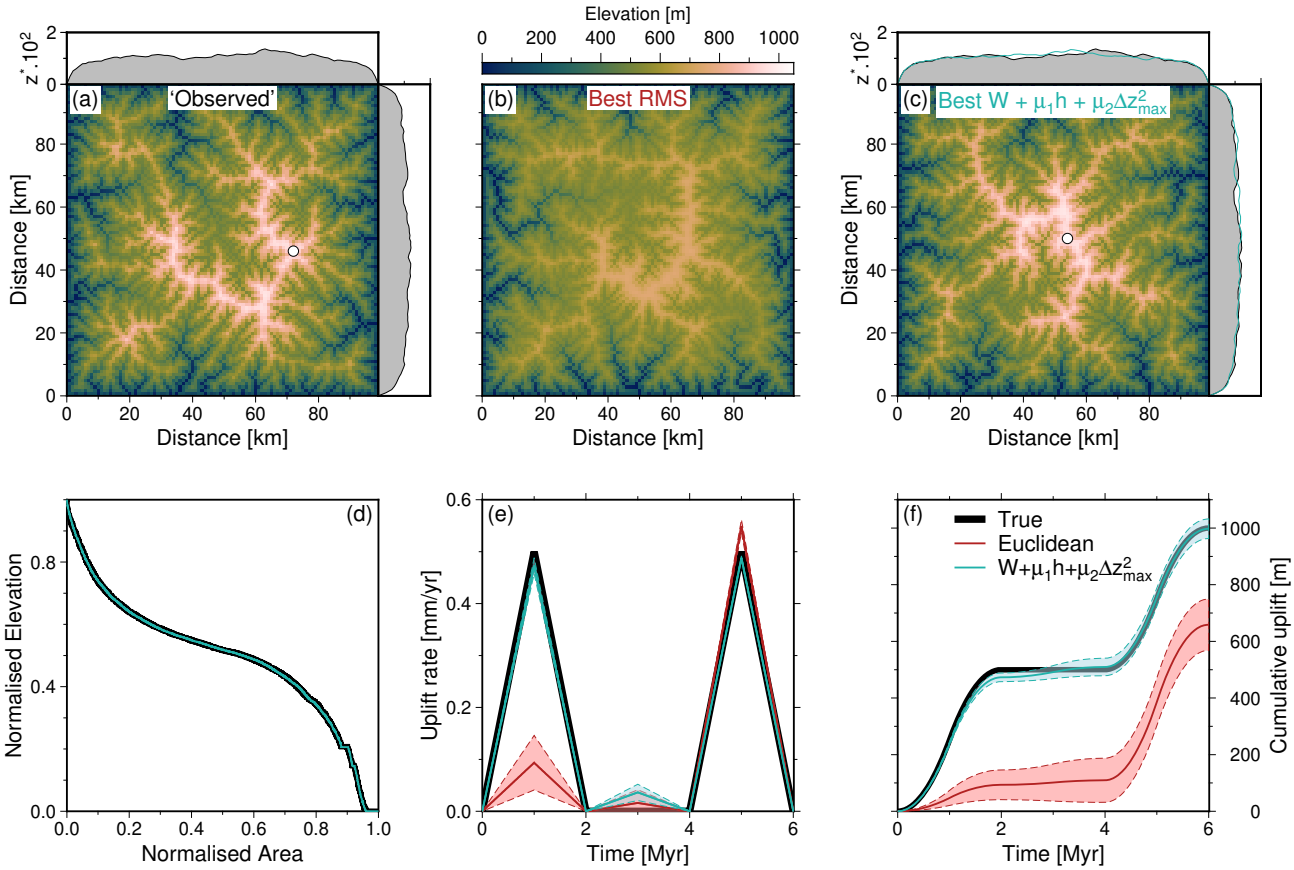


Figure 4.17: **Best-fitting landscapes extracted from ensemble of inverse models with initial conditions different to 'observed' landscape: Comparison of Euclidean and Wasserstein-based approaches.** (a) 'Observed' landscape and its marginals (see Figure 4.1d). (b) The best-fitting landscape from an ensemble of 100 inverse models with uplift rate histories determined by the Neighbourhood Algorithm and Euclidean-based (RMS) statistics (see e.g., Figure 4.16a–f). (c) As per (b), generated with Wasserstein-based metrics (see e.g., Figure 4.16g–l); blue = marginals of best-fitting landscape; grey = marginals corresponding to 'observed' landscape in panel (a). (d) Black = hypsometry of 'observed' 'observed' landscape (panel a). Green = hypsometry of best-fitting landscape shown in panel (c). (e) Black = true uplift history used to generate 'observed' landscape in panel (a); solid red line = mean of calculated uplift rate histories from the best-fitting (maximum likelihood) models generated from 100 inversions with the Neighbourhood Algorithm and Euclidean (RMS) based statistics; shaded region = one standard deviation. Blue = results for Wasserstein-based approach. (f) As per (e), for cumulative uplift.

geometries to even minor variations in the uplift rate history. However, the scenario of identical noise used in the initial conditions is unlikely to be appropriate for understanding origins of topography in the real world where the specific arrangements of noise, and certainly their histories, are usually unknown.

When the noisy starting conditions of 'observed' and theoretical landscapes are different (e.g., because one or both are unknown), the results from this chapter show that Euclidean-based objective functions are likely to be extremely complicated with many local minima. Consequently, they are not likely to be well suited for use in automated optimisation, with searches for uplift rate histories likely to end far

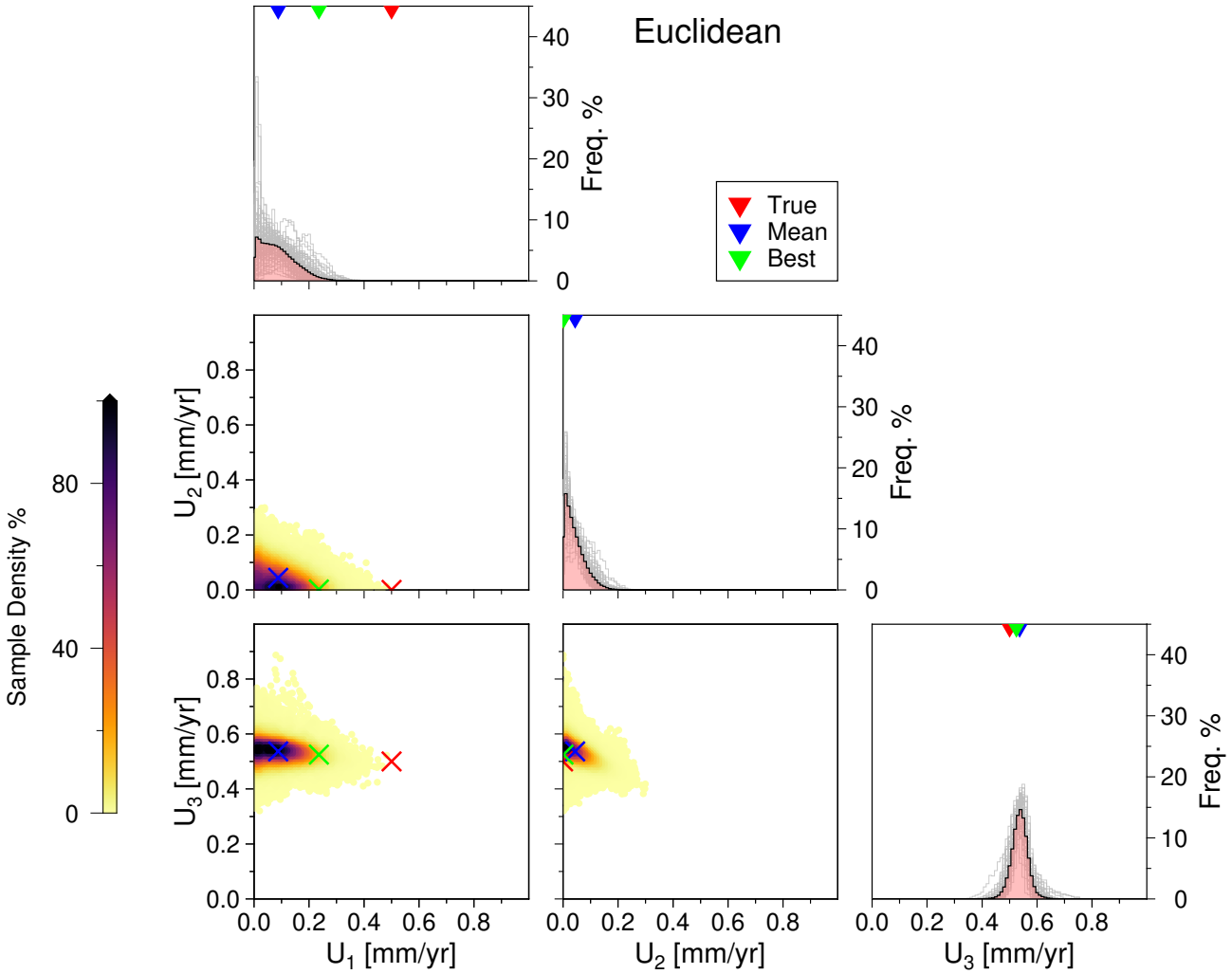


Figure 4.18: **Distribution of calculated uplift rates from ensemble of inverse models generated with Euclidean statistics and different initial noise conditions compared to true uplift rates.** Heat maps = posterior sampling density for each combination of uplift rate parameter values from the *appraisal* phase of 100 inverse models (see body text for details; Figure 4.1c for timings of U_n); note parameter trade-offs. Histograms = Marginal posterior probability distribution for each uplift rate parameter labelled along abscissa. Red arrows/crosses = true uplift rates used to generate the 'observed' landscape shown in Figure 4.1d. Green = best-fitting solutions obtained from *search phase* of the Neighbourhood Algorithm, i.e., the uplift rate values that produce the theoretical landscape with the lowest residual misfit to the 'observed' landscape. Blue = mean of the posterior distributions.

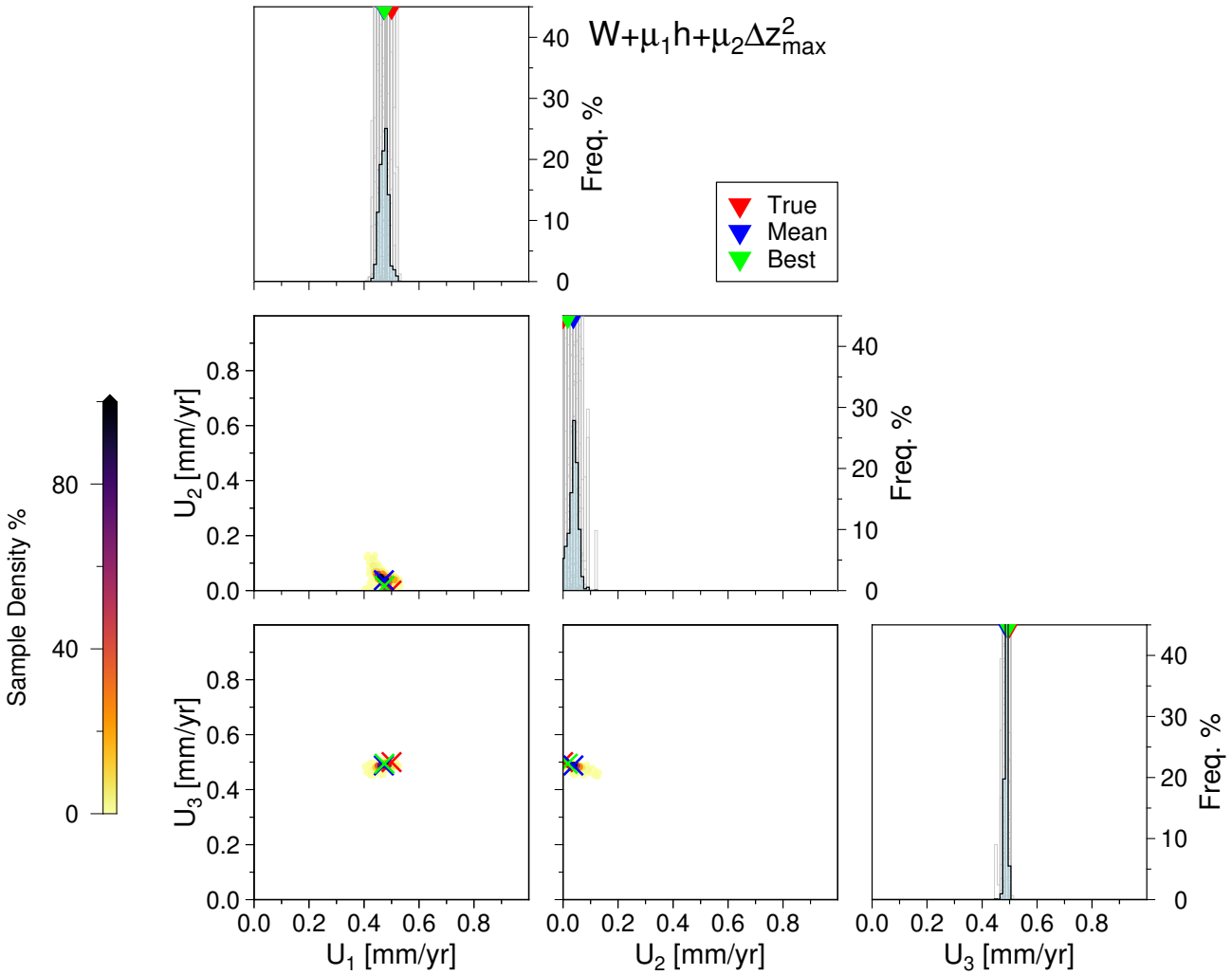


Figure 4.19: **Distribution of calculated uplift rates from ensemble of inverse models generated with different initial conditions and Wasserstein-based objective functions compared to true values.** See Figure 4.18 for extended description.

from the truth. Fortunately, Wasserstein-based approaches outperform Euclidean-based ones and can recover uplift rate histories with accuracy (Figure 4.16). The success of the Wasserstein-based approach stems largely from the relative insensitivity of topographic marginals and landscape hypsometries to local complexity.

The results indicate that inverse modelling of landscapes with Euclidean objective functions may typically underestimate amplitudes of old events (Figures 4.13, 4.17c–e, 4.18, 4.21, 4.20a). Two reasons are suggested for the under-prediction. The first is associated with the removal of tectonic information from topography by erosion. A guide to the length of the record of tectonic events in the landscapes examined is the erosional response time given by Equation 4.3 (see also Figure 4.3). Figure 4.3d demonstrates that the fluvial response time of the longest river of the 'observed' landscape is $\sim$ 6 Myr, it is only $\sim$ 4 Myr for the second, third, and fourth longest rivers. This result is emphasised

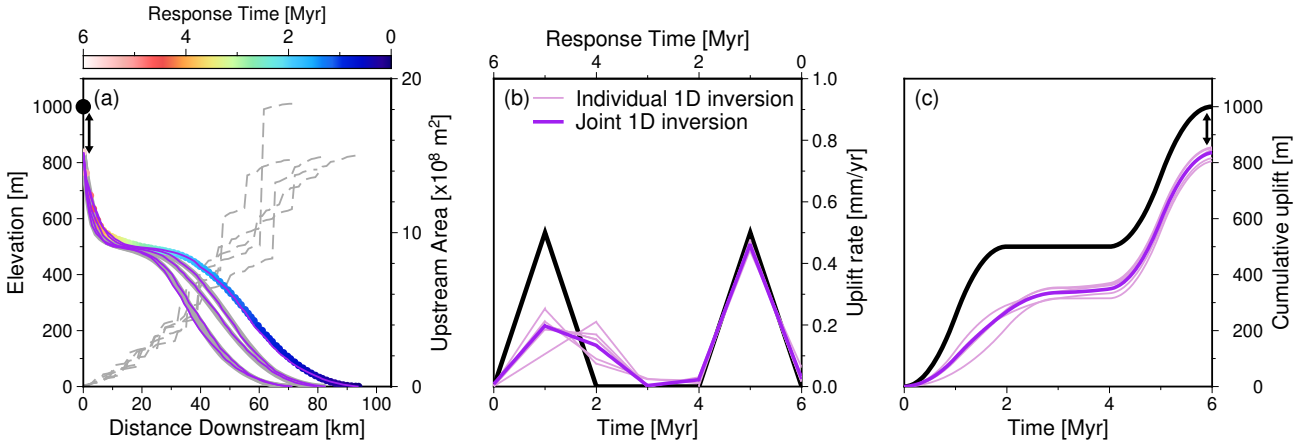


Figure 4.20: **Recovered uplift histories from inverse modelling of river profiles.** (a) Solid grey lines = longitudinal profiles of the longest rivers extracted from five of the 100 best-fitting topographies generated by inverting the 'observed' landscape; longest is overlain with circles coloured by landscape response time (Equation 4.3). Dashed grey lines = upstream drainage area as a function of downstream distance for these rivers. Purple lines show best-fitting profiles from joint-inversion of the observations (grey lines); see Section 4.2.4 for details. Black circle and double-headed arrow indicate difference between river heads and cumulative uplift. (b) Black solid line = true uplift rate. Thin purple lines = calculated uplift rate histories from inverting each river (grey lines) in panel (a) individually. Thick purple line = uplift rate and cumulative uplift history from joint inversion of the river profiles shown in panel (a). Double-headed arrow = difference between cumulation uplift at 0 Myr. (c) As per (b), for cumulative uplift history.

by the histogram of model coverage atop Figure 4.3b, which demonstrates that at least 80% of grid cells within the domain have a response time of less than 5 Myr. In other words, calculated Euclidean misfit is insensitive to changes in uplift rate at times > 5 Myr. The insensitivity can be seen in Figure 4.22a–c, which shows transects through Euclidean misfit functions (see Figures 4.16a–c and g–i). Each figure shows misfit when only one of the uplift rate parameters is varied. This figure emphasises the insensitivity of Euclidean misfit to changing the amplitude of the oldest phase of uplift (U_1). It is unsurprising that inverse modelling of longitudinal river profiles extracted from these landscapes, which have very low model coverage at times > 5 Myr, also fails to accurately recover the earliest uplift phase (Figure 4.20).

Second, Euclidean-based approaches may be unsuited to inverse modelling of noisy landscapes because topography (e.g., valleys and ridges) is unlikely to be located in the same positions in 'observed' and theoretical landscapes. It can then be beneficial, in terms of minimising misfit, for a theoretical landscape to have lower and more consistent elevations than the 'observed' one. Doing so can reduce the differences in elevation between co-located (in the 'observed' and theoretical landscapes) ridges and valleys, for instance (e.g., Figure 4.17b). Consequently, the uplift history used to generate the best-fitting theoretical landscape with a Euclidean scheme will contain less uplift. Given the insensitivity to

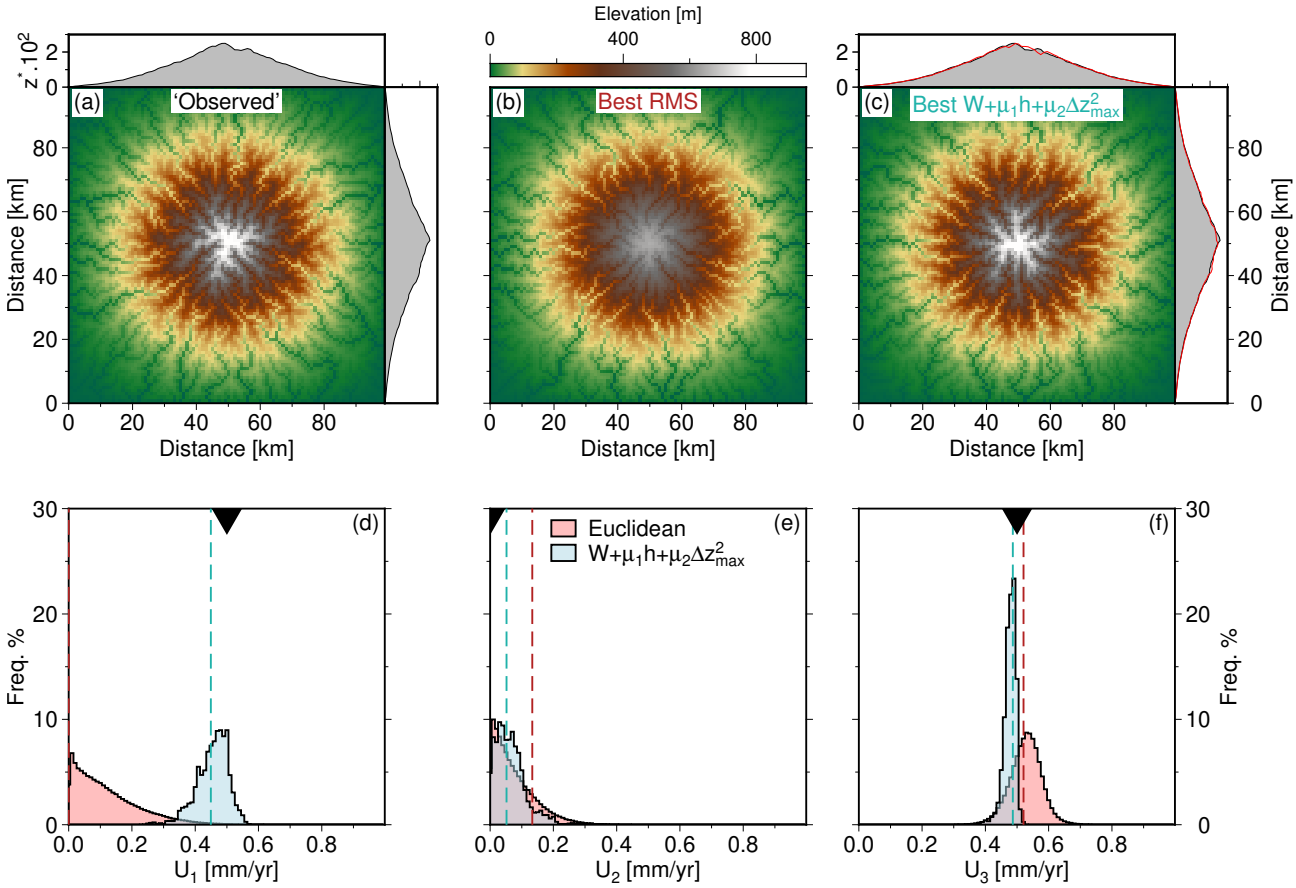


Figure 4.21: **Inverse modelling of domal topography to recover uplift rate histories.** Calculated best-fitting domal topographies and posterior distributions for models with different initial (white noise) conditions identified using the Neighbourhood Algorithm (NA). (a) 'Observed' domal landscape and its topographic marginals, generated with the uplift history shown in Figure 4.1c scaled by Equation 4.2. (b) Best-fitting landscape from NA-based inverse model that uses Euclidean (RMS) statistics. (c) As per (b), using Wasserstein metrics; red = associated marginals; grey = marginals for the 'observed' landscape in panel (a). (d–f) Aggregated posterior probability distributions generated from ensemble of 100 inverse models generated with different noisy starting conditions; red = Euclidean, blue = Wasserstein; coloured dashed lines = calculated uplift rates of single best-fitting model corresponding to the landscapes shown in panels (b–c). Black arrows = parameter values of true solution, i.e., uplift rates used to generate the 'observed' landscape.

old uplift, it is probably generally beneficial for Euclidean-based inverse models to reduce uplift rates at older times, as observed in the experiments in this chapter (e.g., Figure 4.17e–f).

In contrast, the Wasserstein-based methodology can accurately recover rates of uplift when tectonic signals have been eroded from large parts of the landscape (Figures 4.17 & 4.21). Figure 4.22 shows how Wasserstein-based misfit is relatively equally sensitive to changes in each uplift parameter. This efficacy is attributed to the use of marginals, hypsometry and maximum elevations, which combine to provide sufficient information to accurately recover the rate of the oldest uplift events recorded in a landscape.

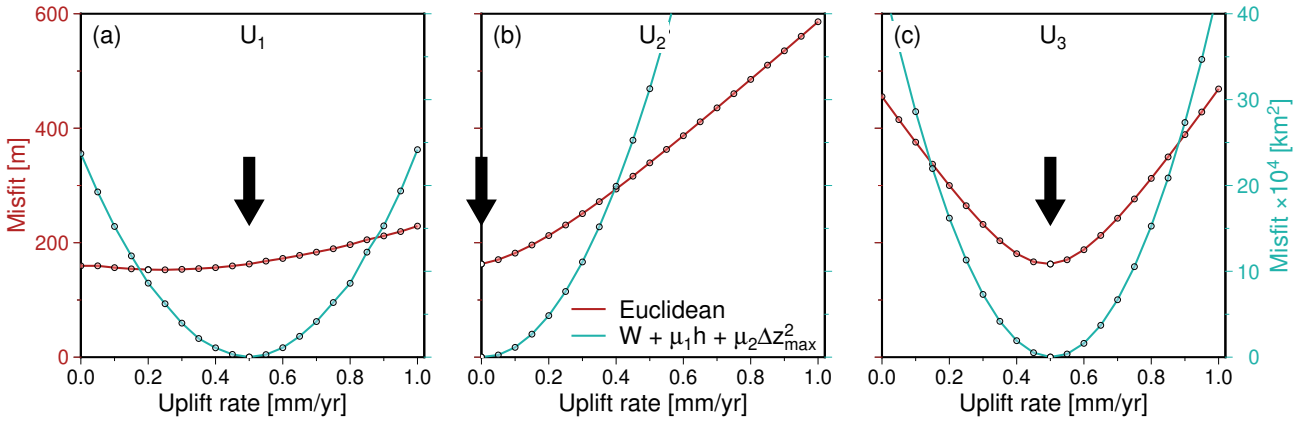


Figure 4.22: **Assessing sensitivity of calculated uplift rates recovered from noisy landscapes.** Euclidean and Wasserstein-based misfit between 'observed' landscape generated with $U_1 = U_3 = 0.5$ mm/yr and $U_2 = 0$, and a theoretical landscape generated with different noise and systematic adjustment of uplift rates. (a) Transects of Euclidean (red) and Wasserstein-based (blue) misfit generated from the misfit maps shown in Figure 4.16a–c and g–i respectively. Here, $0 \leq U_1 \leq 1$ mm/yr every 0.05 mm/yr; U_2 and U_3 are fixed at the values used to generate the 'observed' landscape. White filled circle = minimum misfit. Black arrow = true uplift rate of U_1 used to generate 'observed' landscape. (b) As per (a), varying U_2 and fixing $U_1 = U_3 = 0.5$ mm/yr. (c) As per (a), varying U_3 and fixing $U_1 = 0.5$ and $U_2 = 0$ mm/yr.

4.4.2 Recommendations, implications and future work

The Neighbourhood Algorithm is well suited to searching for true uplift rate histories and performs well even when direction- or simplex-based methods do not (Figures 4.8, 4.13 & 4.16). In contrast, it is found that the Nelder-Mead algorithm is unable to recover the true uplift history with sufficient accuracy to be generally useful, even when starting conditions are identical between the 'observed' and calculated landscapes. This is also true for Powell's algorithm when Euclidean statistics are used to generate the objective function being searched.

An advantage of the Neighbourhood Algorithm is that uncertainties can be straightforwardly quantified from the model ensemble. The calculated uplift rates in Figure 4.17 and the posterior distributions shown in Figures 4.18–4.19 demonstrate that whilst uncertainties can be considerable when Euclidean statistics are used in the inverse model, they may still not overlap with true rates of early uplift (i.e., U_1 in these experiments). In contrast, uncertainties are considerably smaller when Wasserstein-based metrics are used. Moreover, the best-fitting and mean solutions are similar to each other and the true uplift history when Wasserstein-based metrics are used in the inverse model.

It is noted that even in scenarios when noise in the starting conditions of the 'observed' and best-fitting theoretical landscapes are the same, very small amounts of residual misfit remain ($H_w = 0.89$ km^2). These residuals are attributed to the precision with which the optimisation algorithms sample and

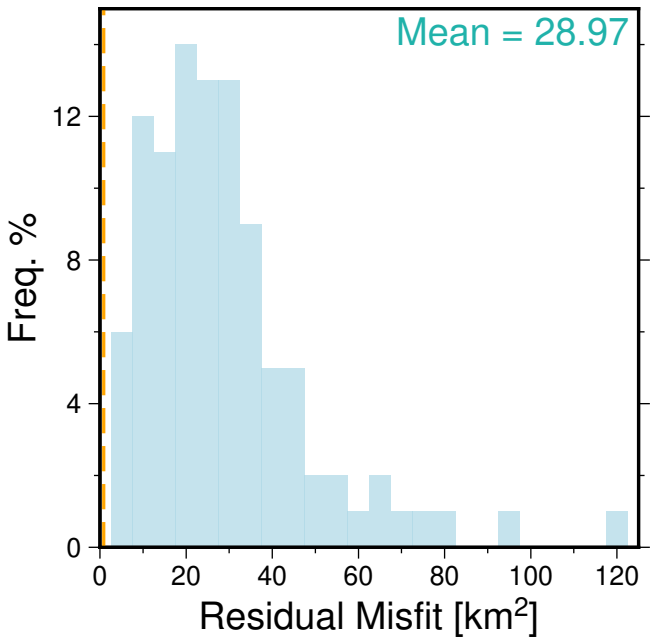


Figure 4.23: **Residual misfit of best-fitting models initialised under different noisy starting conditions.** Histogram shows residual misfit of 100 best-fitting models from Experiment 3 of this chapter, extending the results shown in Figures 4.16–4.17. Mean residual misfit = 28.97 km^2. Orange dashed line shows residual misfit of best-fitting model from Experiment 2: 0.89 km^2.

update parameter values. In contrast, inverting with different initial noisy conditions (i.e., Experiment 3), results in considerably larger residual misfit (mean $H_w = 28.97$ km^2). A histogram showing residual misfits is shown in Figure 4.23.

The results in this chapter have two obvious implications for understanding landscape evolution in general. First, many landscape geometries are plausible for a given history of uplift and erosional model because of the sensitivity of landscape geometries (e.g., positions of drainage networks) to geomorphic noise. This finding is straightforward to demonstrate with simulated landscapes in which different arrangements of computational noise are incorporated as starting conditions. It is suggested that it should also be expected for real landscapes where drainage geometries depend on geomorphic noise and also on lithospheric and sublithospheric tectonic processes operating at larger scales (Castelltort et al., 2012; Willett et al., 2014; Lipp et al., 2020; Kuhasubpasin et al., 2025). This result indicates that attempting to understand the origins of the specific arrangements of valleys, interfluves, hillslopes and rivers, likely requires detailed information about the arrangement of noise, which is unlikely to be available for the majority of the lifetime of a landscape. A corollary is that probabilistic approaches are likely to be necessary for understanding landscape evolution and the origins of topography at a variety of scales.

Secondly, the use of inversion techniques that make use of Euclidean statistics to compare observed

and theoretical landscapes can be unstable and are very sensitive to noise. In contrast, Wasserstein distances, which come from the field of optimal transport, can 'see through' local complexities to more accurately recover histories of uplift. The success of the approach largely stems from the fact that even though landscapes generated with different noisy conditions can be dramatically different at the scales of drainage basins, they contain similar large scale topographic characteristics (e.g., marginals and hypsometries). It is that information that makes it possible to recover tectonics from topography despite the important role that geomorphic noise arising from, for instance, the condition of substrate or the climate can play in determining the precise details of a landscape's evolution. The use of optimisation algorithms within the inversion framework reduces computational burden, however given that evolving entire landscapes is more expensive than inverting river profiles, both approaches remain feasible options when seeking to recover tectonic information from topography.

The modelling in Experiments 3 and 4 used different arrangements of white noise added to theoretical landscapes as initial conditions. In the real world 'noise' might arise as a consequence of, say, climatic, lithologic, or biotic contributions, with different spectral characteristics that change and impact topography as it is being shaped. Figures 4.24–4.26 show that Wasserstein-based inversion can recover uplift rate histories in the presence of red (topography amplitudes increase with scale), pink (amplitudes increase more slowly with scale), white or blue (amplitudes decrease with scale) noise inserted into initial conditions, which perhaps brackets the range of spectral characteristics that landscapes contain (e.g., Pelletier, 1998; Perron et al., 2008; Wapenhans et al., 2021). Birnir et al. (2001) and Wapenhans et al. (2021) showed that addition of quenched (frozen) noise to landscape evolution models can improve their similarities to real landscapes. In future work it would be possible to explore the recoverability of uplift rate histories in the presence of quenched noise by inserting identical arrangements of roughness at every time step, for instance. Alternatively, spatio-temporal noise could be included by inserting different arrangements of roughness, perhaps from different or the same distribution(s) of noise, at every time step by altering the random seed (for instance, how noise is inserted into models produced in Chapter 2).

An obvious direction of future work would be to apply this inverse method to natural topography. Inverting real topography for its uplift rate history will likely require inversion for a substantially increased number of parameters (i.e., U_n). This highlights the need for experiments that explore the efficacy of Wasserstein-based objective functions and optimisation algorithms where solutions are known, such as those in this chapter. The approach could also be adapted to incorporate more complex

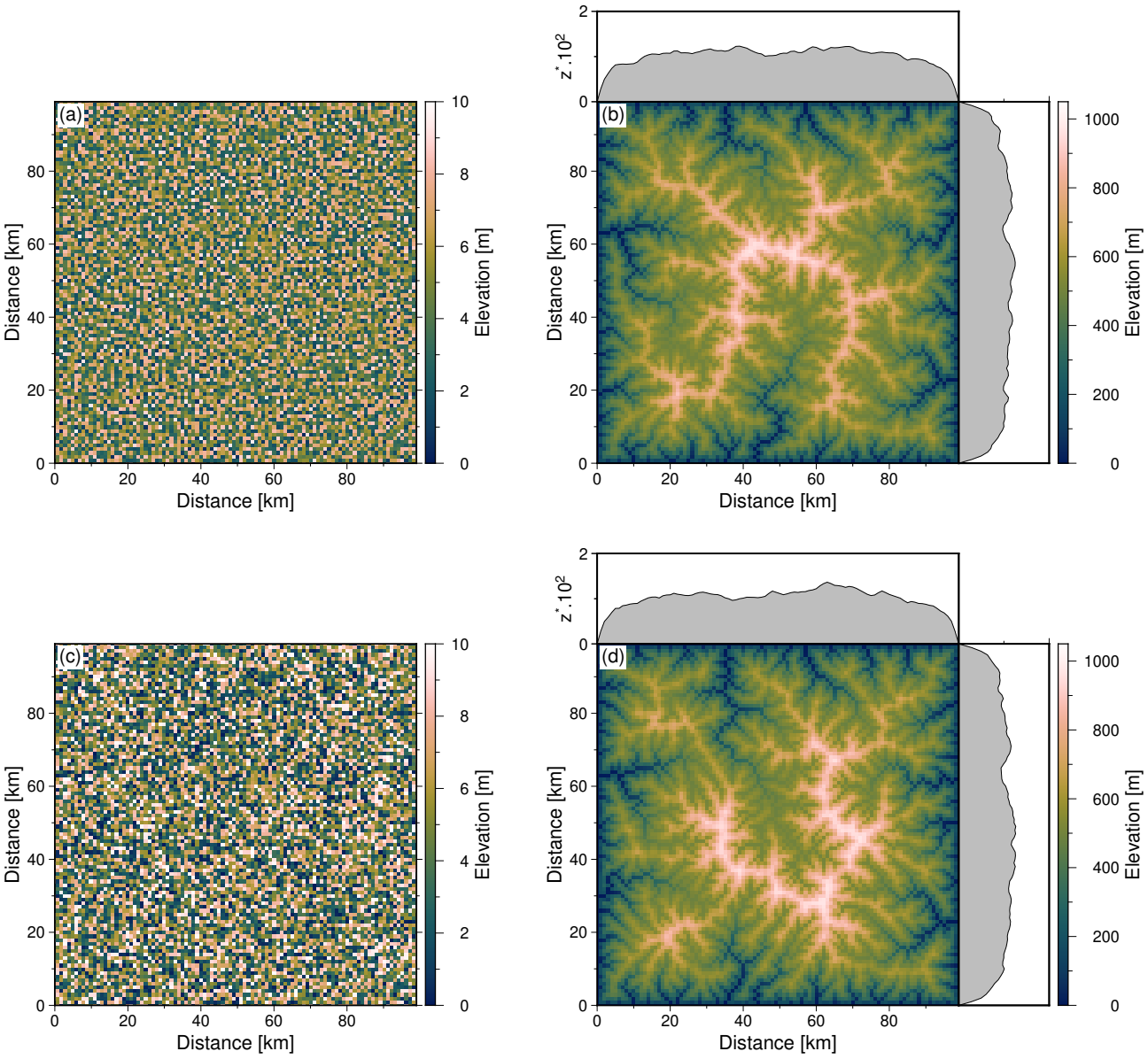


Figure 4.24: **Theoretical landscapes generated with blue and white noise initial conditions.** (a) An example of blue noise with elevations 0–10 m used as an initial condition within a landscape model. (b) Resultant landscape and topographic marginals that evolve from the starting condition in (a) with the model set up as described and the uplift history shown in Figure 2.1c of the main manuscript. (c-d) As above, for white noise initial condition.

erosional models, for instance, transport-limited, glacial and other non-fluvial erosion.

4.5 Conclusions

The form and evolution of landscapes result from a complex interplay of tectonic and geomorphic processes. Establishing contributions of tectonic processes to topography is complicated by the presence of geomorphic noise playing a significant role in determining landscape form. I demonstrate how a probabilistic inverse modelling framework can be used to recover uplift rate histories from landscapes

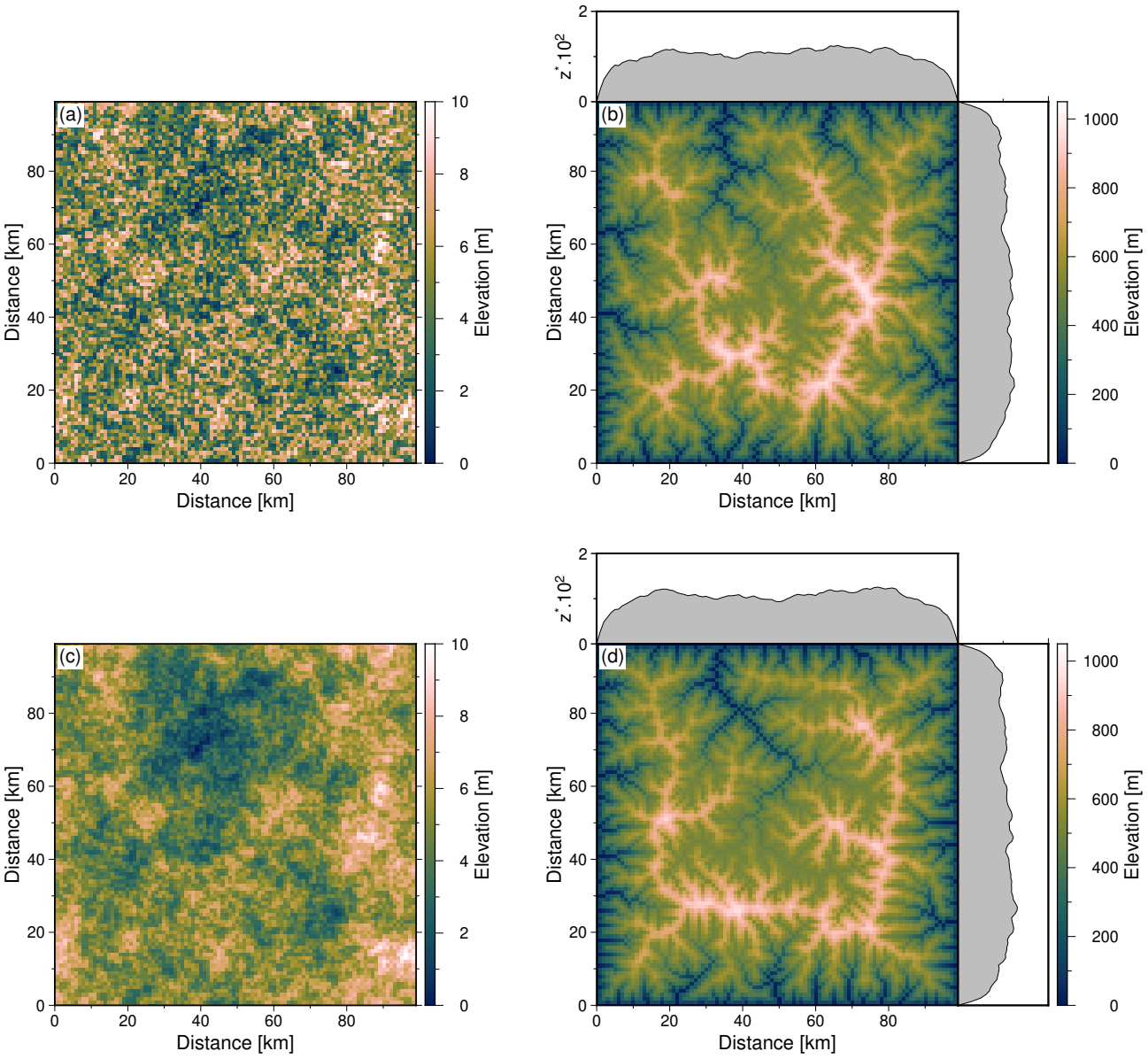


Figure 4.25: **Theoretical landscapes generated with pink and red noise initial conditions.** (a-b) As above in Figure 4.24, for pink noise initial condition. (c-d) As above, for red noise initial condition.

even when the specific arrangement of geomorphic noise is poorly understood. This approach could be useful for recovering tectonics from real landscapes for which one typically has no information about the history of processes contributing to geomorphic noise, such as discharge, changes in substrate, biota, or climate. In this chapter, following procedures widely used in simulations of fluvial landscapes, randomness is applied to models in the form of different noisy initial conditions. The local complexity introduced by noise makes 'standard' Euclidean-based approaches to assess goodness of fit unsuitable for comparing observed and theoretical topography. Instead, it is shown that Wasserstein distances generated using topographic marginals, and the hypsometries and maximum elevation of

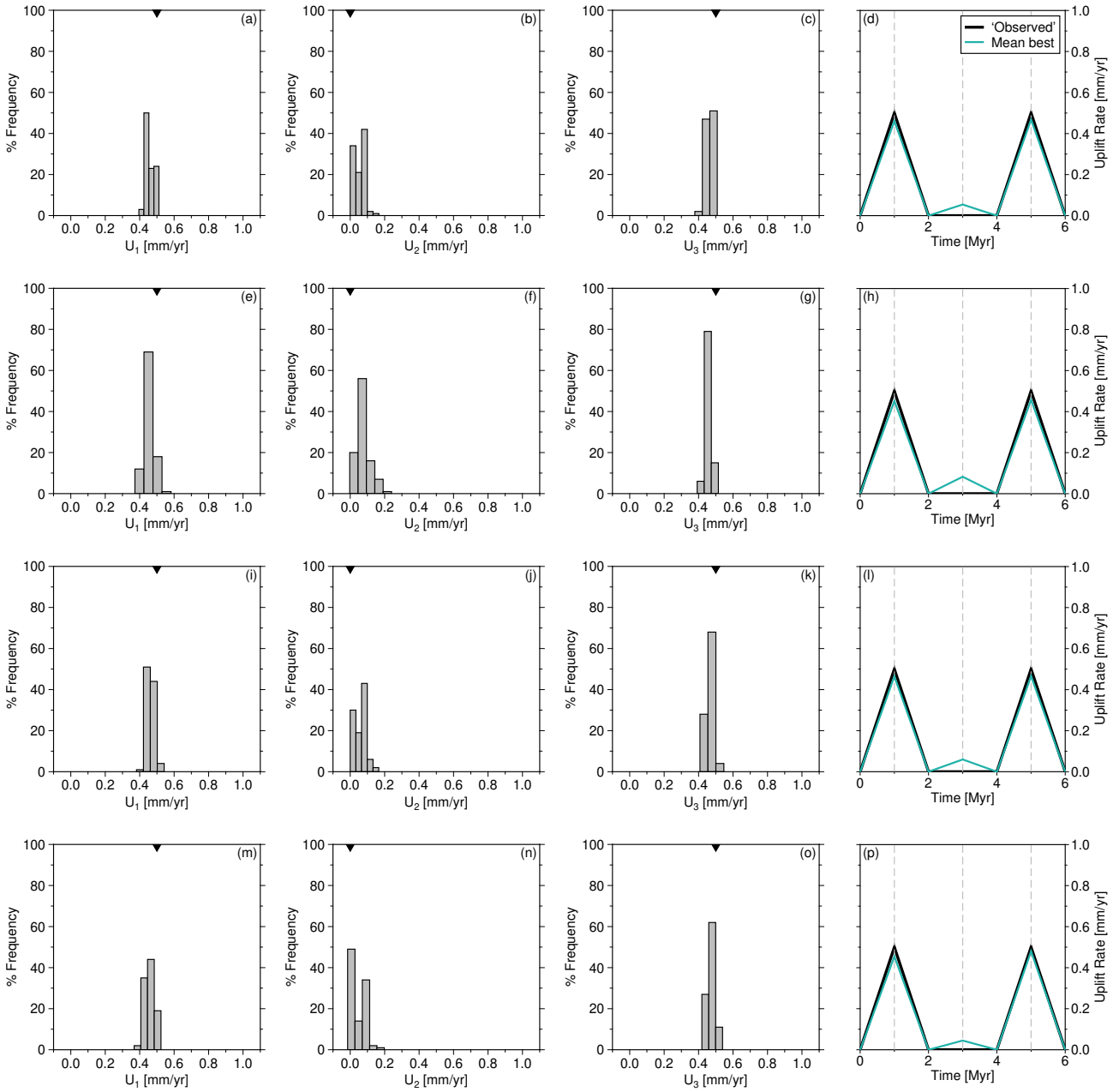


Figure 4.26: **Uplift histories recovered from landscapes with different colours (distributions) of initial noise.** (a-c) Distributions of best-fitting uplift rates calculated using a Wasserstein-based objective function from 100 inversions using the Neighbourhood Algorithm when the 'observed' and theoretical landscapes are generated with different arrangements of blue noise initial conditions. Note that Neighbourhood Algorithm is parameterised with $N_i = 10$, $N_s = 50$, $N_r = 5$, $N = 5$ — i.e., a coarser search than that used for Experiment 3. Black triangle points to value of 'true' solution used to generate 'observed' landscape. (d) Black line shows uplift rate history used to generate 'observed' landscape. Blue line shows the mean of the 100 best-fitting uplift rate histories (mean maximum likelihood) recovered using a Wasserstein-based objective function and the Neighbourhood Algorithm. Dashed grey lines = times at which uplift rates can vary in the inverse models. (e-h) As above, for 'observed' and theoretical landscapes initialised with white noise. (i-l) As above, for pink noise. (m-p) As above, for red noise.

landscapes provides the information needed to recover true histories of uplift. Wasserstein distances are sensitive to the timing of tectonic signals inserted into a landscape. The approach makes it possible

to invert the topography of landscapes generated by block- and domal uplift to recover their true uplift rate histories. The probabilistic nature of the framework enables quantification of uncertainties in recovered uplift rates using posterior probability distributions. I anticipate the approach being useful where knowledge of uplift histories can provide constraints on the geosphere (e.g., natural resource distributions), biosphere (e.g., species evolution), and atmosphere (e.g., palaeoclimate) through time but information available to understand the details of landscape evolution is scant.

Chapter 5

Discussion

5.1 Summary of key findings

The work presented in this dissertation demonstrates how, in spite of geomorphic variability and noise, tectonic information can be recovered from topography using a probabilistic inverse modelling framework. It is demonstrated how landscape evolution models can be used to characterise and quantify variability in geomorphic properties that occurs during the lifetime of a landscape. The importance of such quantification lies not only in its scientific rigour, but crucially in how it permits the respective contributions to topography from tectonic signals and other processes (noise) to be split. Disentangling the roles of climatic and tectonic processes to the shaping of landscapes has been a goal within the geosciences for several decades. Recovering uplift rate histories from topography, as the inverse method developed in this dissertation does, is an important development that enhances the ability to make such distinctions.

In Chapter 2, I set out to describe and characterise sources of geomorphic noise that are present during landscape evolution, develop a method for representing noise within landscape evolution models, and assess its impact on the properties of synthetic landscapes. I first considered how naturally occurring noise can be represented by its spectral properties, and thus conducted a series of experiments in which red, white, and blue noise was added to landscape models. Noise was added in four scenarios: exclusively as an initial condition (as is typical in most landscape evolution models), the same arrangement added as the initial condition and at every subsequent time step, different arrangements added as the initial condition and at every subsequent time step, or as the initial condition and to the final topography. Results of these experiments showed that the geometries and geomorphic properties

of landscapes generated under the same tectonic and erosional conditions can vary substantially due to noise alone. A consequence of this finding is that assumptions underpinning many approaches to assessing landscape evolution, widely applied in studies of real topography, become difficult to justify, at least without acknowledgement and quantification of uncertainties that are present. It emphasises that adding noise to landscape simulators is not an arbitrary choice. Interpreting outputs from single models can be perilous, and should be avoided because they are not representative of underlying mechanisms driving geomorphic processes. Instead, the results imply that probabilistic or ensemble-based approaches to landscape modelling are likely to be required to account for uncertainties that arise from a lack of information about specific arrangements of noise in landscape models and natural landscapes.

A key implication of landscape geometries being variable as a result of noise, either in computational models (as shown in Chapter 2 and previously by Ijjász-Vásquez et al. (1992), for example) or natural systems (e.g., Lipp and Roberts, 2021), is that inverse models comparing topographic observations with modelled predictions using Euclidean statistics can have high misfits even when uplift histories are identical. This impact is highlighted in Chapter 3, where I sought to show how topography can be quantitatively compared in a way that is less sensitive to local complexity than to larger scale structure. I introduced the Wasserstein distance, from the mathematical field of optimal transport, in this chapter as a method to do so. I showed how widely-used Euclidean measures of misfit struggle to consistently and reliably identify best-fitting rates and locations of uplift due to the presence of local minima in objective functions. The Wasserstein distance offers an alternative measure of misfit to quantify similarity between observed and theoretical landscapes, identifying more accurate parameter values even in the presence of noise.

In Chapter 4 I tested whether it is possible to invert noisy topography for its history of uplift using Euclidean or Wasserstein-based objective functions. In a series of experiments that built in their complexity, I showed how Wasserstein-based objective functions that also incorporate calibrated information about landscape hypsometries and maximum elevations can recover the timing and rate of uplift from synthetic topography, even in the presence of noise. In comparison, Euclidean-based objective functions can identify optimal uplift rate histories when the initial noise within observed and predicted topography is identical, but with high uncertainty (in some cases so high that it makes predictions essentially meaningless) when the noise is different, which is a more realistic assumption in the context of real landscapes. Uncertainties in uplift rates are incorporated through a probabilistic optimisation algorithm. The success of this inverse modelling framework indicates that, under certain

conditions (though importantly with no assumptions about a topographic steady state), it is possible to recover tectonic information from real topography. The results from the inverse modelling framework were compared with those produced by inverting longitudinal river profiles. It was shown that river profile inversion failed to recover the oldest uplift, attributed to the absence of sufficient measurements within fluvial networks to constrain tectonic information from that time. It is promising that inverting entire landscapes appears to extend the temporal record on which uplift histories can be determined. Nonetheless, the reduced computational expense involved with inverting longitudinal river profiles compared to simulating the evolution of entire landscapes means it remains a valuable tool.

5.2 Returning to the research questions

In Chapter 1 I laid out four research questions that I sought to answer in this dissertation. I revisit these here to critically reflect on the extent to which they have been answered.

1. How can naturally occurring, geomorphic noise be described, characterised, and represented in landscape evolution modelling strategies?

2. What are the consequences of adding noise to landscape evolution models?

In Chapter 2, I described sources of geomorphic noise that are present during the lifetime of a landscape, and showed that by characterising these sources in terms of their spectral properties, they can be straightforwardly represented in landscape evolution modelling strategies. I demonstrated through a series of experiments that addressed three broad categories of topography (see section 2.2.3) that noise within landscape models generates variability in a range of geomorphic properties derived from topographically stable ($\partial z/\partial t = 0$) landscapes. I concluded from this study that probabilistic or ensemble-based modelling approaches are preferable to analysis of single models because they are more robust to, and can quantify, uncertainties that arise from noise.

3. How can topography be quantitatively compared in a way that 'sees through' local variability?

In Chapter 3, I extended the results of Chapter 2 to highlight how variable landscape geometries that are a consequence of noisy starting conditions are problematic for inverse models that use Euclidean statistics to compare topography. I demonstrated that local complexity generates solutions to Euclidean objective functions that contain local minima, making it challenging for inverse methods to reliably recover uplift parameters. The Wasserstein distance was introduced as an alternative method

to quantitatively compare landscapes, and I showed several examples in which Wasserstein-based objective functions are better suited to seeing through local complexity to recover uplift information from topography (see Figures 3.3, 3.5, and 3.7).

4. Can Euclidean or Wasserstein-based objective functions recover uplift histories from transient topography?

In Chapter 4 I presented an inverse framework that successfully recovers uplift rates from topography. I showed that this was possible using Euclidean- and Wasserstein-based objective functions when the initial conditions in 'observed' and predicted topographies are identical (see Figure 4.13), and that Wasserstein-based objective functions alone are successful when initial conditions differ (see Figures 4.17 and 4.21). Importantly, the probabilistic framework that was advocated for in Chapter 2 was incorporated, permitting uncertainties that arise from noise to be quantified.

5.3 Future work

5.3.1 Application to observed topography

The work presented in this dissertation shows how uplift histories can be recovered from synthetic topography. An obvious next step is to apply the inverse framework to real topography. There are a few considerations when choosing a location to do so. First, it is sensible to identify locations where there exist independent constraints on uplift (e.g., from stratigraphy or thermochronology). These are desirable in order to verify best-fitting solutions obtained from the inverse model. Second, it is desirable to possess information about parameters in the forward model that are not inverted for in this work. For example, knowledge of the parameter v in the stream power model that could be obtained from radiometric dating of basalt channels (e.g., Karlstrom et al., 2007). Two exemplar locations that fulfil these criteria are the African continent, which contains regions of domal topography (such as the Bié and Tibesti domes), and Madagascar.

The African continent has been considered as tectonically stable from the perspective of orogenesis throughout the Cenozoic, notwithstanding the East African Rift. However, its 'basin and swell' topography, characterised by domal topographic highs between sedimentary basins (Figure 5.1a), is long believed to have been generated as a result of convection within the upper mantle (Nyblade and Robinson, 1994; Burke, 1996; McKenzie and Fairhead, 1997; Gurnis et al., 2000; Holdt et al., 2022). Figure 5.1b shows long wavelength ($\geq$ 800 km) free-air gravity anomalies, often used as a proxy for

dynamic support. Positive anomalies are generally correlated with positive residual topography, including at the Hoggar, Tibesti, and Bié domes. Youthful (< 10 Ma) volcanic rocks are also present at these locations, which are located atop seismic shear velocities (at 120 km depth) and thinner lithosphere than surrounding regions (Figure 5.1c-d). Previous studies have made use of stratigraphic constraints, volcanism, sediment flux histories, longitudinal river profiles, combined forward and inverse landscape evolution modelling, and thermochronometry to characterise surface uplift and mantle convection through the Cenozoic (e.g., Bond, 1979; Sahagian, 1988; Rust and Summerfield, 1990; Paul et al., 2014; Deniel et al., 2015; Rudge et al., 2015; Lodhia et al., 2018; Ball et al., 2019; O'Malley et al., 2021). Applying the method developed here to either individual portions of (e.g., single domal swells) or entire African topography would be an attractive starting location in order to assess the method's efficacy in determining uplift histories of real topography, given the diversity of constraints provided by previous studies.

Similarly, debate surrounds the topographic evolution of Madagascar, particularly during the Cenozoic (e.g., de Wit, 2003). As with the African continent, a suite of geological and geophysical observations indicate that surface uplift has occurred during the past 50 Ma and is probably related to upper mantle convection, though its importance is still debated (e.g., Emmel et al., 2012; Roberts et al., 2012b; Stephenson et al., 2019; Stephenson et al., 2021b; Brosens et al., 2023; Clementucci et al., 2025). For instance, it is argued by Clementucci et al. (2025) that knickzones present in modern-day longitudinal river profiles in north Madagascar may have been created by changes in the positions of drainage divides, and that the cause of these changes is unrelated to mantle-driven uplift but instead a consequence of previous rifting and late Cenozoic tilting. Inverting the topography of Madagascar using the approach detailed in this dissertation for its temporally-varying uplift history has the potential to augment previous work and additionally may highlight areas where a spatially-invariant uplift history is inappropriate for explaining present-day Madagascan topography.

Finally, whilst portions of Earth's topography have previously been inverted for their uplift histories on regional to continental scales using information contained within longitudinal river profiles, assumptions around planform fixity have limited its application to regions believed to have longstanding drainage networks (e.g., Roberts et al., 2012b; Paul et al., 2014; Fernandes et al., 2019; O'Malley et al., 2021). The ability to invert entire (two-dimensional) landscapes in the presence of noise explicitly incorporates the ability of drainage planforms to migrate, thus potentially providing opportunity to invert portions of Earth's surface for its uplift history where topography has been advected (e.g., Himalayas, South

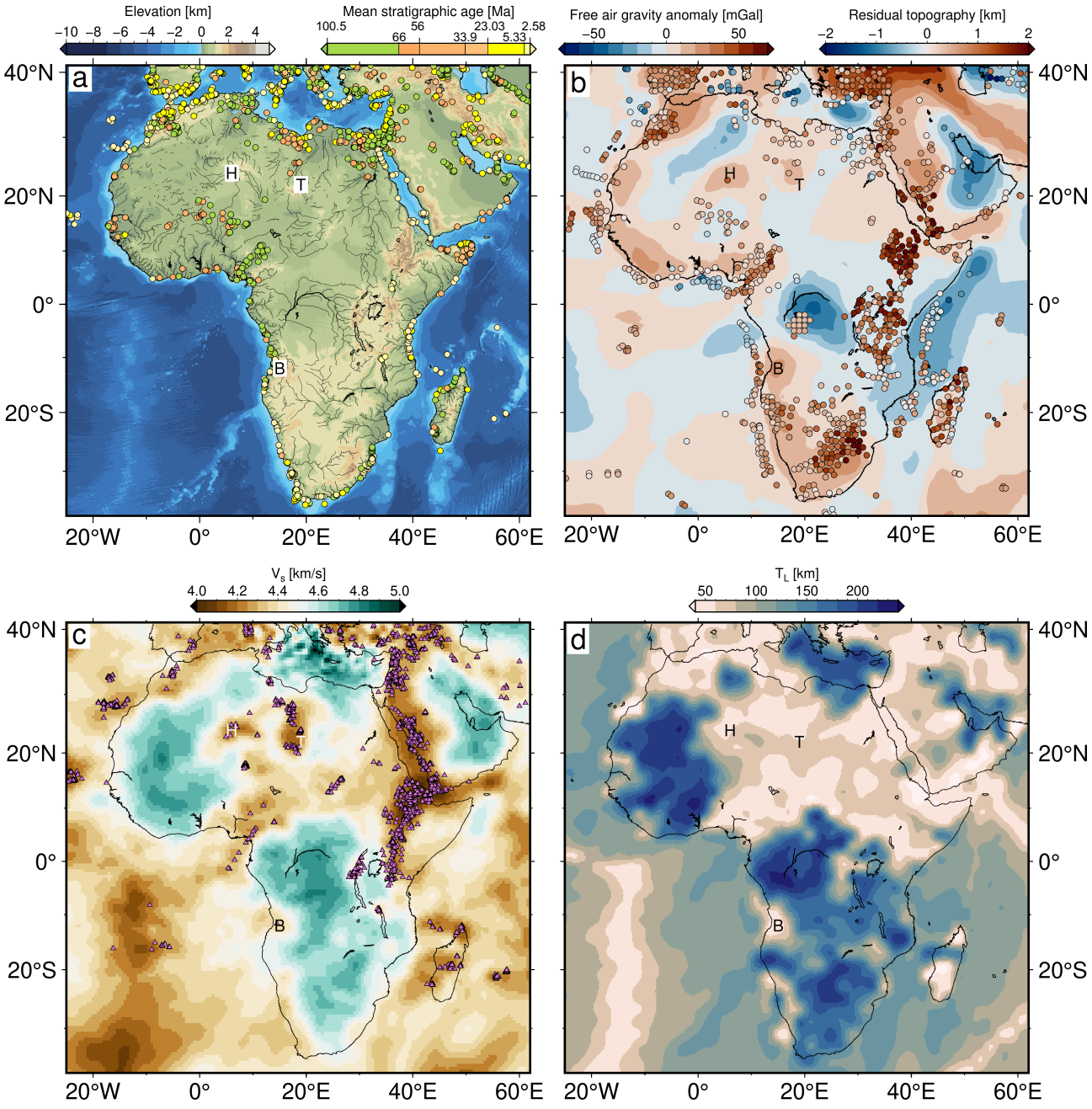


Figure 5.1: **Topographic, geological, and geophysical constraints on the African continent.** (a) Topographic map of Africa (Shuttle Radar Topographic Mission; Tozer et al., 2019). Topography is overlain with drainage networks, from HydroSHEDS database (Lehner and Grill, 2013) and marine fossil data (circles) of Fernandes and Roberts (2020), coloured by mean stratigraphic age. Three topographic swells are labelled: H = Hoggar; T = Tibesti; B = Bié. (b) Long wavelength ($\geq$ 800 km) free-air gravity anomaly field (EGM2008 Pavlis et al., 2012). Overlain with residual topography/bathymetry data of Holdt et al. (2022). (c) Shear-wave velocity at 120 km depth in the CSEM2 tomographic model (Noe et al., 2024). Pink triangles show intraplate magmatic rocks $<$ 10 Ma and located $<$ 400 km from locus of eruption based upon present-day plate speeds, as per Ball et al. (2021). (d) Lithospheric thickness of Africa, Arabia, and Madagascar (Afonso et al., 2019).

American Andes, California).

5.3.2 Further exploration of forward model parameters

In Chapters 3 and 4 I inverted topography for uplift parameters whilst keeping parameter values within the erosional model (Equation 4.9) fixed. Justification for doing so was twofold. First, for simplicity. Second, because it is not clear that other values, or temporally-changing values are any more appropriate on spatial scales of hundreds of kilometres. For example, minimising misfit between observed and predicted longitudinal river profiles indicates that best fits are obtained for $n = 1$ (e.g., Roberts et al., 2012a; Czarnota et al., 2014). Values of $n > 1$ are also likely to create shockwave behaviour, where steeper slopes advect upstream faster than shallower slopes and thus can erase prior signals (Pritchard et al., 2009). Finally, whilst local changes in erodibility can control erosion at small scales, it is unclear that this translates to landscape evolution at large spatial scales and long timescales (e.g., Baynes et al., 2018; Scheingross et al., 2020). Nonetheless, relaxing this constraint could still prove useful for extending the versatility of the inverse modelling framework, and has been addressed in previous work, where trade-offs were observed between erosional parameters and between erosional and uplift parameters (Roberts and White, 2010; Roberts et al., 2012a; Croissant and Braun, 2014).

5.3.3 Extending Optimal Transport-based objective functions

The inverse model presented in this dissertation makes use of the Wasserstein distance, calculated via the marginals approach of Sambridge et al. (2022). Topography is represented by two perpendicular marginal distributions. However, as discussed in Chapter 3, there are alternative ways in which topography could be represented and it may be of interest to explore these. I expand here on two examples. First, making use of more than two marginal distributions may better characterise topography and reduce non-uniqueness in solutions to the inverse model. Doing so could utilise the sliced Wasserstein approach, where a N-dimensional distribution is represented by one-dimensional projections calculated from a hypersphere (Rabin et al., 2012; Bonneel et al., 2015). This approach would add computational cost depending on the number of projections calculated, but is not expected to be prohibitively slow. Second, it may be of interest to explore regularised approaches to the two-dimensional optimal transport problem, such as entropic regularisation (Cuturi, 2013). Where exact solutions to two-dimensional Optimal Transport calculations are computationally expensive (see Figure 3.6), regularised approaches reduce computational burden at the expense of approximating the exact solution. It would be interesting to first test whether a 2-D Optimal Transport problem can be regularised such that the time to

evaluate an objective function is similar to that of the marginals approach, and then to assess whether an uplift history can be accurately recovered, for instance by recreating experiments 2, 3, and 4 of Chapter 4.

Bibliography

Adams, B. A., Hodges, K. V., Whipple, K. X., Ehlers, T. A., Soest, M. C. van, and Wartho, J. (2015). Constraints on the tectonic and landscape evolution of the Bhutan Himalaya from thermochronometry. *Tectonics* **34** (6), 1329–1347. DOI: 10.1002/2015TC003853.

Adams, B. A., Whipple, K. X., Forte, A. M., Heimsath, A. M., and Hodges, K. V. (2020). Climate controls on erosion in tectonically active landscapes. *Science Advances* **6** (42). DOI: 10.1126/sciadv.aaz3166.

Afonso, J. C., Salajegheh, F., Szwillus, W., Ebbing, J., and Gaina, C. (2019). A global reference model of the lithosphere and upper mantle from joint inversion and analysis of multiple data sets. *Geophysical Journal International* **217** (3), 1602–1628. DOI: 10.1093/gji/ggz094.

Altschuler, J., Weed, J., and Rigollet, P. (2018). Near-linear time approximation algorithms for optimal transport via Sinkhorn iteration. DOI: 10.48550/arXiv.1705.09634.

Ancey, C., Bohorquez, P., and Heyman, J. (2015). Stochastic interpretation of the advection-diffusion equation and its relevance to bed load transport. *Journal of Geophysical Research: Earth Surface* **120** (12), 2529–2551. DOI: 10.1002/2014JF003421.

Anderson, R. S. and Anderson, S. P. (2010). *Geomorphology: The Mechanics and Chemistry of Landscapes*. Cambridge University Press. DOI: 10.1017/CBO9780511794827.

Antonelli, A., Kissling, W. D., Flantua, S. G. A., Bermúdez, M. A., Mulch, A., Muellner-Riehl, A. N., Kreft, H., Linder, H. P., Badgley, C., Fjeldså, J., Fritz, S. A., Rahbek, C., Herman, F., Hooghiemstra, H., and Hoorn, C. (2018). Geological and climatic influences on mountain biodiversity. *Nature Geoscience* **11** (10), 718–725. DOI: 10.1038/s41561-018-0236-z.

Ariyanto, P., Syuhada, S. R., T, A., and Y, J. (2017). Crustal structure in the southern part of Central Java based on analysis of tele-seismic receiver function using a neighbourhood algorithm. *Journal of Physics, Conference Series* **985** (02018). DOI: 10.1088/1742-6596/985/1/012018.

Arjovsky, M., Chintala, S., and Bottou, L. (2017). *Wasserstein GAN*. DOI: 10.48550/ARXIV.1701.07875.

Attal, M., Tucker, G. E., Whittaker, A. C., Cowie, P. A., and Roberts, G. P. (2008). Modeling fluvial incision and transient landscape evolution: Influence of dynamic channel adjustment. *Journal of Geophysical Research: Earth Surface* **113** (F3). DOI: 10.1029/2007JF000893.

Attanayake, J., Ferreira, A. M., Berbellini, A., and Morelli, A. (2017). Crustal structure beneath Portugal from teleseismic Rayleigh Wave Ellipticity. *Tectonophysics* **712-713**, 344–361. DOI: 10.1016/j.tecto.2017.06.001.

Audet, P. (2011). Directional wavelet analysis on the sphere: Application to gravity and topography of the terrestrial planets. *Journal of Geophysical Research: Planets* **116** (E1). DOI: 10.1029/2010JE003710.

Backus, G. E. and Gilbert, J. F. (1967). Numerical Applications of a Formalism for Geophysical Inverse Problems. *Geophysical Journal International* **13** (1-3), 247–276. DOI: 10.1111/j.1365-246X.1967.tb02159.x.

Bahadori, A., Holt, W. E., Feng, R., Austermann, J., Loughney, K. M., Salles, T., Moresi, L., Beucher, R., Lu, N., Flesch, L. M., Calvelage, C. M., and E (2022). Coupled influence of tectonics, climate, and surface processes on landscape evolution in southwestern North America. *Nature Communications* **13** (1), 1–18. DOI: 10.1038/s41467-022-31903-.

Baldwin, J. A., Whipple, K. X., and Tucker, G. E. (2003). Implications of the shear stress river incision model for the timescale of postorogenic decay of topography. *Journal of Geophysical Research: Solid Earth* **108** (B3). DOI: 10.1029/2001JB000550.

Ball, P. W., White, N. J., Maclennan, J., and Stephenson, S. N. (2021). Global influence of mantle temperature and plate thickness on intraplate volcanism. *Nature Communications* **12** (1), 2045. DOI: 10.1038/s41467-021-22323-9.

Ball, P. W., White, N. J., Masoud, A., Nixon, S., Hoggard, M. J., Maclennan, J., Stuart, F. M., Oppenheimer, C., and Kröpelin, S. (2019). Quantifying Asthenospheric and Lithospheric Controls on Mafic Magmatism Across North Africa. *Geochemistry, Geophysics, Geosystems* **20** (7), 3520–3555. DOI: 10.1029/2019GC008303.

Balmino, G. (1993). The Spectra of the topography of the Earth, Venus and Mars. *Geophysical Research Letters* **20** (11), 1063–1066. DOI: 10.1029/93GL01214.

Barnes, R., Lehman, C., and Mulla, D. (2014). Priority-flood: An optimal depression-filling and watershed-labeling algorithm for digital elevation models. *Computers & Geosciences* **62**, 117–127. DOI: 10.1016/j.cageo.2013.04.024.

Barnett-Moore, N., Flament, N., Heine, C., Butterworth, N., and Müller, R. D. (2014). Cenozoic uplift of south Western Australia as constrained by river profiles. *Tectonophysics* **622**, 186–197. DOI: 10.1016/j.tecto.2014.03.010.

Barnhart, K. R., Hutton, E. W., Tucker, G. E., Gasparini, N. M., Istanbulluoglu, E., Hobley, D. E., Lyons, N. J., Mouchene, M., Nudurupati, S. S., Adams, J. M., et al. (2020a). Landlab v2. 0: A software package for Earth surface dynamics. *Earth Surface Dynamics* **8** (2), 379–397. DOI: 10.5194/esurf-8-379-2020.

Barnhart, K. R., Tucker, G. E., Doty, S. G., Shobe, C. M., Glade, R. C., Rossi, M. W., and Hill, M. C. (2020b). Inverting Topography for Landscape Evolution Model Process Representation: 2. Calibration and Validation. *Journal of Geophysical Research: Earth Surface* **125** (7), e2018JF004963. DOI: https://doi.org/10.1029/2018JF004963.

Barnhart, K. R., Tucker, G. E., Doty, S. G., Glade, R. C., Shobe, C. M., Rossi, M. W., and Hill, M. C. (2020c). Projections of Landscape Evolution on a 10,000 Year Timescale With Assessment and Partitioning of Uncertainty Sources. *Journal of Geophysical Research: Earth Surface* **125** (12), e2020JF005795. DOI: 10.1029/2020JF005795.

Barnhart, K. R., Tucker, G. E., Doty, S. G., Shobe, C. M., Glade, R. C., Rossi, M. W., and Hill, M. C. (2020d). Inverting Topography for Landscape Evolution Model Process Representation: 1. Conceptualization and Sensitivity Analysis. *Journal of Geophysical Research: Earth Surface* **125** (7). DOI: 10.1029/2018JF004961.

— (2020e). Inverting Topography for Landscape Evolution Model Process Representation: 3. Determining Parameter Ranges for Select Mature Geomorphic Transport Laws and Connecting Changes in Fluvial Erodibility to Changes in Climate. *Journal of Geophysical Research: Earth Surface* **125** (7). DOI: 10.1029/2019JF005287.

Barnosky, A. and Carrasco, M. (2002). Effects of Oligo-Miocene global climate changes on mammalian species richness in the northwestern quarter of the USA. *Evolutionary Ecology Research* **4**.

Baynes, E. R. C., Lague, D., Attal, M., Gangloff, A., Kirstein, L. A., and Dugmore, A. J. (2018). River self-organisation inhibits discharge control on waterfall migration. *Scientific Reports* **8** (1), 2444. DOI: 10.1038/s41598-018-20767-6.

Beaumont, C., Fullsack, P., and Hamilton, J. (1992). Erosional control of active compressional orogens. In: *Thrust Tectonics*. Ed. by K. R. McClay. Springer Netherlands, 1–18. DOI: 10.1007/978-94-011-3066-0_1.

Beeson, H. W., McCoy, S. W., and Keen-Zebert, A. (2017). Geometric disequilibrium of river basins produces long-lived transient landscapes. *Earth and Planetary Science Letters* **475**, 34–43. DOI: 10.1016/j.epsl.2017.07.010.

Bell, T. H. (1975). Statistical features of sea-floor topography. *Deep Sea Research and Oceanographic Abstracts* **22** (12), 883–892. DOI: 10.1016/0011-7471(75)90090-X.

Benamou, J.-D. and Brenier, Y. (2000). A computational fluid mechanics solution to the Monge-Kantorovich mass transfer problem. *Numerische Mathematik* **84** (3), 375–393. DOI: 10.1007/s002110050002.

Benamou, J.-D., Froese, B. D., and Oberman, A. M. (2014). Numerical solution of the Optimal Transportation problem using the Monge–Ampère equation. *Journal of Computational Physics* **260**, 107–126. DOI: 10.1016/j.jcp.2013.12.015.

Berbellini, A., Morelli, A., and G. Ferreira, A. M. (2017). Crustal structure of northern Italy from the ellipticity of Rayleigh waves. *Physics of the Earth and Planetary Interiors* **265**, 1–14. DOI: 10.1016/j.pepi.2016.12.005.

Birnir, B., Smith, T. R., and Merchant, G. E. (2001). The scaling of fluvial landscapes. *Computers & Geosciences* **27** (10), 1189–1216. DOI: 10.1016/S0098-3004(01)00022-X.

Bishop, P. (2007). Long-term landscape evolution: Linking tectonics and surface processes. *Earth Surface Processes and Landforms* **32** (3), 329–365. DOI: 10.1002/esp.1493.

Bond, G. C. (1979). Evidence for some uplifts of large magnitude in continental platforms. *Tectonophysics* **61** (1), 285–305. DOI: 10.1016/0040-1951(79)90302-0.

Bonneel, N., Rabin, J., Peyré, G., and Pfister, H. (2015). Sliced and Radon Wasserstein Barycenters of Measures. *Journal of Mathematical Imaging and Vision* **51** (1), 22–45. DOI: 10.1007/s10851-014-0506-3.

Bonnet, S. and Crave, A. (2003). Landscape response to climate change: Insights from experimental modeling and implications for tectonic versus climatic uplift of topography. *Geology* **31** (2), 123–126. DOI: 10.1130/0091-7613(2003)031<0123:LRTCCI>2.0.CO;2.

Booth, A. M., Roering, J. J., and Perron, J. T. (2009). Automated landslide mapping using spectral analysis and high-resolution topographic data: Puget Sound lowlands, Washington, and Portland Hills, Oregon. *Geomorphology* **109** (3), 132–147. DOI: 10.1016/j.geomorph.2009.02.027.

Borse, D. and Biswal, B. (2025). Emergence of efficient channel networks in fluvial landscapes. *Advances in Water Resources* **200**, 104962. DOI: 10.1016/j.advwatres.2025.104962.

Bovy, B. (2021). *fastscape-lem/fastscape: Release v0.1.0beta3*. Version 0.1.0beta3. DOI: 10.5281/zenodo.4435110.

Braun, J., Robert, X., and Simon-Labric, T. (2013). Eroding dynamic topography. *Geophysical Research Letters* **40** (8), 1494–1499. DOI: 10.1002/grl.50310.

Braun, J. (2002). Quantifying the effect of recent relief changes on age–elevation relationships. *Earth and Planetary Science Letters* **200** (3), 331–343. DOI: 10.1016/S0012-821X(02)00638-6.

Braun, J. and Sambridge, M. (1997). Modelling landscape evolution on geological time scales: a new method based on irregular spatial discretization. *Basin Research* **9** (1), 27–52. DOI: 10.1046/j.1365-2117.1997.00030.x.

Braun, J. and van der Beek, P. (2004). Evolution of passive margin escarpments: What can we learn from low-temperature thermochronology? *Journal of Geophysical Research: Earth Surface* **109** (F4). DOI: 10.1029/2004JF000147.

Braun, J. and Willett, S. D. (2013). A very efficient O(n), implicit and parallel method to solve the stream power equation governing fluvial incision and landscape evolution. *Geomorphology* **180–181**, 170–179. DOI: 10.1016/j.geomorph.2012.10.008.

Brenier, Y. (1991). Polar factorization and monotone rearrangement of vector-valued functions. *Communications on Pure and Applied Mathematics* **44** (4), 375–417. DOI: 10.1002/cpa.3160440402.

Brosens, L., Cox, R., Campforts, B., Jacobs, L., Vanacker, V., Bierman, P., Razanamahandry, V. F., Rakotondrazafy, A. F. M., Razafimbelo, T., Rafolisy, T., and Govers, G. (2023). The slow downwearing of Madagascar: Inferring patterns and controls on long-term basin-averaged erosion rates from *in situ* ^{10} Be at the catchment and regional level. *Earth Surface Processes and Landforms*. DOI: 10.1002/esp.5586.

Bullard, E., Everett, J. E., and Gilbert Smith, A. (1965). The fit of the continents around the Atlantic. *Philosophical Transactions of the Royal Society of London. Series A, Mathematical and Physical Sciences* **258** (1088), 41–51. DOI: 10.1098/rsta.1965.0020.

Burke, K. (1996). The African Plate. *South African Journal of Geology* **99** (4), 341–409. DOI: 10.10520/EJC-942801f20.

Bursztyn, N., Pederson, J. L., Tressler, C., Mackley, R. D., and Mitchell, K. J. (2015). Rock strength along a fluvial transect of the Colorado Plateau – quantifying a fundamental control on geomorphology. *Earth and Planetary Science Letters* **429**, 90–100. DOI: 10.1016/J.EPSL.2015.07.042.

Campforts, B., Schwanghart, W., and Govers, G. (2017). Accurate simulation of transient landscape evolution by eliminating numerical diffusion: the TTLEM 1.0 model. *Earth Surface Dynamics* **5** (1), 47–66. DOI: 10.5194/esurf-5-47-2017.

Campforts, B., Shobe, C. M., Steer, P., Vanmaercke, M., Lague, D., and Braun, J. (2020a). HyLands 1.0: a hybrid landscape evolution model to simulate the impact of landslides and landslide-derived sediment on landscape evolution. *Geoscientific Model Development* **13** (9), 3863–3886. DOI: 10.5194/gmd-13-3863-2020.

Campforts, B., Vanacker, V., Herman, F., Vanmaercke, M., Schwanghart, W., Tenorio, G. E., Willems, P., and Govers, G. (2020b). Parameterization of river incision models requires accounting for environmental heterogeneity: insights from the tropical Andes. *Earth Surface Dynamics* **8** (2), 447–470. DOI: 10.5194/esurf-8-447-2020.

Castelltort, S., Goren, L., Willett, S. D., Champagnac, J.-D., Herman, F., and Braun, J. (2012). River drainage patterns in the New Zealand Alps primarily controlled by plate tectonic strain. *Nature Geoscience* **5** (10), 744–748. DOI: 10.1038/ngeo1582.

Castelltort, S. and Yamato, P. (2013). The influence of surface slope on the shape of river basins: Comparison between nature and numerical landscape simulations. *Geomorphology* **192**, 71–79. DOI: 10.1016/j.geomorph.2013.03.022.

Cawood, P. A. and Hawkesworth, C. J. (2015). Temporal relations between mineral deposits and global tectonic cycles. *Geological Society, London, Special Publications* **393** (1), 9–21. DOI: 10.1144/SP393.1.

Champion, M. E. S., White, N. J., Jones, S. M., and Lovell, J. P. B. (2008). Quantifying transient mantle convective uplift: An example from the Faroe-Shetland basin. *Tectonics* **27** (1). DOI: 10.1029/2007TC002106.

Chandra, R., Azam, D., Müller, R. D., Salles, T., and Cripps, S. (2019a). Bayeslands: A Bayesian inference approach for parameter uncertainty quantification in Badlands. *Computers & Geosciences* **131**, 89–101. DOI: 10.1016/j.cageo.2019.06.012.

Chandra, R., Müller, R. D., Azam, D., Deo, R., Butterworth, N., Salles, T., and Cripps, S. (2019b). Multicore Parallel Tempering Bayeslands for Basin and Landscape Evolution. *Geochemistry, Geophysics, Geosystems* **20** (11), 5082–5104. DOI: 10.1029/2019GC008465.

Chang, C.-P., Ghil, M., Latif, M., and Wallace, J. M. (2015). *A Mathematical Theory of Climate Sensitivity or, How to Deal With Both Anthropogenic Forcing and Natural Variability?* Vol. 6. Climate Change: Multidecadal and Beyond. World Scientific.

Chappell, J. (1974). Geology of Coral Terraces, Huon Peninsula, New Guinea: A Study of Quaternary Tectonic Movements and Sea-Level Changes. *GSA Bulletin* **85**, 553–570. DOI: 10.1130/0016-7606(1974)85<553:GOCTHP>2.0.CO;2.

Chen, T.-Y. K., Hung, C.-Y., Chiang, Y.-C., Hsieh, M.-L., and Capart, H. (2022). A stochastic model of geomorphic risk due to episodic river aggradation and degradation. *Engineering Geology* **309**, 106845. DOI: 10.1016/j.enggeo.2022.106845.

Clementucci, R., Uchusov, E., Wang, Y., and Willett, S. D. (2025). Madagascar's landscape evolution: A tale of two rifts. *Science Advances* **11** (42), eadw6362. DOI: 10.1126/sciadv.adw6362.

Clubb, F. J., Mudd, S. M., Schildgen, T. F., Beek, P. A. van der, Devrani, R., and Sinclair, H. D. (2023). Himalayan valley-floor widths controlled by tectonically driven exhumation. *Nature Geoscience* **16** (8), 739–746. DOI: 10.1038/s41561-023-01238-8.

Cooley, J. W. and Tukey, J. W. (1965). An Algorithm for the Machine Calculation of Complex Fourier Series. *Mathematics of Computation* **19** (90), 297–301. DOI: 10.1090/S0025-5718-1965-0178586-1.

Coulthard, T. J. (2001). Landscape evolution models: a software review. *Hydrological Processes* **15** (1), 165–173. DOI: 10.1002/hyp.426.

Coulthard, T. J., Ramirez, J., Fowler, H. J., and Glenis, V. (2012). Using the UKCP09 probabilistic scenarios to model the amplified impact of climate change on drainage basin sediment yield. *Hydrology and Earth System Sciences* **16** (11), 4401–4416. DOI: 10.5194/hess-16-4401-2012.

Coulthard, T. J., Neal, J. C., Bates, P. D., Ramirez, J., Almeida, G. A. M. de, and Hancock, G. R. (2013). Integrating the LISFLOOD-FP 2D hydrodynamic model with the CAESAR model: implications for modelling landscape evolution. *Earth Surface Processes and Landforms* **38** (15), 1897–1906. DOI: 10.1002/esp.3478.

Croissant, T. and Braun, J. (2014). Constraining the stream power law: A novel approach combining a landscape evolution model and an inversion method. *Earth Surface Dynamics* **2** (1), 155–166. DOI: 10.5194/esurf-2-155-2014.

Cullen, C., Anders, A. M., Lai, J., and Druhan, J. L. (2022). Numerical modeling of groundwater-driven stream network evolution in low-relief post-glacial landscapes. *Earth Surface Processes and Landforms* **47** (2), 658–671. DOI: 10.1002/esp.5278.

Culling, W. E. H. (1960). Analytical Theory of Erosion. *The Journal of Geology* **68** (3), 336–344. DOI: 10.1086/626663.

Curry, M. E. and van der Beek, P. (2025). Exploring Controls on Post-Orogenic Topographic Stasis of the Pyrenees Mountains With Inverse Landscape Evolution Modeling. *Journal of Geophysical Research: Earth Surface* **130** (2), e2024JF007759. DOI: 10.1029/2024JF007759.

Cuturi, M. (2013). Sinkhorn Distances: Lightspeed Computation of Optimal Transport. *Advances in Neural Information Processing Systems*. Ed. by C. Burges, L. Bottou, M. Welling, Z. Ghahramani, and K. Weinberger. Vol. 26. Curran Associates, Inc.

Czarnota, K., Hoggard, M. J., White, N., and Winterbourne, J. (2013). Spatial and temporal patterns of Cenozoic dynamic topography around Australia. *Geochemistry, Geophysics, Geosystems* **14** (3), 634–658. DOI: 10.1029/2012GC004392.

Czarnota, K., Roberts, G. G., White, N. J., and Fishwick, S. (2014). Spatial and temporal patterns of Australian dynamic topography from River Profile Modeling. *Journal of Geophysical Research: Solid Earth* **119** (2), 1384–1424. DOI: 10.1002/2013JB010436.

Davis, W. M. (1899). The geographical cycle. *Geographical Journal* **14**, 481–504. DOI: 10.1007/978-1-349-15508-8_2.

de Wit, M. J. (2003). Madagascar: Heads It's a Continent, Tails It's an Island. *Annual Review of Earth and Planetary Sciences* **31**, 213–248. DOI: 10.1146/annurev.earth.31.100901.141337.

DeLisle, C. and Yanites, B. J. (2024). Modeling Climate and Tectonic Controls on Bias in Measured River Incision Rates. *Geophysical Research Letters* **51** (18), e2024GL109339. DOI: 10.1029/2024GL109339.

Deniel, C., Vincent, P. M., Beauvilain, A., and Gourgaud, A. (2015). The Cenozoic volcanic province of Tibesti (Sahara of Chad): major units, chronology, and structural features. *Bulletin of Volcanology* **77** (9), 74. DOI: 10.1007/s00445-015-0955-6.

DiBiase, R. A. and Whipple, K. X. (2011). The influence of erosion thresholds and runoff variability on the relationships among topography, climate, and erosion rate. *Journal of Geophysical Research* **116** (F4), F04036. DOI: 10.1029/2011JF002095.

Emmel, B., Boger, S. D., Jacobs, J., and Daszinnies, M. C. (2012). Maturity of central Madagascar's landscape — Low-temperature thermochronological constraints. *Gondwana Research*. Special Issue: Western Gondwana **21** (2), 704–713. DOI: 10.1016/j.gr.2011.05.018.

Engquist, B. and Froese, B. (2014). Application of the Wasserstein metric to seismic signals. *Communications in Mathematical Sciences* **12** (5), 979–988. DOI: 10.4310/CMS.2014.v12.n5.a7.

Etherington, T. R. (2022). Perlin noise as a hierarchical neutral landscape model. *Web Ecology* **22** (1), 1–6. DOI: 10.5194/we-22-1-2022.

Faccenna, C. and Becker, T. W. (2020). Topographic expressions of mantle dynamics in the Mediterranean. *Earth-Science Reviews* **209**, 103327. DOI: 10.1016/j.earscirev.2020.103327.

Farr, T. G., Rosen, P. A., Caro, E., Crippen, R., Duren, R., Hensley, S., Kobrick, M., Paller, M., Rodriguez, E., Roth, L., Seal, D., Shaffer, S., Shimada, J., Umland, J., Werner, M., Oskin, M., Burbank, D., and Alsdorf, D. (2007). The Shuttle Radar Topography Mission. *Reviews of Geophysics* **45** (2), 2005RG000183. DOI: 10.1029/2005RG000183.

Fernandes, N. F. and Dietrich, W. E. (1997). Hillslope evolution by diffusive processes: The timescale for equilibrium adjustments. *Water Resources Research* **33** (6), 1307–1318. DOI: 10.1029/97WR00534.

Fernandes, V. M. and Roberts, G. G. (2020). Cretaceous to Recent net continental uplift from paleobiological data: Insights into sub-plate support. *GSA Bulletin* **133** (5-6), 1217–1236. DOI: 10.1130/B35739.1.

Fernandes, V. M., Roberts, G. G., White, N., and Whittaker, A. C. (2019). Continental-Scale Landscape Evolution: A History of North American Topography. *Journal of Geophysical Research: Earth Surface* **123** (11), 2689–2722. DOI: 10.1029/2018JF004979.

Ferreira, A. M. G., Marignier, A., Attanayake, J., Frietsch, M., and Berbellini, A. (2020). Crustal structure of the Azores Archipelago from Rayleigh wave ellipticity data. *Geophysical Journal International* **221** (2), 1232–1247. DOI: 10.1093/gji/ggaa076.

Ferrier, K. L., Huppert, K. L., and Perron, J. T. (2013). Climatic control of bedrock river incision. *Nature* **496** (7444), 206–209. DOI: 10.1038/nature11982.

Finarelli, J. A. and Badgley, C. (2010). Diversity dynamics of Miocene mammals in relation to the history of tectonism and climate. *Proceedings of the Royal Society B: Biological Sciences* **277** (1694), 2721–2726. DOI: 10.1098/rspb.2010.0348.

Fisher, J. A., Pazzaglia, F. J., Anastasio, D. J., and Gallen, S. F. (2022). Linear Inversion of Fluvial Topography in the Northern Apennines: Comparison of Base-Level Fall to Crustal Shortening. *Tectonics* **41** (11). DOI: 10.1029/2022TC007379.

Flint, J. J. (1974). Stream gradient as a function of order, magnitude, and discharge. *Water Resources Research* **10** (5), 969–973. DOI: 10.1029/WR010i005p00969.

Flowers, R. M., Wernicke, B. P., and Farley, K. A. (2008). Unroofing, incision, and uplift history of the southwestern Colorado Plateau from apatite (U-Th)/He thermochronometry. *GSA Bulletin* **120** (5-6), 571–587. DOI: 10.1130/B26231.1.

Forte, A. M. and Rossi, M. W. (2024a). Stochastic in Space and Time: 1. Characterizing Orographic Gradients in Mean Runoff and Daily Runoff Variability. *Journal of Geophysical Research: Earth Surface* **129** (3), e2023JF007326. DOI: 10.1029/2023JF007326.

— (2024b). Stochastic in Space and Time: 2. Effects of Simulating Orographic Gradients in Daily Runoff Variability on Bedrock River Incision. *Journal of Geophysical Research: Earth Surface* **129** (3), e2023JF007327. DOI: 10.1029/2023JF007327.

Forte, A. M., Yanites, B. J., and Whipple, K. X. (2016). Complexities of landscape evolution during incision through layered stratigraphy with contrasts in rock strength. *Earth Surface Processes and Landforms* **41** (12), 1736–1757. DOI: 10.1002/esp.3947.

Fournier, A., Fussell, D., and Carpenter, L. (1982). Computer rendering of stochastic models. *Commun. ACM* **25** (6), 371–384. DOI: 10.1145/358523.358553.

Fox, M., Goren, L., May, D. A., and Willett, S. D. (2014). Inversion of fluvial channels for paleorock uplift rates in Taiwan. *Journal of Geophysical Research: Earth Surface* **119** (9), 1853–1875. DOI: 10.1002/2014JF003196.

Gailleton, B., Malatesta, L. C., Cordonnier, G., and Braun, J. (2024). CHONK 1.0: landscape evolution framework: cellular automata meets graph theory. *Geoscientific Model Development* **17** (1), 71–90. DOI: 10.5194/gmd-17-71-2024.

Gailleton, B., Mudd, S. M., Clubb, F. J., Grieve, S. W. D., and Hurst, M. D. (2021). Impact of Changing Concavity Indices on Channel Steepness and Divide Migration Metrics. *Journal of Geophysical Research: Earth Surface* **126** (10). DOI: 10.1029/2020JF006060.

Gallen, S. F. and Fernández-Blanco, D. (2021). A New Data-Driven Bayesian Inversion of Fluvial Topography Clarifies the Tectonic History of the Corinth Rift and Reveals a Channel Steepness Threshold. *Journal of Geophysical Research: Earth Surface* **126** (3), e2020JF005651. DOI: 10.1029/2020JF005651.

Gallen, S. F. (2018). Lithologic controls on landscape dynamics and aquatic species evolution in post-orogenic mountains. *Earth and Planetary Science Letters* **493**, 150–160. DOI: 10.1016/J.EPSL.2018.04.029.

Gallen, S. F., Seymour, N. M., Glotzbach, C., Stockli, D. F., and O'Sullivan, P. (2023). Calabrian forearc uplift paced by slab–mantle interactions during subduction retreat. *Nature Geoscience* **16** (6), 513–520. DOI: 10.1038/s41561-023-01185-4.

Gao, F. and Han, L. (2012). Implementing the Nelder-Mead simplex algorithm with adaptive parameters. *Computational Optimization and Applications* **51** (1), 259–277. DOI: 10.1007/s10589-010-9329-3.

Garefalakis, P. and Schlunegger, F. (2018). Link between concentrations of sediment flux and deep crustal processes beneath the European Alps. *Scientific Reports* **8** (1), 183. DOI: 10.1038/s41598-017-17182-8.

Gasparini, N. M., Forte, A. M., and Barnhart, K. R. (2024). Short Communication: Numerically simulated time to steady state is not a reliable measure of landscape response time. *Earth Surface Dynamics* **12** (6), 1227–1242. DOI: 10.5194/esurf-12-1227-2024.

Gelman, A. and Rubin, D. B. (1992). Inference from Iterative Simulation Using Multiple Sequences. *Statistical Science* **7** (4), 457–472. DOI: 10.1214/ss/1177011136.

Gelwick, K. D., Willett, S. D., and Yang, R. (2024). Geomorphic indicators of continental-scale landscape transience in the Hengduan Mountains, SE Tibet, China. *Earth Surface Dynamics* **12** (3), 783–800. DOI: 10.5194/esurf-12-783-2024.

Genevay, A., Cuturi, M., Peyré, G., and Bach, F. (2016). Stochastic Optimization for Large-scale Optimal Transport. DOI: 10.48550/arXiv.1605.08527.

Gilbert, G. K. (1877). *Report on the geology of the Henry Mountains (Technical Report)*. Tech. rep. Geographical and Geological Survey of the Rocky Mountain Region, Government Printing Office.

Glotzbach, C. (2015). Deriving rock uplift histories from data-driven inversion of river profiles. *Geology* **43** (6), 467–470. DOI: 10.1130/G36702.1.

Goren, L., Fox, M., and Willett, S. D. (2014a). Tectonics from fluvial topography using formal linear inversion: Theory and applications to the Inyo Mountains, California. *Journal of Geophysical Research: Earth Surface* **119** (8), 1651–1681. DOI: 10.1002/2014JF003079.

Goren, L., Willett, S. D., Herman, F., and Braun, J. (2014b). Coupled numerical–analytical approach to landscape evolution modeling. *Earth Surface Processes and Landforms* **39** (4), 522–545. DOI: 10.1002/esp.3514.

Gray, H. J., Shobe, C. M., Hobley, D. E., Tucker, G. E., Duvall, A. R., Harbert, S. A., and Owen, L. A. (2017). Off-fault deformation rate along the southern San Andreas fault at Mecca Hills, southern California, inferred from landscape modeling of curved drainages. *Geology* **46** (1), 59–62. DOI: 10.1130/G39820.1.

Gurnis, M., Mitrovica, J. X., Ritsema, J., and Heijst, H.-J. van (2000). Constraining mantle density structure using geological evidence of surface uplift rates: The case of the African Superplume. *Geochemistry, Geophysics, Geosystems* **1** (7). DOI: 10.1029/1999GC000035.

Hack, J. T. (1960). Interpretation of erosional topography in humid temperate regions. *American Journal of Science* **258 (A)**, 80–97.

Hack, J. T. (1957). Studies of Longitudinal Stream Profiles in Virginia and Maryland. *Geological Survey Professional Paper 294-B USGS*. United States Government Printing Office, Washington (1957), 45–80.

Hadamard, J. M. (1902). Sur les Problèmes aux Dérivées Partielles et Leur Signification Physique. *Princeton University Bulletin* **13** (4), 49–52.

Hadler Boggiani, B., Salles, T., Mallard, C., and Atwood, N. (2025). The roles of surface processes in porphyry copper deposit preservation. *Earth Surface Dynamics* **13** (4), 683–704. DOI: 10.5194/esurf-13-683-2025.

Hagbi, R., Goren, L., Eiler, J. M., and Ryb, U. (2024). Inferring relative sediment fluxes and landscape evolution trends from C, O and clumped isotopes and mineral composition in detrital carbonate. *Earth and Planetary Science Letters* **647**, 119031. DOI: 10.1016/j.epsl.2024.119031.

Hancock, G. R., Coulthard, T. J., and Lowry, J. B. C. (2016). Predicting uncertainty in sediment transport and landscape evolution – the influence of initial surface conditions. *Computers & Geosciences*. Uncertainty and Sensitivity in Surface Dynamics Modeling **90**, 117–130. DOI: 10.1016/j.cageo.2015.08.014.

Harel, M.-A., Mudd, S. M., and Attal, M. (2016). Global analysis of the stream power law parameters based on worldwide 10Be denudation rates. *Geomorphology* **268**, 184–196. DOI: 10.1016/j.geomorph.2016.05.035.

Harkins, N., Kirby, E., Heimsath, A., Robinson, R., and Reiser, U. (2007). Transient fluvial incision in the headwaters of the Yellow River, northeastern Tibet, China. *China, J. Geophys. Res* **112**, 3–04. DOI: 10.1029/2006JF000570.

Harrison, C. G. A., Miskell, K. J., Brass, G. W., Saltzman, E. S., and Sloan, J. L. (1983). Continental hypsography. *Tectonics* **2** (4), 357–377. DOI: 10.1029/TC002i004p00357.

Hartley, R. A., Roberts, G. G., White, N., and Richardson, C. (2011). Transient convective uplift of an ancient buried landscape. *Nature Geoscience* **4** (8), 562–565. DOI: 10.1038/ngeo1191.

Hasbargen, L. E. and Paola, C. (2000). Landscape instability in an experimental drainage basin. *Geology* **28** (12), 1067–1070. DOI: 10.1130/0091-7613(2000)28<1067:LIIAED>2.0.CO;2.

Haviv, I., Enzel, Y., Whipple, K. X., Zilberman, E., Matmon, A., Stone, J., and Fifield, K. L. (2010). Evolution of vertical knickpoints (waterfalls) with resistant caprock: Insights from numerical modeling. *Journal of Geophysical Research: Earth Surface* **115** (F3). DOI: 10.1029/2008JF001187.

He, C., Yang, C.-J., Turowski, J. M., Ott, R. F., Braun, J., Tang, H., Ghantous, S., Yuan, X., and Stucky de Quay, G. (2024). A global dataset of the shape of drainage systems. *Earth System Science Data* **16** (2), 1151–1166. DOI: 10.5194/essd-16-1151-2024.

Hergarten, S., Robl, J., and Stüwe, K. (2016). Tectonic geomorphology at small catchment sizes – extensions of the stream-power approach and the *χ* method. *Earth Surface Dynamics* **4** (1), 1–9. DOI: 10.5194/esurf-4-1-2016.

Hergarten, S. (2020). Rivers as linear elements in landform evolution models. *Earth Surface Dynamics* **8** (2), 367–377. DOI: 10.5194/esurf-8-367-2020.

Hergarten, S. and Pietrek, A. (2023). Self-organization of channels and hillslopes in models of fluvial landform evolution and its potential for solving scaling issues. *Earth Surface Dynamics* **11** (4), 741–755. DOI: 10.5194/esurf-11-741-2023.

Hobley, D. E., Adams, J. M., Nudurupati, S. S., Hutton, E. W., Gasparini, N. M., Istanbulluoglu, E., and Tucker, G. E. (2017). Creative computing with Landlab: an open-source toolkit for building, coupling, and exploring two-dimensional numerical models of Earth-surface dynamics. *Earth Surface Dynamics* **5** (1), 21–46. DOI: 10.5194/esurf-5-21-2017.

Hoggard, M. J., Czarnota, K., Richards, F. D., Huston, D. L., Jaques, A. L., and Ghelichkhan, S. (2020). Global distribution of sediment-hosted metals controlled by craton edge stability. *Nature Geoscience* **13** (7), 504–510. DOI: 10.1038/s41561-020-0593-2.

Holdt, M. C., White, N. J., Stephenson, S. N., and Conway-Jones, B. W. (2022). Densely Sampled Global Dynamic Topographic Observations and Their Significance. *Journal of Geophysical Research: Solid Earth* **127** (7), e2022JB024391. DOI: 10.1029/2022JB024391.

Hoskins, A. M., Attal, M., Mudd, S. M., and Castillo, M. (2023). Topographic Response to Horizontal Advection in Normal Fault-Bound Mountain Ranges. *Journal of Geophysical Research: Earth Surface* **128** (8), e2023JF007126. DOI: 10.1029/2023JF007126.

Howard, A. D. (1994). A detachment-limited model of drainage basin evolution. *Water Resources Research* **30** (7), 2261–2285. DOI: 10.1029/94WR00757.

Howard, A. D. and Kerby, G. (1983). Channel changes in badlands. *GSA Bulletin* **94** (6), 739–752. DOI: 10.1130/0016-7606(1983)94<739:CCIB>2.0.CO;2.

Hunt, B. R. (1970). The inverse problem of radiography. *Mathematical Biosciences* **8** (1), 161–179. DOI: 10.1016/0025-5564(70)90148-3.

Hurst, M. D., Mudd, S. M., Yoo, K., Attal, M., and Walcott, R. (2013). Influence of lithology on hillslope morphology and response to tectonic forcing in the northern Sierra Nevada of California. *Journal of Geophysical Research: Earth Surface* **118** (2), 832–851. DOI: 10.1002/jgrf.20049.

Hurtrez, J.-E., Sol, C., and Lucazeau, F. (1999). Effect of drainage area on hypsometry from an analysis of small-scale drainage basins in the Siwalik Hills (Central Nepal). *Earth Surface Processes and Landforms* **24** (9), 799–808. DOI: 10.1002/(SICI)1096-9837(199908)24:9<799::AID-ESP12>3.0.CO;2-4.

Hutton, E., Barnhart, K., Hobley, D., Tucker, G., Nudurupati, S., Adams, J., Gasparini, N., Shobe, C., Strauch, R., Knuth, J., Mouchene, M., Lyons, N., Litwin, D., Glade, R., Cipolla, G., Manaster, A., Abby, L., Thyng, K., and Rengers, F. (2020). *Landlab*. DOI: 10.5281/zenodo.595872.

Hyun, S., Mishra, A., Follett, C. L., Jonsson, B., Kulk, G., Forget, G., Racault, M.-F., Jackson, T., Dutkiewicz, S., Müller, C. L., and Bien, J. (2022). Ocean mover's distance: Using optimal transport for analysing oceanographic data. *Proceedings of the Royal Society A: Mathematical, Physical and Engineering Sciences* **478** (2262). DOI: 10.1098/rspa.2021.0875.

Igea, J. and Tanentzap, A. J. (2021). Global topographic uplift has elevated speciation in mammals and birds over the last 3 million years. *Nature Ecology & Evolution* **5** (11), 1530–1535. DOI: 10.1038/s41559-021-01545-6.

Ijjasz-Vasquez, E. J., Bras, R. L., and Rodriguez-Iturbe, I. (1993). Hack's relation and optimal channel networks: The elongation of river basins as a consequence of energy minimization. *Geophysical Research Letters* **20** (15), 1583–1586. DOI: 10.1029/93GL01517.

Ijjász-Vásquez, E. J., Bras, R. L., Rodríguez-Iturbe, I., Rigon, R., and Rinaldo, A. (1993). Are river basins optimal channel networks? *Advances in Water Resources* **16** (1), 69–79. DOI: 10.1016/0309-1708(93)90030-J.

Ijjász-Vásquez, E. J., Bras, R. L., and Moglen, G. E. (1992). Sensitivity of a basin evolution model to the nature of runoff production and to initial conditions. *Water Resources Research* **28** (10), 2733–2741. DOI: 10.1029/92WR01561.

Irpino, A. and Romano, E. (2007). Optimal histogram representation of large data sets: Fisher vs piecewise linear approximation. *European Grid Conference*.

Istanbulluoglu, E. and Bras, R. L. (2005). Vegetation-modulated landscape evolution: Effects of vegetation on landscape processes, drainage density, and topography. *Journal of Geophysical Research: Earth Surface* **110** (F2). DOI: 10.1029/2004JF000249.

Jackson, D. D. (1979). The use of a priori data to resolve non-uniqueness in linear inversion. *Geophysical Journal International* **57** (1), 137–157. DOI: 10.1111/j.1365-246X.1979.tb03777.x.

Jones, G. A., Ferreira, A. M. G., Kulessa, B., Schimmel, M., Berbellini, A., and Morelli, A. (2021). Uppermost crustal structure regulates the flow of the Greenland Ice Sheet. *Nature Communications* **12** (1). DOI: 10.1038/s41467-021-27537-5.

Kantorovich, L. V. (1942). On the Translocation of Masses. *Dokl. Acad. Nauk. USSR* **37**, 7–8, 227–229.

Kaplan, S., McNabb, A., Trujillo, D., and Siemsen, J. K. (1969). The inverse problem of radioisotope diagnosis: A computational method for determining the location and size of tumors. *Mathematical Biosciences* **5** (1), 39–55. DOI: 10.1016/0025-5564(69)90034-0.

Karlstrom, K. E., Crow, R., Crossey, L. J., Coblentz, D., and Wijk, J. W. V. (2008). Model for tectonically driven incision of the younger than 6 Ma Grand Canyon. *Geology* **36** (11), 835–838. DOI: 10.1130/G25032A.1.

Karlstrom, K. E., Crow, R. S., Peters, L., McIntosh, W., Raucci, J., Crossey, L. J., Umhoefer, P., and Dunbar, N. (2007). 40Ar/39Ar and field studies of Quaternary basalts in Grand Canyon and model for carving Grand Canyon: Quantifying the interaction of river incision and normal faulting across the western edge of the Colorado Plateau. *GSA Bulletin* **119** (11-12), 1283–1312. DOI: 10.1130/0016-7606(2007)119[1283:AAFSOQ]2.0.CO;2.

Keilis-Borok, V. I. and Yanovskaja, T. B. (1967). Inverse Problems of Seismology (Structural Review). *Geophysical Journal International* **13** (1-3), 223–234. DOI: 10.1111/j.1365-246X.1967.tb02156.x.

Kent-Corson, M. L., Ritts, B. D., Zhuang, G., Bovet, P. M., Graham, S. A., and Page Chamberlain, C. (2009). Stable isotopic constraints on the tectonic, topographic, and climatic evolution of the northern margin of the Tibetan Plateau. *Earth and Planetary Science Letters* **282** (1), 158–166. DOI: 10.1016/j.epsl.2009.03.011.

King, L. C. (1953). Canons of Landscape Evolution. *GSA Bulletin* **64** (7), 721–752. DOI: 10.1130/0016-7606(1953)64[721:COLE]2.0.CO;2.

Kirby, E. and Whipple, K. (2001). Quantifying differential rock-uplift rates via stream profile analysis. *Geology* **29** (5), 415–418. DOI: 10.1130/0091-7613(2001)029<0415:QDRURV>2.0.CO;2.

Kirby, E., Whipple, K., and Harkins, N. (2008). Topography reveals seismic hazard. *Nature Geoscience* **1** (8), 485–487. DOI: 10.1038/ngeo265.

Kirby, E. and Whipple, K. X. (2012). Expression of active tectonics in erosional landscapes. *Journal of Structural Geology* **44**, 54–75. DOI: 10.1016/j.jsg.2012.07.009.

Kirchner, J. W. and Weil, A. (1998). No fractals in fossil extinction statistics. *Nature* **395** (6700), 337–338. DOI: 10.1038/26384.

Kitoh, A. (2004). Effects of Mountain Uplift on East Asian Summer Climate Investigated by a Coupled Atmosphere–Ocean GCM. *Journal of Climate* **17** (4), 783–802. DOI: 10.1175/1520-0442(2004)017<0783:EOMUOE>2.0.CO;2.

Kooi, H. and Beaumont, C. (1994). Escarpment evolution on high-elevation rifted margins: Insights derived from a surface processes model that combines diffusion, advection, and reaction. *Journal of Geophysical Research: Solid Earth* **99** (B6), 12191–12209. DOI: 10.1029/94JB00047.

Koons, P. O. (1989). The topographic evolution of collisional mountain belts; a numerical look at the Southern Alps, New Zealand. *American Journal of Science* **289** (9). DOI: 10.2475/ajs.289.9.1041.

Krieger, G., Zink, M., Bachmann, M., Bräutigam, B., Schulze, D., Martone, M., Rizzoli, P., Steinbrecher, U., Walter Antony, J., De Zan, F., Hajnsek, I., Papathanassiou, K., Kugler, F., Rodriguez Cassola, M., Younis, M., Baumgartner, S., López-Dekker, P., Prats, P., and Moreira, A. (2013). TanDEM-X: A radar interferometer with two formation-flying satellites. *Acta Astronautica* **89**, 83–98. DOI: 10.1016/j.actaastro.2013.03.008.

Kuhasubpasin, B., Moon, S., and Lithgow-Bertelloni, C. (2025). Unraveling the Connection Between Subsurface Stress and Geomorphic Features. *Geophysical Research Letters* **52** (19), e2025GL116798. DOI: 10.1029/2025GL116798.

Kwang, J. S. and Parker, G. (2019). Extreme Memory of Initial Conditions in Numerical Landscape Evolution Models. *Geophysical Research Letters* **46** (12), 6563–6573. DOI: 10.1029/2019GL083305.

Kwang, J. S., Langston, A. L., and Parker, G. (2021). The role of lateral erosion in the evolution of nondendritic drainage networks to dendricity and the persistence of dynamic networks. *Proceedings of the National Academy of Sciences* **118** (16), e2015770118. DOI: 10.1073/pnas.2015770118.

Lague, D. (2014). The stream power river incision model: evidence, theory and beyond. *Earth Surface Processes and Landforms* **39** (1), 38–61. DOI: 10.1002/esp.3462.

Lamb, M. P., Finnegan, N. J., Scheingross, J. S., and Sklar, L. S. (2015). New insights into the mechanics of fluvial bedrock erosion through flume experiments and theory. *Geomorphology* **244**, 33–55. DOI: 10.1016/J.GEOMORPH.2015.03.003.

Langbein, W. B. (1947). *Topographic Characteristics of Drainage Basins*. USGS Numbered Series 968-C. USGS.

Lehner, B. and Grill, G. (2013). Global river hydrography and network routing: baseline data and new approaches to study the world's large river systems. *Hydrological Processes* **27** (15), 2171–2186. DOI: 10.1002/hyp.9740.

Leonard, J. S. and Whipple, K. X. (2021). Influence of Spatial Rainfall Gradients on River Longitudinal Profiles and the Topographic Expression of Spatially and Temporally Variable Climates in Mountain Landscapes. *Journal of Geophysical Research: Earth Surface* **126** (12), e2021JF006183. DOI: 10.1029/2021JF006183.

Lifton, N. A. and Chase, C. G. (1992). Tectonic, climatic and lithologic influences on landscape fractal dimension and hypsometry: implications for landscape evolution in the San Gabriel Mountains, California. *Geomorphology*. Fractals in Geomorphology **5** (1), 77–114. DOI: 10.1016/0169-555X(92)90059-W.

Lipp, A. G. and Roberts, G. G. (2021). Scale-Dependent Flow Directions of Rivers and the Importance of Subplate Support. *Geophysical Research Letters* **48** (1), e2020GL091107. DOI: 10.1029/2020GL091107.

Lipp, A. G., Roberts, G. G., Whittaker, A. C., Gowing, C. J. B., and Fernandes, V. M. (2020). River Sediment Geochemistry as a Conservative Mixture of Source Regions: Observations and Predictions From the Cairngorms, UK. *Journal of Geophysical Research: Earth Surface* **125** (12), e2020JF005700. DOI: 10.1029/2020JF005700.

— (2021). Source Region Geochemistry From Unmixing Downstream Sedimentary Elemental Compositions. *Geochemistry, Geophysics, Geosystems* **22** (10), e2021GC009838. DOI: 10.1029/2021GC009838.

Lipp, A. G. and Vermeesch, P. (2023). Comparing detrital age spectra, and other geological distributions, using the Wasserstein distance. *Geochronology, in review*. DOI: 10.31223/X5TM02.

Litwin, D. G., Malatesta, L. C., and Sklar, L. S. (2025). Hillslope diffusion and channel steepness in landscape evolution models. *Earth Surface Dynamics* **13** (2), 277–293. DOI: 10.5194/esurf-13-277-2025.

Lodhia, B. H., Roberts, G. G., Fraser, A. J., Fishwick, S., Goes, S., and Jarvis, J. (2018). Continental margin subsidence from shallow mantle convection: Example from West Africa. *Earth and Planetary Science Letters* **481**, 350–361. DOI: 10.1016/j.epsl.2017.10.024.

Lyons, N. J., Val, P., Albert, J. S., Willenbring, J. K., and Gasparini, N. M. (2020). Topographic controls on divide migration, stream capture, and diversification in riverine life. *Earth Surface Dynamics* **8** (4), 893–912. DOI: 10.5194/esurf-8-893-2020.

Magyar, J. C. and Sambridge, M. (2023). Hydrological objective functions and ensemble averaging with the Wasserstein distance. *Hydrology and Earth System Sciences* **27** (5), 991–1010. DOI: 10.5194/hess-27-991-2023.

Malatesta, L. C., Finnegan, N. J., Huppert, K. L., and Carreño, E. I. (2022). The influence of rock uplift rate on the formation and preservation of individual marine terraces during multiple sea-level stands. *Geology* **50** (1), 101–105. DOI: 10.1130/G49245.1.

Mandelbrot, B. B. and Wheeler, J. A. (1983). The Fractal Geometry of Nature. *American Journal of Physics* **51** (3), 286–287. DOI: 10.1119/1.13295.

Marder, E. and Gallen, S. F. (2023). Climate control on the relationship between erosion rate and fluvial topography. *Geology* **51** (5), 424–427. DOI: 10.1130/G50832.1.

Marder, E., Gallen, S. F., and Pazzaglia, F. J. (2023). Late Cenozoic deformation in the U.S. southern Colorado Front Range revealed by river profile analysis and fluvial terraces. *GSA Bulletin* **136** (3-4), 1067–1085. DOI: 10.1130/B36440.1.

McKenzie, D. and Bowin, C. (1976). The relationship between bathymetry and gravity in the Atlantic Ocean. *Journal of Geophysical Research (1896-1977)* **81** (11), 1903–1915. DOI: 10.1029/JB081i011p01903.

McKenzie, D. and Fairhead, D. (1997). Estimates of the effective elastic thickness of the continental lithosphere from Bouguer and free air gravity anomalies. *Journal of Geophysical Research: Solid Earth* **102** (B12), 27523–27552. DOI: 10.1029/97JB02481.

Métivier, L., Brossier, R., Mérigot, Q., Oudet, E., and Virieux, J. (2016a). An optimal transport approach for seismic tomography: Application to 3D full waveform inversion. *Inverse Problems* **32** (11), 115008. DOI: 10.1088/0266-5611/32/11/115008.

— (2016b). Measuring the misfit between seismograms using an optimal transport distance: Application to full waveform inversion. *Geophysical Journal International* **205** (1), 345–377. DOI: 10.1093/gji/ggw014.

Mitchell, N. A. and Yanites, B. J. (2019). Spatially Variable Increase in Rock Uplift in the Northern U.S. Cordillera Recorded in the Distribution of River Knickpoints and Incision Depths. *Journal of Geophysical Research: Earth Surface* **124** (5), 1238–1260. DOI: 10.1029/2018JF004880.

Mitrovica, J., Austermann, J., Coulson, S., Creveling, J., Hoggard, M., Jarvis, G., and Richards, F. (2020). Dynamic Topography and Ice Age Paleoclimate. *Annual Review of Earth and Planetary Sciences* **48** (1), 585–621. DOI: 10.1146/annurev-earth-082517-010225.

Molnar, P. and England, P. (1990). Late Cenozoic uplift of mountain ranges and global climate change: chicken or egg? *Nature* **346** (6279), 29–34. DOI: 10.1038/346029a0.

Monge, G. (1781). Mémoire sur la théorie des déblais et des remplais. *De l'Imprimerie Royale*.

Montgomery, D. R., Balco, G., and Willett, S. D. (2001). Climate, tectonics, and the morphology of the Andes. *Geology* **29** (7), 579–582. DOI: 10.1130/0091-7613(2001)029<0579:CTATMO>2.0.CO;2.

Montgomery, D. R. and Dietrich, W. E. (1992). Channel Initiation and the Problem of Landscape Scale. *Science* **255** (5046), 826–830. DOI: 10.1126/science.255.5046.826.

Montgomery, D. R. and Foufoula-Georgiou, E. (1993). Channel network source representation using digital elevation models. *Water Resources Research* **29** (12), 3925–3934. DOI: 10.1029/93WR02463.

Moretti, I. and Turcotte, D. L. (1985). A model for erosion, sedimentation, and flexure with application to New Caledonia. *Journal of Geodynamics* **3** (1), 155–168. DOI: 10.1016/0264-3707(85)90026-2.

Morisawa, M. E. (1962). Quantitative Geomorphology of Some Watersheds in the Appalachian Plateau. *GSA Bulletin* **73** (9), 1025–1046. DOI: 10.1130/0016-7606(1962)73[1025:QGOSWI]2.0.CO;2.

Morris, M. J., Lipp, A. G., and Roberts, G. G. (2023). Towards inverse modeling of landscapes using the Wasserstein Distance. *Geophysical Research Letters* **50** (14), e2023GL103880. DOI: 10.1029/2023GL103880.

Morris, M. J., Roberts, G. G., Richards, F. D., Lipp, A. G., and Siddle, E. R. (2026). Seeing Through Geomorphic Complexity to Recover Tectonics From Topography: Inverting Landscapes for Uplift Histories Using the Wasserstein Distance. *Journal of Geophysical Research: Earth Surface* **131** (4), e2025JF008966. DOI: https://doi.org/10.1029/2025JF008966.

Morris, M. J. and Roberts, G. G. (2025). Impact of noise on landscapes and metrics generated with stream power models. *Earth Surface Dynamics* **13** (5), 1003–1038. DOI: 10.5194/esurf-13-1003-2025.

Moschetti, M. P., Ritzwoller, M. H., Lin, F.-C., and Yang, Y. (2010). Crustal shear wave velocity structure of the western United States inferred from ambient seismic noise and earthquake data. *Journal of Geophysical Research: Solid Earth* **115** (B10). DOI: 10.1029/2010JB007448.

Mudd, S. M., Clubb, F. J., Gailleton, B., and Hurst, M. D. (2018). How concave are river channels? *Earth Surface Dynamics* **6** (2), 505–523. DOI: 10.5194/esurf-6-505-2018.

Mudd, S. M., Attal, M., Milodowski, D. T., Grieve, S. W. D., and Valters, D. A. (2014). A statistical framework to quantify spatial variation in channel gradients using the integral method of channel profile analysis. *Journal of Geophysical Research: Earth Surface* **119** (2), 138–152. DOI: 10.1002/2013JF002981.

Mueller, J. E. (1972). Re-evaluation of the Relationship of Master Streams and Drainage Basins. *GSA Bulletin* **83** (11), 3471–3474. DOI: 10.1130/0016-7606(1972)83[3471:ROTROM]2.0.CO;2.

Nelder, J. A. and Mead, R. (1965). A Simplex Method for Function Minimization. *The Computer Journal* **7** (4), 308–313. DOI: 10.1093/comjnl/7.4.308.

Neuharth, D., Brune, S., Wrona, T., Glerum, A., Braun, J., and Yuan, X. (2022). Evolution of Rift Systems and Their Fault Networks in Response to Surface Processes. *Tectonics* **41** (3), e2021TC007166. DOI: 10.1029/2021TC007166.

Noe, S., Herwaarden, D.-P. van, Thrastarson, S., Pienkowska, M., Masouminia, N., Ma, J., Bunge, H.-P., Wehner, D., Rawlinson, N., Gao, Y., Tilmann, F., Rodgers, A., and Fichtner, A. (2024). The Collaborative Seismic Earth Model: Generation 2. *Journal of Geophysical Research: Solid Earth* **129** (12), e2024JB029656. DOI: 10.1029/2024JB029656.

Nooteboom, P. D., Delandmeter, P., Sebille, E. van, Bijl, P. K., Dijkstra, H. A., and Heydt, A. S. von der (2020). Resolution dependency of sinking Lagrangian particles in ocean general circulation models. *PLOS ONE* **15** (9), 1–16. DOI: 10.1371/journal.pone.0238650.

Nyblade, A. A. and Robinson, S. W. (1994). The African Superswell. *Geophysical Research Letters* **21** (9), 765–768. DOI: 10.1029/94GL00631.

O'Callaghan, J. F. and Mark, D. M. (1984). The extraction of drainage networks from digital elevation data. *Computer Vision, Graphics, and Image Processing* **28** (3), 323–344. DOI: 10.1016/S0734-189X(84)80011-0.

O'Hara, D., Goren, L., Campforts, B., Wees, R. M. J. van, Zarazúa-Carbajal, M. C., and Kervyn, M. (2025). Landscape evolution on conical landforms with applications to drainage development on volcanoes. *Geomorphology* **489**, 109998. DOI: 10.1016/j.geomorph.2025.109998.

O'Hara, D., Goren, L., Wees, R. M. J. van, Campforts, B., Grosse, P., Lahitte, P., Kereszturi, G., and Kervyn, M. (2024). Time-varying drainage basin development and erosion on volcanic edifices. *Earth Surface Dynamics* **12** (3), 709–726. DOI: 10.5194/esurf-12-709-2024.

O'Malley, C. P. B. (2020). "Quantitative analysis of river profiles and fluvial landscapes". PhD thesis. University of Cambridge. DOI: 10.17863/CAM.51663.

O'Malley, C. P. B., White, N. J., Stephenson, S. N., and Roberts, G. G. (2021). Large-Scale Tectonic Forcing of the African Landscape. *Journal of Geophysical Research: Earth Surface* **126** (12). DOI: 10.1029/2021JF006345.

Paul, J. D., Roberts, G. G., and White, N. (2014). The African landscape through space and time. *Tectonics* **33** (6), 898–935. DOI: 10.1002/2013TC003479.

Pavlis, N. K., Holmes, S. A., Kenyon, S. C., and Factor, J. K. (2012). The development and evaluation of the Earth Gravitational Model 2008 (EGM2008). *Journal of Geophysical Research: Solid Earth* **117** (B4). DOI: 10.1029/2011JB008916.

Paxman, G. J. G., Jamieson, S. S. R., Hochmuth, K., Gohl, K., Bentley, M. J., Leitchenkov, G., and Ferraccioli, F. (2019). Reconstructions of Antarctic topography since the Eocene–Oligocene boundary. *Palaeogeography, Palaeoclimatology, Palaeoecology* **535**, 109346. DOI: 10.1016/j.palaeo.2019.109346.

Pedersen, V. K., Braun, J., and Huismans, R. S. (2018). Eocene to mid-Pliocene landscape evolution in Scandinavia inferred from offshore sediment volumes and pre-glacial topography using inverse modelling. *Geomorphology* **303**, 467–485. DOI: 10.1016/j.geomorph.2017.11.025.

Pelletier, J. D. (1998). The power spectral density of atmospheric temperature from time scales of 10-2 to 106 yr. *Earth and Planetary Science Letters* **158** (3), 157–164. DOI: 10.1016/S0012-821X(98)00051-X.

— (2007). Numerical modeling of the Cenozoic geomorphic evolution of the southern Sierra Nevada, California. *Earth and Planetary Science Letters* **259** (1), 85–96. DOI: 10.1016/j.epsl.2007.04.030.

— (1999). Self-organization and scaling relationships of evolving river networks. *Journal of Geophysical Research: Solid Earth* **104** (B4), 7359–7375. DOI: 10.1029/1998JB900110.

Penck, W. (1953). Morphological Analysis of Land Forms. A Contribution to Physical Geology. *Geological Magazine* **90** (6), 441–442. DOI: 10.1017/S0016756800066048.

Perlin, K. (1985). An image synthesizer. *SIGGRAPH Comput. Graph.* **19** (3), 287–296. DOI: 10.1145/325165.325247.

— (2002). Improving noise. *Proceedings of the 29th Annual Conference on Computer Graphics and Interactive Techniques*. SIGGRAPH '02. San Antonio, Texas: Association for Computing Machinery, 681–682. DOI: 10.1145/566570.566636.

Perron, J. T. and Fagherazzi, S. (2012). The legacy of initial conditions in landscape evolution. *Earth Surface Processes and Landforms* **37** (1), 52–63. DOI: 10.1002/esp.2205.

Perron, J. T., Kirchner, J. W., and Dietrich, W. E. (2008). Spectral signatures of characteristic spatial scales and nonfractal structure in landscapes. *Journal of Geophysical Research: Earth Surface* **113** (F4), 2007JF000866. DOI: 10.1029/2007JF000866.

Perron, J. T. and Royden, L. (2013). An integral approach to bedrock river profile analysis. *Earth Surface Processes and Landforms* **38** (6), 570–576. DOI: 10.1002/esp.3302.

Petit, C., Jourdon, A., and Coltice, N. (2025). Reconstructing landscapes: an adjoint model of the stream power and diffusion erosion equation. *Earth Surface Dynamics* **13** (6), 1263–1280. DOI: 10.5194/esurf-13-1263-2025.

Peyré, G. and Cuturi, M. (2019). Computational Optimal Transport. *Foundations and Trends in Machine Learning* **11**, 355–607. DOI: 10.48550/ARXIV.1803.00567.

Powell, M. J. D. (1964). An efficient method for finding the minimum of a function of several variables without calculating derivatives. *The Computer Journal* **7** (2), 155–162. DOI: 10.1093/comjnl/7.2.155.

Prescott, A. B., Pelletier, J. D., Chataut, S., and Ananthanarayan, S. (2025). An evaluation of flow-routing algorithms for calculating contributing area on regular grids. *Earth Surface Dynamics* **13** (2), 239–256. DOI: 10.5194/esurf-13-239-2025.

Press, W. H., Teukolsky, S. A., Vetterling, W. T., and Flannery, B. P. (1992). *Numerical Recipes in Fortran: The Art of Scientific Computing*. Second. Cambridge, USA: Cambridge University Press.

Pritchard, D., Roberts, G. G., White, N. J., and Richardson, C. N. (2009). Uplift histories from river profiles. *Geophysical Research Letters* **36** (24). DOI: 10.1029/2009GL040928.

Quinn, P., Beven, K., Chevallier, P., and Planchon, O. (1991). The prediction of hillslope flow paths for distributed hydrological modelling using digital terrain models. *Hydrological Processes* **5** (1), 59–79. DOI: 10.1002/hyp.3360050106.

Rabin, J., Peyré, G., Delon, J., and Bernot, M. (2012). Wasserstein Barycenter and Its Application to Texture Mixing. *Scale Space and Variational Methods in Computer Vision*. Ed. by A. M. Bruckstein, B. M. ter Haar Romeny, A. M. Bronstein, and M. M. Bronstein. Berlin, Heidelberg: Springer, 435–446. DOI: 10.1007/978-3-642-24785-9_37.

Racano, S., Jara-Muñoz, J., Cosentino, D., and Melnick, D. (2020). Variable Quaternary Uplift Along the Southern Margin of the Central Anatolian Plateau Inferred From Modeling Marine Terrace Sequences. *Tectonics* **39** (12). DOI: 10.1029/2019TC005921.

Ransome, F. L. (1896). Great Valley of California; a Criticism of the Theory of Isostasy. *The Journal of Geology* **4** (6), 371–428.

Rapp, R. H. (1989). The decay of the spectrum of the gravitational potential and the topography for the Earth. *Geophysical Journal International* **99** (3), 449–455. DOI: 10.1111/j.1365-246X.1989.tb02031.x.

Reiners, P. W., Ehlers, T. A., and Zeitler, P. K. (2005). Past, Present, and Future of Thermochronology. *Reviews in Mineralogy and Geochemistry* **58** (1), 1–18. DOI: 10.2138/rmg.2005.58.1.

Rigon, R., Rinaldo, A., Rodriguez-Iturbe, I., Bras, R. L., and Ijjasz-Vasquez, E. (1993). Optimal channel networks: A framework for the study of river basin morphology. *Water Resources Research* **29** (6), 1635–1646. DOI: 10.1029/92WR02985.

Rigon, R., Rodriguez-Iturbe, I., Maritan, A., Giacometti, A., Tarboton, D. G., and Rinaldo, A. (1996). On Hack's Law. *Water Resources Research* **32** (11), 3367–3374. DOI: 10.1029/96WR02397.

Rinaldo, A., Rodriguez-Iturbe, I., Rigon, R., Bras, R. L., Ijjasz-Vasquez, E., and Marani, A. (1992). Minimum energy and fractal structures of drainage networks. *Water Resources Research* **28** (9), 2183–2195. DOI: 10.1029/92WR00801.

Robert, A. and Roy, A. G. (1990). On the fractal interpretation of the mainstream length-drainage area relationship. *Water Resources Research* **26** (5), 839–842. DOI: 10.1029/WR026i005p00839.

Roberts, G. G., White, N. J., Martin-Brandis, G. L., and Crosby, A. G. (2012a). An uplift history of the Colorado Plateau and its surroundings from inverse modeling of longitudinal river profiles. *Tectonics* **31** (4). DOI: 10.1029/2012TC003107.

Roberts, G. G. and Wani, O. (2024). A theory of stochastic fluvial landscape evolution. *Proceedings of the Royal Society A: Mathematical, Physical and Engineering Sciences* **480** (2283), 20230456. DOI: 10.1098/rspa.2023.0456.

Roberts, G. G., Paul, J. D., White, N., and Winterbourne, J. (2012b). Temporal and spatial evolution of dynamic support from river profiles: A framework for Madagascar. *Geochemistry, Geophysics, Geosystems* **13** (4). DOI: 10.1029/2012GC004040.

Roberts, G. G. and White, N. (2010). Estimating uplift rate histories from river profiles using African examples. *Journal of Geophysical Research: Solid Earth* **115** (B2). DOI: 10.1029/2009JB006692.

Roberts, G. G., White, N., and Lodhia, B. H. (2019). The Generation and Scaling of Longitudinal River Profiles. *Journal of Geophysical Research: Earth Surface* **124** (1), 137–153. DOI: 10.1029/2018JF004796.

Roberts, L. N. R. and Kirschbaum, M. A. (1995). Paleogeography and the Late Cretaceous of the Western Interior of middle North America; coal distribution and sediment accumulation. *Professional Paper*. DOI: 10.3133/pp1561.

Rodríguez-Iturbe, I., Rinaldo, A., Rigon, R., Bras, R. L., Marani, A., and Ijjász-Vásquez, E. (1992). Energy dissipation, runoff production, and the three-dimensional structure of river basins. *Water Resources Research* **28** (4), 1095–1103. DOI: 10.1029/91WR03034.

Rosenbloom, N. A. and Anderson, R. S. (1994). Hillslope and channel evolution in a marine terraced landscape, Santa Cruz, California. *Journal of Geophysical Research: Solid Earth* **99** (B7), 14013–14029. DOI: 10.1029/94JB00048.

Rowley, D. B., Forte, A. M., Moucha, R., Mitrovica, J. X., Simmons, N. A., and Grand, S. P. (2013). Dynamic Topography Change of the Eastern United States Since 3 Million Years Ago. *Science* **340** (6140), 1560–1563. DOI: 10.1126/science.1229180.

Royden, L. H., Clark, M. K., and Whipple, K. X. (2000). Evolution of river elevation profiles by bedrock incision: Analytical solutions for transient river profiles related to changing uplift and precipitation rates. *Eos Trans. AGU, 81(48), Fall Meet. Suppl. Abstract T62F-09.*

Rudge, J. F., Roberts, G. G., White, N. J., and Richardson, C. N. (2015). Uplift histories of Africa and Australia from linear inverse modeling of drainage inventories. *Journal of Geophysical Research: Earth Surface* **120** (5), 894–914. DOI: 10.1002/2014JF003297.

Ruetenik, G. A., Moucha, R., and Hoke, G. D. (2016). Landscape response to changes in dynamic topography. *Terra Nova* **28** (4), 289–296. DOI: 10.1111/ter.12220.

Ruiz Sánchez-Oro, M., Mudd, S. M., and Gailleton, B. (2024). Using Disorder Metrics to Distinguish Discharge-Driven From Drainage Area-Driven Incision and Quantify Deviations in Channel Steepness. *Journal of Geophysical Research: Earth Surface* **129** (9), e2023JF007553. DOI: 10.1029/2023JF007553.

Rust, D. J. and Summerfield, M. A. (1990). Isopach and borehole data as indicators of rifted margin evolution in southwestern Africa. *Marine and Petroleum Geology* **7** (3), 277–287. DOI: 10.1016/0264-8172(90)90005-2.

Sahagian, D. (1988). Epeirogenic motions of Africa as inferred from Cretaceous shoreline deposits. *Tectonics* **7** (1), 125–138. DOI: 10.1029/TC007i001p00125.

Salles, T. (2016). Badlands: A parallel basin and landscape dynamics model. *SoftwareX* **5**, 195–202. DOI: 10.1016/j.softx.2016.08.005.

— (2019). eSCAPE: Regional to Global Scale Landscape Evolution Model v2.0. *Geoscientific Model Development* **12** (9), 4165–4184. DOI: 10.5194/gmd-12-4165-2019.

Salles, T. and Hardiman, L. (2016). Badlands: An open-source, flexible and parallel framework to study landscape dynamics. *Computers & Geosciences* **91**, 77–89. DOI: 10.1016/j.cageo.2016.03.011.

Salles, T., Husson, L., Lorcery, M., and Hadler Boggiani, B. (2023). Landscape dynamics and the Phanerozoic diversification of the biosphere. *Nature* **624**, 115–121. DOI: 10.1038/s41586-023-06777-z.

Salles, T., Mallard, C., and Zahirovic, S. (2020). gospl: Global Scalable Paleo Landscape Evolution. *Journal of Open Source Software* **5** (56), 2804. DOI: 10.21105/joss.02804.

Sambridge, M. (1999a). Geophysical inversion with a neighbourhood algorithm—I. Searching a parameter space. *Geophysical Journal International* **138** (2), 479–494. DOI: 10.1046/j.1365-246X.1999.00876.x.

— (1999b). Geophysical inversion with a neighbourhood algorithm—II. Appraising the ensemble. *Geophysical Journal International* **138** (3), 727–746. DOI: 10.1046/j.1365-246x.1999.00900.x.

Sambridge, M., Jackson, A., and Valentine, A. P. (2022). Geophysical Inversion and Optimal Transport. *Geophysical Journal International* **231** (1), 172–198. DOI: 10.1093/gji/ggac151.

Sassolas-Serrayet, T., Cattin, R., and Ferry, M. (2018). The shape of watersheds. *Nature Communications* **9** (1), 3791. DOI: 10.1038/s41467-018-06210-4.

Scheingross, J. S., Limaye, A. B., McCoy, S. W., and Whittaker, A. C. (2020). The shaping of erosional landscapes by internal dynamics. *Nature Reviews Earth & Environment* **1** (12), 661–676. DOI: 10.1038/s43017-020-0096-0.

Scherler, D., DiBiase, R. A., Fisher, G. B., and Avouac, J.-P. (2017). Testing monsoonal controls on bedrock river incision in the Himalaya and Eastern Tibet with a stochastic-threshold stream power model. *Journal of Geophysical Research: Earth Surface* **122** (7), 1389–1429. DOI: 10.1002/2016JF004011.

Schoenbohm, L., Whipple, K., Burchfiel, B., and Chen, L. (2004). Geomorphic constraints on surface uplift, exhumation, and plateau growth in the Red River region, Yunnan Province, China. *GSA Bulletin* **116** (7-8), 895–909. DOI: 10.1130/B25364.1.

Seguy, V., Damodaran, B. B., Flamary, R., Courty, N., Rolet, A., and Blondel, M. (2018). *Large-Scale Optimal Transport and Mapping Estimation*. DOI: 10.48550/arXiv.1711.02283.

Seibert, J. and McGlynn, B. L. (2007). A new triangular multiple flow direction algorithm for computing upslope areas from gridded digital elevation models. *Water Resources Research* **43** (4). DOI: 10.1029/2006WR005128.

Seifert, N. A., Prozument, K., and Davis, M. J. (2022). Computational optimal transport for molecular spectra: The semi-discrete case. *The Journal of Chemical Physics* **156** (13), 134117. DOI: 10.1063/5.0087385.

Shelef, E. and Hilley, G. E. (2013). Impact of flow routing on catchment area calculations, slope estimates, and numerical simulations of landscape development. *Journal of Geophysical Research: Earth Surface* **118** (4), 2105–2123. DOI: 10.1002/jgrf.20127.

Shen, H., Lynch, B., Poulsen, C. J., and Yanites, B. J. (2021). A modeling framework (WRF-Landlab) for simulating orogen-scale climate-erosion coupling. *Computers & Geosciences* **146**, 104625. DOI: 10.1016/j.cageo.2020.104625.

Shobe, C. M., Tucker, G. E., and Barnhart, K. R. (2017). The SPACE 1.0 model: a Landlab component for 2-D calculation of sediment transport, bedrock erosion, and landscape evolution. *Geoscientific Model Development* **10** (12), 4577–4604. DOI: 10.5194/gmd-10-4577-2017.

Simms, A. R., Rouby, H., and Lambeck, K. (2016). Marine terraces and rates of vertical tectonic motion: The importance of glacio-isostatic adjustment along the Pacific coast of central North America. *GSA Bulletin* **128** (1-2), 81–93. DOI: 10.1130/B31299.1.

Singer, M. B., Grieve, S. W. D., Chen, S.-A., and Michaelides, K. (2024). Climatic Controls on the Length and Shape of the World's Drainage Basins. *Geophysical Research Letters* **51** (24), e2024GL111220. DOI: 10.1029/2024GL111220.

Singh, A., Lanzoni, S., Wilcock, P. R., and Foufoula-Georgiou, E. (2011). Multiscale statistical characterization of migrating bed forms in gravel and sand bed rivers. *Water Resources Research* **47** (12). DOI: 10.1029/2010WR010122.

Sklar, L. and Dietrich, W. E. (1998). River Longitudinal Profiles and Bedrock Incision Models: Stream Power and the Influence of Sediment Supply. In: American Geophysical Union (AGU), 237–260. DOI: 10.1029/GM107p0237.

Sklar, L. S. and Dietrich, W. E. (2001). Sediment and rock strength controls on river incision into bedrock. *Geology* **29** (12), 1087–1090. DOI: 10.1130/0091-7613(2001)029<1087:SARSCO>2.0.CO;2.

Smith, A. G., Fox, M., Schwanghart, W., and Carter, A. (2022). Comparing methods for calculating channel steepness index. *Earth-Science Reviews* **227**, 103970. DOI: /10.1016/j.earscirev.2022.103970.

Smith, T. R., Merchant, G. E., and Birnir, B. (1997). Towards an elementary theory of drainage basin evolution: II. A computational evaluation. *Computers & Geosciences* **23** (8), 823–849. DOI: 10.1016/S0098-3004(97)00067-8.

Snyder, N. P., Whipple, K. X., Tucker, G. E., and Merritts, D. J. (2000). Landscape response to tectonic forcing: Digital elevation model analysis of stream profiles in the Mendocino triple junction region,

northern California. *GSA Bulletin* **112** (8), 1250–1263. DOI: 10.1130/0016-7606(2000)112<1250:LRTTFD>2.0.CO;2.

Solomon, J., Goes, F. de, Peyré, G., Cuturi, M., Butscher, A., Nguyen, A., Du, T., and Guibas, L. (2015). Convolutional Wasserstein Distances: Efficient Optimal Transportation on Geometric Domains. *ACM Trans. Graph.* **34** (4). DOI: 10.1145/2766963.

Stanley, J. R., Braun, J., Baby, G., Guillocheau, F., Robin, C., Flowers, R. M., Brown, R., Wildman, M., and Beucher, R. (2021). Constraining Plateau Uplift in Southern Africa by Combining Thermochronology, Sediment Flux, Topography, and Landscape Evolution Modeling. *Journal of Geophysical Research: Solid Earth* **126** (7), e2020JB021243. DOI: 10.1029/2020JB021243.

Stephenson, J., Tkalčić, H., and Sambridge, M. (2021a). Evidence for the Innermost Inner Core: Robust Parameter Search for Radially Varying Anisotropy Using the Neighborhood Algorithm. *Journal of Geophysical Research: Solid Earth* **126** (1), e2020JB020545. DOI: 10.1029/2020JB020545.

Stephenson, R. and Lambeck, K. (1985). Erosion-isostatic rebound models for uplift: an application to south-eastern Australia. *Geophysical Journal International* **82** (1), 31–55. DOI: 10.1111/j.1365-246X.1985.tb05127.x.

Stephenson, S. N., White, N. J., Carter, A., Seward, D., Ball, P. W., and Klöcking, M. (2021b). Cenozoic Dynamic Topography of Madagascar. *Geochemistry, Geophysics, Geosystems* **22** (6). DOI: 10.1029/2020GC009624.

Stephenson, S. N., Hoggard, M. J., Holdt, M. C., and White, N. (2024). Continental Residual Topography Extracted From Global Analysis of Crustal Structure. *Journal of Geophysical Research: Solid Earth* **129** (4), e2023JB026735. DOI: 10.1029/2023JB026735.

Stephenson, S. N., White, N. J., Li, T., and Robinson, L. F. (2019). Disentangling interglacial sea level and global dynamic topography: Analysis of Madagascar. *Earth and Planetary Science Letters* **519**, 61–69. DOI: 10.1016/J.EPSL.2019.04.029.

Stock, J. D. and Montgomery, D. R. (1999). Geologic constraints on bedrock river incision using the stream power law. *Journal of Geophysical Research: Solid Earth* **104** (B3), 4983–4993. DOI: 10.1029/98JB02139.

Stockli, D. F., Surpless, B. E., Dumitru, T. A., and Farley, K. A. (2002). Thermochronological constraints on the timing and magnitude of Miocene and Pliocene extension in the central Wassuk Range, western Nevada. *Tectonics* **21** (4), 10–1–10–19. DOI: 10.1029/2001TC001295.

Stokes, M. F. and Perron, J. T. (2020). Modeling the Evolution of Aquatic Organisms in Dynamic River Basins. *Journal of Geophysical Research: Earth Surface* **125** (9). DOI: 10.1029/2020JF005652.

Strahler, A. (1957). Quantitative analysis of watershed geomorphology. *Eos, Transactions American Geophysical Union* **38** (6), 913–920. DOI: 10.1029/TR038i006p00913.

Strahler, A. N. (1952). Hypsometric (Area-Altitude) Analysis of Erosional Topography. *GSA Bulletin* **63** (11), 1117–1142. DOI: 10.1130/0016-7606(1952)63[1117:HAAOET]2.0.CO;2.

Stucky de Quay, G., Roberts, G. G., Rood, D. H., and Fernandes, V. M. (2019). Holocene uplift and rapid fluvial erosion of Iceland: A record of post-glacial landscape evolution. *Earth and Planetary Science Letters* **505**, 118–130. DOI: 10.1016/j.epsl.2018.10.026.

Sturgeon, W., Ferreira, A. M. G., Schardong, L., and Marignier, A. (2023). Crustal Structure of the Western U.S. From Rayleigh and Love Wave Amplification Data. *Journal of Geophysical Research: Solid Earth* **128** (8), e2022JB026148. DOI: 10.1029/2022JB026148.

Tanner, W. F. (1971). The River Profile. *The Journal of Geology*. DOI: 10.1086/627653.

Tarboton, D., Bras, R., and Rodriguez-Iturbe, I. (1989). Scale and elevation in river networks. *Water Resources Research* **25**, 2037–2051. DOI: 10.1029/WR025i009p02037.

Tarboton, D. G. (1997). A new method for the determination of flow directions and upslope areas in grid digital elevation models. *Water Resources Research* **33** (2), 309–319. DOI: 10.1029/96WR03137.

Theodoratos, N., Seybold, H., and Kirchner, J. W. (2018). Scaling and similarity of a stream-power incision and linear diffusion landscape evolution model. *Earth Surface Dynamics* **6** (3), 779–808. DOI: 10.5194/esurf-6-779-2018.

Thompson, S. B., Creveling, J. R., and Mitrovica, J. X. (2025). The sensitivity of tectonic uplift corrections to the penultimate deglacial ice volume and configuration. *Quaternary Science Reviews* **353**, 109210. DOI: 10.1016/j.quascirev.2025.109210.

Thompson Jobe, J. A. and Reitman, N. G. (2025). Timescales of Surface Faulting Preservation in Low-Strain Intraplate Regions From Landscape Evolution Modeling and the Geomorphic and Historical Record. *Journal of Geophysical Research: Solid Earth* **130** (6), e2024JB029966. DOI: 10.1029/2024JB029966.

Tozer, B., Sandwell, D. T., Smith, W. H. F., Olson, C., Beale, J. R., and Wessel, P. (2019). Global Bathymetry and Topography at 15 Arc Sec: SRTM15+. *Earth and Space Science* **6** (10), 1847–1864. DOI: 10.1029/2019EA000658.

Tucker, G., Gasparini, N., Bras, R., and Lancaster, S. (2001). The Channel-Hillslope Integrated Landscape Development Model (CHILD). In: *Landscape Erosion and Evolution Modeling*. Ed. by W. W. Harmon and R. S. Doe. Springer US, 349–388. DOI: 10.1007/978-1-4615-0575-4_12.

Tucker, G. E. and Hancock, G. R. (2010). Modelling landscape evolution. *Earth Surface Processes and Landforms* **35** (1), 28–50. DOI: 10.1002/esp.1952.

Tucker, G. E. and Slingerland, R. L. (1994). Erosional dynamics, flexural isostasy, and long-lived escarpments: A numerical modeling study. *Journal of Geophysical Research: Solid Earth* **99** (B6), 12229–12243. DOI: 10.1029/94JB00320.

Turcotte, D. and Schubert, G. (2014). *Geodynamics*. 3rd ed. Cambridge University Press.

Turcotte, D. L. (1997). *Fractals and chaos in geology and geophysics*. 2nd ed. Cambridge: Cambridge University Press.

— (2007). Self-organized complexity in geomorphology: Observations and models. *Geomorphology*. 38th Binghamton Geomorphology Symposium: Complexity in Geomorphology **91** (3), 302–310. DOI: 10.1016/j.geomorph.2007.04.016.

Valentine, A. P. and Davies, D. R. (2020). Global Models From Sparse Data: A Robust Estimate of Earth's Residual Topography Spectrum. *Geochemistry, Geophysics, Geosystems* **21** (8), e2020GC009240. DOI: 10.1029/2020GC009240.

van der Beek, P. and Braun, J. (1999). Controls on post-mid-Cretaceous landscape evolution in the southeastern highlands of Australia: Insights from numerical surface process models. *Journal of Geophysical Research: Solid Earth* **104** (B3), 4945–4966. DOI: 10.1029/1998JB900060.

van der Meij, W. M. (2025). Translating deposition ages into erosion rates: inverse landscape evolution modelling and uncertainty analysis. *Earth Surface Dynamics* **13** (5), 845–860. DOI: 10.5194/esurf-13-845-2025.

Villani, C. (2003). *Topics in Optimal Transportation*. Graduate studies in mathematics. American Mathematical Society.

Vissio, G., Lembo, V., Lucarini, V., and Ghil, M. (2020). Evaluating the Performance of Climate Models Based on Wasserstein Distance. *Geophysical Research Letters* **47** (21). DOI: 10.1029/2020GL089385.

Wang, Y., Goren, L., Zheng, D., and Zhang, H. (2022). Forward and inverse analytic models relating river long profile to tectonic uplift history, assuming a nonlinear slope–erosion dependency. *Earth Surface Dynamics* **10** (4), 833–849. DOI: 10.5194/esurf-10-833-2022.

Wang, Y., Zhang, H., Zheng, D., Yu, J., Pang, J., and Ma, Y. (2017). Coupling slope–area analysis, integral approach and statistic tests to steady-state bedrock river profile analysis. *Earth Surface Dynamics* **5** (1), 145–160. DOI: 10.5194/esurf-5-145-2017.

Wang, Y., Zheng, D., and Zhang, H. (2024). Understanding tectonics from fluvial topography by using the stochastic-threshold incision model: Theory and application to the Dadu River basin, eastern

Tibetan Plateau. *Earth Surface Processes and Landforms* **49** (5), 1653–1666. DOI: 10.1002/esp.5793.

Wapenhans, I., Fernandes, V. M., O'Malley, C., White, N., and Roberts, G. G. (2021). Scale-Dependent Contributors to River Profile Geometry. *Journal of Geophysical Research: Earth Surface* **126** (6). DOI: 10.1029/2020JF005879.

Watts, A. B. and Moore, J. D. P. (2017). Flexural Isostasy: Constraints From Gravity and Topography Power Spectra. *Journal of Geophysical Research: Solid Earth* **122** (10), 8417–8430. DOI: 10.1002/2017JB014571.

Wellman, P. and McDougall, I. (1974). Cainozoic igneous activity in eastern Australia. *Tectonophysics* **23** (1-2), 49–65. DOI: 10.1016/0040-1951(74)90110-3.

Whipple, K. X. and Tucker, G. E. (1999). Dynamics of the stream-power river incision model: Implications for height limits of mountain ranges, landscape response timescales, and research needs. *Journal of Geophysical Research: Solid Earth* **104** (B8), 17661–17674. DOI: 10.1029/1999JB900120.

Willemin, J. H. (2000). Hack's Law: Sinuosity, convexity, elongation. *Water Resources Research* **36** (11), 3365–3374. DOI: 10.1029/2000WR900229.

Willett, S. D. and Brandon, M. T. (2002). On steady states in mountain belts. *Geology* **30** (2), 175–178. DOI: 10.1130/0091-7613(2002)030<0175:OSSIMB>2.0.CO;2.

Willett, S. D., McCoy, S. W., Perron, J. T., Goren, L., and Chen, C.-Y. (2014). Dynamic Reorganization of River Basins. *Science* **343** (6175). DOI: 10.1126/science.1248765.

Willgoose, G. (2018). *Principles of Soilscape and Landscape Evolution*. 1st ed. Cambridge University Press. DOI: 10.1017/9781139029339.

Willgoose, G., Bras, R., and Rodriguez-Iturbe, I. (1991a). A coupled channel network growth and hillslope evolution model: 1. Theory. *Water Resources Research* **27**. DOI: 10.1029/91WR00935.

Willgoose, G., Bras, R. L., and Rodriguez-Iturbe, I. (1991b). Results from a new model of river basin evolution. *Earth Surface Processes and Landforms* **16** (3), 237–254. DOI: 10.1002/esp.3290160305.

Willgoose, G. and Hancock, G. (1998). Revisiting the hypsometric curve as an indicator of form and process in transport-limited catchment. *Earth Surface Processes and Landforms* **23** (7), 611–623. DOI: 10.1002/(SICI)1096-9837(199807)23:7<611::AID-ESP872>3.0.CO;2-Y.

Willgoose, G. R., Hancock, G. R., and Kuczera, G. (2003). A Framework for the Quantitative Testing of Landform Evolution Models. In: *Prediction in Geomorphology*. American Geophysical Union (AGU), 195–216. DOI: 10.1029/135GM14.

Worthington, M. H., Cleary, J. R., and Anderssen, R. S. (1974). Upper and Lower Mantle Shear Velocity Modelling by Monte Carlo Inversion. *Geophysical Journal of the Royal Astronomical Society* **36** (1), 91–103. DOI: 10.1111/j.1365-246X.1974.tb03627.x.

Yacobucci, M. M. (2005). Multifractal and white noise evolutionary dynamics in Jurassic–Cretaceous Ammonoidea. *Geology* **33** (2), 97–100. DOI: 10.1130/G20906.1.

Yi, R. S., Arredondo, Á., Stansifer, E., Seybold, H., and Rothman, D. H. (2018). Shapes of river networks. *Proceedings of the Royal Society A: Mathematical, Physical and Engineering Sciences* **474** (2215), 20180081. DOI: 10.1098/rspa.2018.0081.

Young, R. and McDougall, I. (1993). Long-Term Landscape Evolution: Early Miocene and Modern Rivers in Southern New South Wales, Australia. *The Journal of Geology* **101** (1), 35–49. DOI: 10.1086/648195.

Yuan, X. P., Braun, J., Guerit, L., Rouby, D., and Cordonnier, G. (2019a). A New Efficient Method to Solve the Stream Power Law Model Taking Into Account Sediment Deposition. *Journal of Geophysical Research: Earth Surface* **124** (6), 1346–1365. DOI: 10.1029/2018JF004867.

Yuan, X., Braun, J., Guerit, L., Simon, B., Bovy, B., Rouby, D., Robin, C., and Jiao, R. (2019b). Linking continental erosion to marine sediment transport and deposition: A new implicit and O(N) method for inverse analysis. *Earth and Planetary Science Letters* **524**, 115728. DOI: 10.1016/j.epsl.2019.115728.

Yuan, X., Li, Y., Brune, S., Li, K., Pons, M., and Wolf, S. G. (2024). Coordination between deformation, precipitation, and erosion during orogenic growth. *Nature Communications* **15** (1), 10362. DOI: 10.1038/s41467-024-54690-4.

Yudistira, T., Paulssen, H., and Trampert, J. (2017). The crustal structure beneath The Netherlands derived from ambient seismic noise. *Tectonophysics* **721**, 361–371. DOI: 10.1016/j.tecto.2017.09.025.

Zaprowski, B. J., Pazzaglia, F. J., and Evenson, E. B. (2005). Climatic influences on profile concavity and river incision. *Journal of Geophysical Research: Earth Surface* **110** (F3). DOI: 10.1029/2004JF000138.

Zhou, Z., Whittaker, A. C., Bell, R. E., and Hampson, G. J. (2024). Unravelling tectonic and lithological effects on transient landscapes in the Gulf of Corinth, Greece. *Basin Research* **36** (5), e12901. DOI: 10.1111/bre.12901.

Ziegler, A. M., Rowley, D. B., Lottes, A. L., Sahagian, D. L., Hulver, M. L., and Gierlowski, T. C. (1985). Paleogeographic Interpretation: With an Example From the Mid-Cretaceous. *Annual Review*

of Earth and Planetary Sciences **13** (Volume 13, 1985), 385–428. DOI: 10.1146/annurev.ea.13.050185.002125.

Zink, M., Bachmann, M., Brautigam, B., Fritz, T., Hajnsek, I., Moreira, A., Wessel, B., and Krieger, G. (2014). TanDEM-X: The New Global DEM Takes Shape. *IEEE Geoscience and Remote Sensing Magazine* **2** (2), 8–23. DOI: 10.1109/MGRS.2014.2318895.

Zwaan, F., Brune, S., Glerum, A. C., Vasey, D. A., Naliboff, J. B., Manatschal, G., and Gaucher, E. C. (2025). Rift-inversion orogens are potential hot spots for natural H2 generation. *Science Advances* **11** (8), eadr3418. DOI: 10.1126/sciadv.adr3418.